COPYRIGHT STATEMENT

The copy of this thesis has been supplied on condition that anyone who consults it is understood to recognise that its copyright rests with the author and that no quotation from the thesis and no information derived from it may be published without the author's consent.

MATERIAL CHARACTERISATION OF LASER FORMED DUAL PHASE STEEL COMPONENTS

By

ANNELIZE ELS-BOTES

A thesis submitted in fulfilment of the
full requirements for the degree of

DOCTOR TECHNOLOGIAE: ENGINEERING: MECHANICAL

in the Faculty of Engineering at the
Nelson Mandela Metropolitan University

January 2005

Promoters

Dr PJ McGrath
Prof DG Hattingh

ABSTRACT

Author: **ANNELIZE ELS-BOTES**

Title: **MATERIAL CHARACTERISATION OF LASER FORMED DUAL PHASE STEEL COMPONENTS**

The nature and scope of this thesis can be divided into four categories:

- FORMING PARAMETERS
- Identification of various laser forming parameters in order to produce specimens of similar dimension (radius of curvature).
- TEMPERATURE AND MICROSTRUCTURE
- To study the effect of maximum temperature reached during the forming operation on the microstructure of the various specimens.
- FATIGUE LIFE
- Compare the fatigue life of the specimens produced by various laser parameters to that of the original material, and also the fatigue life of mechanical formed specimens.
- RESIDUAL STRESS PROFILE
  Determine if the laser forming process induces detrimental residual stress magnitudes in the specimens.

The main objective of this thesis was to gain an understanding of the way in which laser forming affects the fatigue performance and residual stress magnitude / distribution of dual phase steel. Although lasers have been used successfully in various manufacturing processes (welding, cutting, marking, etc.), little information is available on the influence of laser forming on many automotive alloys such as dual phase steel. The first part of the work involved a literature review of the process and factors affecting the laser forming process.

It became clear from the literature overview that laser forming of sheet material thicker than 1mm is complex in nature. The variables that can influence the process are complicated and their interaction with each other is not easily controlled.

The main parameters that were thus controlled in this study are as follows:

- Laser power (P)
- Laser head travel speed (v)
- Laser beam size (mm)

The chapters that follow the literature review, deals with the laser forming process of dual phase steel and the production of fatigue specimens using various laser parameters. It was found that the following laser parameters resulted in specimens with approximately the same radius of curvature:

Laser power KW	Beam diameter mm	Interval spacing	% Overlap	Scanning velocity m/min	Line Energy J/m
5	20	10	50	2,5	2000
3,1	14	10,5	25	2	1550
1,5	7,5	7,5	0	1,2	1250

From the results obtained from fatigue testing specimens produced with the above settings, it is clear that the laser forming process has the potential to be employed as a production stage in the manufacture of wheel centre discs while maintaining adequate fatigue strength. Large beam diameters which cause heat penetration through the thickness of the specimen and hence microstructure breakdown should be avoided, since it was shown that these specimens exhibited impaired mechanical properties than those produced with a smaller laser beam diameter.

The microstructural changes observed during the forming process needs to be considered since the mechanical properties of the material changes with a change in microstructure. A dramatic change in microstructure was observed; therefore it is of crucial importance that microstructural evaluation plays an important part in deciding optimum laser parameters for the forming process of ferrous alloys.

During residual stress analysis, trends were observed between measurements taken at the same location of the samples; regardless whether measurements

were taken on the laser irradiated side or the reverse side of the specimen. The
only difference was the magnitude of the relieved residual stress. In most
cases the obtained relieved residual stress was much smaller in magnitude than
that of the original plate (in the bulk of the material). The surface indicated a
slight tensile residual stress for most samples evaluated. A good correlation in
distribution profile was obtained between microhardness and relieved residual
stress distribution at the 'middle of sample' location. This indicates that an
increase in hardness indicates an increase in residual stress magnitude for the
laser formed specimens.

In conclusion, this research has proved that it is possible to deform metal plate
of a 3,5mm thickness with a CO_2 laser system. The research also established
the effect of process parameters on the final product's shape/bend angle and
characterised the effect of the laser forming process on the material's
mechanical properties and structural integrity.

CONTENTS

CHAPTER 3   EXPERIMENTAL SETUP

CHAPTER 4   RESULTS AND DISCUSSION

LIST OF FIGURES

CHAPTER 3   **EXPERIMENTAL SETUP**

LIST OF TABLES

GLOSSARY OF TERMS

A

Age hardening – hardening by ageing, usually after rapid cooling or cold working.

Alloying element – an element added to and remaining in a metal that changes structure and properties.

Alloy steel – Steel containing significant quantities of alloying elements (other than Carbon and the commonly accepted amounts of manganese, silicon, sulphur and phosphorus) added to effect changes in the mechanical or physical properties.

Anisotropy – is a term used for describing the mechanical properties of sheet metal plate depending on the direction relative to a particular axis or plane.

Annealing – heating to and holding at a suitable temperature followed by cooling at a suitable rate.

Apex – refers to the top-most position of a bend.

As manufactured – pertains to sheet metal plate in its as manufactured form.

Automotive wheel – consists of two components, both manufactured by a process known as forming. The inner component is referred to as the centre disc while the outer is referred to as the wheel rim. These components are then welded together to form an automotive wheel.

Axis of rotation – refers to two independent pivotal points, symmetrically positioned about which rotation takes place.

B

Bending stress – if a beam is subjected to a bending moment the fibres in the upper part are extended and these in the lower part compressed. Tensile and compressive stresses are thereby induced which vary from zero at the neutral axis of the beam to a maximum at the outer fibres. Theses stresses are called bending stresses.

Bake hardening – refers to the hardening of the surface of a component subjected to a paint curing temperature.

C

Carbide – a compound of carbon with one or more metallic elements.

Carbo-nitrides – is the precipitation of diffused carbon and nitrogen which usually occurs at the surface of a component when subjected to elevated temperatures.

Centre disc – this is the centre section of an automotive wheel which is welded to the wheel rim.

Coherent light – is light in which all the waves are in phase.

Cycle count – is the number of complete cycles a fatigue specimen undergoes prior to failure.

D

Dislocation – a linear imperfection in a crystalline array of atoms.

Dual phase steel – High Strength Low Alloy (HSLA) steel having a matrix comprising of martensite and ferrite.

E

Electron beam – a stream of electrons in an electron-optical system.

Electron microscopy – the study of materials by means of an electron microscope.

Etchant – a chemical solution used to etch a metal to reveal structural details.

Etching – subjecting the surface of a metal to preferential chemical or electrolytic attack to reveal structural details for metallographic examination.

F

Fatigue – a phenomenon which results in the sudden fracture of a component after a period of cyclic loading in the elastic regime.

Fatigue life – is the number of load cycles a component can withstand prior to failure.

Fatigue limit – refers to the fatigue testing of non-ferrous materials which do not show finite life conditions.

Fatigue performance – see fatigue life

Fatigue strength – The maximum stress that can be sustained for a specified number of cycles without failure.

Ferrite – generally a solid solution of one or more elements in body-centred cuvic iron. In plain carbon steels, the interstitial solid solution of carbon in α-iron.

Final polishing – a polishing process in which the primary objective is to produce a final surface suitable for microscopic examinations.

Flow curve – a diagrammatic representation of data with two measurable parameters, each indicated on mutual perpendicular axis.

Forming – refers to a manufacturing process whereby sheet metal plate is shaped by means of stamping press.

Fracture – is the loss of structural integrity through crack propagation.

Fracture stress – this is the stress magnitude at fracture of a component.

Full stress relief – is the maximum relieved stress obtained, usually associated with residual stress assessment conditions.

G

Grain – an individual crystal in a polycrystalline metal or alloy, including twinned regions or sub-grains if present.

Grain boundary – an interface separating two grains at which the orientation of the lattice changes from that of one grain to that of the other. When the orientation change is very small the boundary is sometimes referred to as a sub-boundary structure.

Grain growth – an increase in the grain size of a metal usually as a result of heating at an elevated temperature.

Grain size – a measure of the areas or volumes of grains in a polycrystalline metal or alloy, usually expressed as an average when the individual sizes are fairly uniform. Grain size is reported in terms of number of grains per unit area or volume, average diameter, or as a number derived from area measurements.

Granular fracture – an irregular surface produced when metal fractures. This fracture is characterized by a rough, grain like appearance. It can be sub-classified into trans-granular and intergranular forms.

Grinding – removing material from a workpiece using a grinding wheel or abrasive belt.

H

Hardness – is an term used for describing the resistance of a material to plastic deformation under the action of an indenter.

Hardenability – the relative ability of a ferrous alloy to harden under cold working conditions.

Hardening – increasing hardness by suitable treatment, usually cold working.

Homogeneous – a chemical composition and physical state of any physical small portion are the same as those of any other portion

Hot working – deformation under conditions that result in re-crystallisation.

Hour-glass type specimen – usually refers to a fatigue type specimen having a waisted hour-glass shape.

I

Impurities – undesirable elements or compounds in a material.

Inclusion count – determination of the number, kind, size and distribution of non-metallic inclusions.

Inclusions – particles of foreign material in a metallic matrix.

Isothermal transformation – Change in phase which occurs in a metal or alloy at constant temperature after cooling or heating through the equilibrium temperature.

Isotropic – having similar mechanical and micro-structural properties in all directions.

Intergranular – within or across crystals or grains. Same as transcrystalline and transgranular.

L

LASER – Light Amplification by Stimulated Emission of Radiation.

Linear drilling evaluation method – a drilling method whose incremental feed rate is of equal amount.

Line heating distribution – This refers to the heating pattern (line spacing and sequence) that will be followed over a specified length of material.

Lamination – an abnormal structure resulting in a separation or weakness aligned generally parallel to the worked surface of the metal.

Longitudinal axis – that direction parallel to the direction of maximum elongation in a worked material.

Longitudinal direction – see longitudinal axis.

Longitudinal plane – is a plane that is normal to the longitudinal axis

M

Macrograph – a graphic reproduction of a prepared surface of a specimen at a magnification not exceeding 25x.

Macrostructure – the structure of metals as revealed by macroscopic examination of the etched surface of a polished specimen.

Magnification – a ratio of the length of a line in the image plane to the length of a line on the imaged material.

Martensite – A metastable phase in steel formed by a transformation of austeninte. It is an interstitial supersaturated solid solution of carbon in iron having a body-centered tetragonal lattice. Its microstructure is characterized by an acicular pattern.

Martensitic – a plate-like constituent having an appearance and a mechanism of formation similar to that of martensite.

Maximum shear strain – a stress of this nature is said to exist on a section of a body if on opposite faces of the section equal and opposite parallel forces exist.

Maximum bending strain – a cylindrical shaft is said to be subject to pure torsion when the torsion is caused by a couple, applied to that the axis of the couple coincides with the axis of the shaft. The state of stress, at any oint in the cross-section of the rod, is one of pure shear, and the strain is such that one cross-section of the shaft moves relative to another.

Mean stress – refers to a pre-strained loading condition.

Mechanical properties – The properties of a material that reveal its elastic and inelastic behaviour where force is applied thereby indicating its suitability for mechanical applications.

Microcrack – a crack of microscopic proportions.

Micrograph – a graphic reproduction of the prepared surface of a specimen at a magnification greater than 25x.

Microstructure – the structure of a prepared surface of a metal as revealed by a microscope at a magnification exceeding 25x.

N

Necking – is a thinning of a material which has been subjected the strain levels beyond its tensile strength.

Non-uniform plasticity – refers to a steel component subjected to strain levels beyond the tensile strength for that particular steel material, usually associated with necking.

Non-uniform stress field – is where the stress along any particular plane are of unequal magnitude.

O

Orientation (crystal) – arrangements in space of the axes of the lattice of a crystal with respect to a chosen reference or co-ordinate system.

Orientated plane – see angle of inclination.

Ovality – slightly out-of-round shape having a major and minor axis.

P

Pearlite – a microconstituent of steel and cast iron comprising an intimate mechanical mixture of ferrite and cementite (iron carbide). It is produced at the eutectoid by the simultaneous formation of ferrite and cementite from austenite, and normally consists of alternate plates or lamellae of these two constituents.

Phase – a physically homogeneous and distinct portion of a material system.

Pitting – localized corrosion of a metal surface that is confined to a small area and takes the form of small cavities.

Plastic deformation – deformation that remains or will remain permanent after release of the stress that caused it.

Plasticity – the capacity of a metal to deform non-elastically without rupturing.

Polished surface – a surface that reflects a large proportion of the incident light in a specular manner.

Polynomial drilling evaluation method – a drilling method whose incremental feed rate increases consecutively.

Principal strains – the maximum and minimum direct strains in a material, subjected to complex stress are called Principal Strains. These strains act in the directions of the principal stresses.

Principal stresses – at any point within a stressed material it will be found that there exist three mutually perpendicular planes on each of which the resultant stress is a normal stress (i.e. no shear stresses occur on these planes). These mutually perpendicular planes are called principal planes, and the resultant normal stresses are called Principal Stresses.

Pure bending conditions – the bending of a material under unconstrained conditions.

Q

Quantitative – identification of relative amounts making up a sample.

Quench hardening – in ferrous alloys, hardening by austenitising, then cooling at a rate to that a substantial amount of austenite transforms to martensite.

Quenching crack – crack formed as a result of thermal stresses produced by rapid cooling from a high temperature.

R

Ra – Arithmetic mean deviation of the profile

Recrystallisation- stage in the annealing process of cold worked metals above $0,4-0,5T_m$, in which deformed crystals are replaced by a new generation of crystals, which begin to grow at certain points in the deformed metal and eventually absorb the deformed crystals. The new crystals have more equal axis and contain far fewer dislocations than the deformed ones.

Relieved – allowing for freedom of movement or relaxation.

Residual stress – are stresses inherent in a component prior to service loading conditions or the stress present in a body that is free of external forces or thermal gradients.

Restrained – hold back movement in any direction.

Rolling – Reducing the cross-sectional area of metal stock, or otherwise shaping metal products, through the use of rotating rolls.

Rolling direction – refers to the direction in which the billet was rolled ruing sheet metal place manufacture.

Rq – Root-mean-square deviation of the profile

Ry – Maximum height of the profile

Rz – Ten-point height of irregularities

S

Scanning electron microscope – an electron microscope in which the image is formed by a beam operating in synchronism with an electron probe scanning the object.

Shear bands – bands in which deformation has been concentrated inhomogeneously in sheets that extend across regional groups of grains.

Sheet metal forming – refer to forming.

Slip – plastic deformation by the irreversible shear displacement of one part of a crystal relative to another in a definite crystallographic direction and usually on a specific crystallographic plane.

Slip band – a group of parallel slip lines so closely spaced as to appear as a single line when observed under an optical microscope.

Spacers – this is shim stock, plate or epoxy type solutions cast into a mould of specific sizes to raise a component or member to a specific height.

Springback – is the elastic recovery after a component has undergone plastic deformation.

Springback load – is the load required to return the material to its original pre-strained condition.

Springback angle – is the angle between the springback position to the original pre-strained position in a pure bend plate component.

Strain – strain is a measure of the deformation of a body acted upon by external forces and can be expressed as a change in dimension per unit of original dimension or in the case of shear as a change in angle between two initially perpendicular planes.

Strain amplifier – the ratio of the voltage supplied to the voltage delivered by the Wheatstone Bridge as a result of the unbalance caused by a change of strain gauge resistance is equivalent to the strain and is amplified into a suitable

voltage or current which can be fed into an analogue or digital indicator or graphic recorder.

Strain rosettes – a combination of three strain gauges set along three axes, usually at 45º or 60º, with each other – used to determine strain at a point of a surface when the strain directions are unknown.

Stress – load applied to a piece of material tends to cause deformation which is resisted by internal forces set up within the material which are referred to as stresses. The intensity of the stress is estimated as the force acting on unit area of the cross-section, namely as Newtons per square metre or Pascals.

Stress amplitude – refers to a stress loading magnitude above and/or below a particular mean stress level.

Stress ratio – is the ratio of minimum to maximum stress levels usually associated with fatigue testing conditions.

Stress raisers – changes in contour or discontinuities in the structure that cause local increases in stress.

Stress relieving – heating to a suitable temperature, holding long enough to reduce residual stresses, then cooling slowly enough to minimise the development of new residual stresses.

Striation – the appearance of faint ridges or furrows; linear markings.

Stringer – a microstructural configuration of alloy constituents or foreign nonmetallic material lined up in the direction of working.

Sub-surface – a location just beneath the surface of a component.

T

Tempered martensite – the decomposition products that result from heating martensite below the ferrite-austenite transformation temperature.

Tempering – in heat treatment, reheating hardened steel to some temperature below the eutectoid temperature to decrease hardness and/or increase toughness.

Transformation temperature – the temperature at which phase changes occur during the heating of iron and steels.

Transmission electron microscope – a microscope in which the image-forming rays pass through the specimen being observed.

Transverse direction – refers to t he perpendicular direction in which the billet was rolled during sheet metal plate manufacture.

True fracture stress – see fracture stress.

U

Uniform stress field – is where the stress along any particular plane are of equal magnitude.

Uniform plasticity – refers to a condition of a component when subjected to plastic deformation between its yield and tensile strength positions.

Unrestrained – free to move in any direction.

V

Venting – refers to a stamping operation producing holes of specific form in a sheet metal component.

Vickers hardness test – a common method of determining the hardness of metals by indenting them with a diamond pyramid under a specified load and measuring the size of the impressions produced.

Void – a defect lowering material strength by concentrating stress.

W

Widmanstätten structure – a mesh-like distribution of a precipitating phase in a solid state transformation which occurs along preferred crystal planes. Usually produced by rapid cooling and when the transforming phase has a large grain size.

Work hardening – the increase in strength and hardness produced by plastic deformation of metals at temperatures below about $0,5T_m$ that results from increasing numbers of dislocations and their entanglement and is accompanied by reduction in ductility.

Y

Yield point – the stress at which a substantial amount of plastic deformation takes place under constant or reduced load. This sudden yielding is a characteristic of iron and annealed steels.

Yield stress – the stress at the onset of plastic deformation determined from the yield point or from a defined amount of plastic strain called the proof stress.

Young's Modulus – it is the ratio (E) of the tensile stress (σ) to the tensile strain (e) in a linear elastic material at loads less than the elastic limit of the material.

Z

Zero mean stress – pertains to the fatigue testing of a component under zero pre-strain conditions.

ACKNOWLEDGEMENTS

"The Lord is the strength of my life; of whom shall I be afraid?"

AUTHOR'S DECLARATION

I declare that this thesis is my own, unaided work. It is being submitted for the degree Doctor of Technology at the Nelson Mandela Metropolitan University. It has not been submitted before for any degree or examination in any other tertiary institution.

A Els-Botes

CHAPTER 1

INTRODUCTION

1.1   INTRODUCTION

Laser forming (bending) is a new flexible metal forming technique using laser-induced thermal distortion to bend sheet metal without external forces. The basic theory of the Laser has been suggested by Albert Einstein in 1917, but due to equipment constraints, the first laser was only built in 1961 by Theodore Maiman. A laser is a device that emits a narrow beam of light and can be used to perform a variety of different processes, e.g. cut metals at high speed, welding, machining of hard and brittle materials, etc. Laser bending is a promising new technology for bending sheet metal with a high thermal conductivity.

1.2   PROBLEM STATEMENT

It has become evident from previous research that the mechanical forming process decrease the dual phase steel (DPS) components fatigue life by as much as 83% during the first draw operation (forming of a bulge shape). This research project will attempt in forming sheet specimens to the same radius of curvature as that formed during the first draw stage of mechanical forming. Laser forming will eliminate the creation of microvoids and will not set-up any detrimental residual stresses and will thereby increase the fatigue life of the component. Although lasers have been used successfully in various manufacturing processes like cutting and welding, little information is available on the effect of laser forming on many automotive alloys such as dual phase steel. This is because of the complexity and number of process parameters involved. Laser forming of sheet metal does not induce detrimental residual stresses as do other conventional forming processes. The laser forming process has the capability of revolutionising the sheet metal forming industry globally because of its high accuracy, speed and ease of automation. The automotive industry

is becoming increasingly dependent on high precision manufactured components to maintain technological and performance superiority.

1.3   OBJECTIVES

The main objectives of this project is as follows:

1.3.1   The effect of process parameters on the final product's shape/radius of curvature.

1.3.2   The effect of process parameters on the final product's mechanical properties (strength, hardness distribution, fatigue strength, residual stress magnitude) and structural integrity (microstructure analysis).

1.4   HYPOTHESIS

Various parameter settings will influence the resultant microstructure and shape (bend angle) of the final product. This in turn will have a direct influence on the material's mechanical properties, and it is envisaged that the laser forming process will lead to enhanced fatigue performance / characteristics compared to conventional stretch forming processes. This will result in the possible use of thinner gauge sheet metal for the manufacture of automotive components, while maintaining the stringent safety requirements of government legislation.

1.5   DELIMITATIONS

This research project will only consider the effect of laser and conventional forming methods of dual phase steel used for the manufacture of automotive wheels. The laser forming process will employ a 5kW continuous wave (CW) CO_2 laser.

1.6   ASSUMPTIONS

It is assumed that different types of lasers will have similar effects on the material as the continuous wave (CW) CO_2 laser, provided that the laser settings, such as line energy and volumetric energy are kept constant. Design of proper heating and cooling processes will be based on the

results obtained from forming simple shape surfaces (two dimensional) from a plate specimen as a first order examination.

1.7   SIGNIFICANCE OF THE RESEARCH

This research resulted in new information with regard to laser forming of dual phase steel, which can be used in the automotive industry. It was proved by previous research that the residual stresses set up in dual phase steel during conventional stretch forming processes are detrimental to the formed component's fatigue strength. Elimination of these detrimental residual stresses and microvoid nucleation from the formed component will lead to a tremendous improvement in wheel design since thinner gauge material can be used and still ensure adequate fatigue strength of the wheel. Laser forming is the ideal forming process since it does not induce any detrimental defects (microvoids) and residual stresses in the material during the forming operation. This research project will also expand existing knowledge and expertise in the metal forming field at the Nelson Mandela Metropolitan University and will also lead to a higher qualification of a full-time staff member.

1.8   RESEARCH METHODOLOGY

Experiments will be performed on 200x50x3.5mm dual phase steel plates with various line heating distributions (line spacing and sequence) and laser parameters.   The resultant shape from the laser application will be measured, and the mechanical and fatigue properties will be assessed. An identical physical shape will be produced using a conventional (mechanical) forming process and the same properties as for laser forming will be assessed. Laser forming parameters considered for this project will include: (i) Laser output power (1,5kW, 3,1kW and 5kW); (ii) Laser head velocity; (iii) Line heating distributions (line spacing and sequence) and (iv) 7,5mm, 14mm and 20mm laser beam diameters. The resultant structures (grain structure and microstructure) will be analyzed both quantitatively and qualitatively by optical and electron

microscopy in order to examine the kind of existing structure zones and their extent.

1.9   PROJECT SPECIFICATIONS

- All mechanical testing will be done in accordance with recommended ASTM testing procedures.
- Fatigue testing will be done in accordance with ASTM E468-82.
- Residual stress analysis will be conducted according to ASTM E837-01.

1.10   PROJECT LAYOUT

This research project will mainly concentrate on section D: Metallurgical and Mechanical property changes, as illustrated in Figure 1.1 below.

```
                          ┌──────────────────────┐
                          │ A.  Energy Influences │
                          └──────────────────────┘
                                     │
                                     ▼
┌──────────────────┐      ┌──────────────────────┐      ┌──────────────────────┐
│ D.  Metallurgical │      │    LASER FORMING     │      │ B.  Process stability │
│    and Mechanical │ ───▶ │                      │ ◀─── │    parameters         │
│   property changes│      │      PROCESS         │      │                       │
└──────────────────┘      └──────────────────────┘      └──────────────────────┘
                                     ▲
                          ┌──────────────────────┐
                          │ C.  Geometry Influences│
                          └──────────────────────┘
```
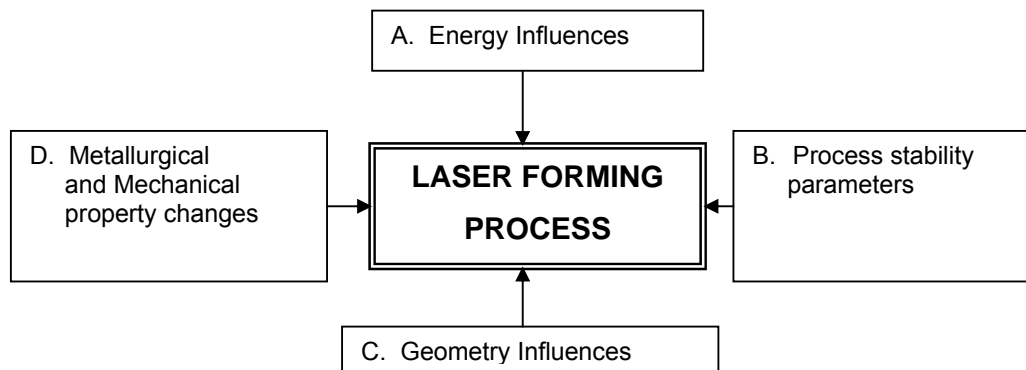
Figure 1.1: Project layout

The results and proof that laser forming can be successfully conducted on dual phase steel will be illustrated in the subsequent Chapters of the thesis. Chapter 2 covers a literature review, Chapter 3 the research methods used to generate results, Chapter 4 covers the results obtained and discussion of the results, and Chapter 5 covers the most important conclusions.

1.11   SUMMARY

The compilation of this thesis gave some insight and background into the field of laser forming. This research will contribute new knowledge to assist with establishing laser forming of dual phase steel as a possible production / forming stage for the manufacture of wheel centre discs. The current forming process leads to the impairment of the dual phase steel's mechanical properties due to the formation of microvoids within the matrix of the material and the magnitude of residual stresses set-up during the forming process.

CHAPTER 2

REVIEW OF RELATED LITERATURE

2.1   INTRODUCTION

The main markets for industrial lasers can be divided geographically into the following: USA (50%), Europe (28%) and Japan (22%). In the USA, the automotive industry and the metal-working industries are the major customers for laser beam sources, whereas in Asia, the electrical and semiconductor industry is the largest. The European market is mainly metal-working and automotive industry related.

To date the African continent is not considered a major market for laser technology. This should change over the next couple of years as many international specifications will call for the use of lasers, (e.g. cutting, welding, surface modification) in order to meet customer demands. As the export of parts/goods becomes increasingly important for a healthy economy, it is of crucial importance that laser technology be developed in South Africa through industry-based research.

The main requirement for the successful introduction of a newly developed laser application, which meets the requirements of the production process, is that the appropriate beam sources and system components are industrially available. What must be taken into consideration is whether the laser method, apart from quality requirements, is more cost effective than conventional forming production methods.

2.2   MARKET SHARES OF LASER TYPES

CO_2 (Carbon dioxide) and Nd:YAG (Neodym:Yttrium-Aluminium-Garnet) lasers are the most important lasers for the industrial materials processing markets. The CO_2 laser has been available for more than twenty years and is obtainable in a wide range of designs and sizes, with output powers of 20kW and more. Nd:YAG lasers are also available

with output powers in the multi-kilowatt range. The advantage of Nd:YAG lasers over CO_2 lasers is that for the Nd:YAG laser, the beam can be delivered via a fiber optic cable, thus these lasers are open to the development of new production methods that were not viable in the past. The diagram in Figure 2.1 illustrates the most important applications for all types of lasers (1998)[1].
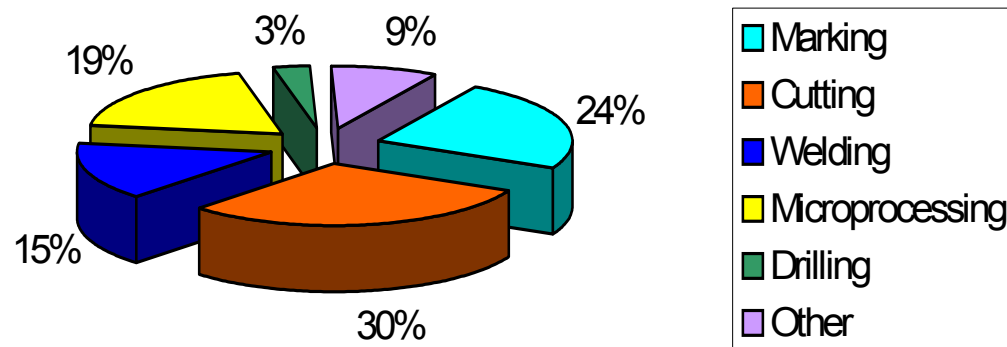
Figure 2.1: Most common applications of lasers in industry

CO_2 lasers are mainly used for cutting applications, however, this is expected to change, as welding applications will show the greatest growth rates, due to the fact that cost-efficient high-power beam sources offer more potential with regard to deeper penetration and higher processing speeds. Nd:YAG lasers on the other hand are most frequently used for marking, welding and cutting of micro- and electronic components and spot welding of delicate structures[1].

2.3   POTENTIAL OF LASER APPLICATIONS

The call for improved production quality, efficiency and flexibility together with those of large-scale manufacturing as well as the need for automation often justify the comparatively costly investment in laser materials processing technology.

It is envisaged that the automotive industry will be one of the most important users of laser technology, and will, to a certain extent, lead the

way in establishing new laser processing methods. The wide range of applications for which laser manufacturing methods have already been successfully implemented is shown in Figure 2.2.

In the manufacture of car bodies, lasers were originally used to cut sheet metal for small batch production. Currently they are used in the full-scale production of car bodies. The use of high power lasers ensures that car body elements can be welded even if the sheets vary in thickness and material (e.g. tailored blanks). This leads to lighter assemblies with very strong weld seams and often also reduces design complexity.
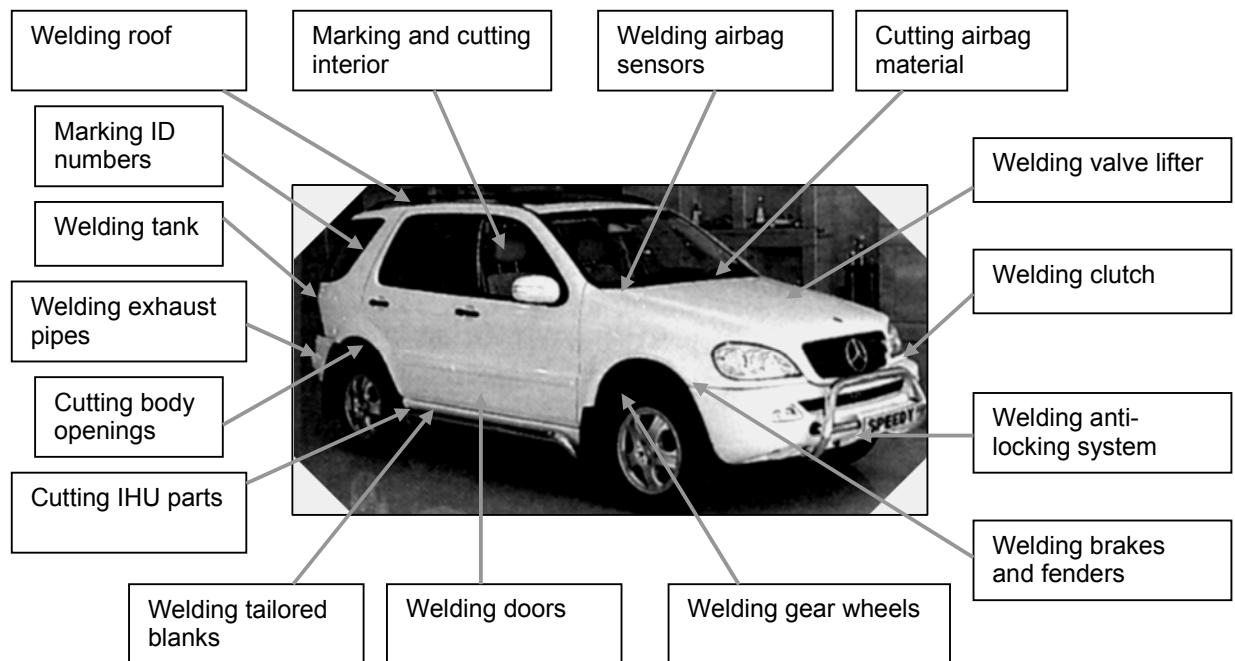
Figure 2.2: Typical applications of lasers in automotive manufacture

It is clear from the brief discussion that the processing of material by means of laser technology holds enormous potential due to its outstanding features, like the economic advantage the process offers. The advantages can be as a direct result from overall cost-reduced fabrication concepts or from the increased use of pioneering design and manufacture[1].

2.4   MANUFACTURING APPLICATIONS

The foremost advantages of laser material processing versus conventional manufacturing processes are:

- Straightforward to manage and computerize
- No expensive tools required
- Non-contact manufacturing process
- No tool wear
- Low heat input on the workpiece due to the very concentrated energy density at the machining point
- High processing speed with good repeatability
- Very hard, brittle or soft materials can be processed
- Almost any shape can be machined by the laser when connected to a suitable CNC system
- Totally different processing geometries are possible without the need to change the tool
- Minimum non-productive times owing to instantaneous response of the beam
- Flexibility when compared to different production methods
- Easy incorporation into conventional manufacture processes

These advantages may already offer sufficient reason for the use of lasers in manufacturing processes, but only technological and financial advantages resulting from specific applications can provide the foundation for investment decisions[1].

2.4.1 Laser cutting

Laser cutting is one of the most significant applications for industrial lasers. Most of the laser cutting methods employ a combination of three separating processes, viz. sublimation cutting, fusion cutting and flame cutting. During laser sublimation cutting, the metal is removed by evaporating the metal. This requires high densities available by suitable modification of the laser radiation and focusing, so that the material removal occurs completely by means of evaporation.

Laser fusion cutting requires reduced power compared to laser sublimation cutting as the metal is only melted and then blown out of the cut with an inert gas jet. Considerably higher processing speeds can be achieved by means of laser flame cutting for low-alloy steels. As a replacement for inert gas, uncontaminated oxygen is used. The metal is heated past its ignition temperature until an extremely exothermal reaction occurs; this supplies energy for the cutting procedure. Compared to sublimation cutting, approximately only five percent (5%) of the energy is required[1].

2.4.2   Laser drilling

The different drilling methods are classified according to the special requirements with regard to

- hole diameter,
- hole depth and
- diameter: depth ratios and the beam parameter and beam guidance adjustments.

Holes with diameters from 20 – 500µm and diameter:depth ratios up to 1:20 can be drilled by the single-pulse technique. For holes with diameters between 0,1 – 1,0mm the percussion method is usually employed. This process uses a sequence of equal laser pulses. Trepanning drilling is used to produce larger hole diameters in the range of 0,4-6mm. This method uses a laser beam that is guided around the hole contour by revolving the optics or the workpiece[1].

2.4.3 Material removal

A variety of three-dimensional structures can be shaped by laser technology employing almost any material. Lasers are used industrially for large-area removal of varnishes, coatings and impurities as well as the removal of material from natural stone, e.g. cleaning of limestone monuments[1].

2.4.4 Laser welding

Compared to conventional welding methods, laser beam welding offers a number of advantages. Figure 2.3 shows these advantages[1].
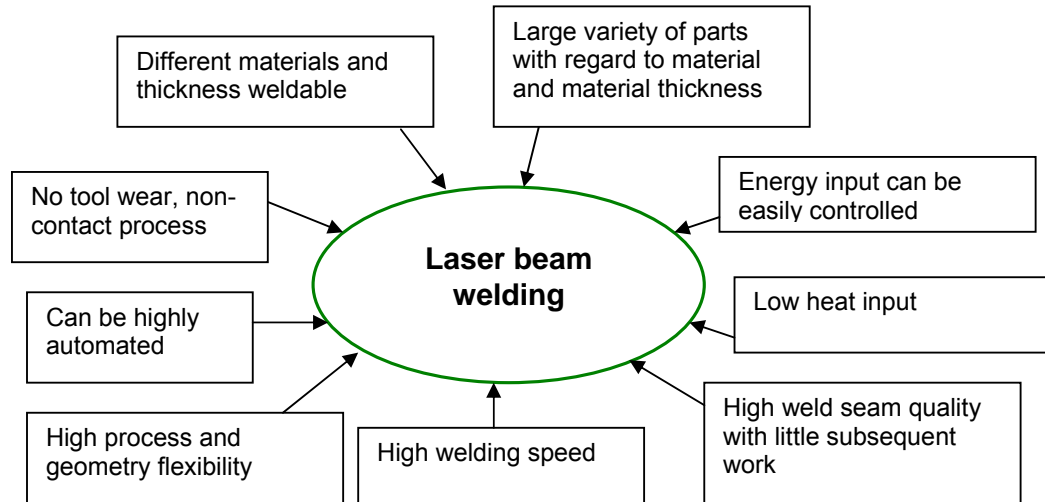
Figure 2.3: Advantages of laser beam welding

The two main processes by which laser beam welding takes place is thermal conduction welding and deep penetration welding (keyhole welding). In the case of thermal conduction welding, the metal melts because of the absorption and the thermal conduction of the laser energy. The limitation of this process is that it only allows for shallow penetration depths.

The fundamental principle of keyhole welding is based on the principle that the metal locally reaches the evaporation temperature due to the focused energy. Because of the evaporation, a capillary (keyhole) is formed with a diameter of one and a half to two times the focused spot.

The vapour pressure prevents the capillary from closing, which acts against the hydrostatic pressure of the neighbouring melt and its surface tension. Laser-induced plasma is formed in the metal vapour streaming away above the workpiece and in the capillary. Energy input is conducted into the solid metal by means of thermal conduction. This is

the method that allows the laser beam to make deep penetration welds. The energy of the laser beam can totally penetrate the metal and increase the deep penetration welding effect after the plasma has been established. Most metals can be welded without inert shielding gas as long as plasma can be created and the surface oxidation is acceptable[1].

2.4.5 Laser soldering

When joining very small metallic components (10-200μm), problems are often experienced that cannot by solved by conventional methods. Soldering is the best joining method to use in these cases. Soldering can be divided into brazing (T>800°C) and soft soldering (T<230°C). During soldering, laser light is employed to melt an additional material with a considerably lower melting temperature than that of the component's material to be joined. High process repeatability can be achieved for laser beam soldering if the laser power and beam interaction time is controlled. The process is controlled by monitoring the surface temperature as a function of time[1].

2.4.6 Laser surface treatment

Surface treatment usually requires low intensity laser radiation and a comparatively long reaction time. The basic principle of laser surface treatment is illustrated in Figure 2.4.

1. Laser
2. Alloy layer
3. Base material
4. Alloyed zone
5. Heat affected zone
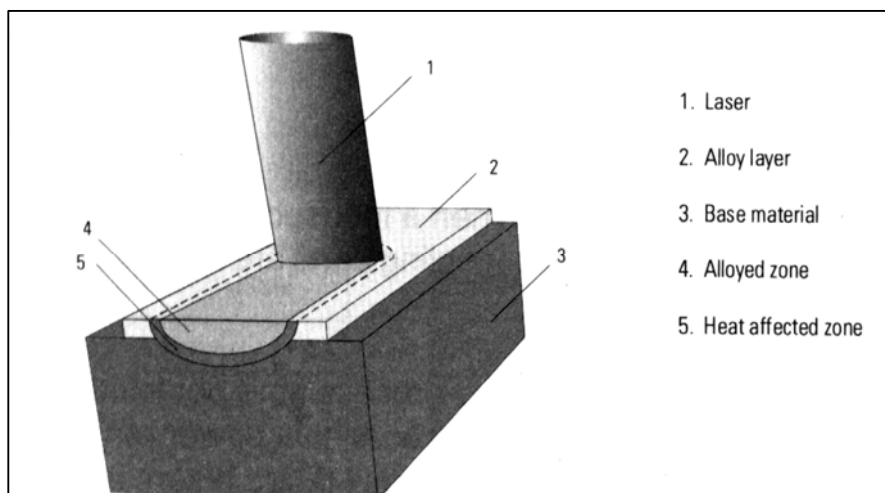
Figure 2.4: Basic principle of surface treatment[1]

Surface treatments can be classified into four main groups:

- Hardening

  Laser surface hardening corresponds closely to conventional hardening mechanisms. A defocused laser beam supplies the heat and self-quenching is achieved by rapid thermal conductivity into the cold base metal. The main advantages of laser surface hardening are:

  - Improved processing of inaccessible areas

  - Localised hardened areas

  - Low distortion

  - Short processing times

  Because the method employs a defocused beam without contact, it is very flexible with respect to the geometry of the component[1].

- Laser re-melting

  Laser beam re-melting is mainly used to assist with minimizing wear on highly stressed surfaces. Re-melting can also be performed to add additional alloying elements to the surface layers.

- Cladding

  This application employs the deposition of wear resistant layers or depositing layers for repairs. The process commonly involves feeding a powder to the laser heated zone through a special nozzle.

- Alloying

  This process is similar to laser beam cladding but the aim is to mix two materials, forming a third material with the desired properties. Carbides, nitrides and borides are usually added to improve wear resistance and/or increase corrosion properties[1]. Figure 2.5 illustrates the main two types of laser beam alloying processes.
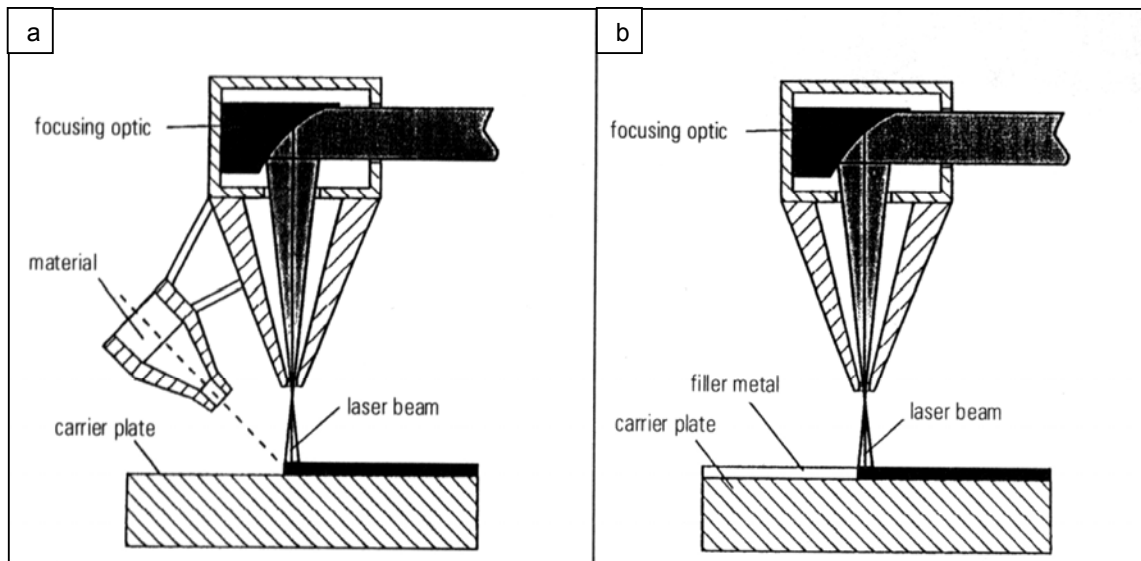
Figure 2.5: Laser beam alloying processes[1]

The process of laser surface alloying is similar to surface melting with the laser, except that desired alloying elements are externally added to the melt pool to modify the surface chemical composition as best suited for the part being treated. Such modification of the surface composition to achieve the desired properties can be obtained by introducing the alloying elements in (a) gaseous or (b) powder form as a prior coating. Thickness of the alloyed layer can be up to 2000 µm.

2.4.7 Laser marking

Nd:YAG lasers are most commonly used for marking applications (90%). The most important difference between cutting or welding lasers and lasers used for marking are that the latter are generally lower power continuous wave and are normally Q-switched.   Typical output powers are in the range of three to 150 Watts. High power lasers are only used for special applications such as metal engraving. Nd:YAG lasers are used for marking almost all metals, many types of polymers, coated materials, enamel, and many other materials.

CO_2 lasers are more commonly used for marking glass, wood, leather and acrylics. CO_2 lasers can be set to engrave the material with (wood, leather) or without contrast (plastics), dependent on the material[1]. When marking involves the visible removal of material (10-50μm deep), it is termed engraving. If only the effects of heat and oxygen change the colour of the metal, without any material actually being removed, the process is referred to as marking by annealing. Laser beams can also be used to effect a change in the colour of many plastics. When the plastic is exposed to high intensity laser light, the material changes colour due to the pigments in the plastic material and / or the expansion of the plastic[1].

2.4.8   Rapid product development (laser assisted)
Stereo lithography

Stereo lithography machines convert three-dimensional CAD data into perpendicular stacks of slices to form a three dimensional object from the data. A low power laser beam is then traced across a vat (holder) containing photo curable liquid polymer, producing a single layer of solidified resin. The initial layer is then lowered incrementally by the height of the next section, where upon the layer is recoated with resin and another is traced on top of it. The process is repeated until the entire part is fabricated[1].

Selective sintering

A modulated laser beam follows the shape of a section of a CAD generated object; it traces the object across a bin of special heat fusible powders. This causes the particles to fuse or sinter together as the laser passes. After the initial layer is formed, powder is reapplied and the laser processes the next layer. Figure 2.6 illustrates the process of selective sintering.
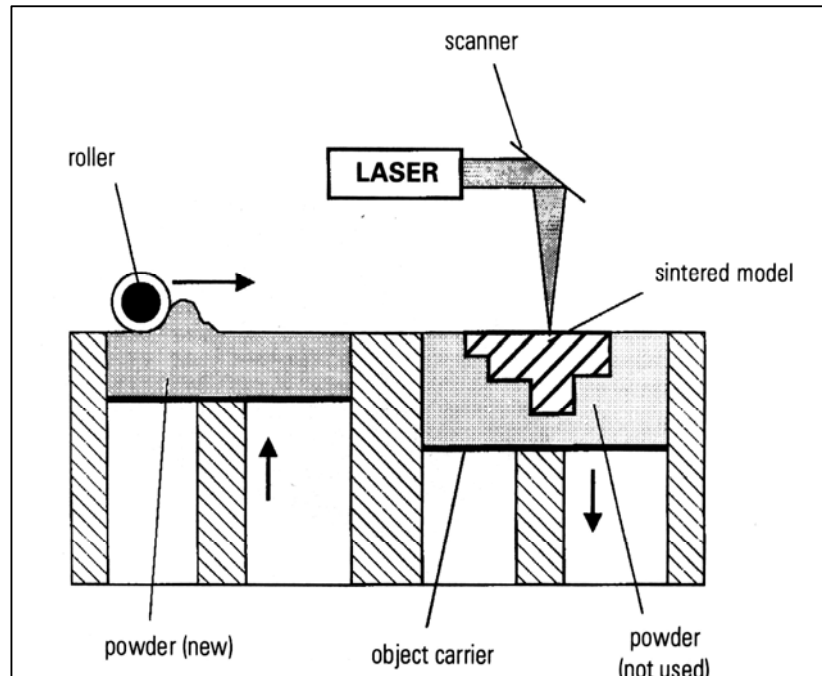
Figure 2.6: Schematic illustration of the selective sintering process[1]

Laser forming

The controlled energy of the laser can be used to generate defined thermal compressive strains or tensile stresses in the material, which can then be used to change the shape of the workpiece. This process is commercially used in the manufacture of micro relays[1].

Laser systems are considered an ideal tool for the industrial processing of materials because of their ability to accurately focus energy. Laser forming (LF) is the process of bending a metal or alloy sheet into various shapes by thermal stresses due to laser irradiation. In order to analyse the process, a good understanding of the process and its parameters is of great importance.

2.5   THE LASER FORMING PROCESS

The laser forming process can be simplified by the following flow diagram: [2]

```
┌─────────────────────────────┐
│ Laser beam irradiation      │
└─────────────────────────────┘
              │
              ▼
┌─────────────────────────────┐
│ Absorption                  │
└─────────────────────────────┘
              │
              ▼
┌─────────────────────────────┐
│ Temperature rise            │
└─────────────────────────────┘
              │
              ▼
┌─────────────────────────────┐
│ Thermal expansion           │
└─────────────────────────────┘
              │
              ▼
┌─────────────────────────────┐        ┌─────────────────────────────┐
│ Thermal stress              │───────▶│ Plastic deformation         │
└─────────────────────────────┘        └─────────────────────────────┘
              │
              ▼
┌─────────────────────────────┐
│ Heat conduction             │
└─────────────────────────────┘
              │
              ▼
┌─────────────────────────────┐
│ Temperature fall (cooling)  │
└─────────────────────────────┘
              │
              ▼
┌─────────────────────────────┐
│ Thermal contraction         │
└─────────────────────────────┘
              │                          ┌─────────────────────────────┐
              ▼                          │ Plastic deformation         │
┌─────────────────────────────┐         └─────────────────────────────┘
│ Thermal stress              │────────▶            │
└─────────────────────────────┘                     ▼
                                         ┌─────────────────────────────┐
                                         │ **Laser forming**           │
                                         └─────────────────────────────┘
```
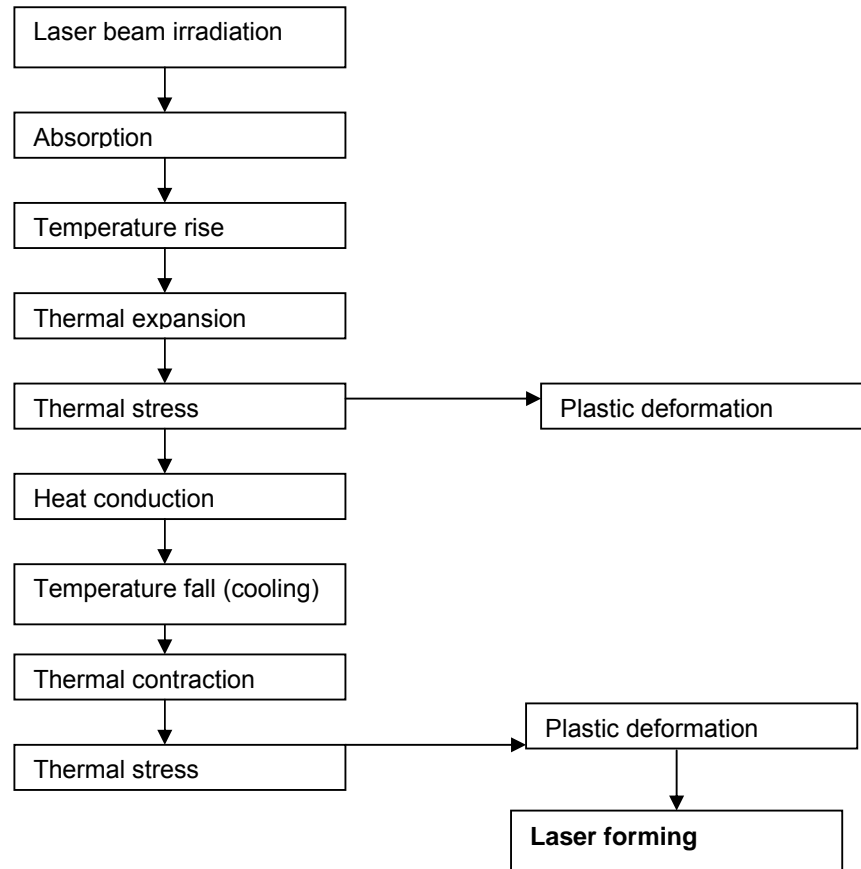
Figure 2.7: Flow diagram of the laser forming process

Mechanical forming is a manufacturing process by which the shape of a part is altered by the application of a force that induces stresses in the part that are greater than the yield strength and less than the fracture strength of the material. In laser forming on the other hand, when a laser beam of sufficiently high power density, which has a Gaussian distribution, is irradiating a metal sheet, the sheet will absorb some of the laser energy on the surface. This thermal energy is then conducted into the metal and a temperature gradient is set up between the top and bottom surfaces of the metal sheet. The area of the metal being irradiated expands in volume due to a rise in temperature.

As a material's temperature changes, so do its mechanical properties. When a temperature is reached where the material's thermal stress exceeds the flow stress of the metal at that temperature, plastic deformation occurs. After the irradiation scan, the heated area cools by heat conduction into the material. Since no melting is involved, radiation loss is negligible. Because of the cooling, the material contracts non-uniformly due to the temperature distribution, which causes high thermal stresses in the metal. The metal part will plastically deform to accommodate these high stresses and will thus deform without any external applied forces. Laser forming limits material degradation to thin layers near the plate surface[3].

The following variables have been identified as important factors affecting the laser forming process[2]:

- Incident laser beam power
- Laser beam diameter
- Power density distribution of laser beam
- Absorbtivity of metal
- Laser scanning speed
- Numbers of repetitions of laser beam scan
- Density of metal
- Thermal conductivity of metal
- Specific heat of metal
- Thermal expansion coefficient of metal
- Yield strength of metal
- Modulus of elasticity of the metal
- Poisson's ratio of the metal
- Strain hardening exponent of the metal
- Dimensions of sample
- Melting temperature of metal
- Fracture strength of metal

As stated earlier, all mechanical properties of materials are functions of temperature, and since laser forming is temperature based, it is important that these variables be noted in order to predict/analyse the laser forming process.

It was stated in literature that multiple heating using low heat input can minimize the reduction in fracture toughness of the material due to laser line heating. No graphical evidence of this statement could be found in the relevant technical paper. Fracture toughness was measured by taking V-notch Charpy test specimens from laser heated plates[3].

2.6   MAIN BENDING MECHANISMS

Three main bending mechanisms have been established through research to explain forming due to laser line heating. Each of the three methods can be characterized by the gradient of compression created by the heat distribution through the sheet's thickness.

2.6.1 Temperature Gradient Mechanism (TGM)

This mechanism requires the use of a small beam diameter and a fast processing speed. Due to the high processing speed, the heat is not given enough time to penetrate to the bottom of the sheet, resulting in a temperature gradient through the sheet's thickness. This results in a tapered compression region through the material. There is no loss of material and the plastically compressed area forms a ridge on the heated side, while the bottom of the sheet remains largely unaffected. This results the sheet bending towards the laser beam. Multiple scans may be required to achieve the desired bend angle[4]. Creating out-of-plane positive bend angles (towards the laser beam) is mostly achievable by choosing parameters of laser power and scanning velocity that produce a bend by the TGM.

Figure 2.8 shows a schematic illustration of the temperature gradient mechanism.

Laser beam

Out-of-plane
bending,
positive angle
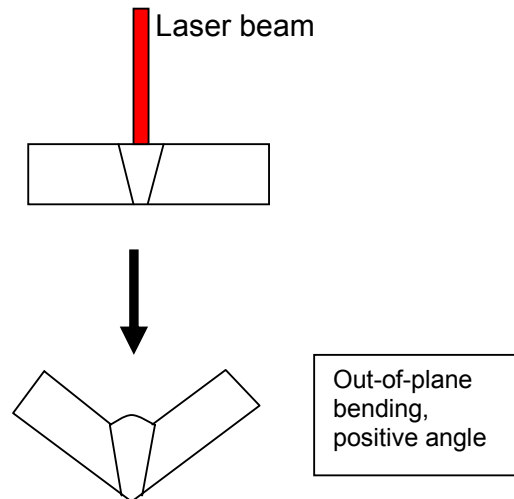
Figure 2.8: Schematic illustration of temperature gradient mechanism

An influence on the direction of the bend angle is the residual stresses
present in the sheet material before the laser forming process. If there
are compressive stresses at the surface and tensile stresses in the core
of the sheet, the stress released during heating will result in the
generation of a positive 'prebend' and advance to a positive bend angle
on subsequent scans. From the TGM it has been observed that during
heating, a negative bend angle develops[5]. The positive bend angle
results due to the relaxation of the residual stresses, which occurs first at
the irradiated surface of the sheet. As this occurs, the sheet acquires a
concave form, which leads to a positive bend angle. A maximum
curvature will be attained if the compressive stresses at one surface are
totally relaxed[5]. Steep temperature gradients, which are promoted by
three-dimensional heat flow, create non-uniform stress, strain or
temperature distributions, causing bending through the TGM.   This
bending mechanism occurs when the beam radius (R) is smaller than the
sheet thickness (D)[6].

2.6.2 Buckling Mechanism

This mechanism is characterised by the bending of the sheet away from
the laser beam. Both positive and negative bend angles can be
achieved by this mechanism. The absence of a temperature gradient

through the material's thickness, a condition established by a two dimensional heat flow, results in distortion of the material.

It is expected that yielded widths smaller than the sheet thickness are unlikely to create noticeable distortions when the heat flow is two dimensional[6].   A large beam diameter is employed together with a slow processing speed, which results in almost homogeneous heating. The bend angles are usually large and a single scan can produce a bend angle of up to 15°. The bend angle is also more rounded in shape than those produced by the temperature gradient mechanism[4]. This process is illustrated in Figure 2.9 and Figure 2.10.
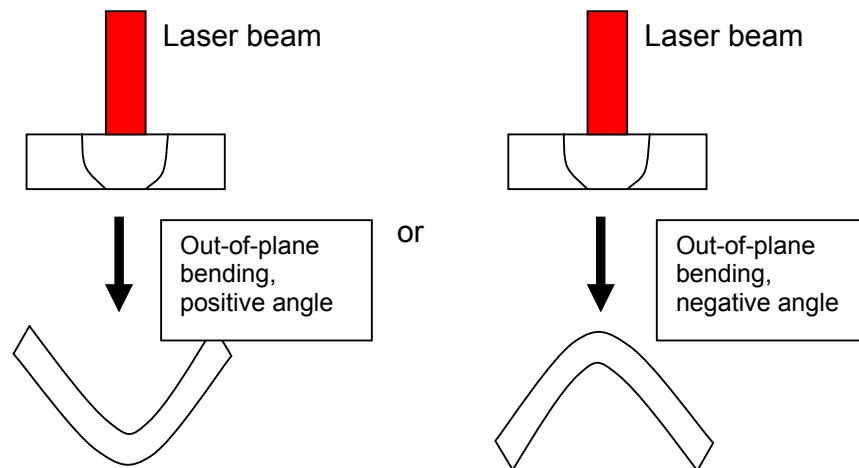
Figure 2.9: Schematic illustration of buckling mechanism
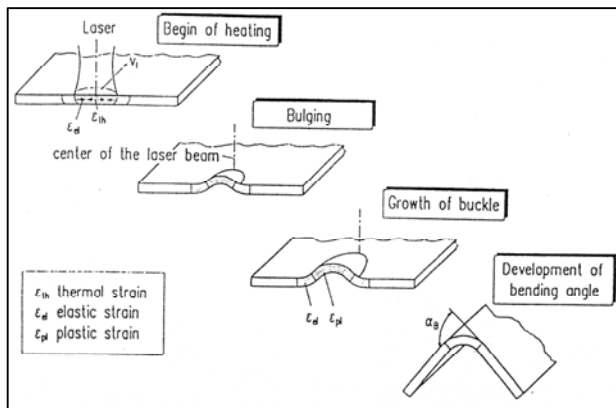
Figure 2.10: Stages of laser forming by the buckling mechanism[4]

2.6.3 Upsetting Mechanism

The upsetting mechanism involves homogeneous heating that result in parallel plastic compression, which causes a shortening of the sheet. This mechanism is used to form spatial parts like bowls, which require a loss of surface area[4]. This mechanism is simplistically illustrated in Figure 2.11 and is known as in-plane shrinkage.

Laser beam

In-plane shrinkage
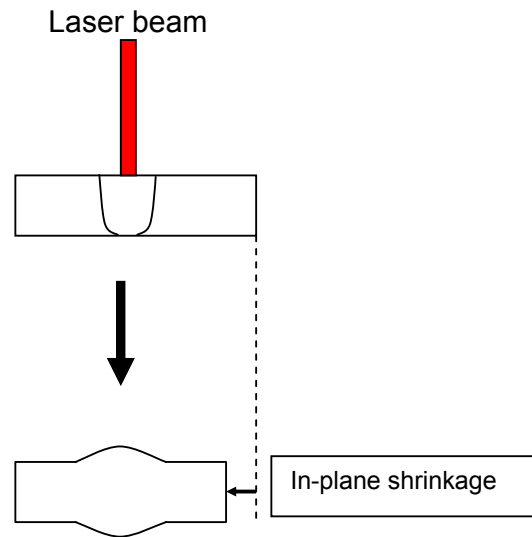
Figure 2.11: Schematic illustration of the upsetting mechanism

2.7   INFLUENCE OF PROCESS PARAMETERS

2.7.1 Angular distortion

Masubuchi found that a parameter 'm' can be used to indicate the amount of angular distortion[3]. The parameter 'm' is defined by the following equation:

$$m = \frac{P}{t\sqrt{v}} \tag{2.1}$$

Where: P = power of the laser beam (kW)

t = plate thickness (inch)

v = travel speed of laser beam (inches per minute)

In his study, Masubuchi found that the amount of angular distortion increases as the parameter 'm' increases, however, when 'm' exceeds a value of approximately six (6), the amount of angular distortion starts to decrease. This was based on studying the effects of various experimental parameters on angular distortion in low-carbon steel plates having thickness of 6,4; 12,7; 19,1 and 25,4mm respectively. It is not clear if the relationship in equation 2.1 can be applied to steel plates of lower thickness and varying carbon content or microstructure[3].

2.7.2 Line Energy

Apparently there is a threshold line energy, which is defined by the ratio between laser power and laser beam velocity, below which bending is unlikely to occur. From KC Chan's study it was stated that the bending angle varies linearly with laser beam power[7]. A schematic illustration of the laser line heating process, using a CO_2 laser is shown in Figure 2.12.
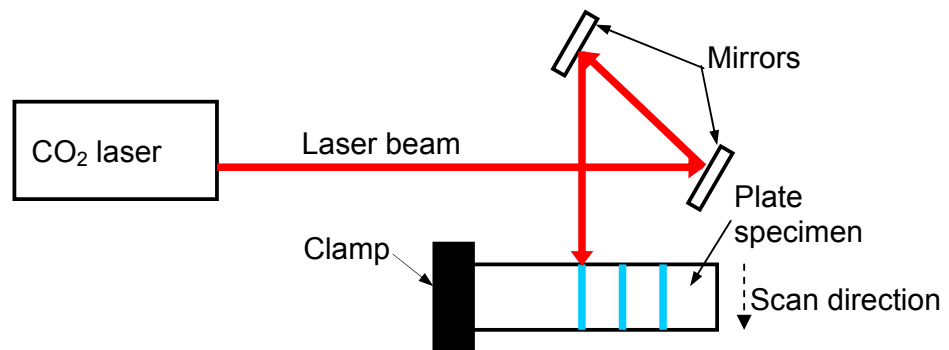
Figure 2.12: Laser line heating process

2.7.3 Relationships for stainless steel and aluminium alloys

Studying the process of laser plate bending on stainless steel and aluminium alloys, the following general relationships were found:

- Increased number of laser scans results in an increased bend angle (laser power and travel speed remain constant).
- It was observed that the effect of material properties on bend angle was remarkable and will be briefly explained in the following section. Most significant were the effects of temperature dependence of yield stress and thermal expansion coefficient. Metals with a low thermal expansion

coefficient and high proof stress values in the temperature range, where bending takes place, produced smaller bend angles.

- Bend angle can be approximated by the total residual strain[8].

Total residual strain = Compressive plastic strain – Tensile plastic strain

Although these researchers claim to have predicted bend angle relatively accurately, no mathematical relationship was published in their paper[8].

2.7.4 Yielded zone

When explaining the process of laser bending, another important factor that needs attention is the shape and size of the plastic zone. The yielded zone can be seen as a group of rectangular elements as shown in Figure 2.13.
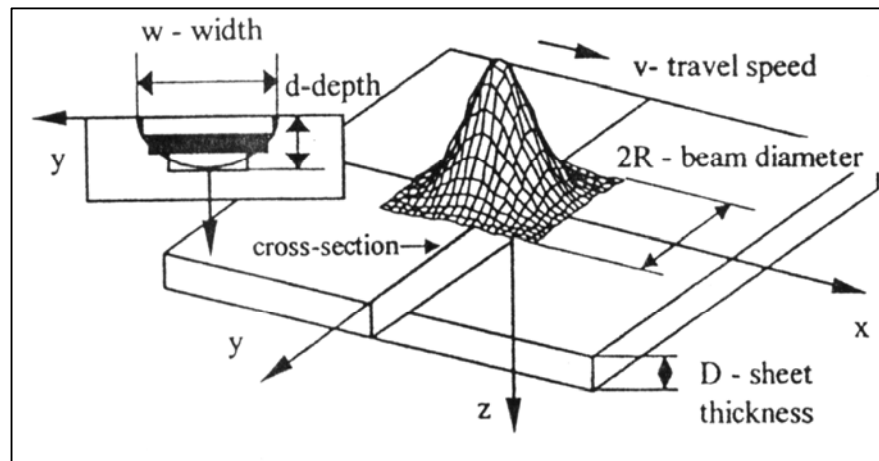
Figure 2.13:   Schematic illustration of the yielded zone[9]

When heated, the various rectangular elements of the plastic zone heat up and expand. This expansion is then transformed into plastic compression when the temperature exceeds the yielding temperature (T_{yield}). This temperature can be estimated from the condition at which the elastic strain (ε_{es}) reaches its elastic limit (ε_{el}); i.e. the flow stress (σ_y) divided by the Modulus of Elasticity (E) equals the thermal expansion (α) times the temperature increase ($T - T_o$)[9]:

$$\varepsilon_{es} = \frac{\sigma_y}{E} = \alpha(T_{yield} - T_o) = \varepsilon_{el} \qquad\qquad (2.2)$$

$$\therefore \sigma_y = E\alpha(T_{yield} - T_o) \qquad\qquad (2.3)$$

It is widely accepted that the value $\frac{\sigma_y}{E}$ strongly decreases with temperature, and can be resolved / calculated for most engineering materials[9]. The extent of the constraint caused by the colder and therefore more rigid part of the sheet has a key influence, regardless of the mechanism (temperature gradient or buckling mechanism). A specimen free to expand upon heating and contract on cooling will have no net shape change when cooled down to room temperature. Because of the constraint (various temperature regions), determining a single yielding temperature is a simplification, but can be a useful estimate for a better understanding of the process[9].

2.7.5 Temperature gradient, heat flow and yielded zone

From literature it is clear that the temperature gradient through the sheet thickness ($\frac{dT}{dz}$ or $\frac{\Delta T}{D}$) will play an important role in controlling the resulting bend angle, as will the gradient in the y-direction (see Figure 2.13) [9]. Figure 2.14 illustrates the effect of temperature gradient, expressed in terms of heat flow and the resulting bending mechanism.

Figure 2.14 shows that when the temperature gradient through the thickness of the material is large (three dimensional heat flow), the resulting bending mechanism is the Temperature Gradient Mechanism, whereas when there is virtually no temperature gradient through the material thickness (two dimensional heat flow), the resulting bending mechanism is the buckling mechanism.

The strains resulting from the temperature gradient should result in bending, but only if the sheet is adequately warmed through its thickness

to become easily formable. In order to obtain maximum angular
distortion at least three criteria must be satisfied simultaneously:

- A high enough temperature must be reached to lower the yield
  strength over a large enough volume of material, which includes
  the whole thickness (D).

- A large thermal gradient through the thickness of the sheet.

- Thermal expansion (heating) and contraction (cooling) must be as
  high as possible; therefore, the surface temperature must
  approach the melting temperature of the material[9].
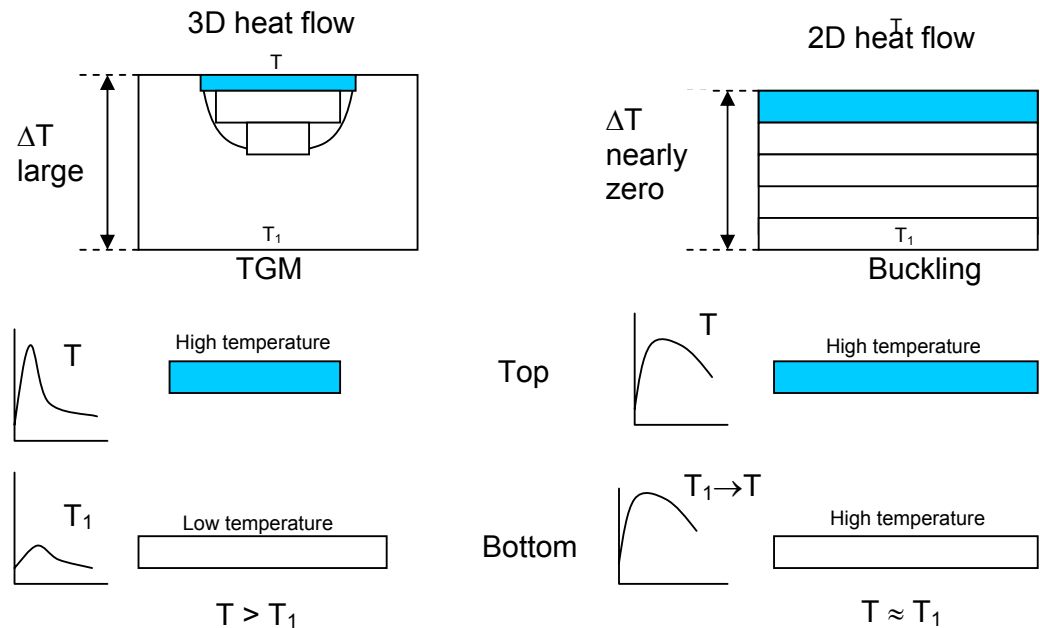
Figure 2.14: Illustration of the effect of temperature gradient on the
resulting bending mechanism

To obtain maximum bending angle, a perfect combination of yield zone
depth and width must be achieved. If the yield zone depth is shallow or
the yield zone width is too narrow, no bending is likely to occur since the
amount of strained material would be insufficient. Even if the heat flow is
three dimensional, no bending would occur because the material remains
too rigid throughout its thickness. On the other hand, conditions that lead

to complete penetration of heat will lead to perfect two-dimensional heat flow, which will more likely result in minor angular changes. Even though the sheet thickness would be heated enough to make it easily formable, the absence of a temperature gradient might not induce significant bending[9]. From this study it was also observed that as the beam size increased, the heat flow became more two dimensional.

Other important observations are that the bending angle responded better to small variations in power when the beam spot size is small. This can be attributed to the high sensitivity of heat flow changes with power. At first the bend angle increased, as the size of the plastic zone grows (depth and width). As the power increased, the heat flow was gradually affected by the bottom surface, which leads to two-dimensional heat flow. When the maximum bend angle was obtained, the bend angle started to decrease while the yielded zone still increased in size (width and depth). The decrease in bend angle is most likely to occur when the thermal stresses and strains above and below the neutral axis start to cancel out each other. The exact depth where the bend angle starts to decrease is still unknown, but can probably be predicted with knowledge of the residual stress distribution through the thickness of the sheet[9].

Laser forming is a complex process in that variables such as depth, width, temperature and thermal strains change when only one parameter, e.g. power, travel speed or focus depth, is altered. Vollersten[9] derived a relatively simple equation for bend angle (θ) for the temperature gradient mechanism, assuming thermoelastic strains and an arbitrary stress distribution within the plastic zone:

$$\theta_{Bending} = \frac{\alpha(T - T_o)wd}{2D^3}\left(3\pi D - 8d\right) \qquad\qquad (2.4)$$

Where: D = plate thickness (mm)

                    d = yield depth (penetration depth of T_{yield} isotherm, mm)

w = yield width (top width of T_{yield} isotherm, mm)

α = thermal expansion ($10^{-6}.°C^{-1}$)

T = temperature (at which bending takes place) (°C)

T_o = original temperature of plate (room temperature) (°C)

Equation 2.4 shows that the bend angle is at maximum when the surface temperature is highest and when the ratio of $\dfrac{d}{D}$ reaches a critical value. It also shows that the bend angle increases with an increase in yielded width[9].

2.7.6 Thickening effect

It has been shown that bending occurs when cooling takes place, leading to various degrees of contraction through the thickness of the sheet. When an element contracts it becomes thicker since its volume remains constant. This phenomenon is generally referred to as the thickening effect and is usually quantified as $\dfrac{\Delta D}{D}$ where D is the thickness of the sheet. Experimental results suggest that there is a correlation between thickening and beam power (the higher the power, the greater the thickening). This is expected since larger powers produce larger thermal expansions and contractions[9].

2.7.7 Energy influences

As discussed earlier, the energy input to the sheet metal surface critically affects the laser forming process and the forming mechanism that takes place. Studies on titanium alloys revealed that the bend angle increased with an increase in power or line energy. This is because at a constant speed the isotherm defining the elastic-plastic interface becomes wider with increasing power. This in turn results in a larger plasticized zone and a resulting larger bend angle as a greater volume of plasticized material is available to overcome the opposing bending moment

(constraint) of the sheet compared to the case where there is a low magnitude of energy input.

It was also observed that at high energy input and slow velocities there is a loss of efficiency from overheating the material that resulted in a decrease in bend angle. Phase transformations which show an accompanying volumetric expansion had a negative effect on the bend angle[10].

2.7.8 Geometry and process stability influences

As the thickness of a material increases, the bend angle decreases because according to the strength of materials theory, the moment of resistance is proportional to the square of the sheet thickness[10]. The moment of inertia of the workpiece increases with an increase in the number of scans over an identical track, hence more energy is required for subsequent scans in order to maintain the rate of bending. In aluminium alloys the decrease in microhardness resulting from heat input reduces this effect to some extent for subsequent scans. In the case of titanium alloys the increase in hardness, the increase in phase change effects and the increase in thickness with increasing scans all contribute to greater a decrease in the bending angle rate[10].

Laser forming is a complex process involving thermal-mechanical processes[11]. The laser beam has the ability to heat a metal plate and create local thermal gradients, which allows thermo-mechanical forming of complex shapes. Thermal gradients exist through the thickness direction and laterally in constricted areas[12]. Obvious reasons to study the laser forming process are listed below:

- It would be easier to incorporate laser forming into an automatic fabrication system than the traditional line heating forming technique, which employs the use of oxyacetylene torches.

- Material degradation is limited to thin layers near the surface of the material provided the correct laser settings are used. Laser forming can thus be used on materials (steels) which are sensitive to heat[12].

A schematic illustration of the changes in temperature and the resulting out-of-plane deformation that occurs during line heating is shown in Figure 2.15. Figure 2.15 (a) indicates line heating and shows the heat source travelling at a constant speed along the x-axis of the plate surface. The shaded area/region shows where plastic deformation occurs on and near the surface during the thermal cycle.
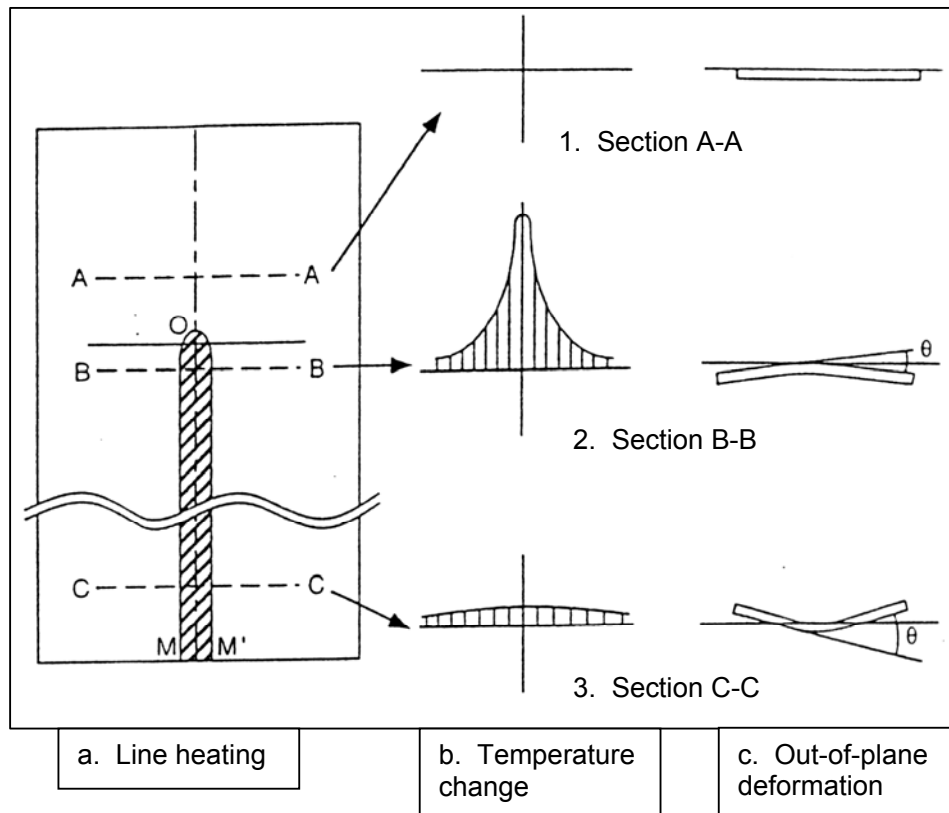
Figure 2.15(a), (b) and (c): Illustration of changes in temperature and angular distortion experienced during laser line heating[12]

The temperature distributions on the surface through three cross-sections as shown in Figure 2.15 (b) indicates the temperature changes. It should be noted that subsurface regions will have lower temperatures associated with them and are not indicated in Figure 2.15.

Out-of-plane deformation is shown in Figure 2.15 (c). Section A-A shows that thermal stresses caused by heating, are relatively small and resulted in negligible out-of-plane deformation. Noticeable deformation is shown at section B-B. The regions near the surface are heated to high temperatures while further away the regions are less heated; this resulted in a concave shape with a negative bend angle (θ). The regions near the surface want to expand due to heating, but are restrained by the regions below. This causes compressive stresses to be set up in the regions near the surface. It is well documented that yield stress decreases with an increase in temperature. Therefore, since the yield stress in the highly heated area is low, compressive plastic strains are produced in these regions. When the heat source passes by, the metal starts to cool which results in elastic shrinking of the region to occur. Because of the existence of the compressive plastic strains formed in regions near the heated zone, the plate bends into a convex shape with a positive bend angle (θ) as shown by section C-C[12].

The strain rate at elevated temperatures has a much higher influence on the material's flow stress than at lower temperatures[13]. Previous experimental results have shown that the resulting bend angle is directly proportional to $\sqrt{v}$ for low-carbon steel plates, where v is the laser scanning velocity (associated with strain rate).

The main reason that the bend angle decreases with increasing velocity (for constant laser power) is that the laser energy input per unit time reduces when the scanning velocities increase. There is also a decrease in bend angle due to flow stress increase because the higher the velocity, the higher the strain rate, which causes the flow stress to rise[13].

Even if the laser energy input per unit length is kept constant, the net energy input available to cause forming may still vary due to different heat dissipation rates associated with different scanning velocities. Laser forming is best studied by keeping the peak temperature reached at the top surface of the workpiece, constant. This will ensure that the constant net energy input available for the forming process can be maintained under varying scanning velocities (strain rate)[13].

It has been observed that for a low-carbon steel (AISI 1010) and constant line energy, the lower velocities resulted in a smaller bend angle. This is due to the fact that the through-thickness temperature is smaller thus resulting in smaller thermally induced distortions between top and bottom surfaces. Also, heat dissipation is more significant at lower speeds and reduces the efficiency of the forming process. It was proved by previous research that the peak temperature increased with an increase in velocity even when line energy was kept constant. This is because there is less heat dissipation at higher scanning velocities, which leads to an increase in temperature difference between the top and bottom surfaces of the workpiece[13].

The main trends identified when studying laser forming of AISI 1010 low-carbon steel is that bend angle decreased and residual stress increased with an increase in scanning velocity (strain rate). Plastic strain was found to be compressive on the upper surface and tensile on the bottom surface, which is consistent for the temperature gradient mechanism (TGM).

Due to heating by the laser, a steep thermal gradient is set up through the thickness of the material which leads to a higher tendency of thermal expansion at the top surface. The surrounding cooler material restricts the expansion, resulting in considerable plastic deformation at the top surface. During cooling, the material that was compressed in the surface layers contracts so that shortening of these layers makes the workpiece

bend towards the laser beam, while the bottom layers experiences slight tension.
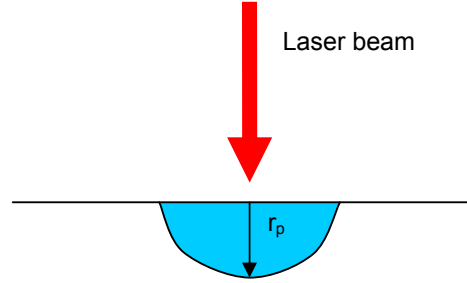
Figure 2.16: Schematic illustration of derivation of Peak Temperature

As shown in Figure 2.16, r_p corresponds to the radius of critical temperature region (plastic region). Based on Rosenthal's solution[14]:

$$T = T_o + \frac{q}{2\pi kvt}\exp\left[\frac{r_p^2}{4\lambda t}\right]$$

(2.5)

Where: T_o = room temperature

q = heat input

k = thermal conductivity

r_p = radius where T_p occurs from source (radius of plastic zone)

λ = thermal diffusivity

v = travel speed

t = time

Further refined, equation 2.5 can predict peak temperature at any given point by:

$$T_{peak} = T_o + \frac{2\lambda q}{\pi kevr^2}$$

(2.6)

Where: e = 2,71828

When T_p is the critical temperature corresponding to the plastic deformation limit and r_p is the radius of the critical temperature region, then the following equation is valid:

$$r_p = \left[\frac{2\lambda q}{\pi kve(T_p - T_o)} \right]^{\frac{1}{2}}$$ (2.7)

Further, assuming that the semicircular region is equivalent to a rectangular region of the same area as shown in Figure 2.17:
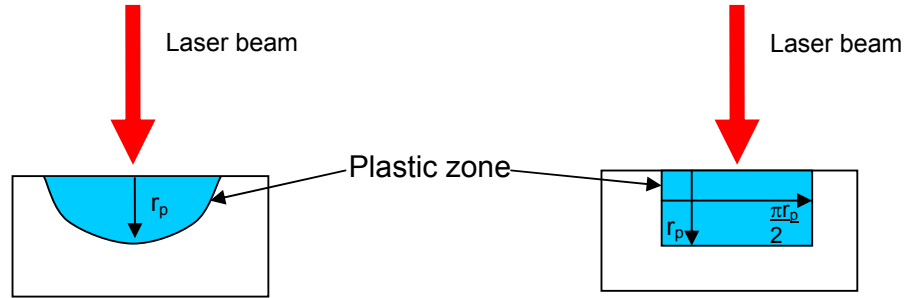
Figure 2.17: Comparison of semicircular and rectangular plastic zone

The formula for vertical displacement in terms of material properties, plate thickness and heat input can be determined as follows[14]:

$$\mu_3 = \frac{3\alpha q(1-v)(T_m - T_o)}{8\rho cveh^3(T_o - T_p)} \left\{ h - \left[\frac{2q}{\pi\rho cve(T_p - T_o)} \right]^{\frac{1}{2}} \right\} \left\{ \left[\frac{2q\pi}{\rho cve(T_p - T_o)} \right]^{\frac{1}{2}} - 8|x_2| \right\}$$ (2.8)

Therefore, angular distortion is:

$$\delta = \frac{\mu_3}{l}$$ (2.9)

Where: α = Thermal expansion coefficient

T_p = Temperature for plastic strain

c = Specific heat capacity (at critical temperature)

h^3 = Height of deformed zone

l = Distance from centre of heated zone (weld centre)

Over the last two decades the international manufacturing community has shown great interest in the forming or shaping of sheets using a high power laser beam[15]. The main benefit of the laser process is that it requires no hard tooling, and is particularly suitable for small batch production and rapid prototyping. For titanium sheet, it was found that bending was initiated when a surface temperature reached $0,45T_m$ where T_m indicates the melting temperature of the alloy, and a maximum bending angle was achieved at approximately $0,65T_m$. This corresponds with conditions where the thermal gradients within the thickness and yielded widths were both large[16].

2.8   OVERVIEW OF FORMING PROCESSES

All methods of metal forming are based on a mixture of plastic and elastic actions. It is well documented that any metal forming operation will induce residual stresses in the metal. Residual stresses are generated by non-uniform plastic deformation, and the degree of induced residual stresses will fluctuate from one forming operation to the next. These locked-in (residual) stresses contribute to distortion problems in operations subsequent to the plate-forming operation. Currently mechanical forming is the most suitable technique for repeatedly forming thin sheets into the same shape in large volumes[17].

2.9   CHANGES OF TEMPERATURE AND STRAIN

It was found that for mild steel plate, with a constant travel speed, the maximum temperature reached by the specimen increases with an increase in laser input power (P). A typical plot of strain changes that occur in mild steel plate is illustrated in Figure 2.18. The profile in Figure 2.18 was observed for strain experienced by the bottom surface (away from the laser beam). When the laser beam heated the top surface, high compressive strains were produced at the bottom surface. After the

laser line passed, the high compressive strains transformed to tensile strains and then stabilized.
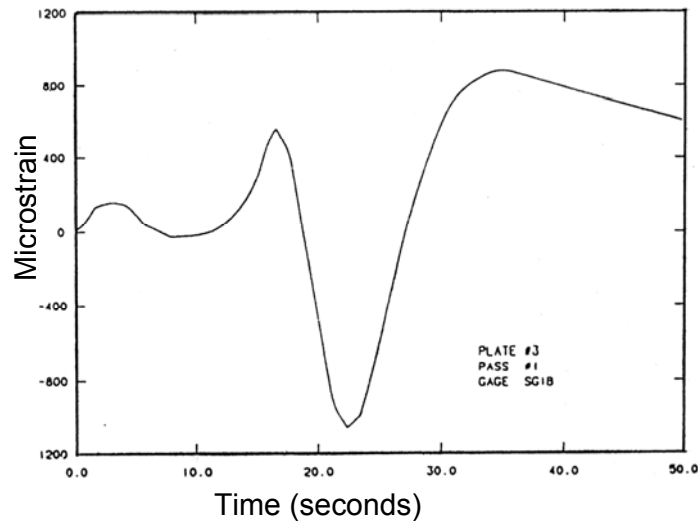
Figure 2.18: Strain changes during a single scan[17]

This plot demonstrates that strain changes during laser line heating and cooling are complex. According to literature there is a linear relationship between the number of passes and angular distortion (residual strain)[17].

2.10   PRIMARY FACTORS AFFECTING LASER FORMING

The main factors affecting laser forming are laser power (P), laser head travel speed (v) and plate thickness (t). For a given plate thickness, the amount of angular distortion increases with an increase in heat input ($\frac{P}{v}$). It was also determined by experiments that there is an optimum heat input for each plate thickness. Experimental results suggest the following:

- The basic mechanisms by which process parameters and plate thickness affect the amount of distortion are similar in laser line heating, flame heating and arc welding.

- The parameter $\frac{P}{t\sqrt{v}}$ may be used effectively for estimating the amount of angular distortion.

2.11   SECONDARY FACTORS

Because there are no boundary constraints, a decreased distortion near the plate edge will be observed. This can be attributed to the following:

- Heat flow: When the heat line is close to an edge, the heat flow pattern is altered by the presence of the edge. The temperature reached by the areas near the edge are higher than those in areas further away, resulting in a smaller temperature difference, hence causing less distortion near the edge.

- Plate restraint: When the heating line is close to an edge, the restraint or bending rigidity of the plate becomes non-symmetric, resulting in less distortion[17].

Angular distortion is produced by the temperature gradient between the irradiated top surface and the cool bottom surface. The bending process should become more efficient by developing a means for increasing the temperature gradient. Experimental results showing the effect of the cooling method on angular distortion are shown in Table 2.1.

From Table 2.1 it can be concluded that the cooling method has a negligible effect on angular distortion when using laser line heating for plate forming[17].

Table 2.1: Effects of cooling method on angular distortion[17]

Cooling method	Angular distortion (degrees)
Water bath, natural convection, with steel support underneath HAZ	1,16
Water bath, natural convection, no steel support underneath HAZ	1,08
Dry ice, entire plate rested on a block of dry ice	1,11
Forced air convection, plate suspended by clamp on one edge	1,13
Natural air convection, plate rested on an aluminium table	1,28

It is important to take into account the microstructural changes during laser forming because the high temperature experienced by the material causes the flow stress to be more significantly influenced by microstructural changes. Work hardening and simultaneous stress relieving by dynamic softening processes characterise laser forming. Not only does dynamic recrystallization lead to recovery/stress relieving, it is also the primary softening mechanism which influences the stress-strain behaviour of the material and therefore its flow stress. This is especially true for steels, for they exhibit relatively low stacking fault energy[18]. The high cooling rates experienced by the material during laser forming precludes significant diffusion controlled transformations near the top surface being irradiated[18].

2.12 MICROSTRUCTURAL CHANGES ASSOCIATED WITH HEATING DPS

The laser forming process employs a laser beam to supply sufficient energy to the material to result in bending by means of the various bending mechanisms as discussed earlier in this Chapter. It is thus important to know the microstructural changes taking place during heating and cooling of dual phase steel. Since the laser forming process involves deformation by the buckling mechanism and heat supplied by the diffused laser beam, the heat will have an influence on the microstructure of the dual phase steel. The microstructure of dual phase steel consists of approximately 20-25% islands of lath martensite in a ferritic matrix. In order to predict or classify the type of microstructural changes that could be expected, it will be necessary to determine the maximum temperature reached by the specimens during the forming process. The rate of cooling will also play an important role. The heat generated during the laser forming process will lead to martensite breakdown to iron carbide/cementite (Fe_3C) globules within a ferritic matrix in regions near the heated/irradiated surface.

The degree of microstructural change will depend on the maximum temperature reached and the rate of heat dissipation (cooling) through

the thickness of the sample. Sections of the sample further away from
the heated surface will only reveal slight over tempering of the martensite
phase. Depending on the time at high temperature, grain growth is also
an important factor that needs to be considered. It is very important
to quantify the amount of microstructural breakdown / change, as this will
have a direct influence on the final component's mechanical properties.

In order to understand the changes in microstructure due to heating /
cooling the iron iron-carbide diagram will be used to illustrate the various
phases present. The iron-iron carbide phase diagram is shown in
Figure 2.19 with an expanded view of the delta (high temperature)
region.
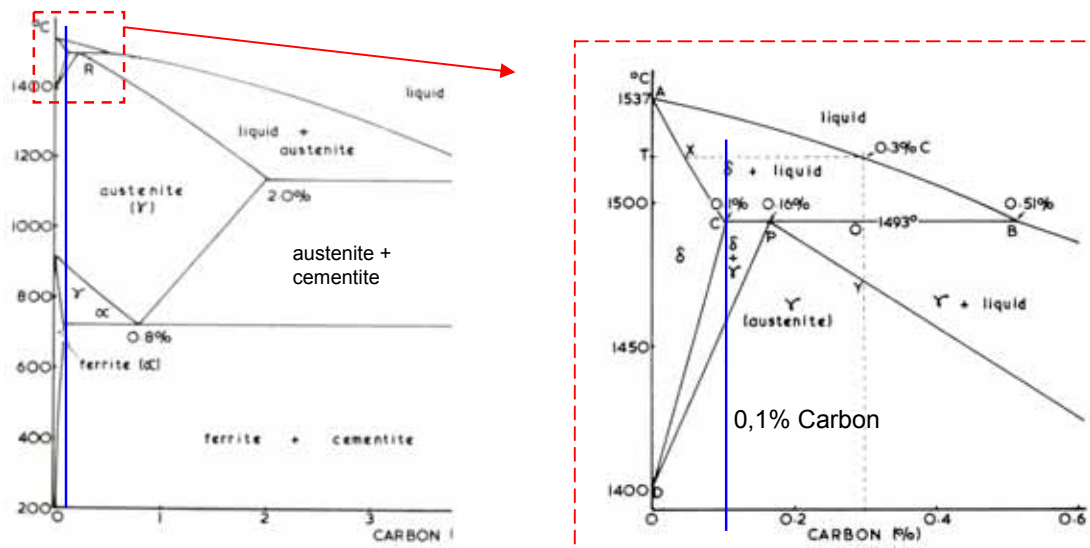
Figure 2.19: Fe-Fe$_3$C phase diagram with expanded view of delta
region[70]

A steel with a 0,1% carbon content is shown by the blue vertical line on
both graphs. This composition corresponds to the dual phase steel's
carbon content of 0,09%. From the above diagrams it can be seen that
temperatures that approach melting temperature can be as high as
1493°C.

Another important factor to consider when looking at laser forming of dual phase steel is the volume changes experienced by the material due to phase changes, and not only due to expansion by the heat supplied by the laser. When steel is heated above approximately 910°C, the microstructure undergoes a polymorphic change from ferrite (α) to austenite (γ). Ferrite has a body-centred crystal (BCC) structure and austenite has a face-centred (FCC) crystal structure. The FCC crystal structure is more closely packed than the BCC crystal structure, and therefore steel shows a decrease in volume when heated through 910°C. This phenomenon is illustrated in Figure 2.20.
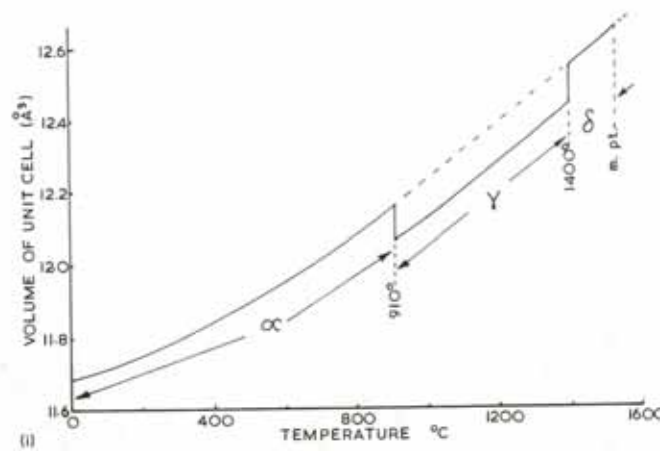
Figure 2.20: The effect of polymorphic transformations on expansion of steel[19]

This transformation is also characterised by heat liberation when cooling from temperatures above 910°C ($\gamma \rightarrow \alpha$ transformation). These changes are important to note, since the laser forming mechanisms utilise the fact that expansion in the volume of material irradiated will set up plastic strains in the material which will lead to deformation of cooling. It can thus be said that transformations which leads to a decrease in volume of material when heated will not assist the laser forming process as the volume of strained material is less, whereas transformation which shows an increase in volume (martensitic transformation) will assist the laser forming mechanism. Before one attempts to try and correlate the microstructural changes to a Time-Temperature-Transformation diagram,

which is more relevant than the Fe-Fe$_3$C diagram since it takes non-
equilibrium cooling into account, it is important to understand the
mechanism by which the various transformation products of austenite
form.

The decomposition of austenite occurs according to three separate, but
sometimes overlapping mechanisms, and results in three different
reaction products, i.e. pearlite, bainite and martensite. The bainite
reaction can be explained as follows: In the region between 350°C and
500°C (normal steel), initial nuclei of ferrite are formed which is coherent
with the austenite matrix. The cementite then precipitates from the
carbon enriched layer of austenite, allowing further growth of the
ferrite. The precipitated carbide tends to lie parallel with the long axis of
the bainite needle to form the typical open feathery structure of upper
bainite.
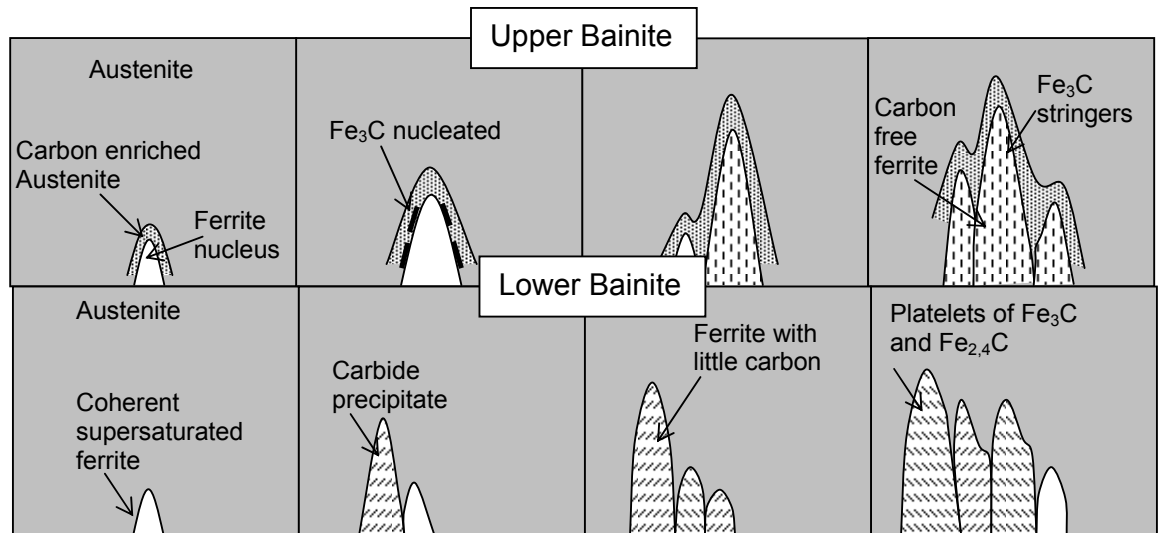
Figure 2.21: Schematic illustration of bainite formation

Below approximately 350°C, coherent ferrite, supersaturated with carbon,
forms first and is then followed by the precipitation of carbide within the
ferrite needle, transversely at an angle of 55°. A proportion of the

carbide is epsilon carbide ($Fe_{2,4}C$) and the ferrite contains a little dissolved carbon. This lower bainite structure is somewhat similar to lightly tempered martensite. These two mechanisms are shown graphically in Figure 2.21.

Martensite formation takes place during fast cooling (quenching) to approximately 250°C, the temperature decreases rapidly enough through the interval in which nucleation could occur, to a temperature so low that the molecular mobility (diffusion) becomes too small for the formation of nuclei. The austenite therefore changes incompletely to a distorted body-centered structure (Body-Centered Tetragonal (BCT)), with little or no diffusion of the carbon into particles of cementite, to form martensite (which is formed at high speed – less than 0,002 seconds). The mechanism of formation of this structure is not nucleation and growth but a shearing process. This mechanism resembles the process of mechanical twinning and involves very little atomic movement, but considerable internal stress due to the shear and to the position of the carbon atoms.

As the temperature decreases, the elastic energy increases and eventually causes a shear in a part of the matrix, which stabilises the rest. Further shear can only take place when the temperature is decreased and more energy gained. The amount of martensite formed is practically independent of time and depends principally on the temperature at which the steel is held. Therefore, a proportion of austenite is usually retained in quenched steel which can be reduced by a decrease in temperature. The temperature at which martensite begins to form (M_s) is progressively lowered as the carbon content of the steel increases.

The temperature is also affected by the alloy content, but the following empirical formula can be used for calculating the M_s from the chemical analysis, provided all carbides have been dissolved in the austenite:

$$M_s \ (°C) = 561\text{-}474(\%C)\text{-}33(\%Mn)\text{-}17(\%Ni)\text{-}17(\%Cr)\text{-}21(\%Mo) \qquad (2.10)$$

Therefore, the calculated M_s for this grade of dual phase steel equals 475,68°C.

This value correlates closely with the values indicated on the TTT diagrams found in literature. The temperature at which the transformation is complete (M_f) is about 215°C below the M_s[20].

Plastic and elastic stresses promote the formation of martensite, but it is retarded when cooling is interrupted. When cooling is resumed after such a stabilisation arrest, martensite only begins to form again after cooling to a lower temperature. Two forms of martensite have been identified depending on carbon content. In low carbon steels, laths, containing many dislocations, are found, while in high carbon steels, plate martensite is found in which the plates are heavily twinned[20].

2.13   DUAL PHASE STEEL PRODUCTION

Dual phase steels are low-carbon steels that have been micro-alloyed with small amounts of elements such as vanadium, niobium or titanium. These steels have a microstructure consisting of islands of hard martensite phase in a matrix of softer ferrite. Dual phase steels behave similarly to low-strength steel during the initial stages of deformation.

Due to work-hardening in subsequent forming stages, the final product could have a high yield strength of typically 550-760MPa. Deformation increases the yield strength at a rate typically about 6MPa for each 0,1% of strain[21].

The microstructure of dual phase steel can be developed by two methods:
- by heat treatment after rolling or
- directly through conventional hot-rolling processes.

In the first method, the steel is heated to a critical temperature within the ferrite-austenite (α-γ) region of the phase diagram for a specific time and then quenched. In the second method, the hot-rolled strip is coiled in the transformation gap as illustrated in Figure 2.22. From previous research it was established that coiling temperature was the parameter that must be carefully controlled and it should be kept below 610°C, preferably in the 510-610°C range and that the microstructure and mechanical properties of the dual phase steels are very sensitive to carbon content[21].
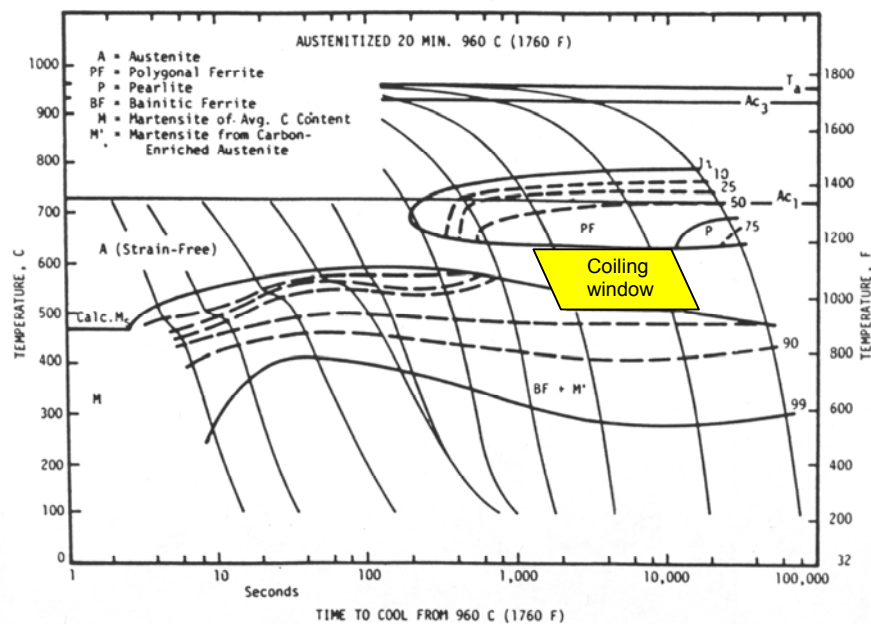
Figure 2.22: Time-Temperature-Transformation diagram for dual phase steel[22]

The term bainitic ferrite refers to acicular ferrite which forms by means of a bainitic transformation and the term refers to a microstructure which is carbide-free and thus different to upper or lower bainite and should not be confused with these phases when using the diagram.

2.14   MATERIAL CHARACTERISTICS

Dual phase steel can be produced directly from the rolling mill by the use of a thermo-mechanical treatment (TMT) well suited to the alloy

composition[23]. The finishing temperature of the rolling process must be close to the upper critical temperature to maximise the acceleration effect that the hot deformation has on the ferrite reaction, but intercritical rolling that can result in the formation of work hardened ferrite (that is detrimental to the cold formability of the steel) must be avoided. The coiling temperature is another important factor, and must be kept below 600°C in order to avoid the formation of pearlite which suppresses the continuous yielding of the metal during tensile testing and lowers its work hardening rate. Amongst the various hardening mechanisms of steels, the distribution of a hard second phase in the ferritic matrix is one of the best methods to optimise the strength/ductility ratio i.e. its formability[24]. To achieve weight reductions and fuel saving in automobiles, designers have concentrated on dual phase steels (DPS) containing ferrite and martensite phases. It has been documented that the volume fraction and shape of grains in dual phase steels strongly influences the material's stress-strain behaviour[25].

The ferrite-martensite structure is obtained by heating the steel to approximately 800°C, which is in the austenite-ferrite region, and quenching it back to room temperature. The structure that is quenched contains ferrite and austenite that is enriched in carbon. The exceptional properties of dual phase steel are low yield strength and a high work hardening rate. The importance of a high work hardening rate is that the strength of the steel increases rapidly as it is deformed. A high work hardening rate is considered to be typical of a mixed microstructure consisting of a hard phase in a soft matrix[26]. It has been found that dual phase steels frequently contain, in addition to ferrite and martensite,

between 2% and 9% of retained austenite. These particles of retained austenite increase the work hardening rate during the first few percent strain during a tensile test. This is due to strain-induced transformation of the retained austenite into martensite[27].

2.14.1 Chemical composition

The chemical composition of the dual phase steel used in this study is shown in Table 2.2.

Table 2.2: Chemical composition of dual phase steel (DPS)

% Carbon	0,09	% Copper	0,025
% Silicon	0,22	% Tin	0,004
% Manganese	0,90	% Vanadium	0,001
% Sulphur	0,04	% Aluminium	0,04
% Chromium	0,71	% Titanium	0,004
% Nickel	0,04	% Boron	0,0003
% Molybdenum	0,01	% Iron	96,696
% Phosphorus	0,04		

The main difference in chemical composition as compared to C2 steel (conventional steel used for manufacture of wheel rims) is given in Table 2.3. Both C2 and dual phase steel are currently used for the manufacture of the same wheel rims and C2 material are sometimes used in place of dual phase steel as it is easier to obtain.

Table 2.3: Difference in main alloying elements between C2 and dual phase steel

Alloying element	C2	Dual Phase Steel
% Silicon	0,03	0,22
%Phosphorus	0,015	0,04
% Chromium	0,05	0,71

The comparison to the C2 chemical composition is just to indicate the main difference in steel composition and hence the different microstructures obtained. The matrix microstructure of C2 consists of ferrite and pearlite compared to the ferrite and martensite matrix of dual phase steel. Elements such as nickel, aluminium, silicon and copper are

all found largely dissolved in ferrite[4]. The carbide forming tendencies of some of these elements are only apparent when there is a significant amount of carbon present. Any element dissolved in ferrite increases its hardness and strength due to solid solution strengthening. The strengthening effect of the dissolved elements contributes relatively little to the overall strength of the steel[26].

The change in critical temperature produced by the presence of alloying elements is important in the heat treatment of alloy steels, since it will either raise or lower the hardening temperature compared to plain-carbon steel. All alloying elements tend to reduce the carbon content of the eutectoid, but only nickel and manganese reduce the eutectoid temperature.

2.14.2 Mechanical properties

The mechanical properties, as determined by the tensile test, are given in Table 2.4.

Table 2.4: Mechanical properties of dual phase steel

0,2% Proof stress	Tensile strength	Modulus of Elasticity	% Elongation	% Reduction of cross-sectional area
341,3 MPa	577,8 MPa	198,7 GPa	23,8	52,5

The average hardness of the material in the as-received condition was found to be approximately $HV_{0,5}$ 157. From Table 2.3 it is clear that the material has a high ductility, based on percentage elongation and percentage reduction in cross-sectional area.

It is well known that the dual phase steels developed over the past decades show low yield strengths, continuous yielding, high work hardening rate, good formability and good ductility[28]. This work hardening process in dual phase steels under axial loading is complex. The work hardening process can be divided into three strain regions,

each region exhibiting a different work hardening rate. The rapid work hardening in the first phase leads to the removal of residual stresses and the rapid build-up of back stress in the ferrite caused by plastic instability of the two phases. During the second phase, the work hardening rate decreases due to the constrained deformation of the ferrite caused by the presence of the rigid martensite phase. The third stage shows the formation of dislocation cell structures and further deformation in the ferrite is governed by dynamic recovery and cross-slip and by ultimate yielding of the hard martensite phase.

It has been shown in previous work that the initiation of microviods occurs by decohesion of ferrite-martensite interfaces or by the shear cracking of martensite particles[28]. It has also been observed that the majority of microvoids are formed at the ferrite-martensite interface rather than at the cracked martensite, and eventually these microvoids coalesce to cause failure during subsequent tensile loading. It is therefore preferred that the martensite produced by heat treatment be kept as deformable as possible to remain coherent with the matrix during

cold forming operations. Amongst the various martensite morphologies produced by heat treatment, the fibrous lath martensite, with a high degree of structural coherency with the surrounding ferrite, leads to the lowest microvoid density during cold deformation[28].

2.15   RESIDUAL STRESSES

It is well documented in literature that residual stresses are an important factor to consider in design, especially when designing against fatigue failure. Because residual stresses are generated by non-uniform plastic deformation, it is important to consider the residual stresses developed in metalworking / forming processes. It is envisaged that the laser forming process will induce less detrimental residual stresses than the conventional forming process. This in turn should lead to an increase in the fatigue life of the component. Residual stress analyses of the laser

formed samples need to be done in order to determine if the laser forming method can be considered a 'stress relieving' process. It is important to note that cooling can produce residual stresses in the same way as non-uniform plastic deformation.

The main objective of this chapter is to compare the residual stress magnitude of the samples produced by the various laser parameters and the results will then be used to make a correlation between residual stress magnitude and fatigue life. Fatigue properties of materials have become progressively more important as technology has developed a larger quantity of equipment / machinery that is subjected to repeated loading and / or vibration (e.g. automobiles).

It is expected that laser forming will have less of an effect on the reduction of fatigue strength of dual phase steel compared to the mechanical stretch forming operations currently used in the manufacture of automotive wheel rims. During conventional forming operations, microvoids are formed between the hard (martensite) and soft (ferrite) phases in dual phase steel. These microvoids lead to a decrease in fatigue strength of the material since these microvoids can be considered to be 'microcracks' already present in the material. It is envisaged that the heat absorbed by the material during laser forming will influence the microstructure and hence the fatigue performance, but to a lesser degree than conventional stretch forming since no microvoids will be generated within the microstructure.

Residual stresses are a system of stresses within a component when it is free from external forces[29]. During deformation, a small portion of the applied stress is stored within the component as a tangled network of dislocations[30]. These residual stresses increase the total energy of the component.

The residual stress distribution is not necessarily uniform throughout the deformed component. Residual stress can either be beneficial or detrimental depending on magnitude, nature, and distribution of the stress in relation to the applied load. Because residual stresses are only elastic in nature, the maximum value which a residual stress can reach is the yield stress of the material. For analytical purposes, residual stresses can be treated the same as ordinary applied stresses. Thus, effectively a compressive residual stress subtracts from the applied tensile stress, and a tensile residual stress adds to an applied tensile stress.

Metals are commonly 'stress relieved' by heating to a temperature where the yield strength of the material is the same or less than the value of the residual stress. Because the material's yield strength has been lowered due to heating, the material can now deform and release the stress as the residual stress magnitude is now larger than the yield strength, and plastic deformation can take place. Non-uniform thermal expansion and contraction can also produce residual stresses and it is therefore important to slow cool from the stress relief temperature. The differential strains that produce residual stresses can be reduced at room temperature by plastic deformation. It is common practice for products like sheet and plate to be stretched beyond the yield stress to relieve differential strains by plastic deformation.

Allowing for residual stresses in the assessment of service performance will vary according to the failure mechanism. In most cases it is not necessary to take residual stresses into account in calculations of the static strength of ductile materials. When designing against fatigue or buckling of structures, appropriate allowances for residual stresses need to be made. Residual stresses play a major role in fracture in the brittle and transitional regimes. Therefore, the stress intensity, K or energy release rate, J, due to residual stresses, must be calculated and included in fracture assessments.

2.16   RESIDUAL STRESS MEASURING TECHNIQUES

Due to the fact that it is difficult to accurately calculate residual stresses by analytical methods, they are usually determined by a variety of experimental methods. Residual stresses may be measured by non-destructive techniques which include: X-ray diffraction, neutron diffraction and magnetic and ultrasonic methods. Destructive techniques include: hole drilling and the ring core and deep hole methods; and by sectioning methods which include block removal, splitting, slicing and layering. Depending on the scale at which the metal is analysed, different kinds of stresses are defined: the macro stresses (stresses of the first kind) over a few grains, the stresses of the second kind over a particular grain and the stresses of the third kind across sub-microscopic areas (several atomic distances within the grain).

The only residual stress evaluation method available to analyse laser formed specimens was the hole drilling method. It should be noted that the residual stress measurements on the various laser formed specimens are for comparative purposes only. Therefore, only the hole drilling method will be explained in this chapter.

2.17   HOLE-DRILLING METHOD FOR MEASURING RESIDUAL STRESSES

The hole drilling method is one of the most commonly used semi-destructive mechanical methods for experimental stress analysis[31]. The hole-drilling method can be summarized by the following steps:

- Application of a special three-element strain gauge rosette onto the surface of the component to be analysed.
- A small hole is drilled into the component through the centre of the rosette.
- Measurements are taken of the relaxed strains, corresponding with the initial residual stress.
- These strain measurements are then used to calculate the principal residual stresses and their angular orientation[32].

The aforementioned procedure is relatively simple and has been standardized in ASTM E837-01[33]. The key features of this method are:

- This method is only valid for residual stresses up to 60% of the yield strength.

- Highly sensitive to position and shape of drilled hole.

- Residual stresses determined are the average over the depth of the drilled hole.

- Incremental drilling techniques offer qualitative results only.

2.17.1 Residual Stress Calculation

The minimum and maximum relieved residual stresses can be calculated according to ASTM E837-01[33]. In the case of thick specimens (thickness greater than 1,2D where D is equal to the diameter of the gauge circle), the stresses are assumed to be uniform throughout the hole depth. The three combination stresses P, Q and T are calculated and correspond with the three combination strains p, q and t. The following formulae are used:

$$P = -E(\Sigma \bar{a}.p)/\bar{a}^2 /(1+v) \tag{2.11}$$

$$Q = -E(\Sigma \bar{b}.q)/(\Sigma \bar{b}^2) \tag{2.12}$$

$$T = -E(\Sigma \bar{b}.t)/(\Sigma \bar{b}^2) \tag{2.13}$$

Where: $p = (\varepsilon_3 + \varepsilon_1)/2 \;\; ; \;\; q = (\varepsilon_3 - \varepsilon_1)/2$ (2.14 ; 2.15)

$$t = (\varepsilon_3 + \varepsilon_1 - 2\varepsilon_2)/2 \tag{2.16}$$

$\bar{a}$ and $\bar{b}$ are dimensionless, almost material independent constants[33], the complete table acquired from ASTM 837-01 is given in Appendix C.

where: $\bar{a} = -\dfrac{\bar{A}(2E)}{(1+v)}$ and $\bar{b} = -\bar{B}(2E)$ (2.17 ; 2.18)

E = Modulus of Elasticity and v = Poisson's ratio

Therefore, σ_{max} and σ_{min} is:

$$\sigma_{max}, \sigma_{min} = P \pm \sqrt{Q^2 + T^2} \tag{2.19}$$

Figure 2.23 is a schematic illustration of the residual stress and typical surface strain relieved when a hole is drilled into the specimen.
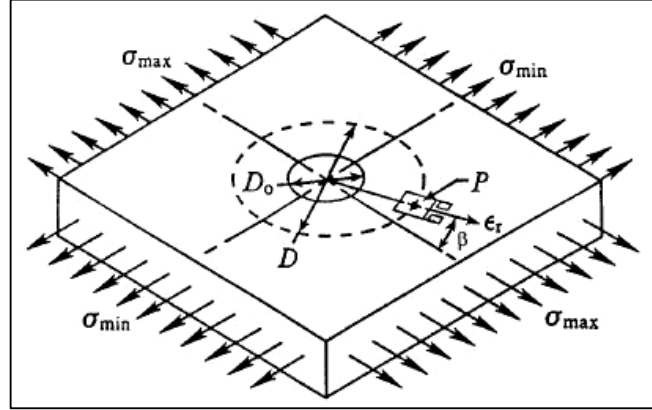
Figure 2.23: Schematic illustration of surface reaction when a hole is drilled into a specimen[33]

The following equation relates relieved surface strain to the relieved principal stresses:

$$\varepsilon_r = (\overline{A} + \overline{B}\cos 2\beta)\sigma_{max} + (\overline{A} - \overline{B}\cos 2\beta)\sigma_{min} \qquad (2.20)$$

Nomenclature:

ε_r = Relieved strain measured by a radially aligned strain gauge at P

$\overline{A}, \overline{B}$ = Calibration constants

σ_{max} = Maximum (most tensile) principal stresses present at hole location before drilling

σ_{min} = Minimum (most compressive) principal stresses present at hole location before drilling

β = Angle measured clockwise from the direction of gauge 1 to the direction of σ_{max}

D = Diameter of gauge circle

D_o = Diameter of the drilled hole

2.17.2 Hole-drilling procedure using the RESTAN system

The system consists of four main components as illustrated in Figure 2.24. Appendix E gives a brief description of the operation of the various components.
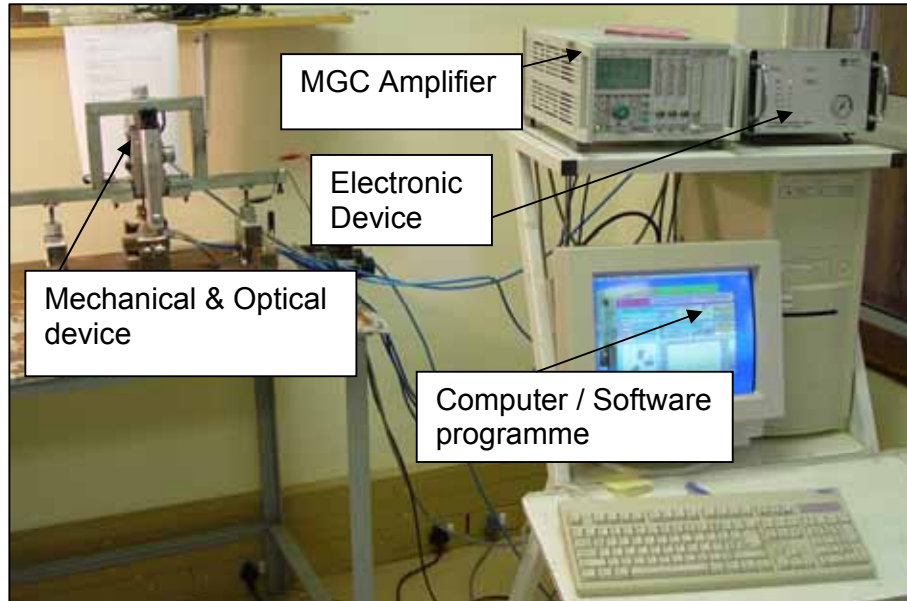
Figure 2.24: System used for hole-drilling residual stress measurements

2.18   FATIGUE OF METALS

Fatigue failure is a phenomenon occurring when cyclic stresses, often at values well below a given material's tensile strength, causes microscopic damage to accumulate and causes ultimate failure of the component[22]. There are currently three major approaches for analysing and designing against fatigue failures. The *stress-based approach*, which was developed by 1955, is based on an analysis of the nominal (average) stresses in the region of the component being analysed. The nominal stress that can be resisted under cyclic loading is determined by considering mean stresses and by making adjustments for the effects of stress raisers. The *strain-base approach* involves a more detailed analysis of the localised yielding that may occur at stress raisers during

cyclic loading. The *fracture mechanics approach* treats growing cracks using the methods of fracture mechanics.

The two most common methods for obtaining fatigue data are the rotate bend and reverse bend fatigue tests. In both cases, samples are machined to provide a wasted (hour-glass) gauge length which is then loaded to the required testing conditions. The data obtained from such tests are usually presented on a graph (S-N curve) of alternating stress (σ_a or S_a) against the number of cycles to failure (N_f)[34]. Some materials, especially plain-carbon and low-alloy steels, exhibit a distinct stress level below which fatigue failure does not occur under ordinary conditions. This is illustrated on the S-N curve where it appears to become flat.

These lower limiting stress amplitudes are called fatigue limits or endurance limits (σ_e or S_e). For materials like aluminium and copper where the S-N curve does not appear to approach an asymptote, a fatigue limit is usually specified at a specific long life, e.g. 10^7 or 10^8 cycles.

Fatigue strength is the term used to specify a stress amplitude value from an S-N curve at a particular number of cycles of interest. High-cycle fatigue refers to situations of long fatigue life where the stress is sufficiently low that yielding effects do not dominate the behaviour. High-cycle fatigue starts typically in the range 10^2 to 10^4 cycles, but this value varies with material. In low-cycle fatigue, the strain-based approach is more useful as this deals specifically with the effects of yielding[35].

Figure 2.25(a), (b) and (c) illustrates the nomenclature associated with constant amplitude cycling.

(a)

(b)

(c)
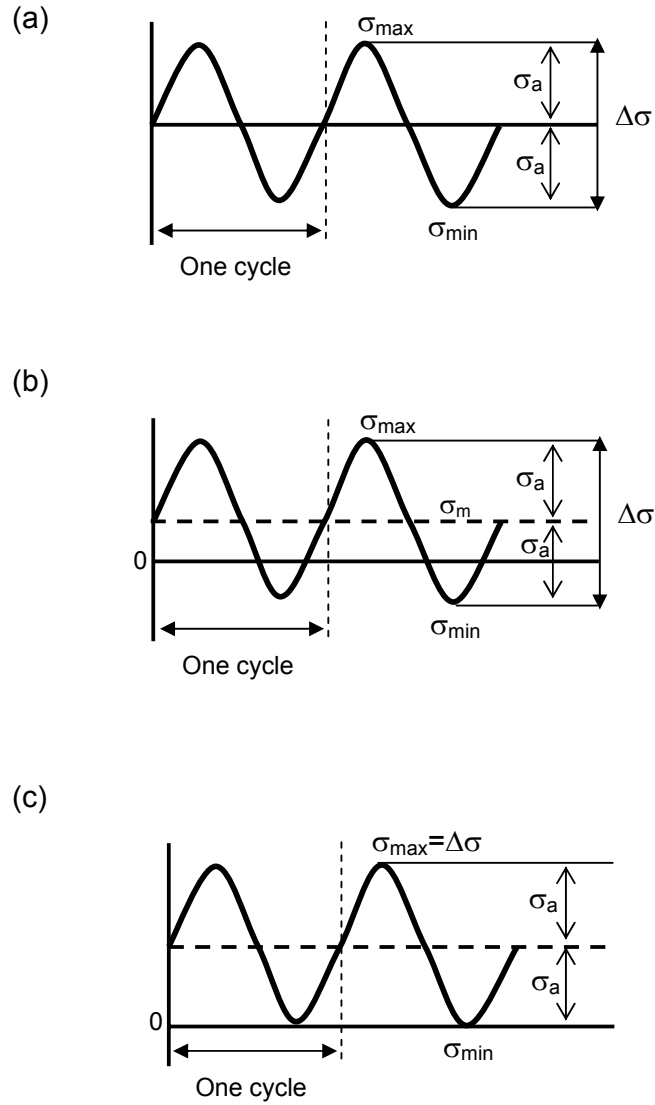
Figure 2.25: (a) Completely reversed stressing, $\sigma_m = 0$; (b) Nonzero mean stress, σ_m; (c) Zero to tension stressing, $\sigma_{min} = 0$

The following relationships and terms are generally used when discussing mean and alternating stress:

Stress range: $\Delta\sigma = \sigma_{max} - \sigma_{min}$ (2.21)

Stress amplitude: $\sigma_a = \dfrac{\sigma_{max} - \sigma_{min}}{2}$ (2.22)

Mean stress: $$\sigma_m = \frac{\sigma_{max} + \sigma_{min}}{2}$$ (2.23)

Stress ratio: $$R = \frac{\sigma_{min}}{\sigma_{max}}$$ (2.24)

Amplitude ratio: $$A = \frac{\sigma_a}{\sigma_m}$$ (2.25)

The stress ratio and amplitude ratio values corresponding with several general loading conditions are shown in Table 2.5.

Table 2.5: Values for general loading conditions

Fully reversed	R = -1	A = ∞
Zero to maximum	R = 0	A = 1
Zero to minimum	R = ∞	A = -1

The ratio of fatigue limit (S_e) to tensile strength (S_u) for a material is known as the fatigue ratio. Most steels with a tensile strength below 1400 MPa have a fatigue ratio of 0,5. It should be noted that this ratio can range form 0,35 to 0,6. It is generally assumed that the alternating stress level corresponding with a life of 1000 cycles can be estimated as $0,9S_u$[35]. The following relationships to Brinell hardness exist:

$$S_u(MPa) \approx 0,5BH(6,89476)$$ (2.26)

$$S_e(MPa) \approx 0,25BH(6,89476) \quad \text{for BH} \leq 400$$ (2.27)

$$S_e \approx 690MPa \quad \text{for BH > 400}$$ (2.28)

The relationship between fatigue limit and tensile strength are given by the following equations:

$$S_e \approx 0,5S_u \quad \text{when } S_u \leq 1400MPa$$ (2.29)

$$S_e \approx 690MPa \quad \text{when } S_u > 1400MPa$$ (2.30)

2.19 ESTIMATED S-N CURVE

In Juvinall and Marshek (1991) a procedure was suggested that can be applied to a variety of engineering materials[36]. The method uses log-log coordinates, a point at 1000 cycles is established and a straight line is then drawn to an estimated fatigue limit at a specified number of cycles, N_e. The estimated curve corresponds with completely reversed loading, that is, to zero mean stress conditions[36].   The effect of various surface finishes on the fatigue limit of steels is shown graphically in Figure 2.26.
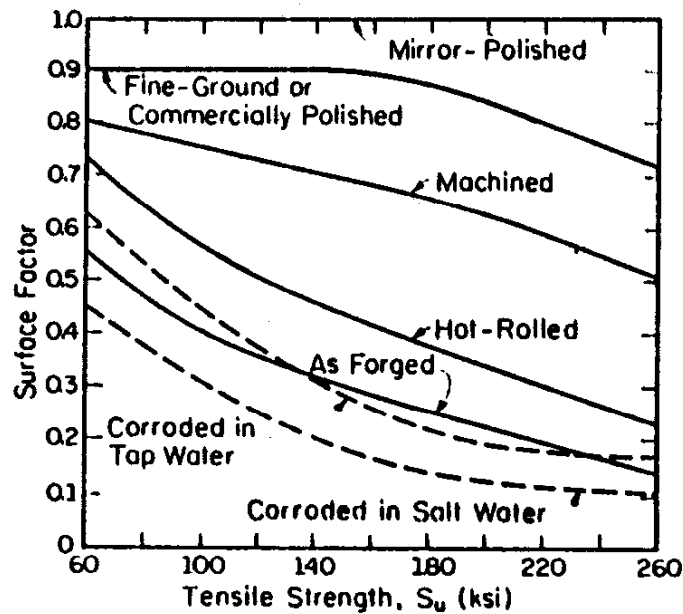
Figure 2.26: Effect of various surface finishes on fatigue limit of steels[36]

The parameters used for producing an estimated S-N curve are shown in Table 2.6.

Table 2.6: Parameters for estimated S-N curve[36]

Parameter	Applicability	Juvinall (1991)
Bending fatigue limit factor: m_e	Steels, $S_u \le 1400$MPa Higher strength steels Cast iron, Al alloys if $S_u \le 325$MPa Magnesium alloys	0,5 $\le$0,5 0,4 0,35
Load type factor: m_t	Bending Axial Torsion	1,0 1,0 0,58
Size (stress gradient) factor: m_d	Bending or torsion d < 10mm d = 10 to 50mm d = 50 to 100mm Axial	 1,0 0,9 0,8 0,7 to 0,9
Surface finish factor: m_s	Polished Ground Machined	1,0 See figure 5.2 See figure 5.2
Life for fatigue limit point: N_e, cycles	Steels, cast irons Aluminium alloys Magnesium alloys	10^6 5×10^8 10^8
Constants for point at $N_f = 10^3$ m' ; k_f'	Bending or torsion	$m' = 0,75$ $k_f' = k_f$
	Axial, small eccentricity	$m' = 0,75$ $k_f' = k_f$

2.19.1 Theory calculations for Dual Phase Steel

For bending: $S_u' = S_u$

Point 1: $(S_a, N_f) = (m'S_u', 10^3)$ (2.31)

Point 2: $(S_e, N_f) = (mS_u, 10^6)$ (2.32)

Where $S_a = AN_f^B$ $(10^3 \le N_f \le 10^6)$ (2.33)

From Table 6.4 and Figure 6.21 the following values were obtained:

$m_e = 0,5$ $m_t = 1,0$ $m_d = 1,0$ $m_s = 0,9$ (fine ground)

It must be noted that the value for m_d was estimated by comparing cross-sectional areas between the plate specimen and a round hour-glass specimen.

The combined reduction factor, m, therefore is:

$$m = m_e \times m_t \times m_d \times m_s \qquad\qquad (2.34)$$

$$m = 0,5 \times 1 \times 1 \times 0,9 = 0,45$$

Point 1: S_{1000} = m'S_u'

                            = 0,75(577,78 MPa)

                            = **433,34 MPa**   **at 10^3 cycles**

Point 2: S_e = mS_u

                            = 0,45(577,78 MPa)

                            = **260 MPa**   **at 10^6 cycles**

The estimated S-N curve according to the Juvinall and Marshek method for dual phase steel, with a fine ground surface finish, is illustrated in Figure 2.27.
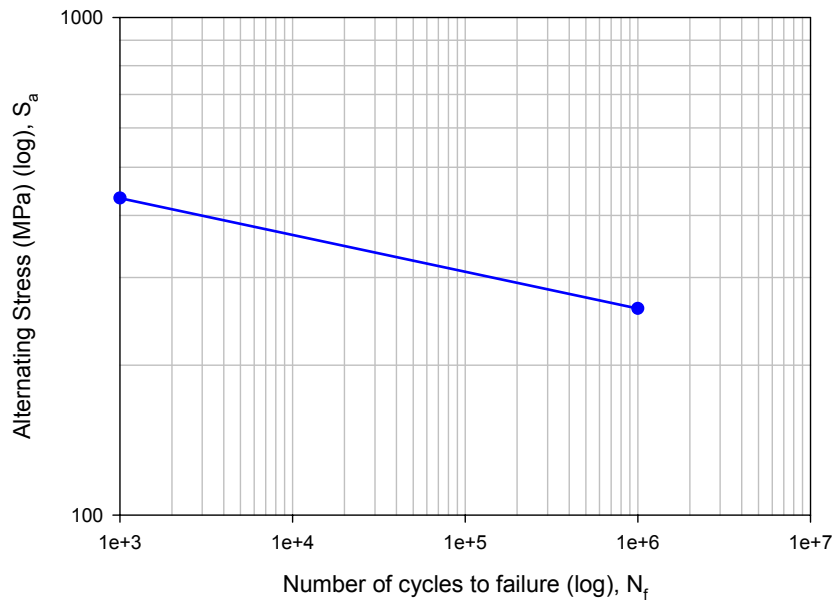
Figure 2.27: Estimated S-N curve for Dual Phase Steel

The equation corresponding with the estimated curve is:

$$S_a = A N_f{}^B$$

$$B = \frac{\log 433,34 - \log 260}{\log 10^3 - \log 10^6} = -0,0740$$

$$A = \frac{S_a}{N_f{}^B} = \frac{433,34}{1000^{-0,0740}} = 722,48 MPa$$

$$\therefore \quad S_a = 722,48 Nf^{-0,0740} MPa \qquad (10^3 \le N_f \le 10^6) \qquad (2.35)$$

2.20 SUMMARY

Laser bending is a promising technology for bending sheet metal with a high thermal conductivity (all metals). Although lasers have been used successfully in various manufacturing processes (welding, cutting, marking, etc), little information is available on the influence of laser forming on many automotive alloys such as dual phase steel. It is envisaged that the laser forming process will enhance fatigue performance/characteristics of automotive formed components as compared to conventional forming processes. This will result in the use of thinner gauge sheet metal for the manufacture of automotive components, while maintaining the rigorous safety requirements.

It is clear from this thorough literature overview that laser forming of sheet material of thickness greater than 1mm is complex in nature. The variables that can influence the process are complicated and their interaction with each other is not easily controlled. The main parameters that will be controlled in this study are as follows:

- Laser power (P)
- Laser head travel speed (v)
- Laser beam size (mm)

Other parameters that are important are plate thickness, t, and laser beam energy distribution, which will be kept constant in all the

experiments done for this study. Changes in microstructure are also important to note since the forming process takes place at relatively high temperatures (approaching melting temperature). These high temperatures can also act as a stress-relief or softening heat treatment process.

It is clear that a wide variety of industrial lasers are available to provide laser solutions for a large number of manufacturing tasks. The main disadvantage of incorporating laser technology into the manufacturing process is the initial cost involved in acquiring the laser system. Although the initial cost of setting up a laser system is high, the advantages of the process over the long term can be economically viable. It is envisaged that with further research into the field of the laser forming process, it could become a major forming technique, especially for very hard and difficult to form metallic materials.

The laser forming (LF) technique can only become a competitive production process once the complexity of the process is well defined. The effect of process parameters, material properties, initial cost, are all important considerations before a decision with regard to the applicable forming process can be made. Some of the complexities of this forming process will be the influence of the laser beam intensity on the material's microstructural changes. A change in a material's microstructure has a direct influence on its mechanical properties, and it will be of critical importance to be able to predict the resultant mechanical properties of the material after the laser forming process.

CHAPTER 3

EXPERIMENTAL SETUP

3.1   INTRODUCTION

The method of producing laser formed specimens and how they were
tested will be explained in this Chapter. Experimental setup for the
following procedures are described: Laser forming of specimens;
Temperature analysis (IR camera); Residual stress measurements; and
Fatigue testing.

3.2   LASER FORMING – EXPERIMENTAL SETUP

Dual phase steel samples of dimensions 200x50x3,5 mm were irradiated
with a laser beam with various powers, scanning velocities and beam
diameters. The specimens were graphite coated (later coated with matt
black lacquer) to maximise absorptivity of laser energy. The energy
distribution of the laser beam (beam's mode) was kept constant as a
doughnut shape during all trials. A non-dimensional sketch of the beam
profile is illustrated in Figure 3.1.
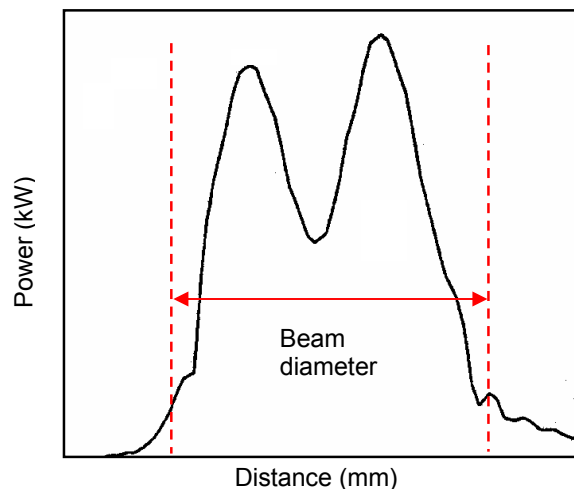
Figure 3.1: Non-dimensional beam profile

The instrument used for forming the dual phase steel samples was a
5kW Trumpf continuous wave CO_2 laser system. Gas flow rate through

the laser head was 10ℓ/min and the shielding gas was Argon. The Trumpf laser system used for the experiments is shown in Figure 3.2. The unit is classified as a Class 1 laser system and has a maximum output power of 5kW.
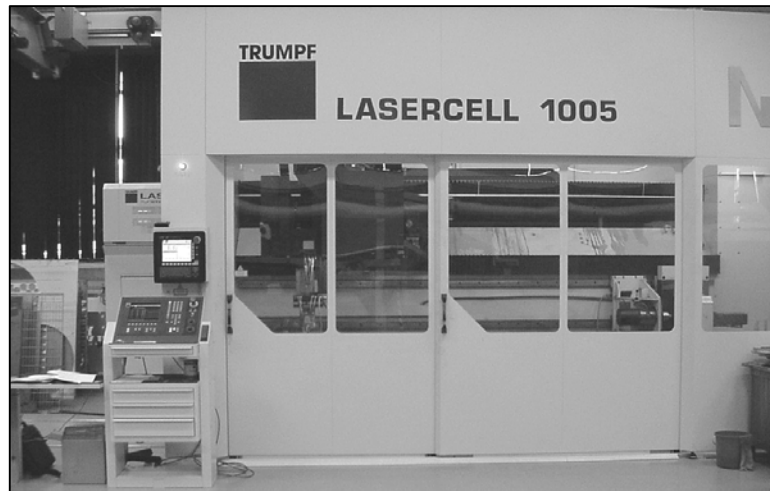
Figure 3.2: Trumpf laser system

Actual bend height (i.e. the change in height due to bending) was measured after various scanning intervals. The specimens to be irradiated were clamped at one end in a clamping device and radiation was started from the free end of the specimen as to obtain maximum deformation. The experimental setup is shown in Figure 3.3.
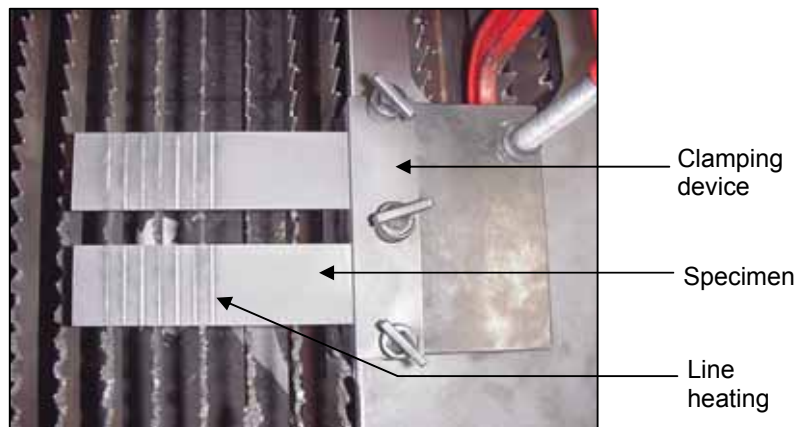
Figure 3.3: Experimental setup

Typical bend specimens formed during laser line heating are shown in Figure 3.4. Change in bend height measurements were taken from the free end as indicated in Figure 3.4. After the forming process was completed, the samples' radii of curvature were measured according to the method explained in Appendix A.
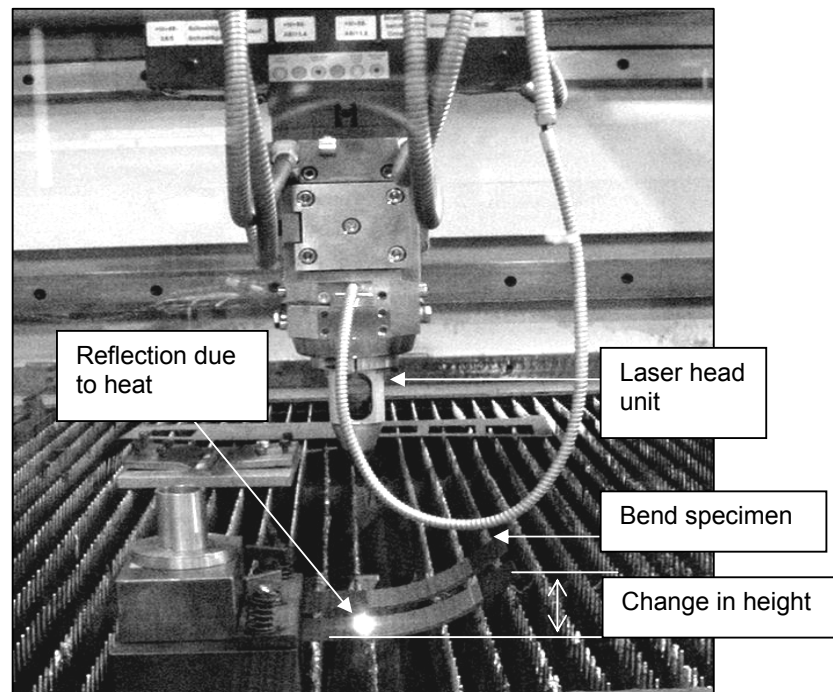
Figure 3.4: Typical bend specimens during laser line heating

3.3   TEMPERATURE ANALYSIS – EXPERIMENTAL SETUP

Temperature analysis was done using a FLIR SC1000 infrared camera. The camera was fitted with a special filter so as not to damage the detector by the radiation of the CO_2 laser. The most important parameter to note during temperature analysis is the emissivity of the material. This is quite difficult to do as the emissivity changes with changes in the temperature of the specimen.

According to literature, the values listed in Table 5.1 can be used for steel with various surface conditions[37]. The emissivities of metals are low, and only increases with temperature. Non-oxidised metals

represent an extreme case of almost perfect opacity and high specular reflectivity, which does not vary greatly with wavelength[38].

Table 3.1: Emissivity values[26]

Material	Surface condition	Temperature	Emissivity, $\in$
Steel	Polished	100°C	0,066
Mild steel		232-1065°C	0,20-0,32
Sheet steel	Oxidised	24°C	0,80
Matte black lacquer		77-146°C	0,91

The emissivities of materials vary greatly with wavelength, temperature, and surface condition. Verification of emissivity values for this study was done by heating uncoated samples to known temperatures and measuring temperature with the infrared camera. The emissivity value was then set to correspond with the correct temperature reading. At temperatures above 1000°C, the dual phase steel samples exhibited emissivities between 0,76 and 0,72. It was decided to use a mean value of 0,74, which is the average value obtained during temperature calibration, for all thermal analyses. Microstructure analysis was also used as a confirmation tool. It is estimated that the error involved in temperature readings is ±10°C based on the calibration which showed this type of temperature range.

The results from the infrared camera were then analysed using ThermaCAM Researcher 2002 software. Temperature measurements were taken at positions as shown in Figure 3.5.
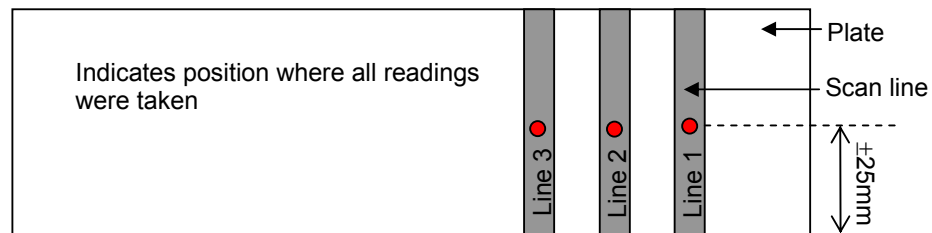
Figure 3.5: Schematic diagram showing position of temperature measurement

Measurements were taken at:

1) **just before the first scan** (reading taken at ⬤ when the laser beam was at position A),

2) **maximum temperature during the fifth scan** (reading taken at ⊗
when laser the beam was at position B) and

3) **just after the fifth scan** (reading taken at ⊗ when the laser beam
was at position C).

The measurement setup is graphically illustrated in Figure 3.6. Each
laser line was scanned five times with the laser beam with a 15 second
time interval (delay) between each line.
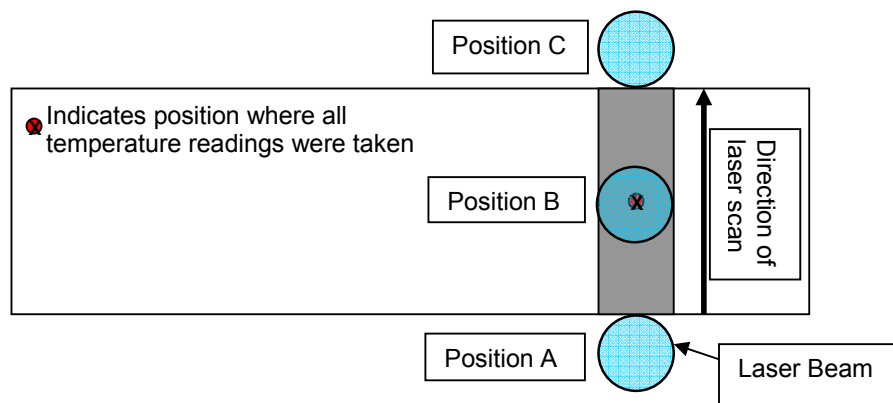
Figure 3.6: Graphic illustration of position of temperature measurement

After the fifth scan, the matt black lacquer coating was completely burned
off; hence there was a difference in emissivity values for the first scan
line and the fifth scan line. Figure 3.7 shows the setup followed during
the recording of the laser forming process with the FLIR SC1000 thermal
camera. Time-temperature measurements for the complete processes
are given in Appendix B.
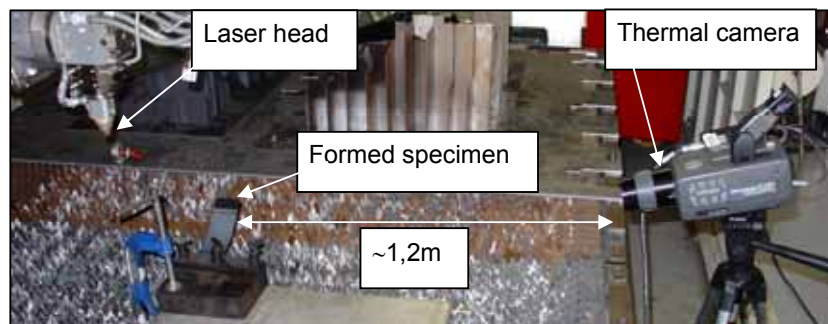
Figure 3.7: Thermal camera setup

3.4   RESIDUAL STRESS MEASUREMENT SETUP

For residual stress evaluation of the laser formed specimens, the following test parameters were used:

- Drilling depth: 2mm
- Drilling method: Automatic
- Evaluation method: Polynomial
- Number of incremental drilling steps: 20
- Feed rate: 0,2mm/min
- Delay time: 10 seconds

The above test parameters have been chosen on the basis of previous research results obtained on dual phase steel[36].

The rosette strain gauge used for evaluations was Micro Measurement's type EA-06-031RE-120. It was necessary to use a rosette strain gauge with a small diameter as the space between consecutive laser lines are relatively small / narrow. The limitation of using this type of gauge is loss of sensitivity/accuracy during measurement. This does not constitute a major problem, as the residual stress results obtained in this study will only be used for comparative purposes between samples created with various laser parameters and not to quantify magnitudes of induced stresses. Locations of the strain gauges and identification of result sets are shown in Figure 3.8. All measurements were taken on the centre-line of the specimens.
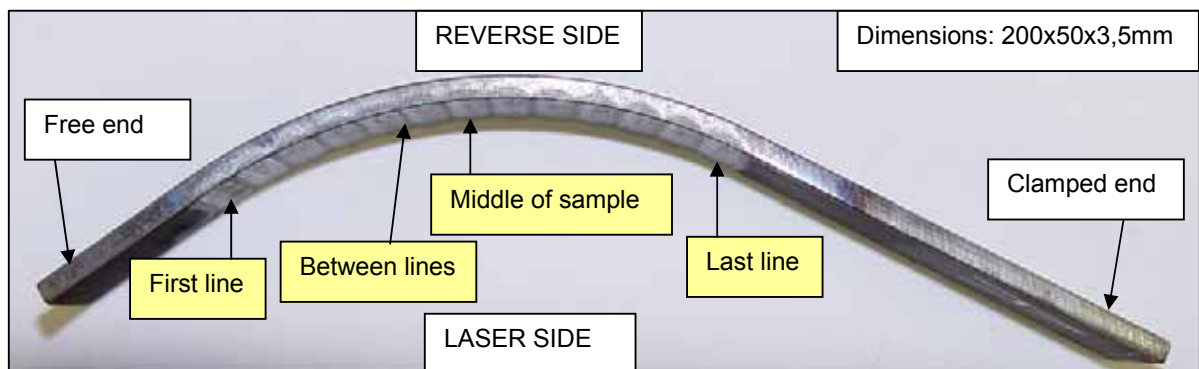
Figure 3.8: Indication of strain gauge location (yellow) for residual stress measurements

Surface preparation and strain gauge application was done according to the manufacturer's recommendations.

3.5   FATIGUE TESTING – EXPERIMENTAL SETUP

The main components of the TMS fatigue testing machine are an electrical motor with an adjustable double eccentric, connecting rod with bending arm and load transducer. The TMS testing machine adheres to the following design specifications:

- Capacity: 650Nm
- Load ranges: 0 to 2000kg
- Reversed bending moment: 325Nm
- Swing angle: $\pm12°$ maximum
- Stress cycles: 1 to 1420 revolutions per minute
                                            (2 to 50Hz)

The TMS fatigue testing machine is shown in Figure3.9. The fatigue testing setup procedure is explained in Appendix C.
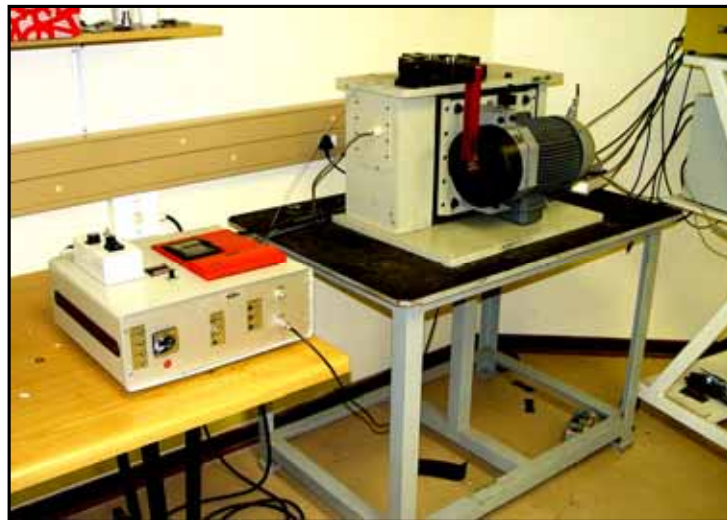
Figure 3.9: TMS fatigue testing machine setup

3.5.1 Fatigue specimens

Fatigue specimens were produced by laser forming plate specimens with dimensions of 200x50x3,5mm. The plate specimens were laser irradiated from the free end as discussed in Section 3.2. The various laser parameters used to produce the specimens are given in Table 3.2.

Table 3.2: Laser parameters used to produce fatigue specimens

Laser Power (kW)	Beam Diameter (mm)	Scanning Velocity (m/min)	Line Energy (P/v) (J/m)	Interval spacing (mm)
1,5	7,5	1,2	1250	7,5
5	20	2,5	2000	10

The deformed plate were then set up as shown in Figure 3.10 and laser cut into the shape (hour-glass) of the fatigue specimen. The specimen appearance after the laser cutting operation is shown in Figure 3.11.
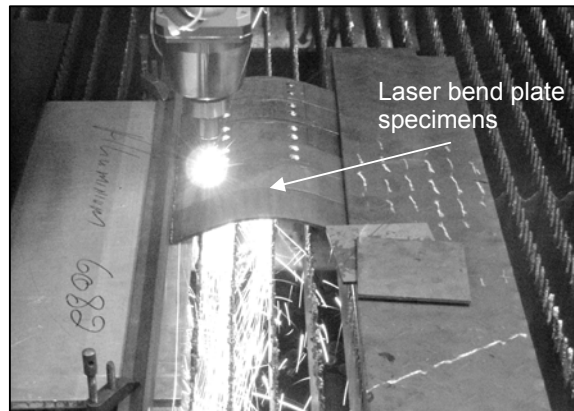
Figure 3.10: Cutting of fatigue specimens from laser formed plate
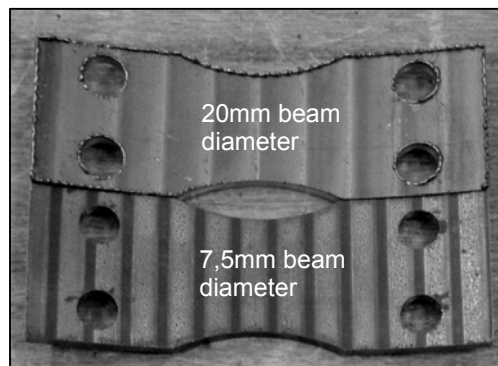
Figure 3.11: Specimen appearance after laser cutting

The melted edge was removed during the final machining operation on the CNC milling machine. A schematic illustration of the dimensions of the final specimen is shown in Figure 3.12.
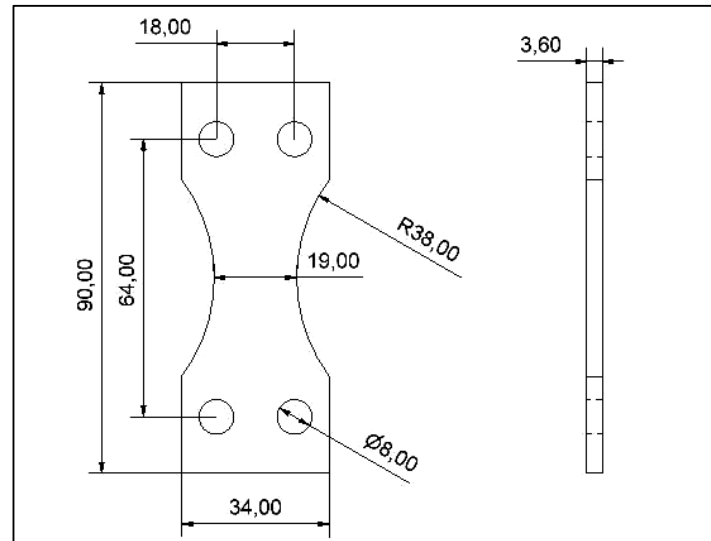
Figure 3.12: Dimensions of hour glass fatigue specimen (mm)

After final machining, the specimen surfaces were cleaned using a flapper wheel with a 120 grit roughness. The average surface roughness of the samples' surfaces after the flapping operation is given in Table 3.4. Appendix D shows the actual surface roughness readings obtained. Surface roughness measurements were done according to DIN specification (see Table 3.3 for specification table) using a Mitutoyo surface roughness tester (model SJ-201).

Table 3.3: Standard cut off length for Ra from non-periodic roughness profile

	Cutoff length (mm)	Evaluation length (mm)
$0,1\mu m < Ra \leq 2\mu m$	0,8	4

After the flapping operation, the fatigue samples were cleaned with acetone and coated with a layer of non-conductive paint and a strain gauge applied on the smallest cross-sectional area.

Table 3.4: Average surface roughness results

Sample number	Location of measurement	Ra (μm)	Ry (μm)	Rz (μm)	Rq (μm)
Sample 1 (1,5kW)	Back surface (opposite laser irradiated surface)	0,98	6,95	6,95	1,07
	Radiated surface – on laser line	1,01	5,99	5,99	1,23
	Radiated surface – between laser lines	0,82	5,16	5,16	1,00
Sample 2 (5kW)	Back surface (opposite laser irradiated surface)	1,01	6,51	6,51	1,24
	Radiated surface – on laser line	0,98	6,32	6,32	1,21

A conductive path was painted on the sample surface with silver conductive paint to serve as a crack detection mechanism. The specimen was then mounted in the TMS fatigue testing machine and the load set up using the strain gauge and strain amplifier. Due to material constraints, only five specimens were tested per load.

The final specimen after being coating with non-conductive spray and the silver conductive path painted on is shown in Figure 3.13.

Silver conductive path
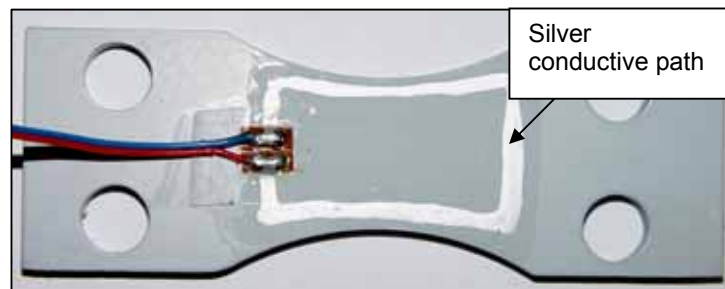
Figure 3.13: Final fatigue specimen

The bend/formed specimens were accommodated in the grips of the machine by manufacturing specialised spacers so that the specimen would be installed correctly into the grips. A side view of this setup is shown in Figure 3.14. The spacers were manufactured using a special mould and then casting Lecoset cold curing resin in the desired shape.
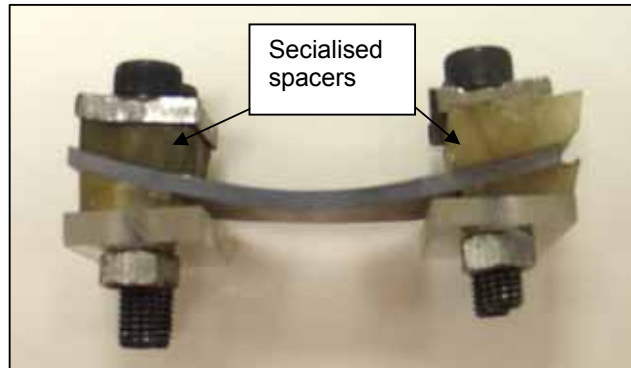
Figure 3.14: Formed fatigue specimen setup

3.6   SUMMARY

Information if this Chapter is very important in order to ensure reproducibility of results. All experimental setups were discussed and clarified so as to establish confidence in the results that will be discussed in the next Chapter.

CHAPTER 4

RESULTS AND DISCUSSION

4.1   INTRODUCTION

In this Chapter it will be proved that it was possible to deform dual phase steel by means of laser irradiation. The properties of the material will be analysed and the results showed. It was established that the laser forming process does not induce residual stresses of great magnitude into the material. Although the fatigue results all indicated a decrease in fatigue life compared to the original flat plate material, compared to the final mechanically formed centre disc, the results showed an increase in fatigue life.

4.2   DIMENSIONAL ANALYSIS

Table 4.1 shows the various experimental settings investigated. Only those settings who yielded significant bending results were investigated further (e.g. microstructure analysis and microhardness profiling).

Table 4.1: Experimental parameters

Power (kW)	Beam diameter (mm)	Scan velocity (m/min)	No. of scans	P/V (J/m)	Interval spacing (mm)	Deformation
4	15	5	20 (5/line)	800	7,5	Significant
3	10	5	20 (5/line)	600	10	Significant
4	15	5	20 (5/line)	800	15	Significant
4	15	5	20 (5/line)	800	7,5	Significant
5	30	2,5	20 (5/line)	2000	10	Significant
5	20	2,5	20 (5/line)	2000	10	Significant
1,5	7,5	1,20	20 (5/line)	1250	7,5	Significant
3,1	14	2	20 (5/line)	1550	10,5	Significant

The full table of experimental values is given in Appendix E. Details of deformation are classified as follows:

- Less than 0,3 mm change in bend height   =   Slight

- Between 0,3 - 0,6 mm change in bend height   =   Bending

- More than 0,6 mm change in bend height   =   Significant

Figure 4.1 graphically shows the increase in actual bend height versus distance from the free end of the various specimens produced. The values indicated by arrows on Figure 4.1 are the line energies associated with the various test parameters used. Line energy is the quotient of laser power (W) and scanning velocity (m/min), and the resultant unit is J/m.
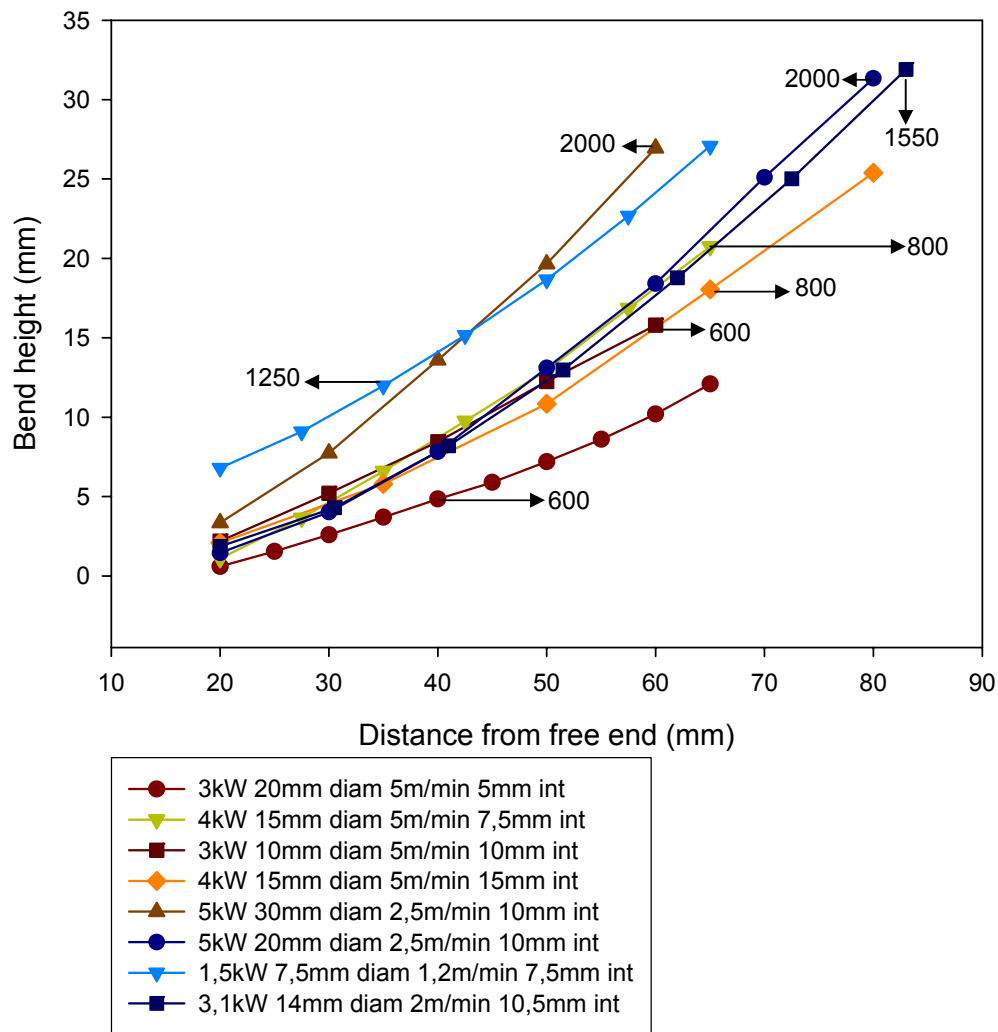
Figure 4.1: Comparison after 15 scans/line for various settings

Initially it was thought that very little correlation exists between line energy and bend characteristics. For the same line energy (with different laser powers and scanning velocities), there is a difference in the bending characteristics of the specimen. Therefore, even if the line energy is kept constant, there does not seem to be a constant corresponding bend angle.

On further investigation, it became apparent that the interval spacing between scanning lines or percent overlap by consecutive heating lines is a very important consideration. The percentage overlap influence the maximum temperature the material reaches as well as the time at temperature for a specific volume of material. This in turn affects the microstructural changes which also affects the materials yield strength at that specific temperature. It is thus understandable that all these changes / effects will influence the final bend angle / radius of curvature of the specimen. Figure 4.2 (a) and (b) shows the comparison of two settings with various interval spacing (percent overlap).
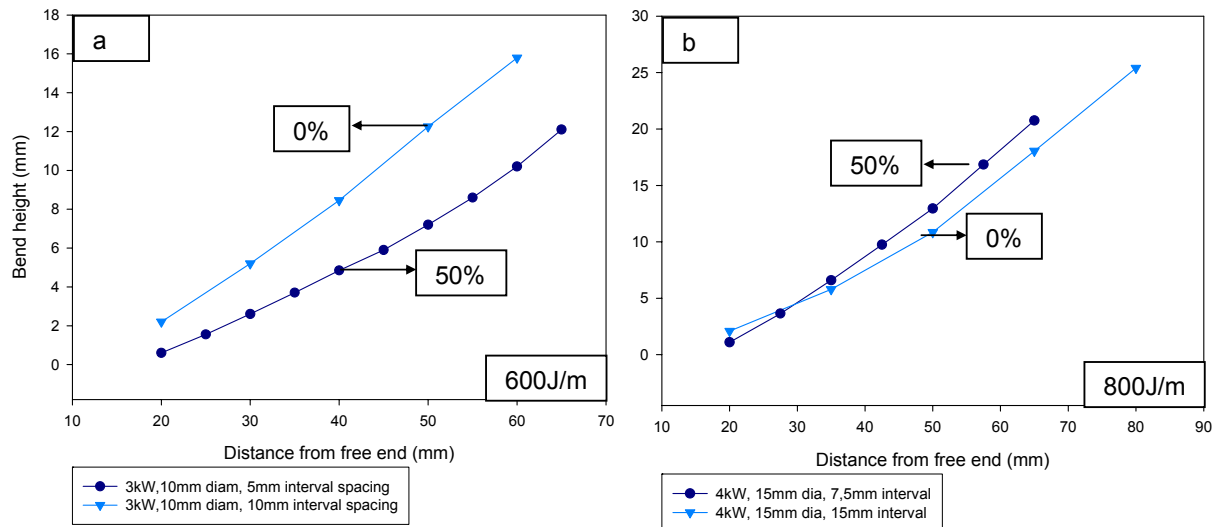
Figure 4.2 (a) and (b): Effect of percentage overlap between scan lines and bend characteristics

For lower line energies, like those indicated in Figure 4.2(a), the temperature gradient mechanism seems to play a more important role in the deformation experienced by the specimen. The deformation mechanisms experienced by these specimens are a combination of the temperature gradient mechanism and the buckling mechanism as little or no thickening of these samples was observed.

At higher line energies such as those indicated in Figure 4.2(b), the buckling mechanism is the foremost deformation mechanism with the temperature gradient and upsetting mechanism only contributing to a small part of the total deformation. It has been well documented that for two dimensional heat flow conditions (no temperature gradient through the thickness of the material), the buckling and the upsetting mechanism are the main contributors to deformation experienced by the sample. The upsetting mechanism results in a shortening of the samples which could be linked to the thickening effect experienced by the samples irradiated with the laser beam.

Therefore, at lower line energies, as the percentage overlap increase, the specimen is heated to a greater extent and thereby destroys the temperature gradient through the thickness of the sheet specimen completely. The buckling mechanism does not contribute a great deal either, since the temperature reached by the specimen is not sufficient to ensure a plasticised zone (yielded zone) of adequate size. The increase in temperature does not lower the flow stress of the material enough so that plastic deformation can take place with ease.

As the line energy increases, the main deformation mechanism changes to the buckling mechanism. The temperature reached by the specimen penetrates through the thickness of the plate and generates a plastic zone of adequate width and depth. Yielded widths and depths smaller than the sheet thickness is unlikely to create noticeable distortions when heat flow is two dimensional[17].

$$\theta_{Bending} = \frac{\alpha(T - T_o)wd}{2D^3}(3\pi D - 8d) \tag{4.1}$$

Equation 4.1 shows that bend angle increase (based on yield zone width (w) and yield zone depth (d)) with an increase in plasticized zone (yielded zone) when the buckling mechanism is the main contributor to deformation. There is an optimum plastic zone width to plastic zone depth ratio (w:d) and exceeding this ratio will not lead to an increased bend angle as the limiting element for plastic zone depth is the material thickness.

Percentage overlap does not cause an increase in the ratio of plastic zone width to plastic zone depth (w:d) and therefore it is expected that the only reason for a better response in terms of bend height is that the radius of curvature for the higher percentage overlap specimens is smaller (i.e. tighter bend).
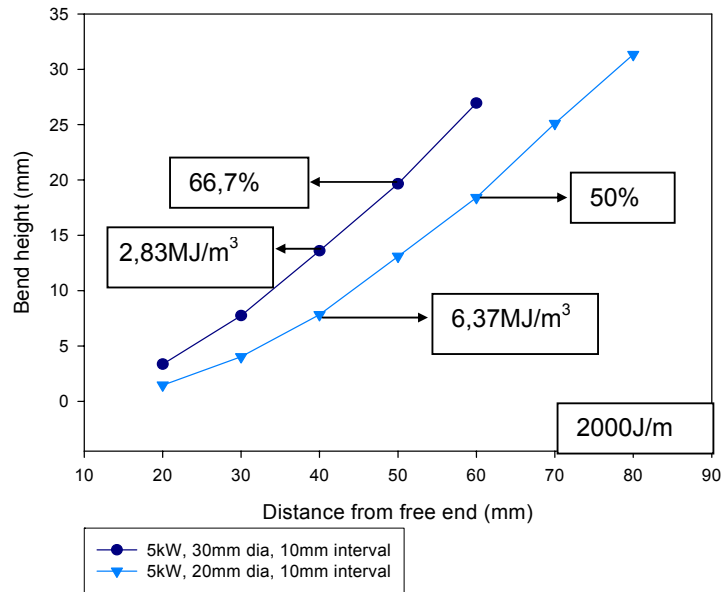
Figure 4.3: Constant laser power but different laser beam spot size, and percentage overlap

There seems to be a correlation between Figure 4.2(b) and Figure 4.3. An increase in percentage overlap for constant line energy, increased the bending response of the specimen. On the other hand, if one looks at the volumetric energy density of the two specimens in Figure 4.3, the two specimens are not similar, since the one employs a 20mm diameter beam and the other a 30mm diameter beam. If volumetric energy distribution is measured in J/m^3, the 20mm beam diameter sample is exposed to a higher value than the 30mm beam diameter sample since the power settings are the same.

Specimens were reproduced according to the settings shown in Table 4.2 based on findings during preliminary testing. These settings were found to produce specimens with approximately the same radius of curvature (average radius of curvature = 130mm).

Table 4.2: Settings to produce specimens of similar geometry

Laser power (kW)	Beam diameter (mm)	Interval spacing (mm)	% Overlap	Scanning velocity (m/min)	Line Energy (J/m)
5,0	20	10,0	50	2,50	2000
3,1	14	10,5	25	2,00	1550
1,5	7,5	7,5	0	1,20	1250

From Figure 4.4 it can be seen that the plotted curves are very close to each other. It can thus be assumed that when the curves follow the same path on the bend height vs. distance from free end plot, the geometrical shape will be similar if all other variables (ambient temperature, etc.) are kept constant.
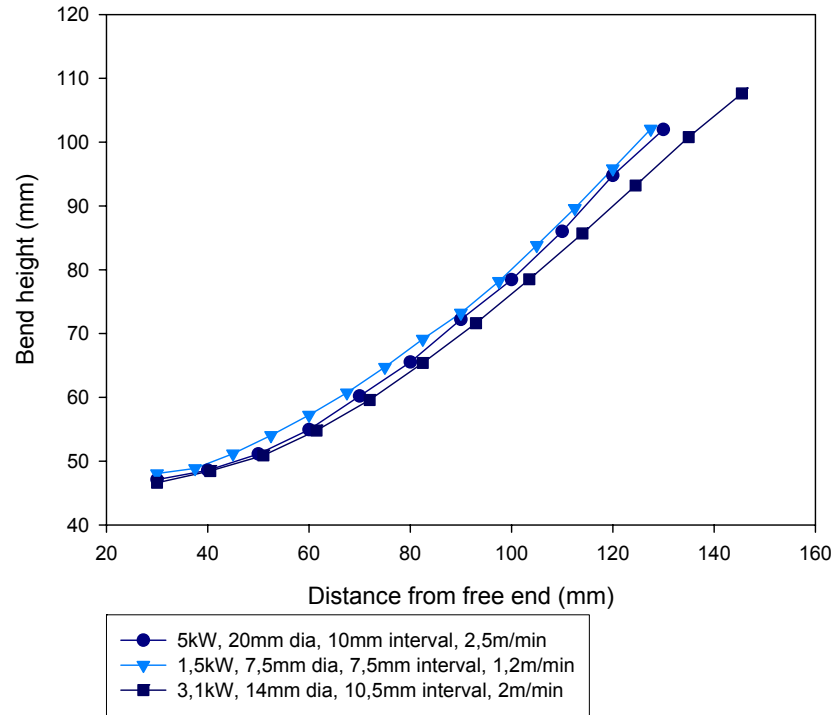
Figure 4.4: Graphic representation of specimens produced with settings
in Table 4.2

Mathematical solutions of the curves in Figure 4.4 yielded the following
equations (laser forming equations), all with an R^2 = 0,99 indicating an
almost perfect fit of the curve to the mathematical solution. The
specimens will be identified by the laser power as indicated in Table 4.2.

- 5kW: $y = 34,8e^{0,0082x}$ (4.2)
- 3,1kW: $y = 35,1e^{0,0077x}$ (4.3)
- 1,5kW: $y = 35,9e^{0,0081x}$ (4.4)

In the previous equations y represents bend height (mm) and x
represents the distance from the free end (mm). It is clear that all the
curves follow the same trend and are similar to the formula used to
characterize the uniform plastic region (flow curve) of the stress-strain
curve of a tensile test. The flow curve equation is given as:

$$\sigma_{true} = K\varepsilon^n \tag{4.5}$$

Where n = strain hardening exponent and K = strength coefficient.

Equation 4.5 is frequently used in calculations with regard to plastic deformation in the plastic regime of the stress-strain curve. Equations 4.2, 4.3 and 4.4 can be combined to form a generalized equation valid only for dual phase steel between line energies of 1250J/m and 2000J/m.

Combined equation: $\mathbf{y = 35,3e^{0,008x}}$ \hfill (4.6)

The constants 35,3 and 0,008 are only valid for dual phase steel between settings as given in Table 4.2. The influence of number of laser scans per line on the resulting bend height was also investigated and typical results are shown in Figure 4.5.
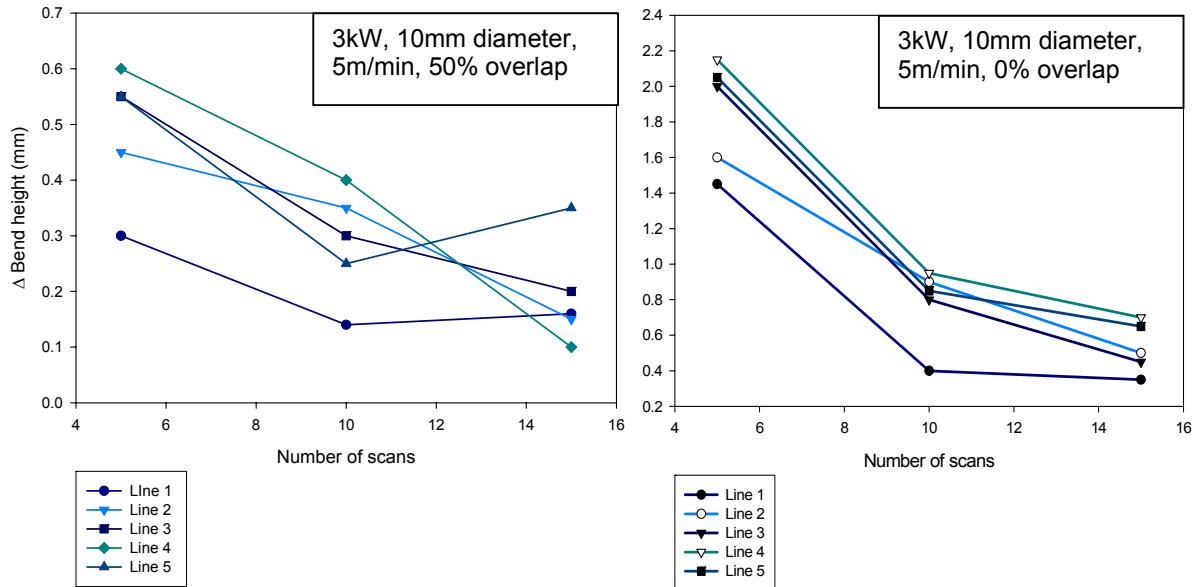
Figure 4.5: Influence of number of laser scans on bend characteristics (3kW)

It is clear from Figure 4.5 that for all the successive laser lines with a line energy of 600J/m, the most deformation was observed during the first

five scans of the scanning cycle of 15 scans per line. Continuing to laser scan the same position, more than five scans will not result in a significant increase in bend height and hence bend angle. There is also a better consistency in results for the specimens with zero percent overlap than those who were produced employing a 50 percent overlap.

Figure 4.6 also indicates that the specimen experiences the most deformation during the first five laser scans. The specimens were irradiated with a line energy of 800J/m and it was observed that the specimens that were irradiated with a zero percent overlap behaved differently to those who employed a 50 percent overlap. The zero percent overlap samples revealed less of a difference between the first five scans and the second set of five scans, except for the very last scanning line. The difference in change of bend height is more drastic for the specimens where the laser line pattern did not employ any overlap between scanning lines.
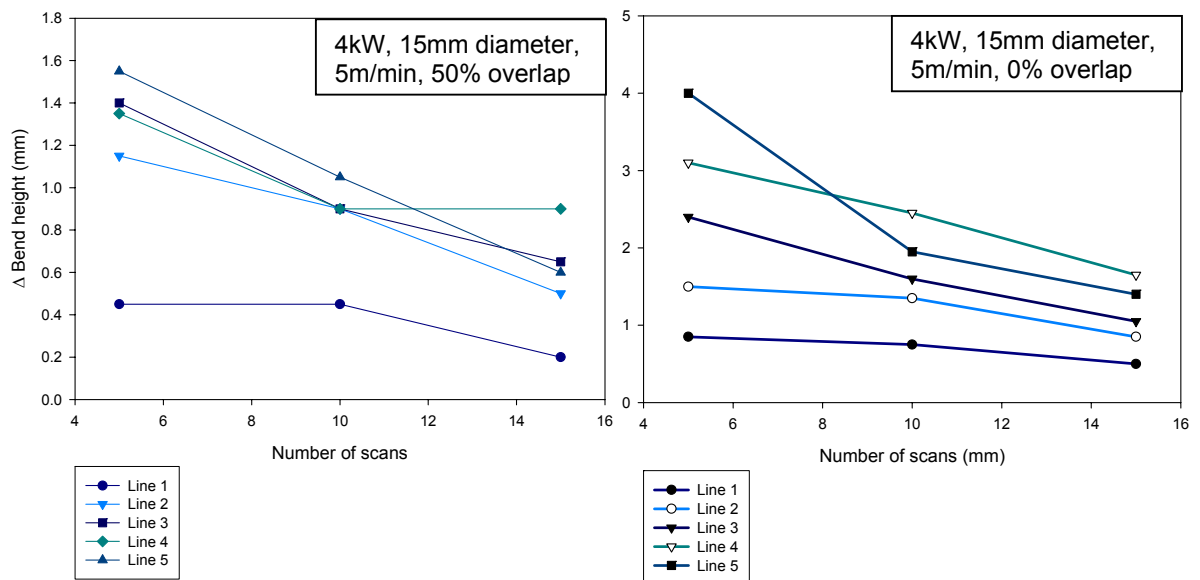
Figure 4.6: Influence of number of laser scans on bend characteristics (4kW)

This less drastic deformation experienced by the samples deformed by a line pattern with overlap between the lines can be attributed to the fact

that the yielded zone width and depth are now differently sized than those with no overlap between the lines. This influences the resulting bend angle as it was shown in Chapter 2 that the yielded width and depth reach a critical value beyond which very little deformation is experienced. The y-axis of Figure 4.5 and 4.6 indicate incremental change in bend height.

The change in total bend height between each set of five laser scans shows that the increase in bend height is approximately linear in nature. This trend is graphically illustrated in Figure 4.7 which shows the difference in total bend height vs. number of scans per line.
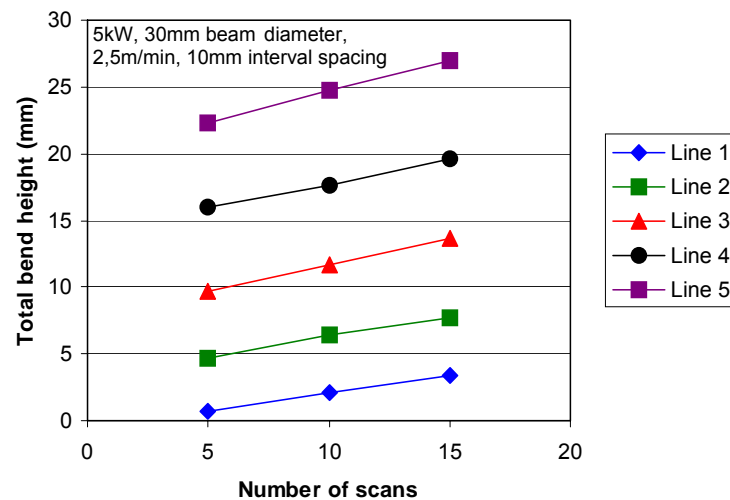
Figure 4.7 Graphic representations of difference in total bend height vs. number of scans per line

The bend height increases more rapidly as the number of line heating cycles the sample has experienced, increases. The lines shown on Figure 4.7 are of a linear nature and approximately parallel to each other. The distance between the lines is (with a tendency to increase spacing) an indication that deformation is taking place more rapidly with time or number of line scans. This is because as the temperature of the specimen increases with an increasing number of scans, so the yield strength decreases and makes deformation easier.

The forming processes with the process parameters as given in Table 4.2 can be shown on a 'master diagram' and is graphically indicated on Figure 4.8. This master diagram was developed by equating the following four parameters:

- Laser power, kW
- Scanning velocity, m/min
- Beam diameter, mm
- % Overlap between consecutive laser lines
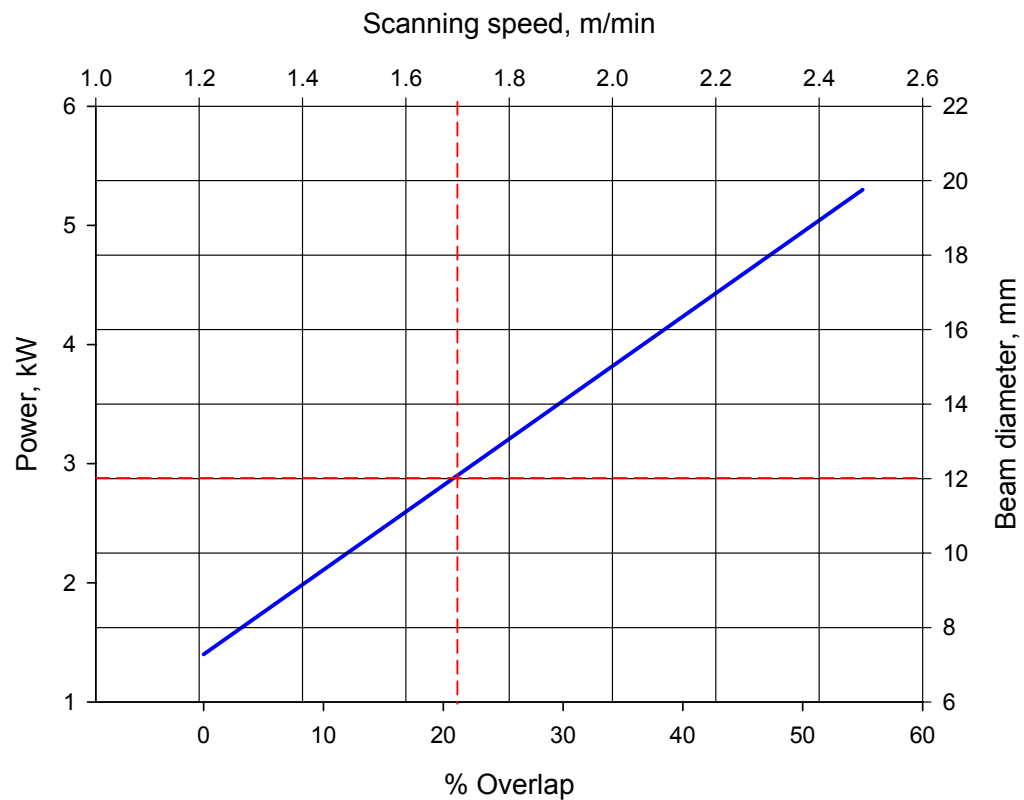
Figure 4.8: Master diagram obtained for dual phase steel

This master diagram could be obtained because the relationship between the properties showed a linear correlation. This diagram can now be used to determine process parameters that will result in approximately the same radius of curvature than that obtained for the settings analysed in this research project i.e. 130mm. An example of the use of this diagram can be illustrated by the following:

The coordinates of any point on the blue line should result in the same radius of curvature, e.g. by following the red dashed lines on the graph, the following settings can be read off and will result in a radius of curvature of 130mm (for the same size of specimen):

- 2,83kW Beam power
- 21% Overlap between consecutive scan lines
- 12mm Diameter beam
- 1,7m/min Scanning velocity

4.3.   CALCULATION OF PARAMETER 'M' ACCORDING TO MASUBUCHI

Employing the formula derived by Masubuchi (see section 2.7.1) to calculate a parameter which is referred to as 'm', yielded the following results:

$$m = \frac{P}{t\sqrt{v}}$$ (4.7)

5kW: (thickness = 3,5mm   velocity = 2,5m/min)   m = 3,66
3,1kW: (thickness = 3,5mm   velocity = 2m/min)   m = 2,54
1,5kW: (thickness = 3,5mm   velocity = 1,2m/min)   m = 1,58

It is clear that in all cases the parameter 'm' is below the value of six (6) which was found to be the limit above which deformation becomes negligible. For the 5kW setting, the radius of curvature obtained was slightly smaller than that produced by the 1,5kW setting. Therefore, it can be assumed that an increase in parameter 'm' for dual phase steel will result in a tighter bend i.e. smaller radius of curvature of the final specimen.

4.4   CALCULATION OF BEND ANGLE

Since the thermal expansion coefficient for dual phase steel was not known, the average value was taken for alloy steels[37]. Table 4.3 indicates the range of results obtained from literature which shows that there is not a significant difference in thermal expansion coefficient values.

Table 4.3: Thermal expansion coefficient values for the temperature range
between 540° - 980°C

	High ($\times 10^{-5}.°C^{-1}$)	Low ($\times 10^{-5}.°C^{-1}$)
Alloy steels	1,5	1,1
Carbon Free-cutting steels	1,5	1,5
Alloy steels (cast)	1,5	1,4
High temperature steels	1,4	1,1
Ultra high strength steels	1,4	1,0

The average value for alloy steels is thus $1,3 \times 10^{-5}.°C^{-1}$, and this value
will be used for the calculations. The theoretical bend angle can be
calculated by applying equation 4.1 (see Chapter 2).

$$\theta = \frac{\alpha(T - T_o)wd}{2D^3}(3\pi D - 8d)$$
(4.1)

Where: D = Plate thickness, mm

d = Yield depth (penetration depth of T_{yield} isotherm, mm)

w = Yield width (top width of T_{yield} isotherm, mm)

α = Thermal expansion coefficient

T = Temperature, °C

By measuring the visible outer heat lines / isotherms on the 1,5kW
specimens, the following values were obtained:

w = 6,1mm   and   d = 1,1mm

No measurements could be made on the 5kW specimens as they did not
exhibit any heat lines / isotherms due to the percentage overlap between
consecutive irradiation cycles / lines. The calculation of the bend angle
for the 1,5kW specimens are shown in the following section:

$$\theta = \frac{\alpha(T - T_o)wd}{2D^3}(3\pi D - 8d)$$

$$\theta = \frac{1{,}35x10^{-5}(1392{,}99 - 23)(6{,}1x1{,}1)}{2(3{,}5)^3}\left(3\pi 3{,}5 - 8(1{,}1)\right)$$

$$\theta = 33{,}707x10^{-3}$$

$$\therefore \boldsymbol{\theta = 0,0337^\circ}$$

This calculation can not be applied directly to this research, since it was derived from the temperature gradient mechanism of laser deformation.

It has been explained in section 4.2 that the main bending mechanism operating during the forming process of dual phase steel of 3,5mm thickness is a combination of the buckling and upsetting mechanism with the TGM only contributing a small amount to the overall deformation. This has now been proved since the above result only indicates that a small angle of 0,0337° can be attributed to the temperature gradient mechanism.

4.5   MICROSTRUCTURAL ANALYSIS

4.5.1 7,5mm Beam diameter specimens

The original microstructure of the dual phase steel in the as-received condition is shown in Figure 4.9. The grain size of the original sample corresponds with ASTM 7 and smaller.
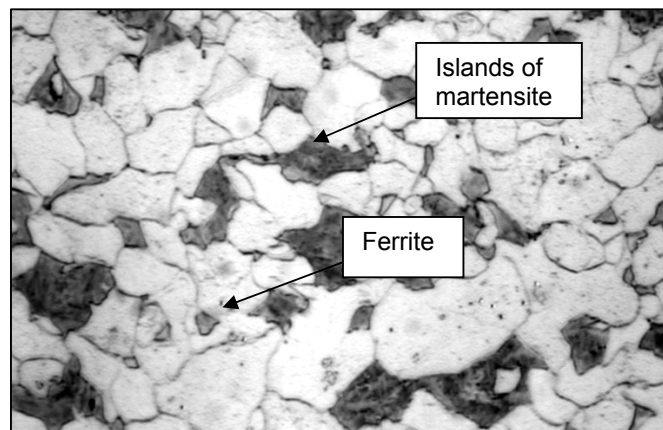
Figure 4.9: Original microstructure of dual phase steel
(x1000, 2% Nital)

The microstructural changes observed on the laser formed specimens are mainly at the top surface where irradiation has taken place. A typical microstructure observed on the 7,5mm samples are shown in Figure 4.10. It is evident that the material was heated well above the upper transformation limit as the ferrite grains have recrystallised into a different form.
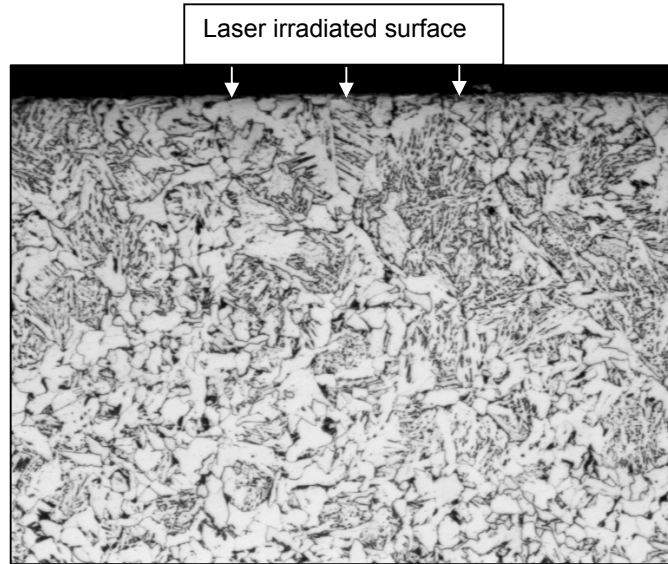
Figure 4.10: Microstructure of top surface of 7,5mm beam diameter sample (x200, 2%Nital)

There is evidence of Widmanstätten ferrite (Bainitic ferrite) near the top surface, which forms by the transformation of the interior of the austenite grain (wholly or in part) and form the acicular (needle-like) structure observed. Widmanstätten ferrite is a result of relatively fast cooling and therefore undercooling of the austenite, thus it forms at temperatures below those associated with slow cooling rates. At higher magnification this microstructure is better resolved and there is an aligned second phase present (carbide) in or between certain ferrite grains. Figure 4.11 shows the microstructure at a higher magnification.
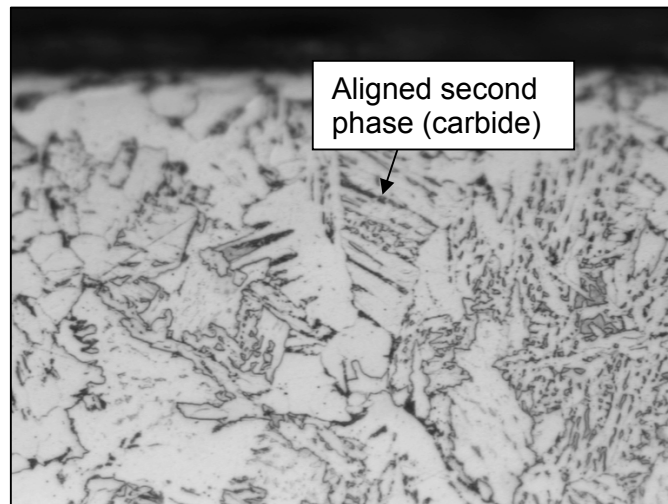
Figure 4.11: Microstructure at top surface of 7,5mm beam diameter sample (x500, 2%Nital)

At the high temperatures at which Widmanstätten ferrite grows, the driving force is not adequate to support the strain energy associated with a single plate. Widmanstätten ferrite formation therefore involves the simultaneous and adjoining cooperative growth of two plates, which are crystallographic variants in such a way that their shape deformations are equally accommodated. This has the effect of cancelling a large amount of the strain energy. The orientation is that of the lowest interfacial energy. Due to the fact that Widmanstätten ferrite forms at elevated temperatures, it is thermodynamically necessary that the carbon is redistributed during growth. The ferrite thus always has a para-equilibrium carbon content and grows at a rate which is restricted by the diffusion of carbon in the austenite ahead of the plate tip. Since the transformation is displacive, substitutional atoms do not partition and an atomic association is maintained between the parent and product lattices[39].

The second phase observed within the ferrite grains are angular patches of martensite. Microstructures with aligned second phase within the ferrite grains are usually undesirable when considering notch toughness of the material[40]. The dark patches within the microstructure are a mixture of various transformation products (ferrite carbide aggregate).

Some grain boundary precipitation of carbides is also visible. The description of the microstructure above can clearly be seen in Figure 4.12, which is a micrograph of the top region of the 7,5mm beam diameter sample at x1000 magnification. This microstructure also indicates an increase in ferrite grain size compared to the original material, although it is not very clear.
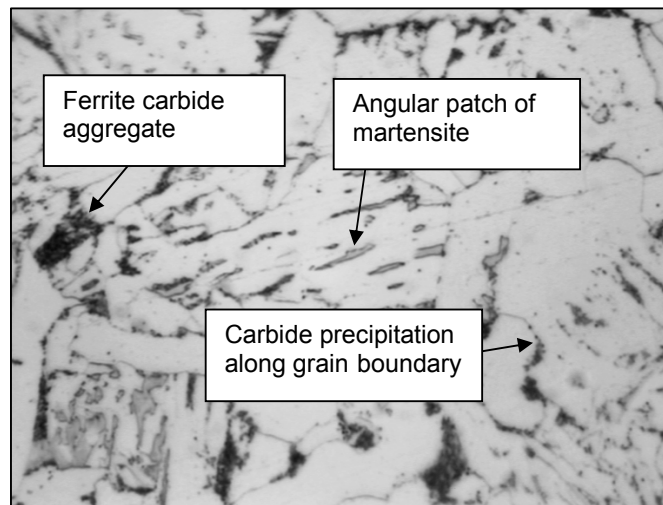
Figure 4.12: Micrograph identifying the various phases present
(x1000, 2%Nital)

Factors that affect the microstructure include cooling rate, composition, the presence of non-metallic nuclei and plastic strain. The overall grain size depends on the amount of energy input (heat input), with higher energy inputs usually leading to larger grains. Non-metallics are important as they may act as nuclei for transformation products. These nuclei may range from relatively coarse inclusions to micro sized particles within the matrix (coherent and non-coherent). Plastic strain occurs during the cooling of the sample and may have an influence on the properties of the final sample[40].

The microstructure in the centre of the sample showed some banding and breakdown of the martensite phase is evident. The martensite showed an over-tempered structure with spheroids of carbide within a

ferrite matrix. This microstructure is shown in Figure 4.13.
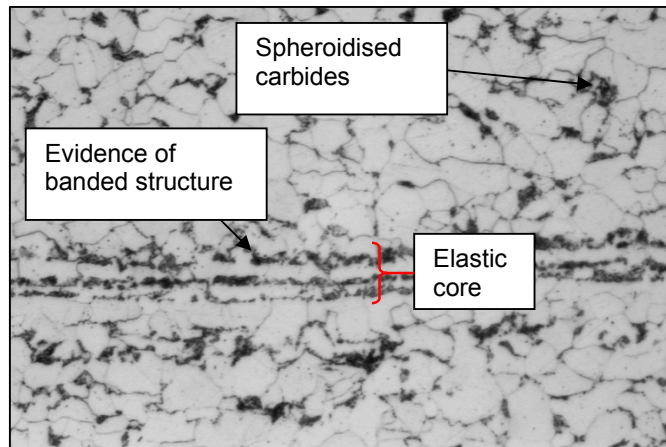
Figure 4.13: Microstructure in centre of sample (x500, 2% Nital)

The bottom surface of the sample also showed some evidence of
martensite over-tempering and negligible grain growth. Figure 4.14
shows the structure at the bottom surface (furthest away from the
irradiated surface) of the specimen.
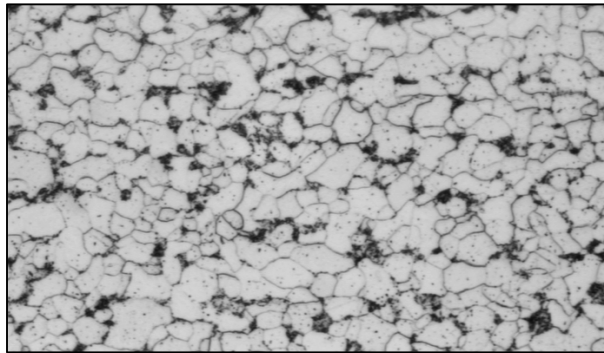
Figure 4.14: Microstructure at bottom surface of sample (x500, 2% Nital)

4.5.2 14mm Beam diameter specimens

As previously stated, the major microstructural changes took place at the
top surface (irradiated surface) of the sample. There is limited evidence
of Widmanstätten ferrite, but grain growth is clearly visible. The
microstructure consists mainly of ferrite with some grains of martensite /
bainite. Some alignment of the second phase can be seen in Figure 4.15
(a) and (b).
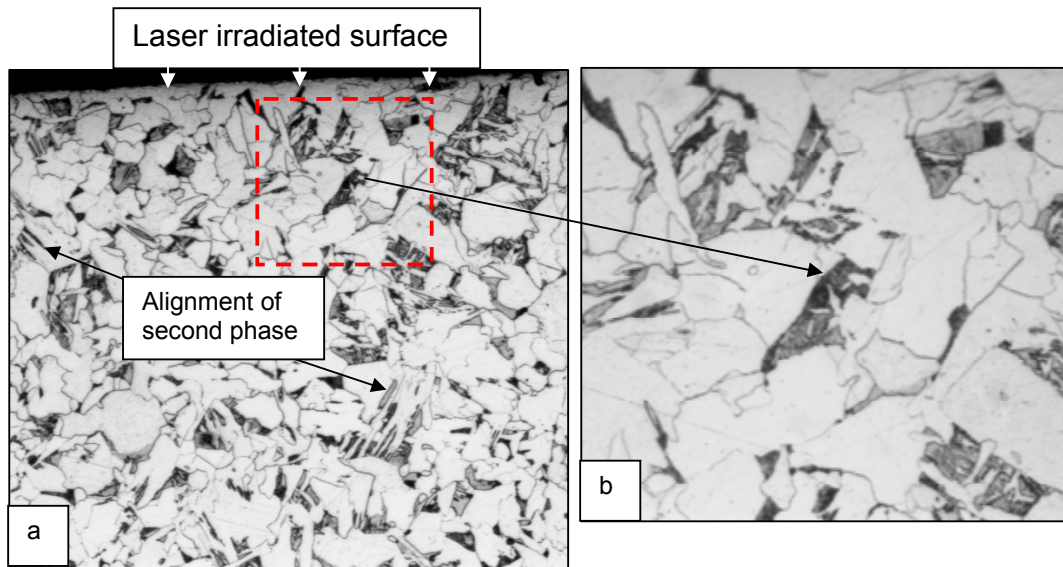
Figure 4.15: (a) Microstructure of top surface irradiated with 3,1kW beam power (x200, 2%Nital), (b) Microstructure of same area at higher magnification (x500, 2%Nital)

The grains showing the martensite/bainite microstructure are shown in Figure 4.16. This microstructure is formed when austenite is rapidly cooled, which prevents the precipitation of iron carbide, although less severe quenching is needed to give rise to the bainitic structure. Bainite growth takes place rapidly because the driving force is increased by a greater degree of non-equilibrium at the lower temperatures at which it is formed. Because of this, particle size is too small to be seen by low power optical microscopy.
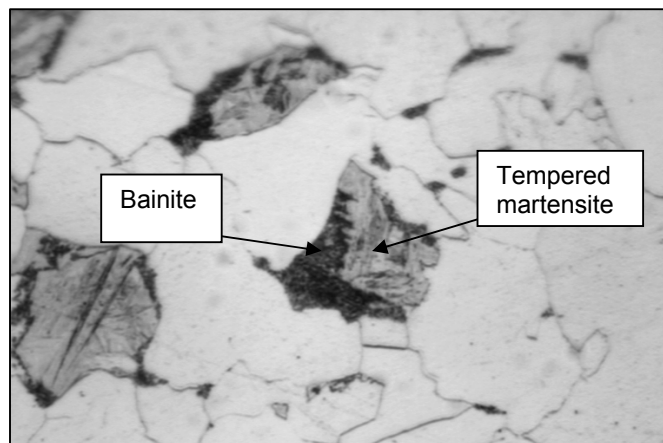
Figure 4.16: Typical microstructure showing martensite / bainite in ferrite matrix (x1000, 2%Nital)

This microstructure can be expected since during the heating cycle of the laser forming process, the microstructure changes to austenite, and given that the cooling rate is very fast, areas of high enough carbon content transforms to martensite with some retained austenite in the ferritic matrix. Because the forming process entails the overlap between consecutive laser scan lines, the subsequent heating can be seen as similar to a tempering process for the normal martensite that formed from the first cooling.

Any retained austenite transforms to bainite on subsequent heating since the temperature is high enough to ensure the transformation process. The final microstructure consists of a ferritic matrix with tempered (sometimes over-tempered) martensite and bainite. Subsequent heating during overlap of laser scans keeps the specimen at a specific temperature long enough to ensure bainite transformation (similar to austempering).

Just further inward from the top surface, the microstructure resembles a pearlitic/ferritic structure rather than martensitic or bainitic. Figure 4.17 shows a typical microstructure just inward from the top surface. This implies that the laser beam heated the sample to a high enough temperature to be austenitic in that region but the cooling rate that that region experiences was not fast enough to result in a martensitic structure. The cooling rate was such that fine pearlite formed from the austenite.
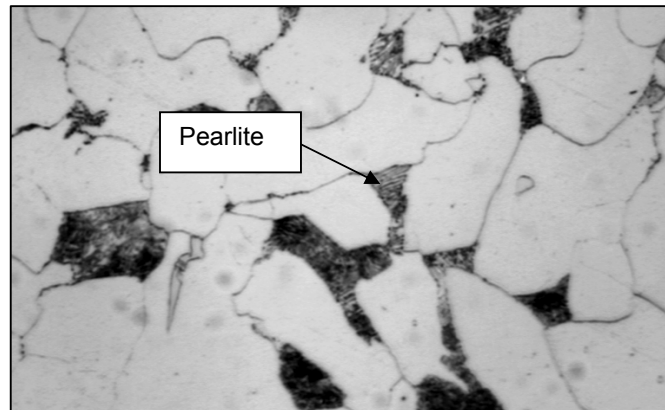
Figure 4.17: Microstructure resembling pearlite (x1000, 2%Nital)

In the centre of the specimen the banded structure is still visible, with a microstructure of over-tempered martensite in a ferritic matrix. The grain size in this region is similar to that observed on the 7,5mm beam diameter samples. The typical microstructure in the centre of the sample is shown in Figure 4.18.
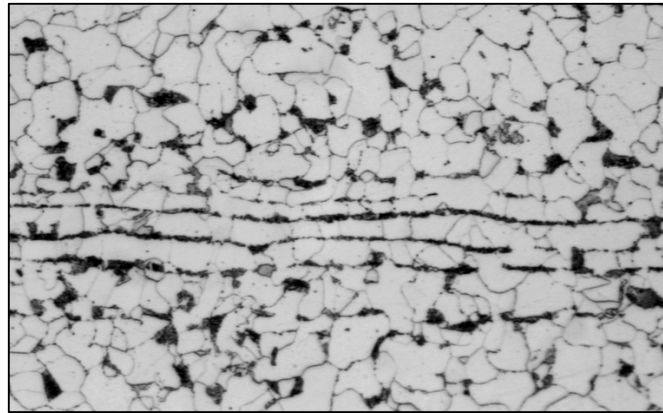
Figure 4.18: Microstructure in the centre of the sample (x500, 2%Nital)

The bottom surface of the sample showed only slight increase in grain size accompanied by the breakdown of the martensite phase due to the tempering effect of the laser forming process. The typical microstructure is shown in Figure 4.19. Dark patches in the microstructure can be explained as carbide/ferrite aggregated, probably overtempered martensite i.e. fine globular carbide particles in a ferritic matrix.
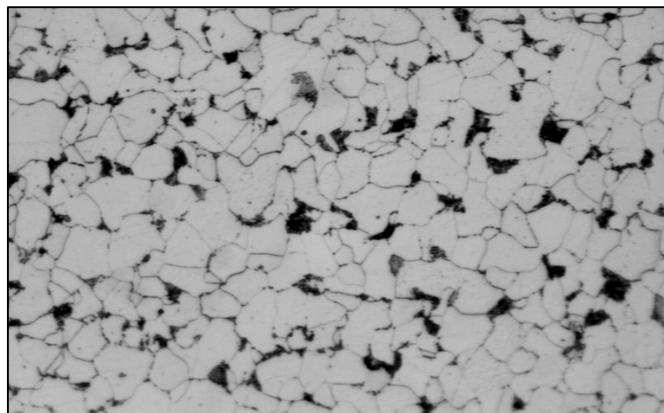
Figure 4.19: Microstructure of bottom region of sample (x500, 2%Nital)

4.5.3 20mm Beam diameter specimens

The 20mm beam diameter specimens experienced the highest temperature of all the samples produced by the various laser parameters. The typical microstructure observed at the top surface of the specimen is shown in Figure 4.20(a) and (b).
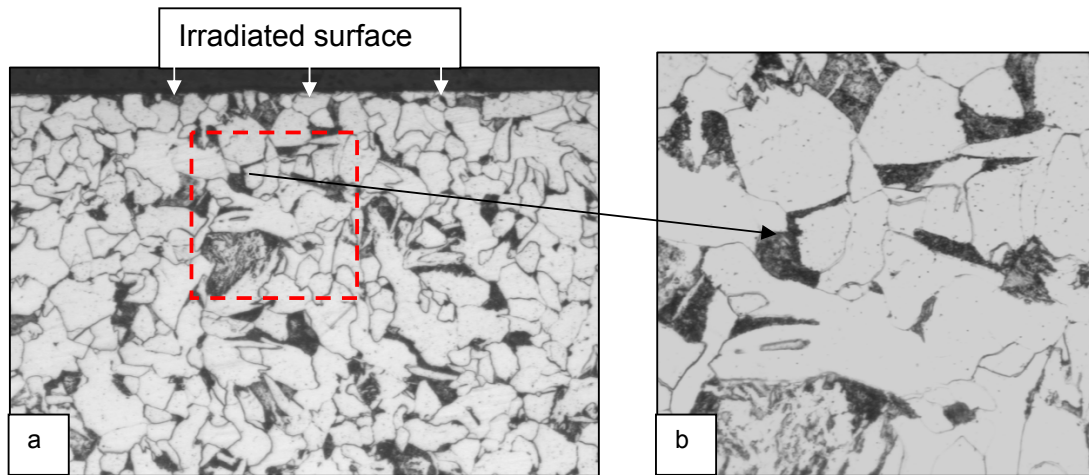
Figure 4.20: (a) Microstructure of top surface irradiated with 5kW beam power (x200), (b) Microstructure of same area at higher magnification (x500, 2%Nital)

The major microstructural changes observed on the top surface (laser irradiated side) of the samples, are severe grain growth and phase changes. The original martensite in the microstructure is replaced by grains of ferrite/carbide aggregate. These grains resemble spheroidised pearlite.
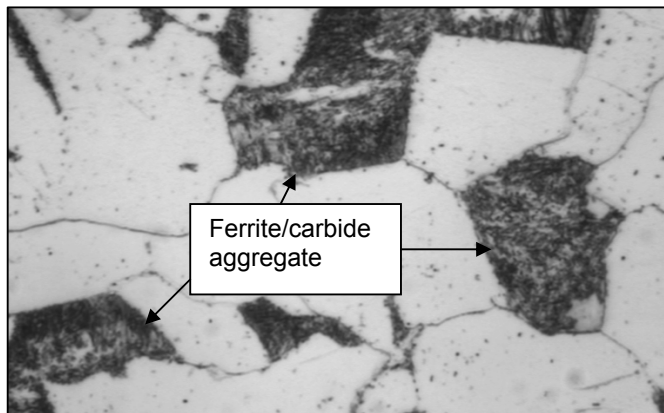
Figure 4.21: Typical microstructure at top region of sample (x1000, 2%Nital)

At still higher magnifications these structures consisting of ferrite/carbide aggregate (spheroidised pearlite) are more clearly visible. Figure 4.21 shows the microstructure similar to those in Figure 4.20 but at a higher magnification.

The microstructure in the centre of the sample showed that the banding effect that was clearly visible on the other samples has been largely eliminated. This is because of the amount of heat supplied by the laser forming process. The sample experienced a phase change as well as a heat treatment process as the consecutive laser lines overlapped with each other. The typical microstructure is shown in Figure 4.22. Some grain growth is also visible. The microstructure consists of ferrite and some islands of very fine pearlite.
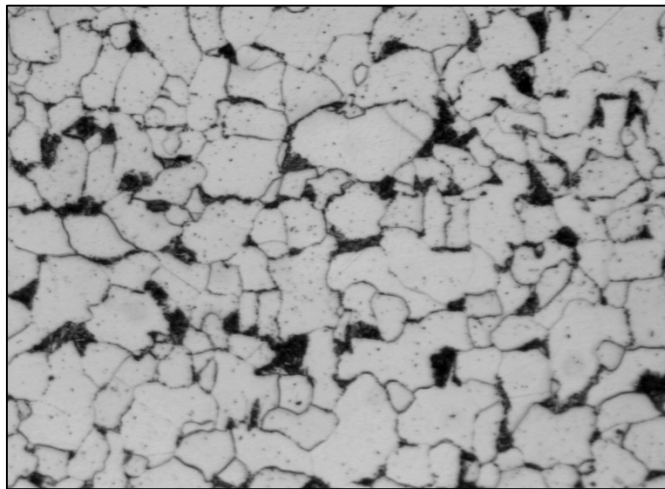
Figure 4.22: Microstructure in the centre of the sample (x500, 2%Nital)

The microstructure at the bottom surface does not look much different to the microstructures in the centre of the sample and are shown in Figure 4.23. The grains are slightly smaller than those observed in the centre of the sample. Once again the microstructure consists of a ferrite matrix with some grains of pearlite. There is no evidence of martensite or bainite in the microstructure. This means that the rate of cooling through

the transformation range was slow enough to allow the formation of a pearlitic structure.
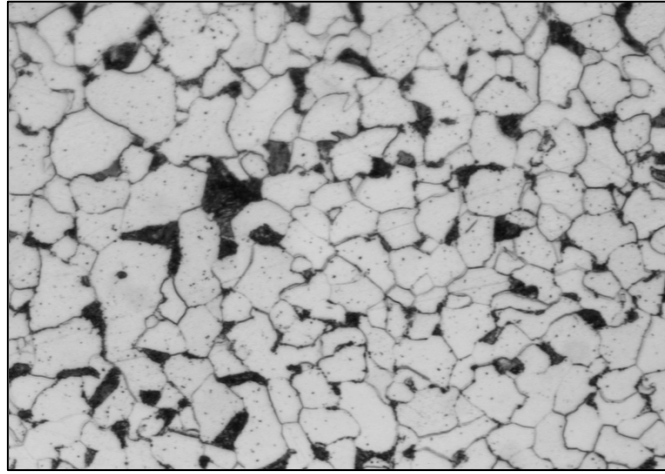
Figure 4.23: Typical microstructure of bottom region of sample (x500, 2%Nital)

From the data presented it is clear that an increase in line energy (E_L) results in a higher temperature experienced by the specimen. When the line energies of the above samples are converted to a volumetric energy by taking into account the beam spot size/area, the following values were calculated:

$$E_V = \frac{E_L}{A_B}$$ (4.8)

Where: E_V = Volumetric Energy (J/m^3)

                E_L= Line Energy (J/m)

                A_B = Area of laser beam (m^2)

- 5kW   -   6,37MJ/m^3
- 3,1kW   -   10,07MJ/m^3
- 1,5kW   -   28,29MJ/m^3

From the results it can be observed that a decrease in beam spot size leads to a higher value of volumetric energy absorbed by the specimen.

Table 4.4: Summarising table of resultant microstructures

	0,5mm below irradiated surface	Grain size	Middle of sample	Grain size	Bottom of sample	Grain size
Original material	Ferrite and Martensite	ASTM E112 7				
5kW	Ferrite and Ferrite/Carbide aggregate	70% increase	Ferrite and fine Pearlite	40% increase	Ferrite and Pearlite	15% increase
3,1kW	Ferrite and Martensite / Bainite	50% increase	Ferrite and Pearlite	50% increase	Ferrite and Ferrite/Carbide aggregate	15% increase
1,5kW	Acicular Ferrite, Fine carbides and small patches of martensite	-	Ferrite and Spheroidised carbides (overtempered martensite)	40% increase	Ferrite and overtempered martensite	Less than 10%

4.6   MICROHARDNESS ANALYSIS

Analysis of the microhardness values through the thickness of the specimens deformed by laser line heating yielded results as illustrated in Figure 4.24. Vickers microhardness measurements were done using a 500g load. The hardness indentations were made in the centre of the irradiated line and measured from the irradiated surface.
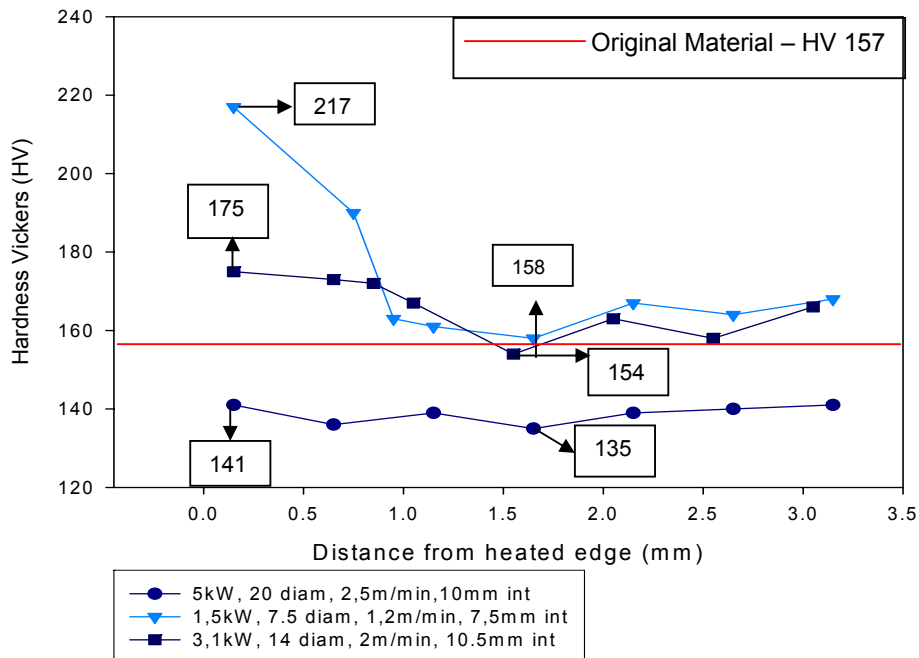
Figure 4.24: Microhardness analysis of laser formed specimens (through the thickness)

It is clear from Figure 4.24 that the most dramatic change in hardness can be seen on the specimen irradiated with the 1,5kW laser power. The range of results obtained for each set of measurements is shown here:

- 5kW   -   6 HV units
- 3,1kW   -   21 HV units
- 1,5kW   -   59 HV units

Hardness evaluations along the length of the irradiated samples yielded the results as shown in Figure 4.25. Hardness indentations were made approximately 0,1mm below the irradiated surface and along the length of the specimens across a few laser scan widths. The hardness profile of the sample formed employing a 1,5kW laser power showed a markedly different hardness profile to the sample that was deformed using a 5kW laser power.
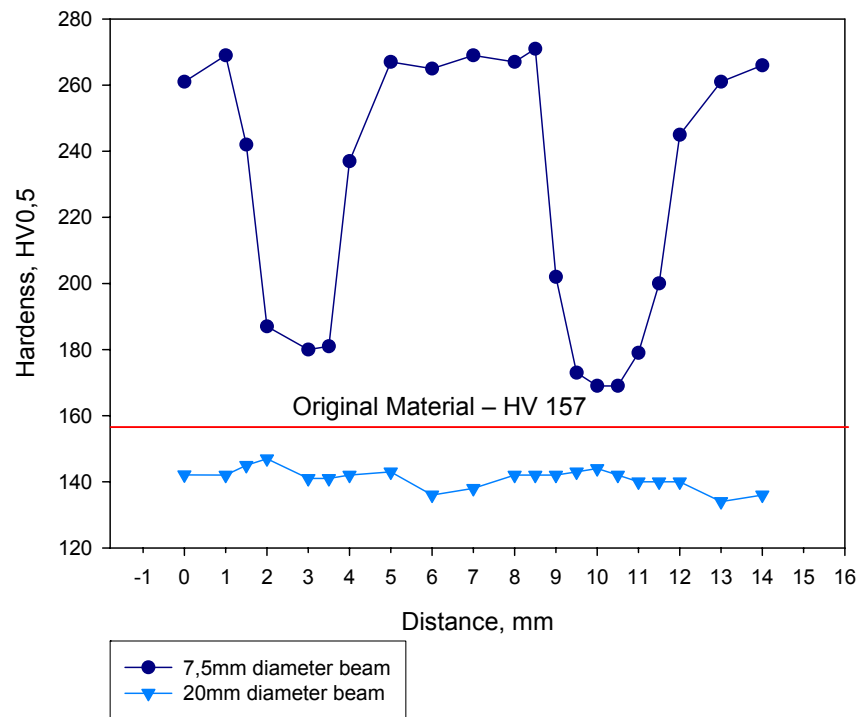
Figure 4.25: Microhardness analysis of laser formed specimens (along length)

4.7 TEMPERATURE ANALYSIS

4.7.1 7,5mm Beam diameter

Three samples were produced using the following laser parameters:

- Laser power: 1,5kW
- Beam diameter: 7,5mm
- Interval spacing: 7,5mm
- Scanning velocity: 1,2m/min
- % Overlap between scans: 0%
- Line energy: 1250J/m

Real-time recordings were made of the laser forming process using the infrared thermal camera, after which the recordings were analysed. Time-temperature readings are shown in Table 4.5.

Table 4.5: Time-temperature readings for 7,5mm beam diameter

Line (Scanning cycle)	Just before 1st scan		Max at 5th scan		Just after 5th scan	
	Temperature °C	Time sec	Temperature °C	Time sec	Temperature °C	Time sec
1	23	0	1182,5	18,9	514,2	20,74
2	230	40,4	1348,2	65,7	660,4	67,38
3	386,6	86,92	1359,9	112,06	697,9	114,10
4	442,8	133,46	1390,3	158,48	728,7	160,46
5	477,4	179,86	1427,7	205,14	731,1	206,98
6	488,4	226,12	1451,6	251,66	737,6	253,56
7	496,6	272,76	1429,0	297,96	747,2	299,76
8	490,2	319,30	1420,6	344,68	745,8	346,44
9	487,7	365,82	1377,7	391,12	743,2	392,96
10	485,8	412,32	1376,0	437,74	735,3	439,40
11	484,0	458,84	1374,9	484,66	730,8	486,14
12	477,1	505,46	1373,4	530,92	726,9	532,54
13	473,2	551,66	1340,7	577,48	720,5	579,10

From Table 4.5 it is clear that the maximum temperature is reached at the ninth scanning cycle (line). The **maximum temperature** observed during the fifth scan per line, range from 1182,5°C to1377,7°C, i.e. a temperature difference of 195,2°C. Similarly, the temperature difference for readings taken **just before each first scan** is 266,6°C (disregarding the 23°C, which was room temperature before the forming process started) and 233°C for measurements taken **just after the fifth scan**. Figure 4.26 shows a graphic representation of the data displayed in Table 4.5. It is clear from Figure 4.26 that the temperature stabilises after the third scanning cycle. This is to be expected since during the first two scanning cycles, the bulk of the material is still cold compared to the irradiated region. This large temperature difference causes heat to be conducted away to cooler regions at a higher rate. After the third scanning cycle, the temperature profile has stabilised thus leading to the plateau observed in Figure 4.26.
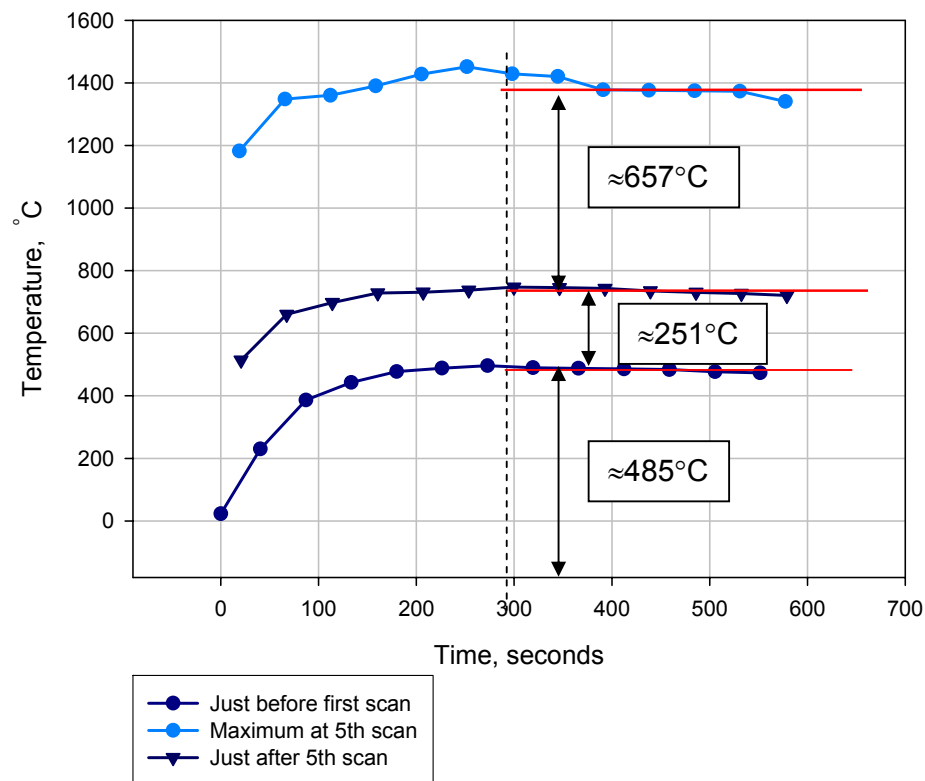
Figure 4.26: Graphic representation of temperature measurements for 7,5mm beam diameter specimens

The average temperature difference (last eight readings) between the readings observed on the plateau region of the graph are as follows: Between **just before the first scan** and **just after the fifth scan** – 250,55°C and between **maximum temperature** and **just after the fifth scan** – 657,06°C. This indicates fast cooling between the maximum temperature reached and measurements taken just after the fifth scan.

An image taken with the infrared camera revealed that the beam does have a donut shape. This is indicated in Figure 4.27 by the peaks observed on the line graph. Also clear from this image is that the rest of the plate specimen is below 200°C and thus appears the same as the background since the high temperature filter eliminates all temperatures below 200°C.
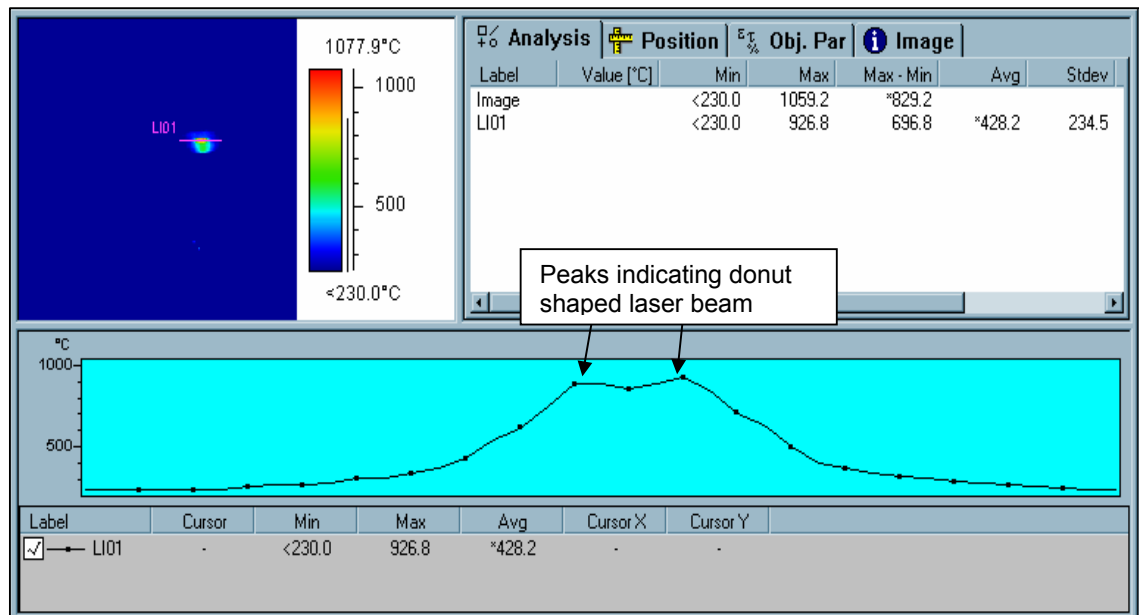
Figure 4.27: Image of first scanning line for 7,5mm beam diameter

Figures 4.28(a), (b) and (c) show images of the second, third and fourth scanning cycles/lines.
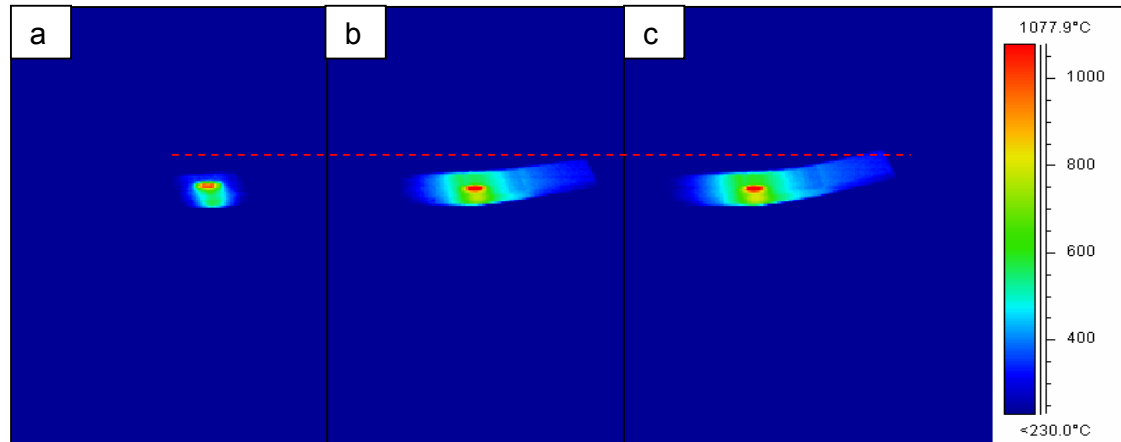
Figure 4.28: (a) Second scan cycle, (b) third scan cycle and (c) fourth scan cycle

It is clear from these images that the sample is getting progressively hotter as the forming process proceeds. It is also clear from Figure 4.28 (b) and (c) that the bend is now noticeable. The bending mechanism takes place during the cooling cycle. As the laser line scans over the metal surface, the samples first bend towards the negative direction (opposite to final bend direction i.e. away from the laser beam).

By the time the laser scan has been completed, the sample has bent towards the positive direction i.e. towards the laser beam. The various bending mechanisms are explained in detail in Chapter 2 and it is believed that the deformation mechanism in this case is a combination of the buckling mechanism and the upsetting mechanism. Some thickening of the samples in the irradiated areas was observed, however only slightly.

After ten scanning cycles (five scans per cycle) the temperature profile indicated in Figure 4.29 could be observed.
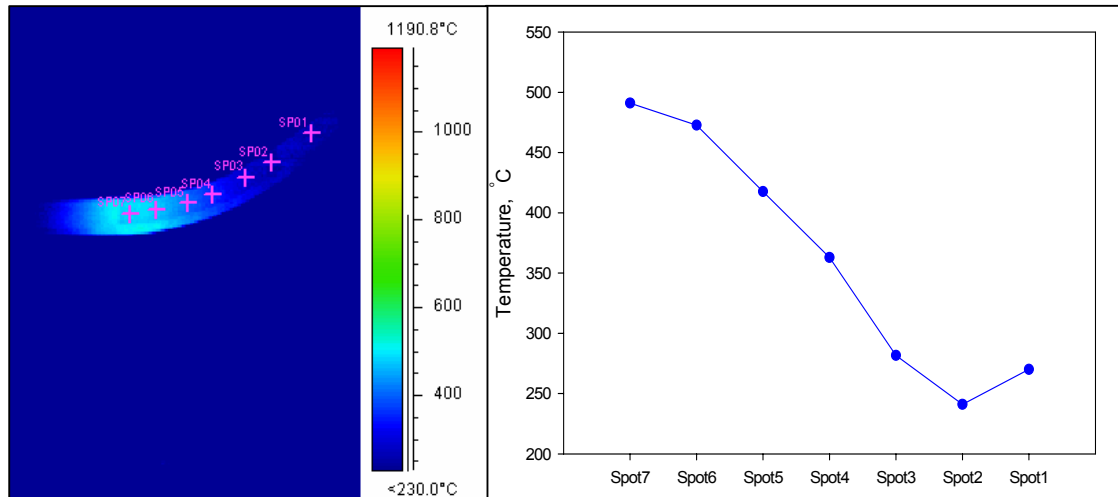
Figure 4.29: Temperature profile at tenth scanning cycle

The complete forming process consisted of thirteen scanning cycles and lasted 9 minutes 39 seconds (time measured from first laser contact until last laser scan). After the last scan, the sample cooled down to 350,9°C in 35,66 seconds. The cooling rate the sample experiences is very important to note, as this influences the microstructural changes that could take place. The total scanning cycle are graphically depicted in Figure 4.30. From this, it can be seen that the sample experiences a maximum temperature for a very short time. On average (for last eight readings), the temperature falls from 1392,99°C to 735,93°C in 1,71 seconds i.e. ≈ 384,25°C/s.
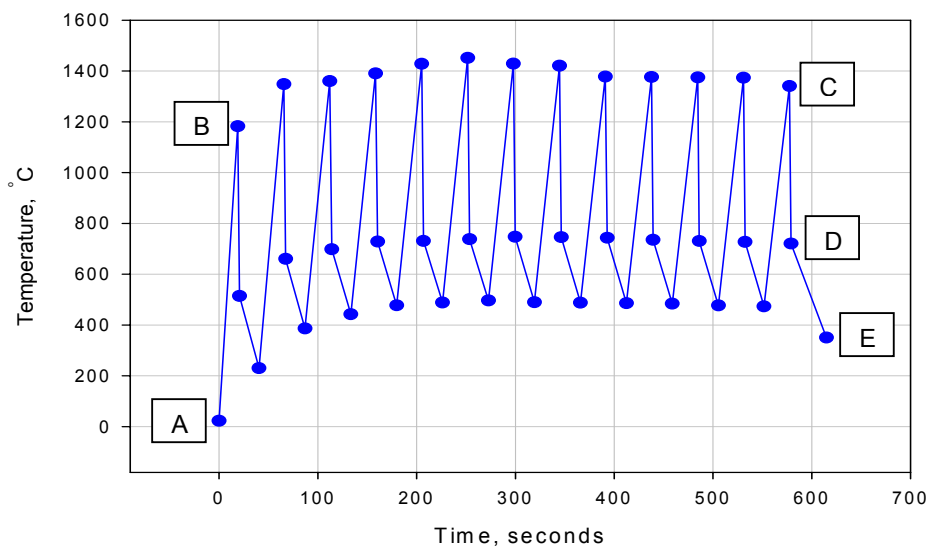
Figure 4.30: Total scanning cycle for 7,5mm beam diameter

The heating/cooling rates of the various regions indicated on Figure 4.30 are:

- Heating between points A and B: 61°C/s

- Cooling between points C and D: 383°C/s

- Cooling between points D and E: 10°C/s

The heat pattern (heat flow) between scanning cycles is shown in Figure 4.31. It can be observed that the previous scan lines (difference in temperature) are also still visible.
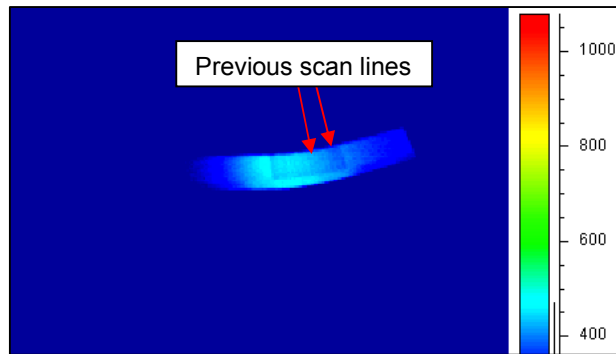
Figure 4.31: Temperature profile between scanning cycles

4.7.2 14mm Beam diameter

The three samples investigated were produced using the following laser parameters:

- Laser power: 3,1kW
- Beam diameter: 14mm
- Interval spacing: 10,5mm
- Scanning velocity: 2m/min
- %Overlap between scans: 25%
- Line energy: 1550J/m

Time-temperature readings taken from the infrared camera recordings are shown in Table 4.6. Maximum temperature is reached at the seventh scanning cycle (line). The temperature difference between maximum readings taken while scanning is 267,7°C. The difference in temperature

observed for readings taken just before each first scan is 294,1°C
(disregarding the 23°C, which was room temperature before forming) and
268,7°C for measurements taken just after the fifth scan.

Table 4.6: Time-temperature readings for 14mm beam diameter

Line	Just before 1st scan		Max at 5th scan		Just after 5th scan	
(Scanning cycle)	Temperature °C	Time sec	Temperature °C	Time sec	Temperature °C	Time sec
1	23	0	1176.7	18.54	718.9	19.42
2	353.1	38.42	1309.9	56.98	819.7	58.28
3	511.9	76.98	1385.1	95.62	931.5	96.64
4	594.4	115.54	1422.5	134.08	971.1	135.14
5	629.1	153.98	1426.3	172.8	984.4	173.68
6	641.4	192.74	1431.7	211.22	984.7	212.3
7	647.2	231.22	1444.4	249.7	987.3	250.78
8	643.5	269.94	1428.8	288.44	987.6	289.46
9	643.0	308.38	1412.6	316.14	978.8	317.18
10	625.9	336.08	1402.8	354.7	959.7	355.64

Figure 4.32 is an image obtained from the infrared camera and shows
the temperature distribution after the last scan of the first scanning cycle.
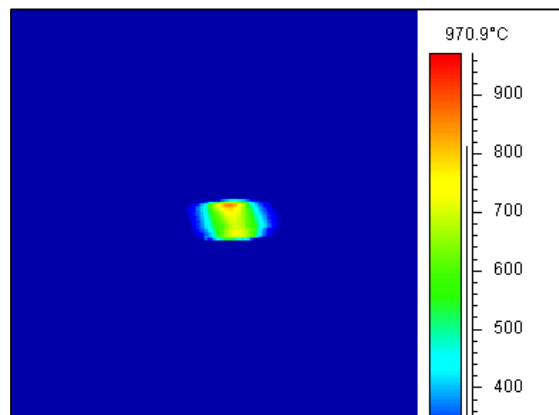
Figure 4.32: Infrared image of first scanning cycle, 14mm beam diameter

Figure 4.33 shows a graphic representation of the data displayed in Table 4.6. From Figure 4.33 it is clear that the temperature levels off (reaches a plateau) as the process continues.
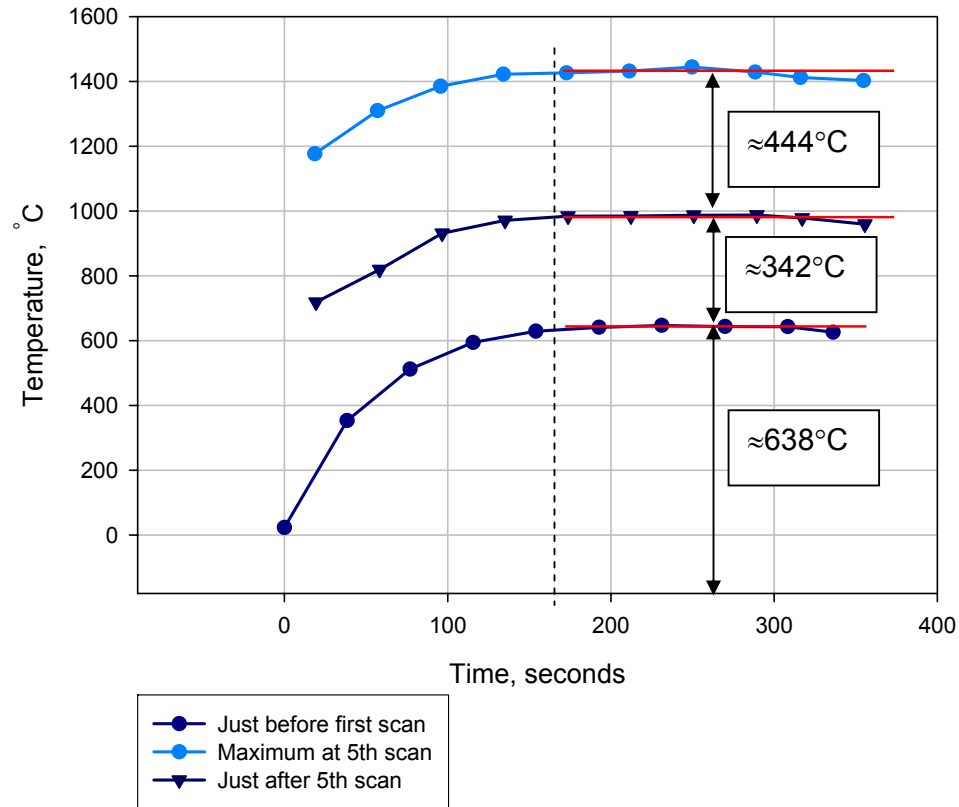
Figure 4.33: Graph showing time-temperature data for 14mm beam diameter

The temperature ranges stabilizes at the fifth scanning cycle. The average temperature difference between the times at which measurements were taken is also indicated on Figure 4.33. The average temperature differences between lines on Figure 4.33 were calculated using values of the last six readings (plateau region).

The complete forming process lasted 5 minutes 55,8 seconds and the specimen cooled to 420,2°C (from 1402,8°C) in 41,04 seconds from the time the laser beam left the sample. The heat distribution pattern shown in Figure 4.32 is more clearly illustrated in Figure 4.34, which shows the sample just after the fifth scan of the second scanning cycle. This concentration in temperature at the edge of the specimen has been

discussed in Chapter 2 and leads to a decrease in bend angle in those regions, due to a smaller temperature gradient.
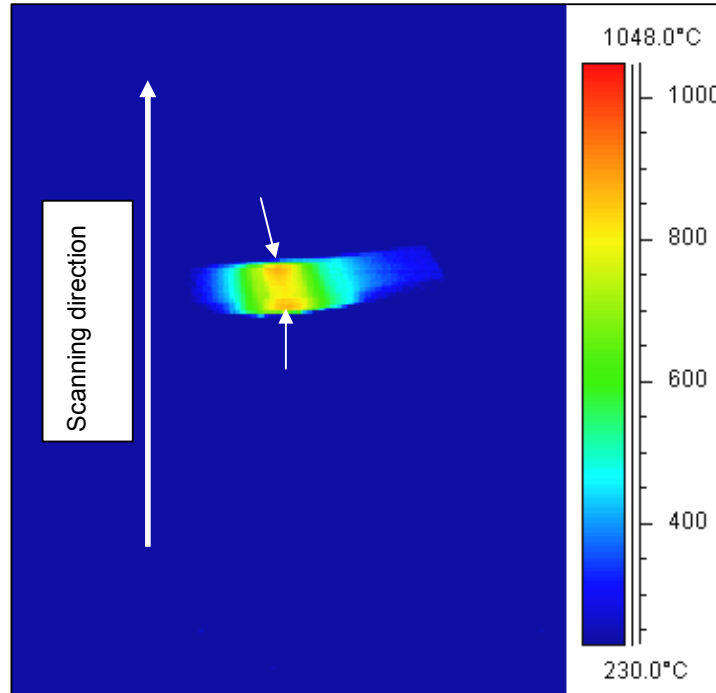
Figure 4.34: Heat distribution pattern – 14mm beam diameter

From Figure 4.34 it can be observed that the edges of the sample (indicated by white arrows) show a higher temperature distribution than the rest of the sample. The front edge (beginning of scan) experiences a higher temperature because the beam also interacts with the side surface which also absorbs heat. The same happens at the back edge and hence the temperature in these two regions are slightly higher than the rest of the sample which only has one surface (top) exposed to the laser beam. The heat flow around an edge is different than through the body of the sample and this contributed to the heat pattern observed. This pattern was present during all stages of the forming process. The progressive increase in bend height is shown in Figure 4.35(a), (b) and (c).
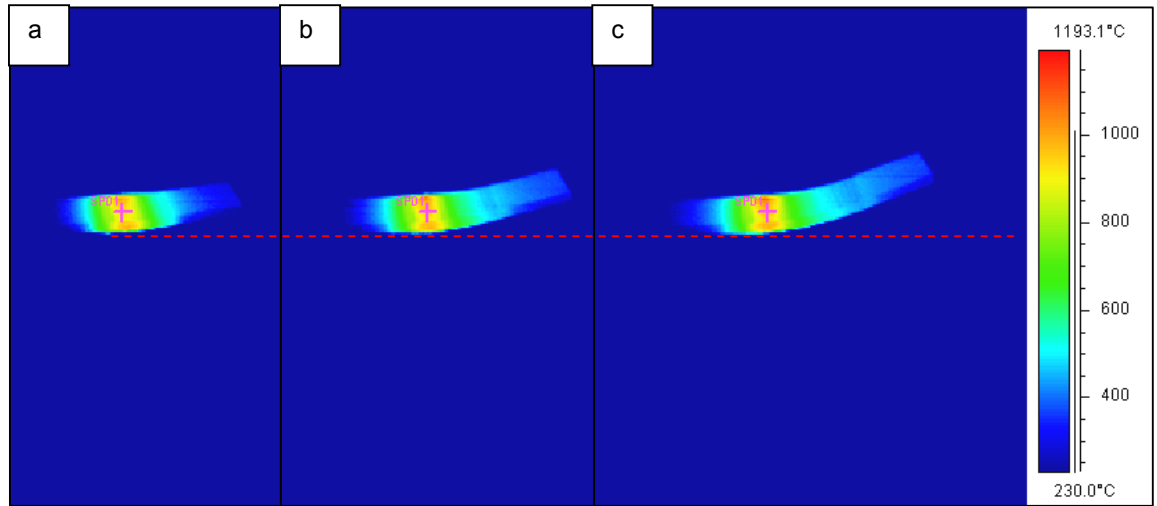
Figure 4.35: (a) Second scan cycle, (b) third scan cycle and (c) fourth scan cycle

It is also clear that the sample reached a higher temperature than the samples produced with the 7,5mm beam diameter settings. The bending mechanism (buckling) was observed during the forming process. Negative bending was observed during the forming process, although it was very slight. The temperature profile of the specimen after completion of seven scanning cycles is shown graphically in Figure 4.36.
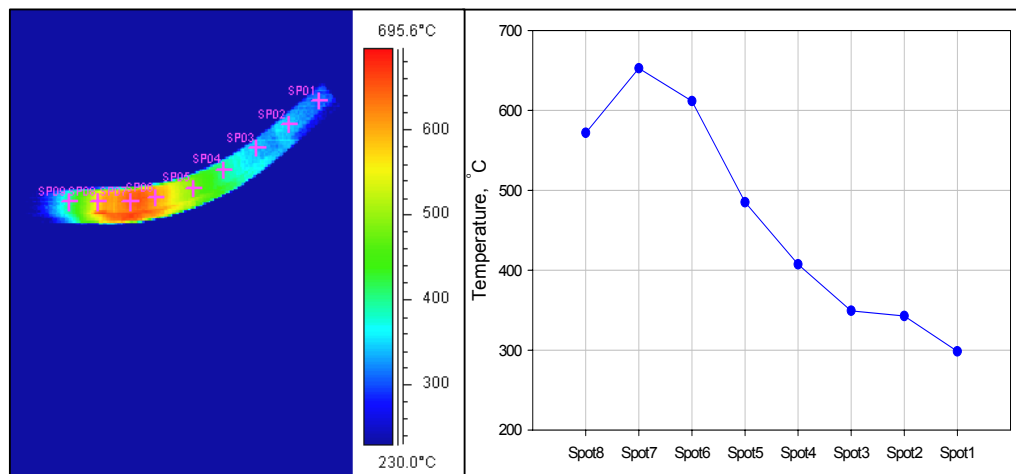
Figure 4.36: Temperature profile after seventh scanning cycle

It can be observed that the temperature, on the edge from which irradiation started, is significantly higher than that observed on the 7,5mm beam diameter samples (80,8°C). This is due to a combination of factors such as higher line energy and an increased percentage overlap between scanning lines.

The complete forming process consisted of ten scanning cycles (five lines per cycle) which are graphically displayed in Figure 4.37. On average the temperature falls from 1384,08°C to 932,37°C in 1,03 seconds i.e. ≈439°C/s.
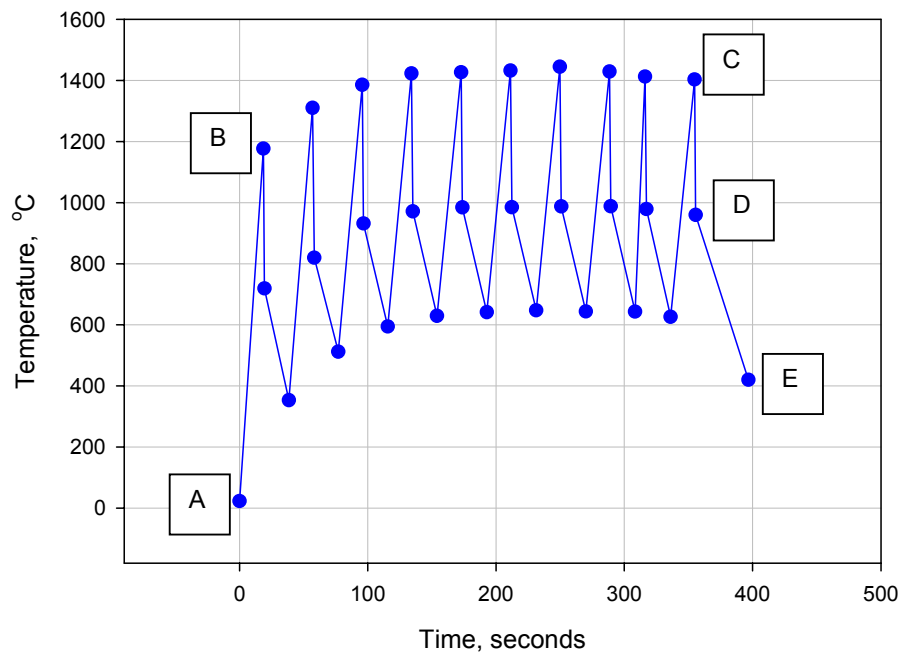
Figure 4.37: Total scanning cycle for 14mm beam diameter

The heating/cooling rates of the various regions indicated on Figure 4.37 are:

- Heating between points A and B: 62°C/s
- Cooling between points C and D: 471°C/s
- Cooling between points D and E: 13°C/s

4.7.3 20mm Beam diameter

Three samples were produced for analysis using the following laser parameters:

- Laser power: 5kW
- Beam diameter: 20mm
- Interval spacing: 10mm
- Scanning velocity: 2,5m/min
- %Overlap between scans: 50%
- Line energy: 2000J/m

Time-temperature readings taken from the infrared camera recordings are shown in Table 4.7.

Table 4.7: Time-temperature readings for 20mm beam diameter

Line (Scanning cycle)	Just before 1st scan		Max at 5th scan		Just after 5th scan	
	Temperature °C	Time sec	Temperature °C	Time sec	Temperature °C	Time sec
1	23	0	1238.3	16.44	827.1	17.3
2	447.9	35.88	1358.4	52.6	1025.3	53.5
3	653.6	72.14	1401.3	88.72	1105.8	89.54
4	706.8	108.22	1413.9	124.82	1114.8	125.86
5	719.2	144.42	1423.3	160.84	1144.4	161.84
6	707.2	180.5	1471.6	196.94	1142.4	197.92
7	724.3	216.48	1482.2	233.14	1150	234
8	720.7	252.62	1486.2	269.32	1153.6	270.2
9	722.4	288.78	1481.1	305.2	1156.2	306.2
10	720.3	324.82	1480.5	341.32	1136.3	342.24

A maximum temperature of 1486,2°C was reached during the eighth scanning cycle. The temperature range observed for the **maximum temperature** readings is 247,9°C. The temperature range for **just before the first scan** readings is 276,4°C (disregarding the 23°C reading), for **just after the fifth scan** readings the value is 329,1°C.

The temperature differences between the various scanning lines were calculated using the average of the last five readings. The cooling rate from maximum temperature to the readings taken just after the fifth scan is slower than those observed on the previous samples. On average the sample cools from a temperature of 1423,68°C to 1095,59°C in 0,926 seconds i.e. ≈354°C/s.

A graphical representation of the data in Table 4.7 is shown in Figure 4.38.
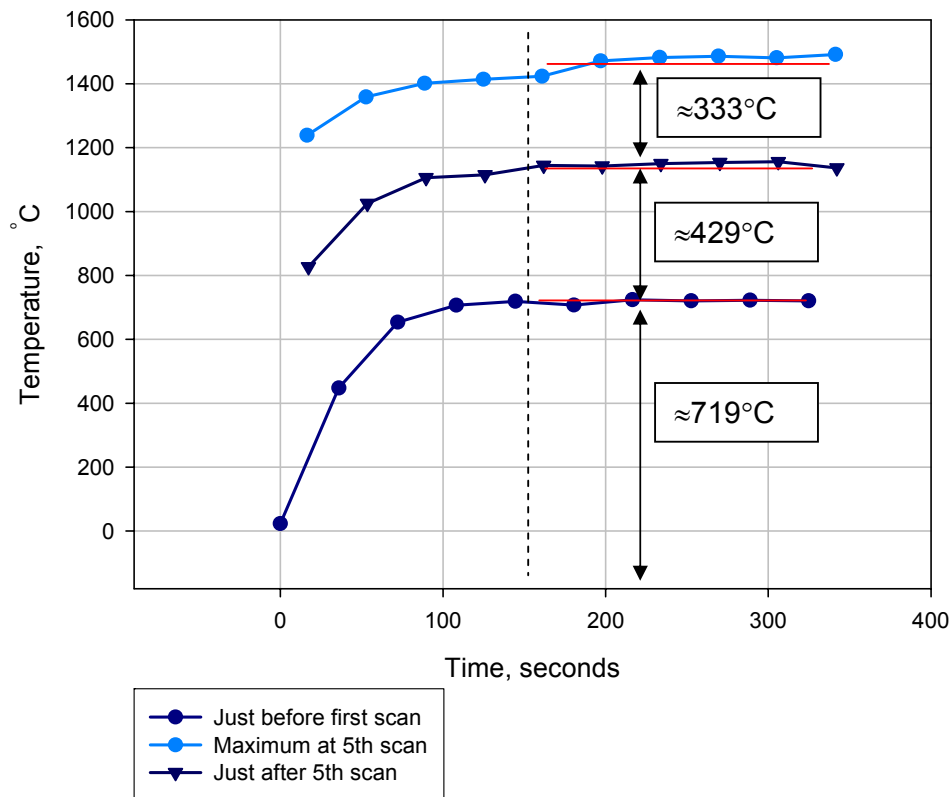
Figure 4.38: Graphic representation of time-temperature data for 20mm beam diameter

Because the beam diameter is relatively large (diffused beam), a clear donut shape (ring) can be observed in Figure 4.39, which is an image taken during the first scan of the first cycle. The coloured plume that is visible, is in fact the gaseous products from the matte black paint which is being burned off by the heat of the laser beam.
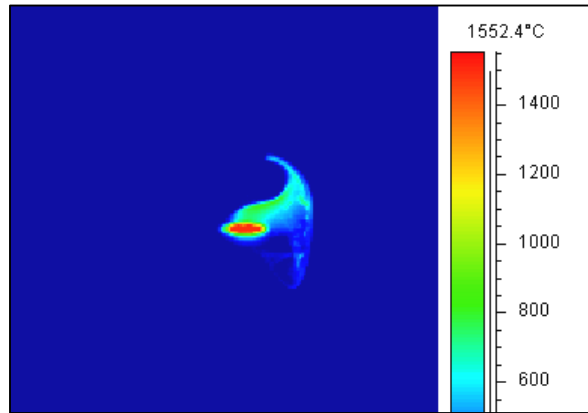
Figure 4.39: Image of first scan during first scanning cycle

Figure 4.40 shows the temperature distribution on the sample during the fifth scan of the first cycle. The heat pattern is wider than those obtained previously due to the larger beam diameter.
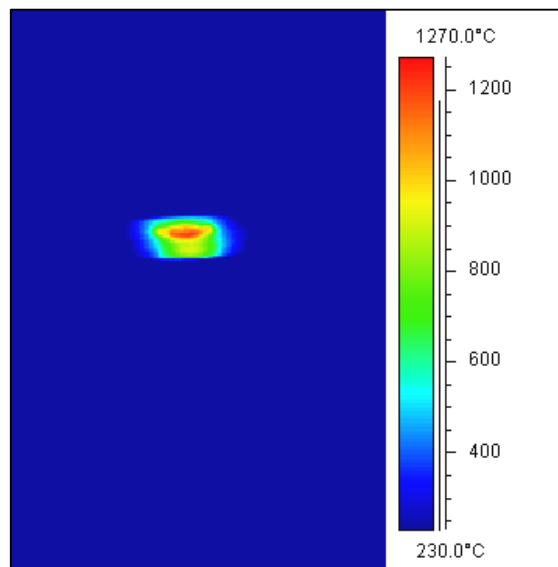
Figure 4.40: Image of fifth scan during first scanning cycle

The sequential increase in bend height can be seen in Figure 4.41(a), (b) and (c).
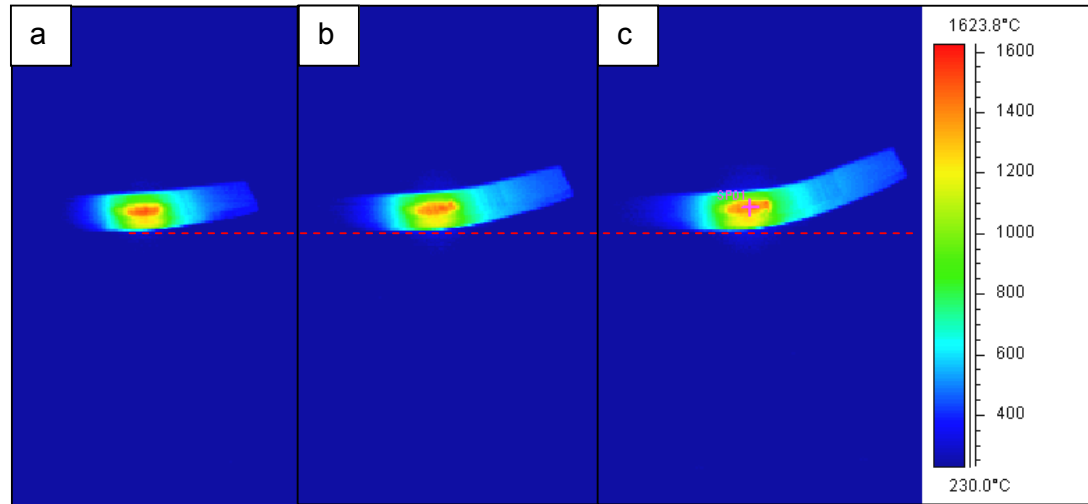
Figure 4.41: (a) Second scan cycle, (b) third scan cycle and (c) fourth scan cycle

The heat pattern after scanning is similar to those observed on previous samples, except that a higher temperature is achieved. Figure 4.42 shows the image displaying the temperature/heat distribution pattern.
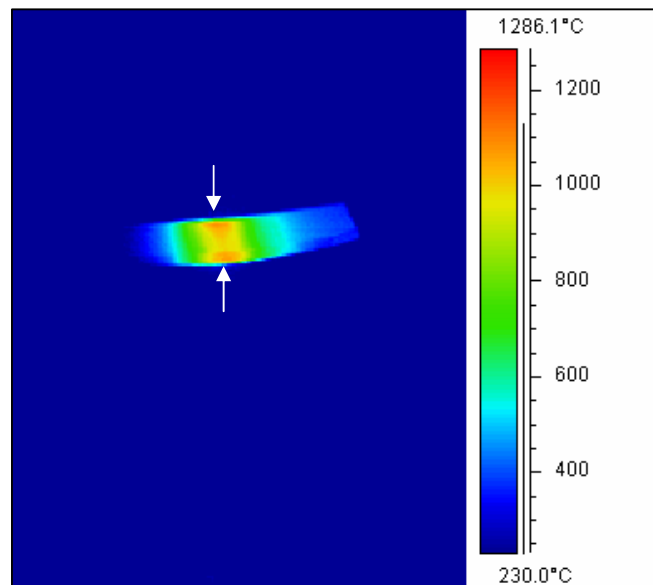
Figure 4.42: Temperature distribution pattern – 20mm beam diameter

The bending mechanism is illustrated with the aid of thermal images in Figure 4.43. This process is more observable using these settings, as

the negative bending observed on previous samples were only very slight in comparison as the size of their plasticized zones is considerably smaller.
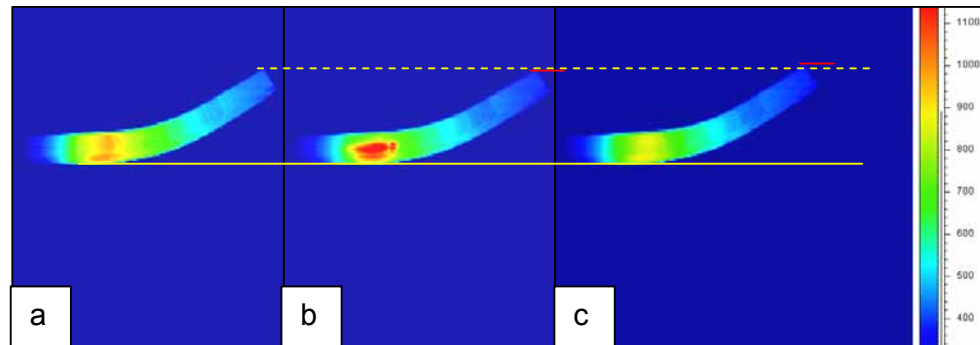
Figure 4.43: Thermal images illustrating bending mechanism

Figure 4.43(a) shows the sample just after the laser beam has left the metal surface. The material is already heated in the region of the laser material interaction. Figure 4.43(b) is an image of the sample at the beginning of the radiation cycle. The regions near the surface are heated to high temperatures while further away the regions are cooler, this resulting in a relaxation of the bend angle. The regions near the surface wants to expand due to heating, but are restrained by the regions below. This causes compressive stresses to be set up in these regions.

From Figure 4.43(c) it is clear that the bend angle has increased again. This is because the metal starts to cool which results in elastic shrinking of the region. Because of the existence of compressive plastic strains formed in regions near the heated zone, the sample bends upwards (positive bend angle).

The temperature profile of the sample just after the final laser scan has been completed, is shown in Figure 4.44.
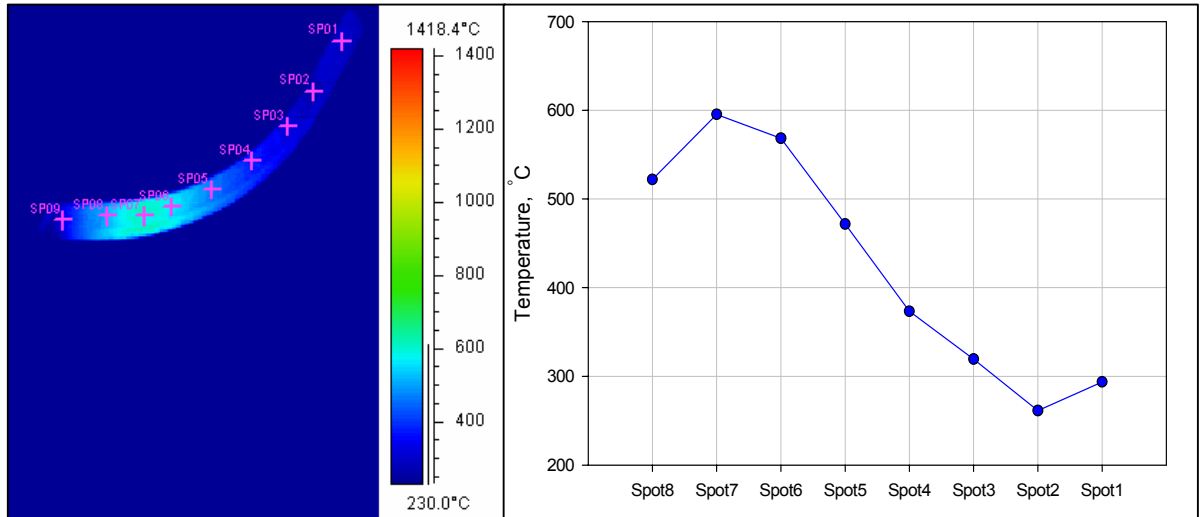
Figure 4.44: Temperature profile after tenth (final) scanning cycle

The complete forming process consisted of ten scanning cycles (five scans per cycle) and lasted 8 minutes 33,6 seconds. After completing the laser forming process, the sample cooled down to 433,3°C in 57,55 seconds. The complete scanning cycle (forming process) is shown graphically in Figure 4.45.
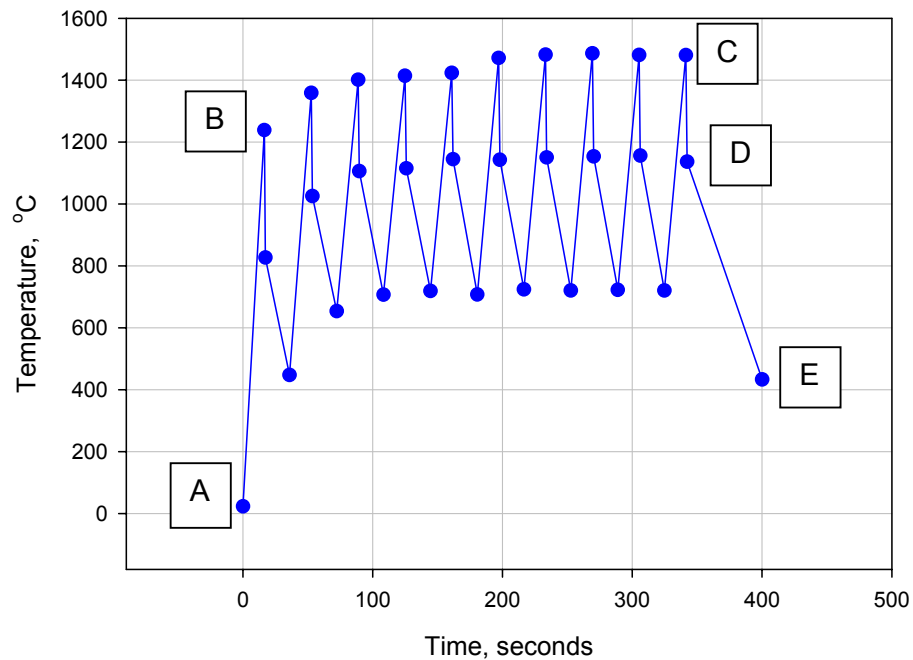
Figure 4.45: Total scanning cycle for 20mm beam diameter

The heating/cooling rates of the various regions indicated on Figure 4.45 are:

- Heating between points A and B: 76°C/s

- Cooling between points C and D: 374°C/s

- Cooling between points D and E: 12°C/s

4.7.4 Laser parameters correlation

The graph depicted in Figure 4.46 shows the relationship between the complete forming cycles for the various parameters used to produce the specimens. It is clear from Figure 4.46 that the total length of the forming cycle for the 7,5mm beam diameter settings took much longer to complete than the other two laser settings used. This means that the sample is exposed to heat for a longer time period than for the other sets of parameters. It is also clear that the maximum temperatures reached by all the samples are very close in temperature scale, whereas the temperature measurement after the complete scanning cycle shows a larger variance between samples.
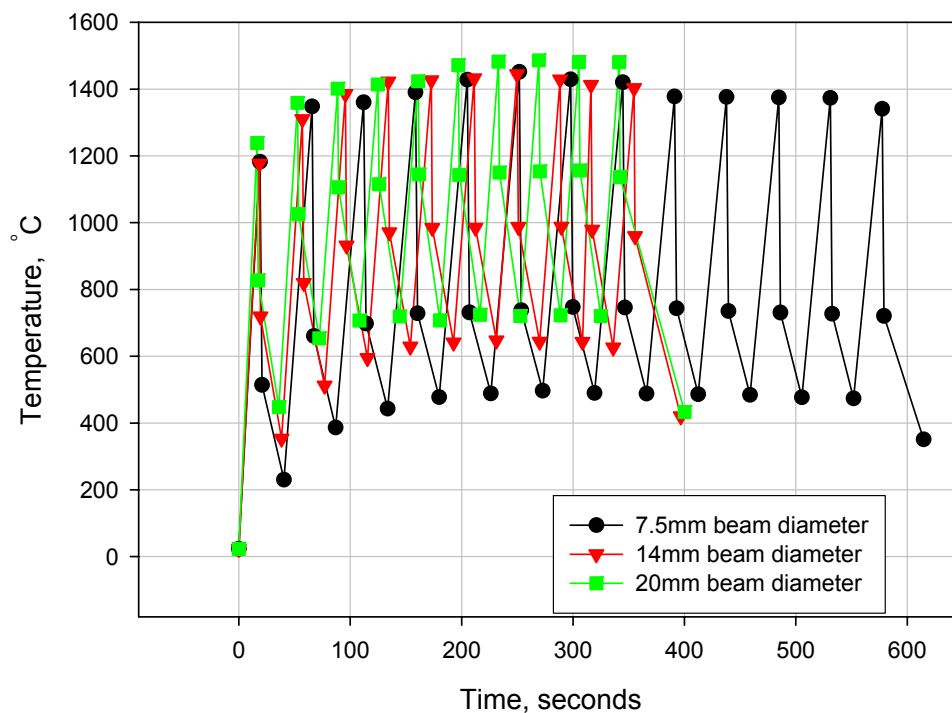
Figure 4.46: Comparison between complete forming cycles for various laser parameters

Figure 4.47 is a graphic representation of maximum temperature readings taken during the forming cycle of the various settings used.
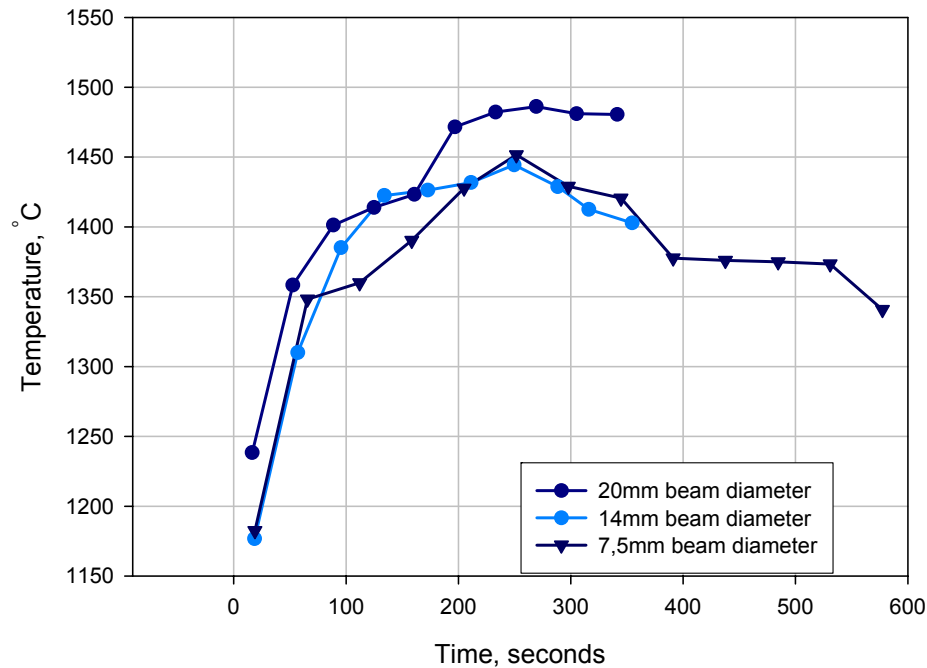
Figure 4.47: Correlation between maximum temperature measurements for the various settings

Due to the scale of the graph it seems that there is a large variation in temperature readings taken at various time intervals during the forming process.   The 7,5mm beam diameter samples exhibited the same trend as those of the 14mm beam diameter. Since it was suggested that the laser forming process must be controlled by maximum temperature readings, it is important to know what range of maximum temperature will result in deformation and if there is any significant differences in final sample dimension due to temperature variation.

The graph shows an increase to a maximum temperature, after which the temperature decreases due to the clamping device acting as a heat sink. The 20mm beam diameter line shows an increase in temperature and no dramatic decrease in temperature as the clamping device is approached. This is because the 20mm beam diameter employs a laser power of 5kW and a scanning velocity of 2,5m/min, which means the sample heats up

quickly and does not cool to the same extent as the others because the scanning velocity is faster than for the other settings.

Figure 4.48 is graphically displaying the temperature measurements just after the fifth scan of each scanning cycle of the three sets of parameters used.
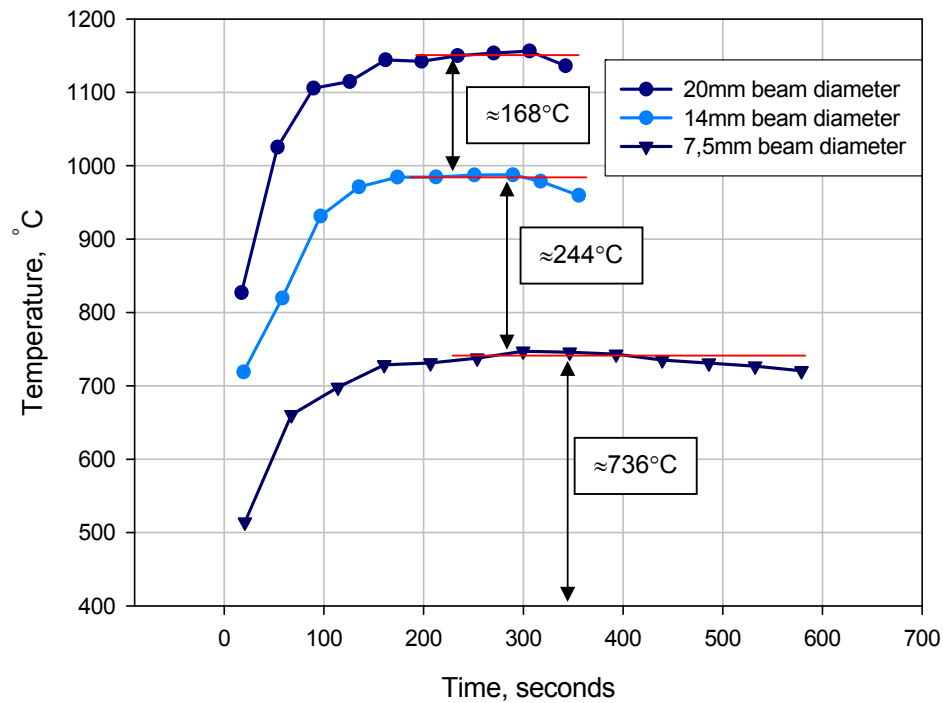
Figure 4.48: Comparison of temperature measurement taken just after the fifth scan

It is clear that as the line energy increased, so did the temperature measured just after the fifth scan. The temperature increased by 33% from the 7,5mm beam diameter readings to the 14mm beam diameter readings. Similarly there was a 17% increase in temperature between the 14mm beam diameter readings and the 20mm beam diameter readings.   The temperature increase between the 7,5mm beam diameter readings and the 20mm beam diameter readings correspond with a value of 56%.

Figure 4.49 graphically displays the temperature readings taken just before the first scan of each scanning line.
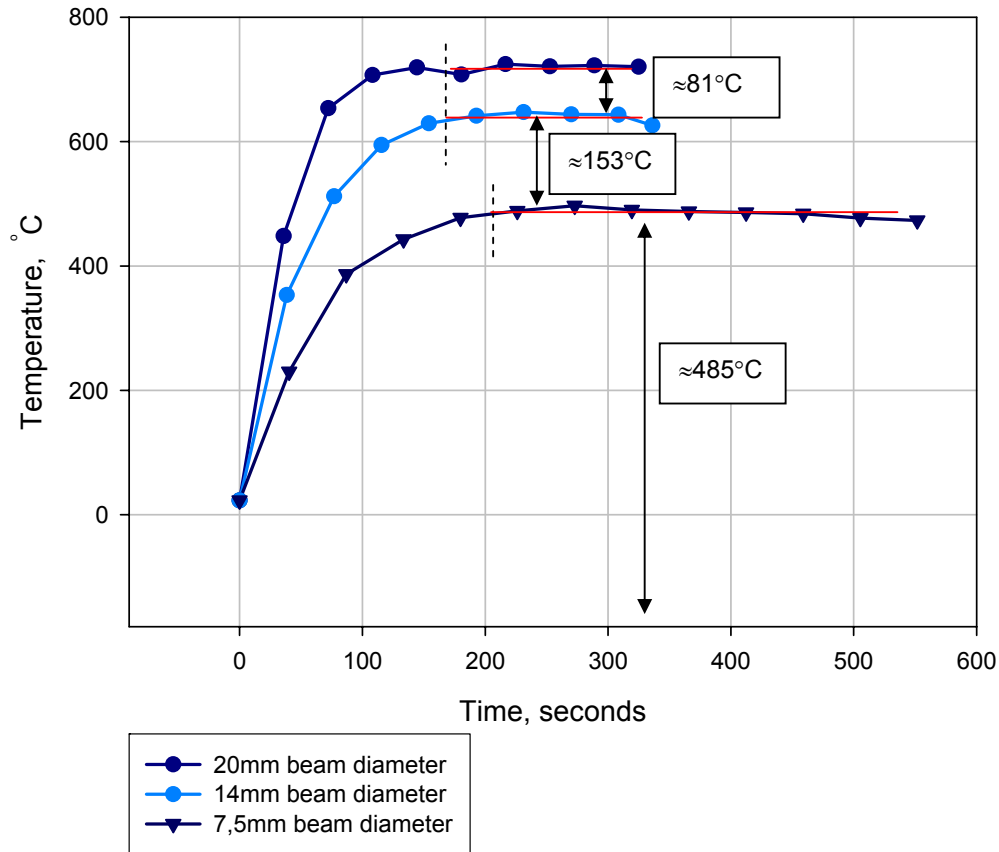
Figure 4.49: Graphic representation of temperature readings just before the first scan

Once again the settings using the highest line energy also exhibited the highest temperature. The increase between the temperature readings of the 7,5mm beam diameter and the 14mm beam diameter samples showed a 32% increase. The increase in temperature readings between the 14mm beam diameter and the 20mm beam diameter corresponds with a value of 13%. There was a 48% increase between the 7,5mm beam diameter and 20mm beam diameter readings.

A graph, on an expanded scale, of the first few readings of the complete scanning cycles for the three different sets of parameters used, are shown in Figure 4.50.
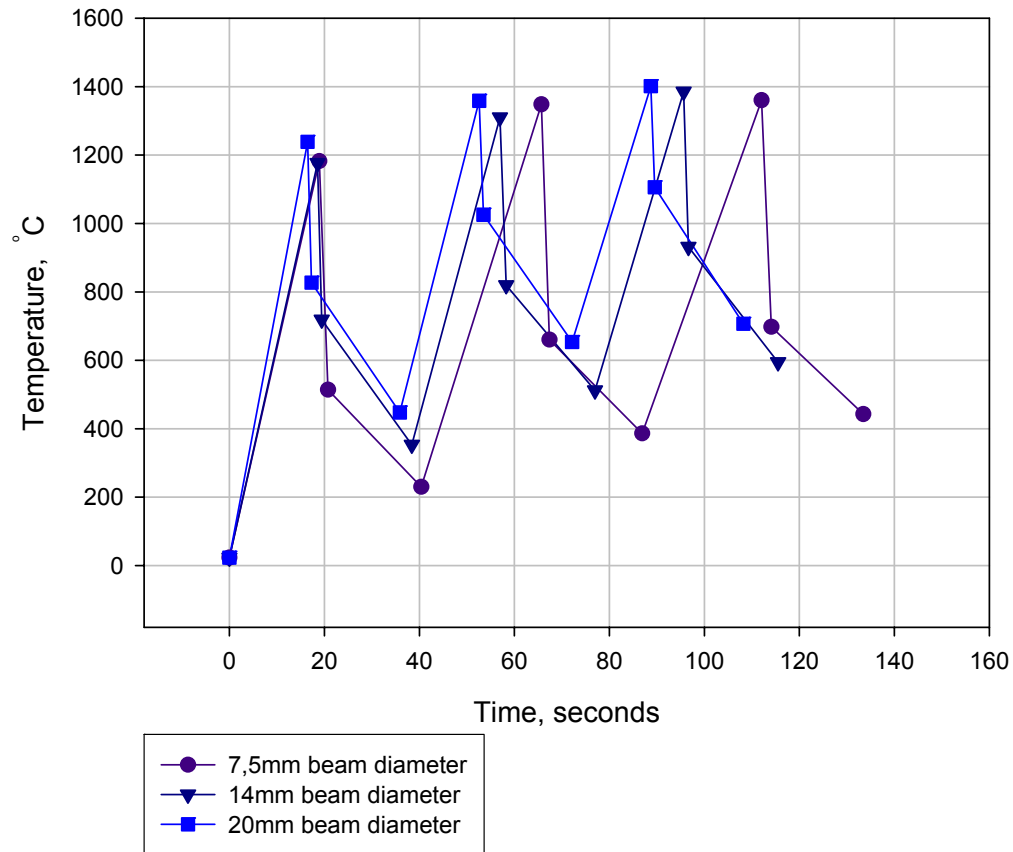
Figure 4.50: Expanded region of first section of scanning cycles of various laser parameters

The variations between the various laser parameters are now more evident. It is also clear that the 7,5mm beam diameter settings exhibit the slowest process speed.

4.7.5   Relationship to Time-Temperature-Transformation (TTT) diagram

It is clear from the microstructures observed in the previous section that there should be a correlation to the TTT diagram. It was difficult to try and predict the type of microstructure from the TTT diagram obtained from literature or to forecast the cooling rate required for the

microstructures observed on the various samples. In order to determine the microstructure, accurate measurements of the cooling rate at a single point had to be made on the various samples. The point on all samples was taken in the centre of the sample, i.e. after half of the irradiation cycles were completed. Samples for metallurgical investigation were taken from the centre of the specimen. The time-temperature readings for the various samples are given in Appendix B. A graphic representation of the time-temperature data for the 7,5mm beam diameter samples are shown in Figure 4.51.
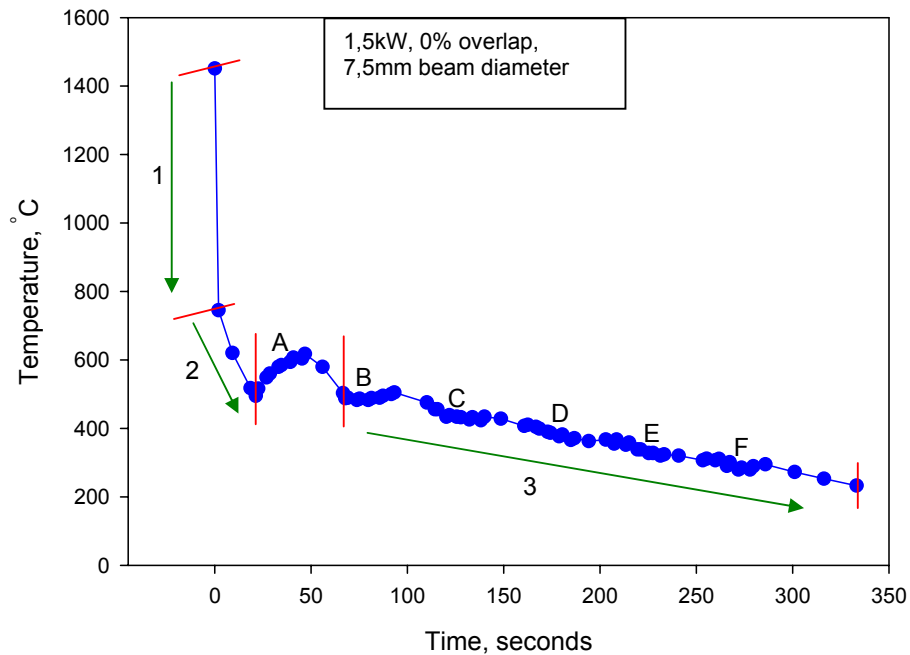
Figure 4.51: Graphic representation of time-temperature data for 7,5mm beam diameter

From Figure 4.51 it is clear that the maximum temperature is reached during laser irradiation of the specific point at which measurements were taken. The first irradiation cycle adjacent (next scanning cycle) to this point seems to have an influence on the cooling rate as indicated by point A on the graph. Subsequent irradiation cycles (scanning cycles) seem to have less of an effect, except for slowing down the cooling rate (of the specific point in the center of the sample where all temperature

readings were taken). The subsequent irradiation cycles (scanning cycles) are indicated by points B, C, D, E and F on the graph.

The cooling rates at the various regions on Figure 4.51 are indicated by green arrows. The cooling rate is most severe when cooling from the original laser irradiation at the point of measurement (first region indicated by **1** on Figure 4.51) and corresponds with a value of 364°C/s. The second region (indicated by **2** on Figure 4.51) indicates a slower cooling rate of 13°C/s and the third region (indicated by **3** on Figure 4.51) shows an even slower cooling rate of only 1,1°C/s. The cooling rate is significant because if cooling is slow enough and above the temperature at which martensite forms, no martensite will be present in the final microstructure. On the other hand, if the cooling rate is fast enough, martensite will be present.

Figure 4.52 shows the location of the temperature measurement during subsequent laser irradiation cycles (cross).
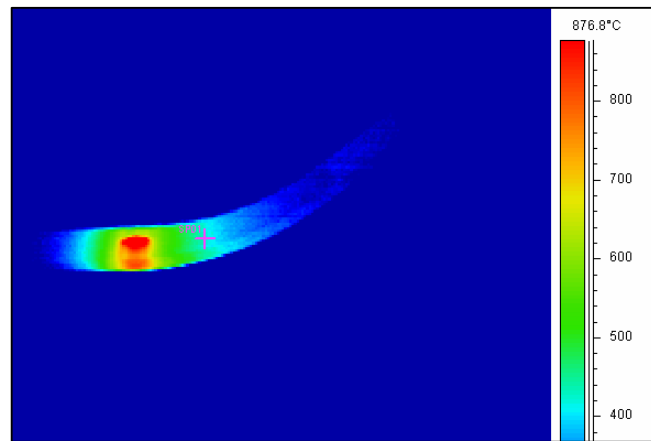
Figure 4.52: Point of temperature measurement

The graphic representation of the samples formed with the 3,1kW and 14mm beam diameter settings are shown in Figure 4.53.
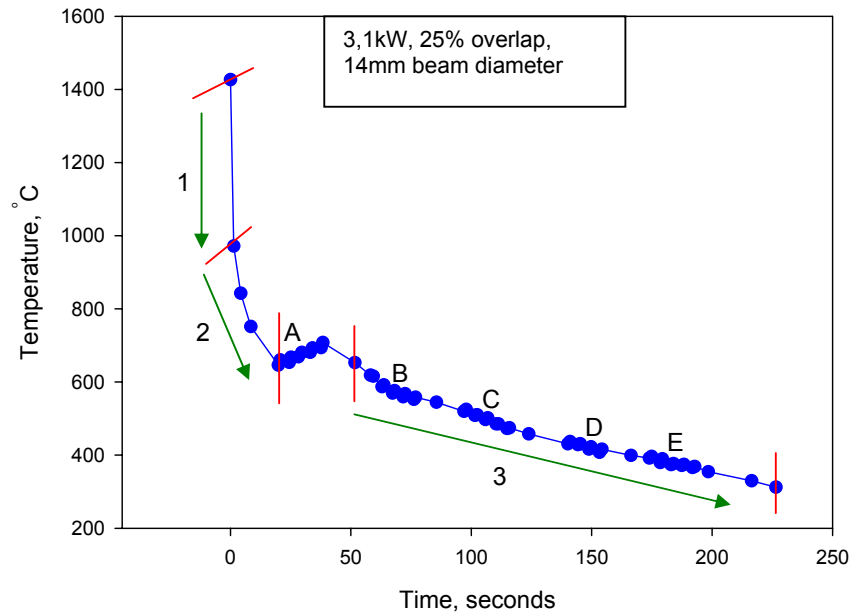
Figure 4.53: Graphic representation of time-temperature data for 14mm beam diameter

The shape of the curve in Figure 4.51 and Figure 4.53 is very similar except that the temperature ranges differ slightly. It can thus be said that an overlap of 25% between consecutive laser irradiation lines only seems to influence the temperature experienced at the point being measured.

The cooling rate in region one (green arrows) is the fastest and corresponds with a value of 334°C/s. In region two, the cooling rate is slower and corresponds with a value of 9°C/s. Region three has the slowest cooling rate on the graph and corresponds with a value of 1,9°C/s. The values of the cooling rates of the various regions on the graph shown in Figure 4.53 are very similar to those observed for the previous sample with a 0% overlap between consecutive laser irradiations.

Figure 4.54 shows the graphic representation of time-temperature data for the 5kW and 20mm beam diameter setting. It is clear that the graph displayed in Figure 4.54 appears different to the previous two graphs.
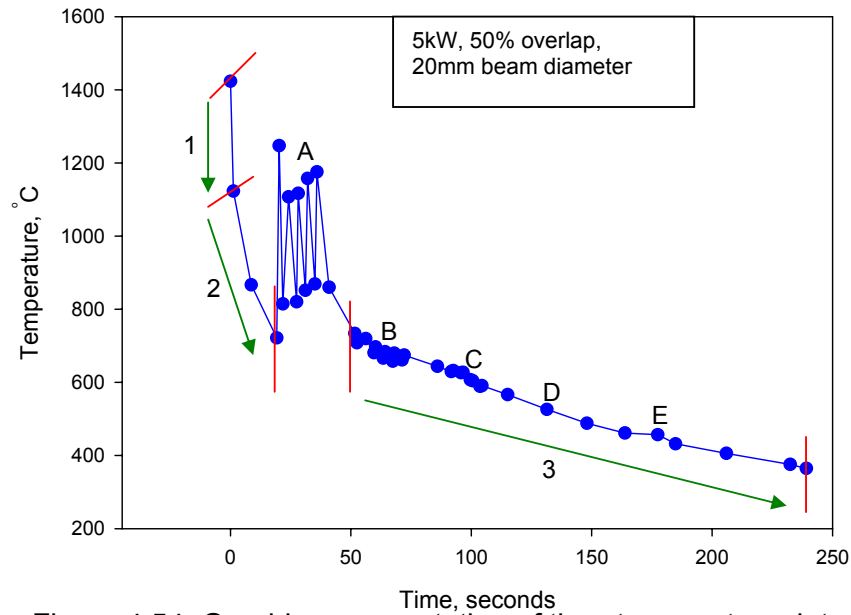
Figure 4.54: Graphic representation of time-temperature data for 20mm beam diameter

The 50% overlap between consecutive laser irradiations definitely increased the temperature at the point of measurement. This means that the point in question remains basically at a temperature above 800°C for two laser irradiation cycles. The fastest cooling rate was observed in region one (green arrows) with a value of 255°C/s. Region two exhibited a cooling rate corresponding with 22°C/s and in region three the cooling rate corresponded with a value of 2°C/s.

Table 4.8 shows the cooling rates of the different samples for the respective regions as indicated by the green arrows on the various time-temperature plots.

Table 4.8: Comparison of cooling rates of the samples

	1,5kW (1250J/m) 7,5mm beam dia. 0% overlap	3,1kW (1550J/m) 14mm beam dia. 25% overlap	5kW (2000J/m) 20mm beam dia. 50% overlap
Region 1	364°C/s	334°C/s	255°C/s
Region 2	13°C/s	9°C/s	22°C/s
Region 3	1,1°C/s	1,9°C/s	2°C/s

From Table 4.8 it is clear that the 1,5kW samples showed the fastest cooling rate in region 1, the 5kW samples the fastest cooling rate in region 2 and region 3. The comparative graph of the cooling cycles of the various samples is shown in Figure 4.55. This graph shows the trend experienced by the samples at a specific point (centre of sample's width and length) while cooling.
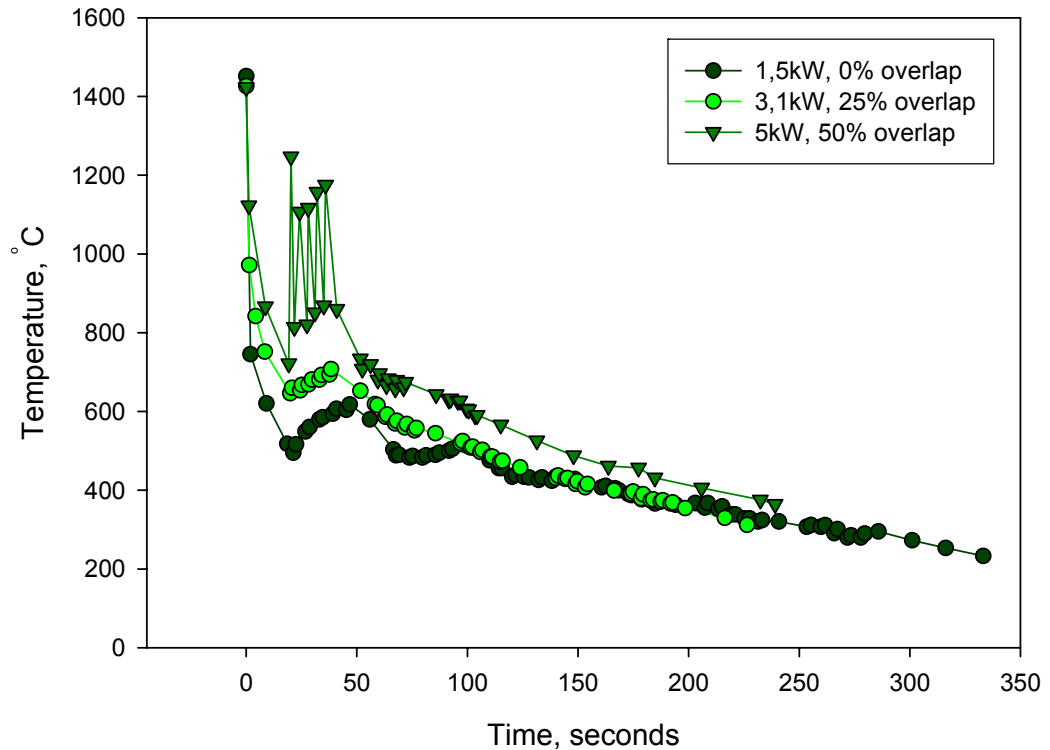
Figure 4.55: Comparative graph indicating cooling rate trends for the various samples

It is clear from the microstructural analysis that both (martensitic and bainitic) transformations have taken place. Due to the percentage overlap between consecutive laser scans, it is difficult to accurately determine the heating/cooling cycle at one specific area.

Taking the TTT diagram into account, the following cooling curves can be superimposed to show the possible resulting microstructure. Figure 4.56(a), (b) and (c) shows the average cooling curves for the various samples evaluated.
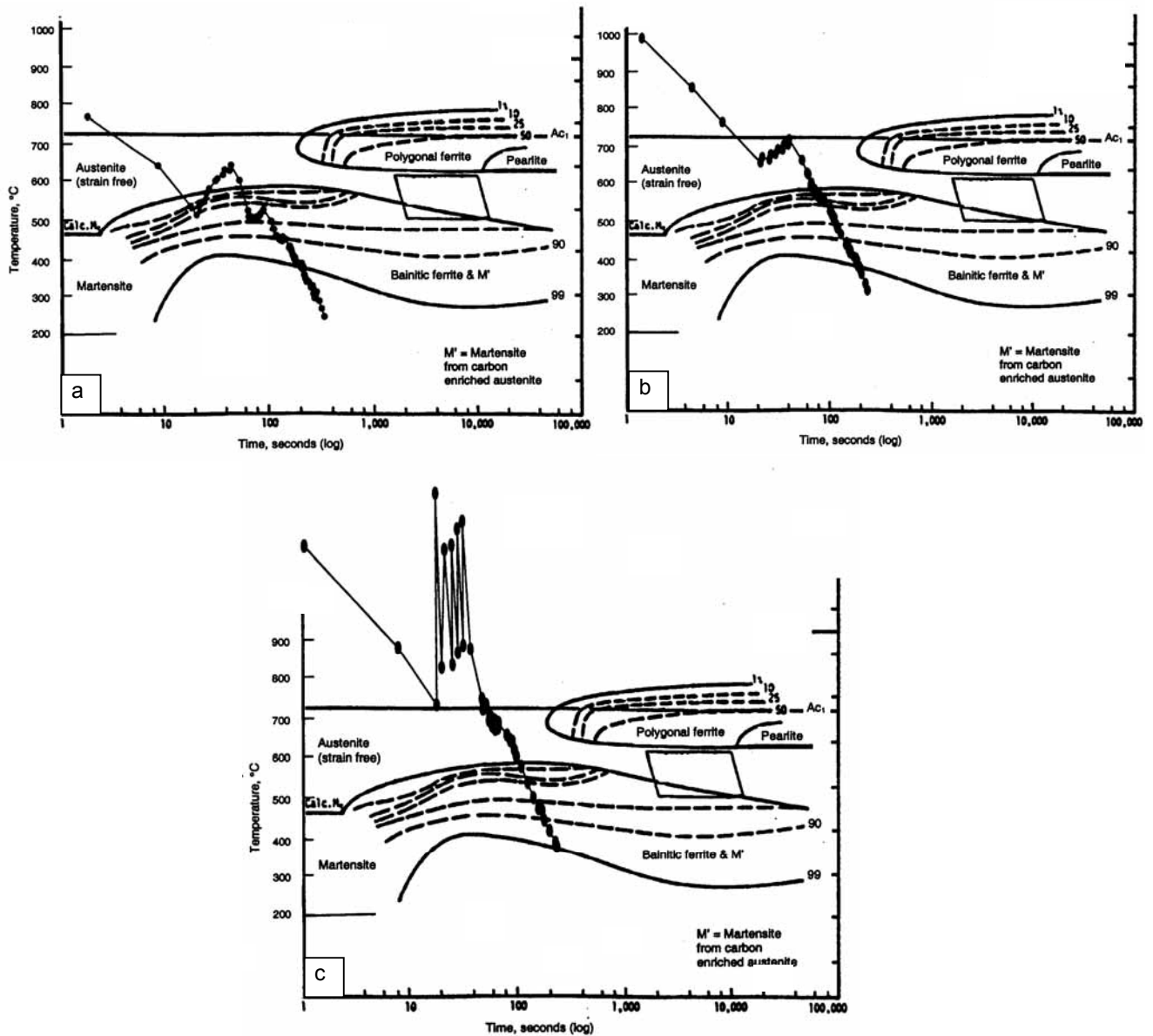
Figure 4.56: (a) Superimposed cooling curve of a sample irradiated with 1,5kW; (b) 3,1kW and (c) 5kW

Figure 4.56(a), (b) and (c) shows that the samples all cool through the same region of the TTT graph i.e. the Bainitic ferrite and Martensitic (M' – martensite formed from carbon enriched austenite) region. There is, however, a difference in the temperature to which the samples are heated during the laser forming process. It is clear that the samples irradiated with 5kW laser power, are at a temperature higher than the

lower critical (Ac1) and upper critical temperature (Ac3) for a longer time than the other samples. This affects the amount of austenite formed during the heating cycle, and also the amount of carbides being dissolved in the austenite. This is the only reason that could be found that could attribute to the variance in microstructure observed using the different laser parameters. It is only the 1,5kW samples that exhibited a microstructure consisting of acicular ferrite (bainitic ferrite) and martensite. It is thus proposed that the 3,1kW and 5kW samples followed a cooling curve similar to what is shown schematically in Figure 4.57.
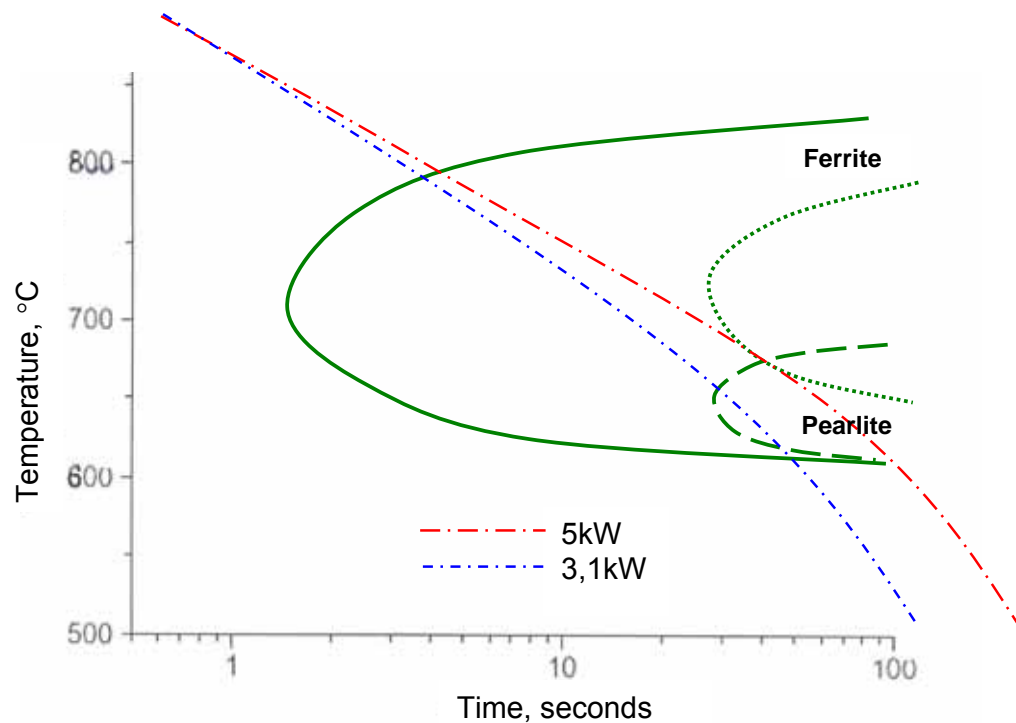
Figure 4.57: Schematic TTT diagram indicating probable cooling rates for 3,1kW and 5kW samples

4.8   RESIDUAL STRESS ANALYSIS

According to ASTM E837-01, the following information should be included when reporting on residual stress analysis:

- Description of test specimen

  Material

  Pertinent mechanical properties

- Model and type of strain gauge used

  Strain gauge geometry

- The method used to drill the hole

- Plot of strain versus depth for each gauge

- Tabulation of strains e1, e2, and e3 at all locations, and

- Tabulation of stresses and direction of stresses at all locations

Most of the required information has already been given in previous sections of this chapter. This section will therefore only concentrate on the last three points listed above.

4.8.1 Original flat plate

Analysis of the relieved residual stress magnitude in the original material before forming is given in the following section. Figure 4.58 shows a plot of measured strains versus hole depth for the original DPS plate.
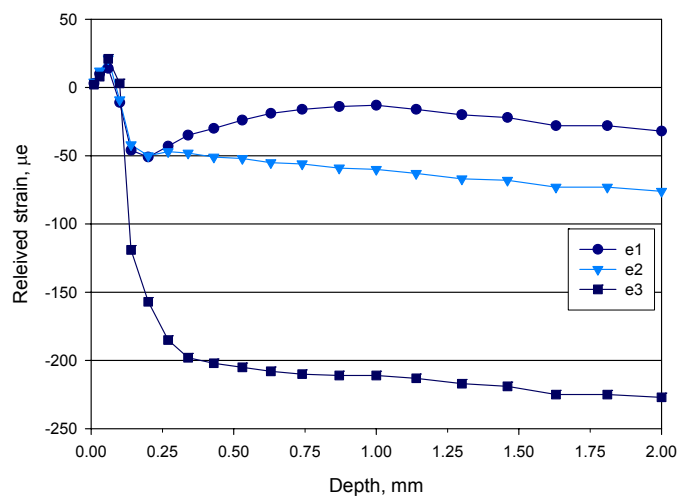
Figure 4.58: Strain relaxation curve as a function of drilling depth – Original plate

The actual results obtained and the magnitude and direction of the principal relieved stresses as calculated according to ASTM E837-01 are tabulated in Appendix F. From Figure 4.58 it is clear that there is a steep gradient from the surface inwards. It is therefore evident that the sample exhibits a non-uniform residual stress distribution which renders the Uniform Stress Method as specified in ASTM E837-01 inadequate for residual stress analysis.

The Average Stress Method or Equivalent Uniform Stress Method will be used to compare the results obtained for the various samples. By definition, the equivalent uniform stress is that   stress magnitude which, if uniformly distributed, would produce the same total relieved strain at any depth, as measured during hole drilling[32].

The results from this technique will provide qualitative information about the stress variation with depth. Using the data generated in Appendix F, the graph in Figure 4.59 of relieved residual stress (maximum and minimum principal stress) versus hole depth can be plotted.
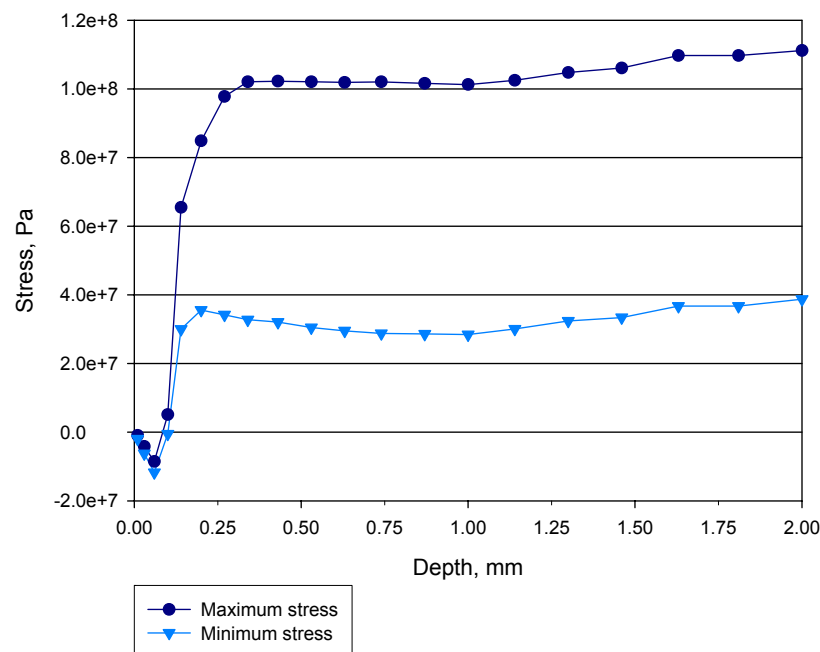
Figure 4.59: Plot of relieved residual stress versus hole depth – Original

No conclusions can be drawn from Figure 4.59, except that both the maximum and minimum calculated principal stresses are mostly tensile in the deeper layers of the material and slightly compressive in the surface layer.

4.8.2 7,5mm Beam diameter (1,5kW) laser formed samples

For comparitive purposes this section will be divided into two sub-sections, viz. LASER SIDE and REVERSE SIDE (opposite to laser irradiated surface).

4.8.2.1 Laser side

Measurements were taken at the following positions on the samples:

- Between lines (coincided with middle of sample)
- Last line

Positions are indicated on Figure 3.8. The results plotted as relieved strains as a function of hole depth are shown in Figure 4.60.
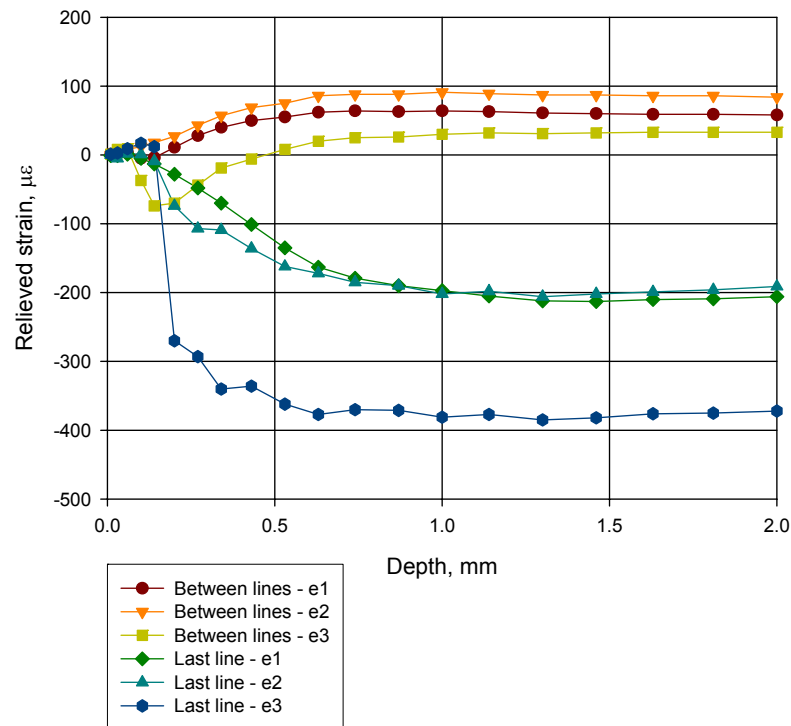
Figure 4.60: Strain relaxation curves for 'between lines' location and 'last line' location – (7,5mm)

From the strain relaxation curves it is evident that there is a difference in relieved strain magnitude and direction. Measurements between the laser lines yielded more positive relieved strain than measurements taken on the last line. The calculated principal stresses and angles are given in Appendix F for the previous samples.

A plot of the calculated principal stresses (minimum and maximum) for both measurement locations is shown on Figure 4.61. The measurements taken between the laser lines indicate residual stress of a compressive nature deeper into the material and also at the surface layer. In between these two sections there is a small region which indicates tensile residual stresses. Measurements taken on the last heating line indicates a relatively large (compared to previous sample) tensile residual stress deeper in the material and a very slight compressive (almost zero) tendency at the surface layer.
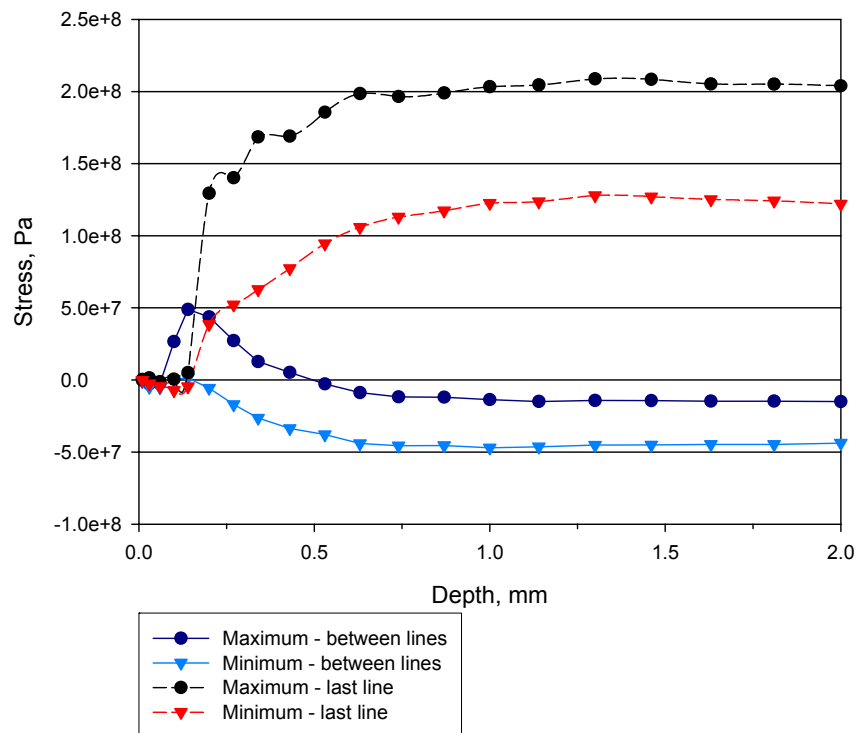
Figure 4.61: Plot of relieved residual stress versus hole depth – 7,5mm LASER SIDE

4.8.2.2 Reverse side

Measurements were taken on the following positions:

- Middle of sample
- Between lines
- Last line

Strain relaxation curves as a function of hole depth for the above positions are shown in Figure 4.62. It is clear that the trends in Figure 4.62 are similar, although the magnitude of relieved strain is vastly different.
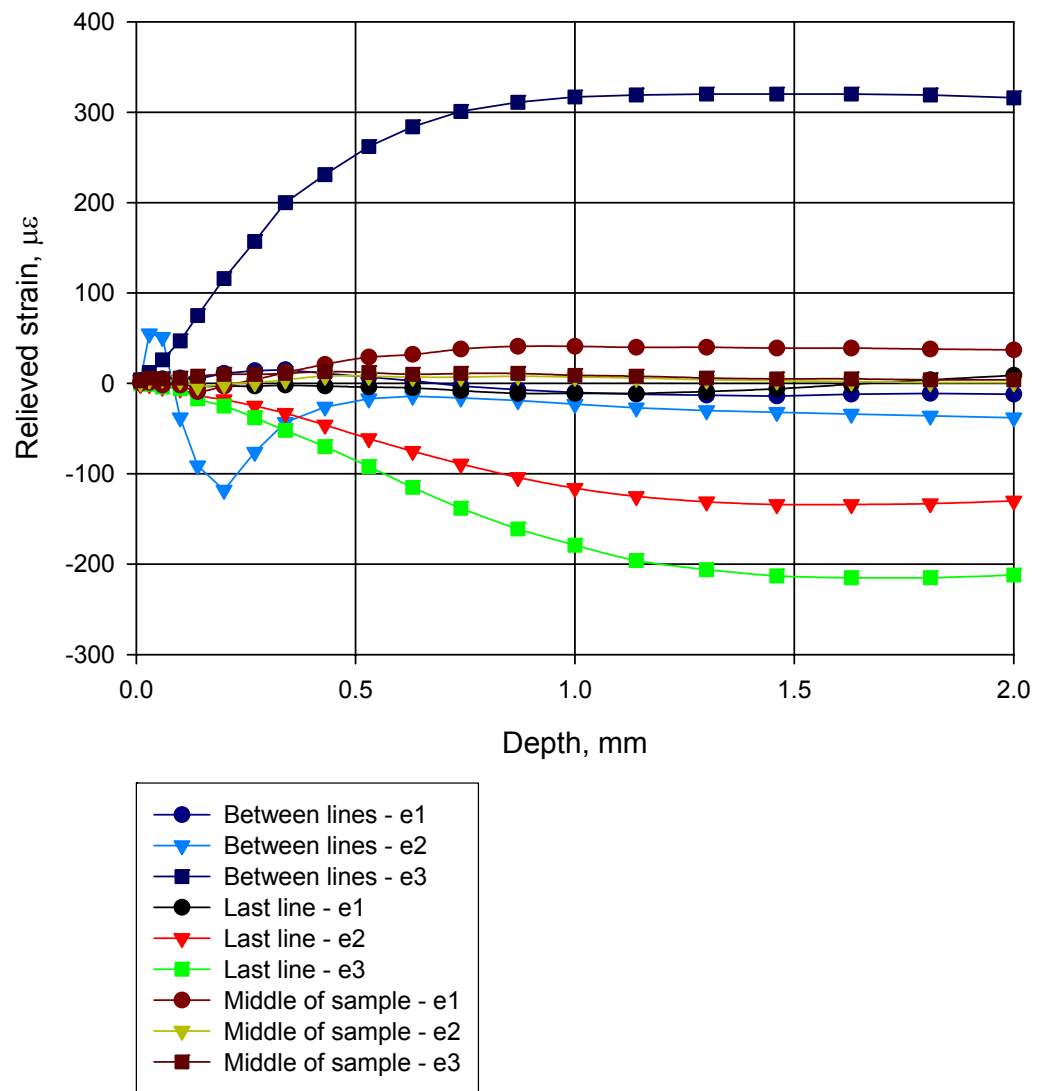
Figure 4.62: Strain relaxation curves for 'middle of sample', 'between lines' and 'last line' locations

The calculated principal stress (min & max) values are given in Appendix F and their matching relieved stress curves are shown in Figure 4.63.
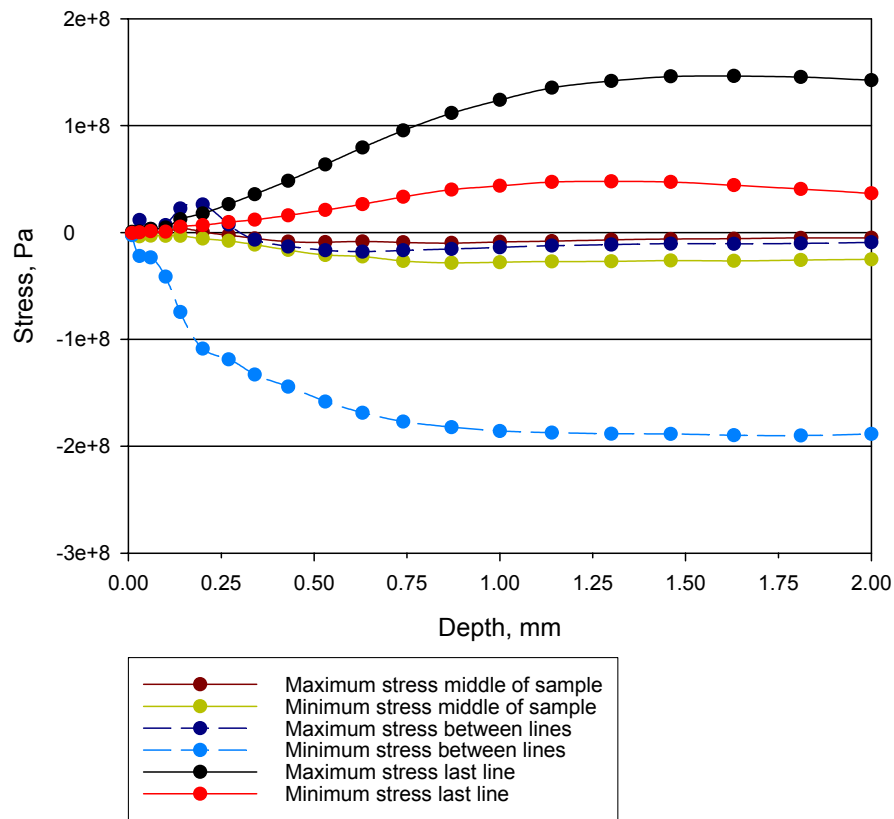
Figure 4.63: Plot of relieved residual stress vs. hole depth – 7,5mm
REVERSE SIDE

4.8.3 20mm Beam diameter (5kW) laser formed samples

4.8.3.1 Laser side

Measurements were taken at the following locations:

- First line
- Middle of sample

The strain relaxation curves as a function of hole depth is shown in Figure 4.64. From Figure 4.64 it seems that the relieved strains are mostly tensile. The results of the calculated principal stresses and corresponding angles are given in Appendix F.
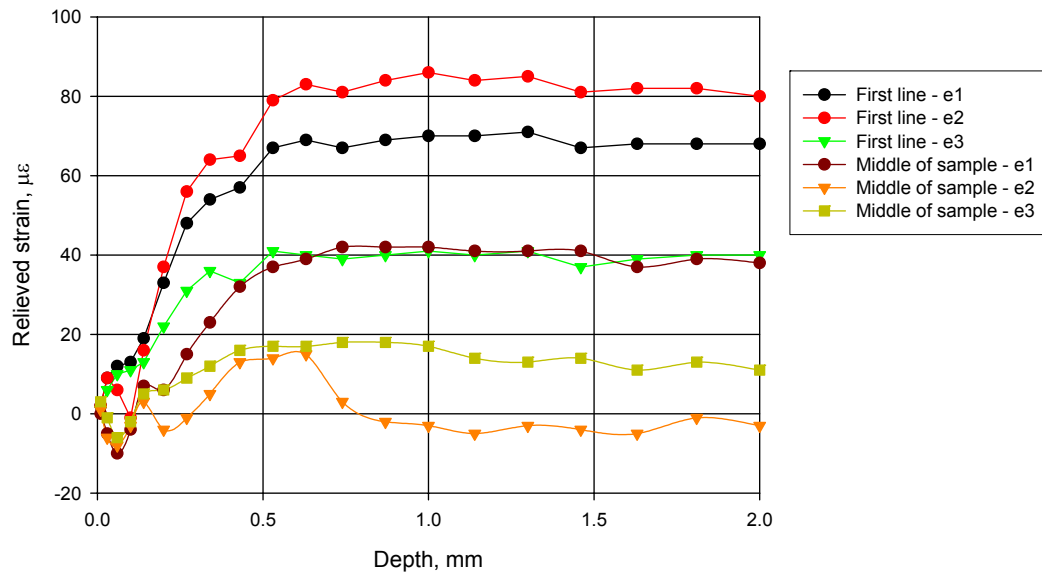
Figure 4.64: Strain relaxation curves for 'first line' and 'middle of sample'
locations – (20mm)

Figure 4.65 is a plot of relieved stress versus hole depth for the above
samples. It is clear that the relieved stress is mostly compressive in the
regions with increasing depth.
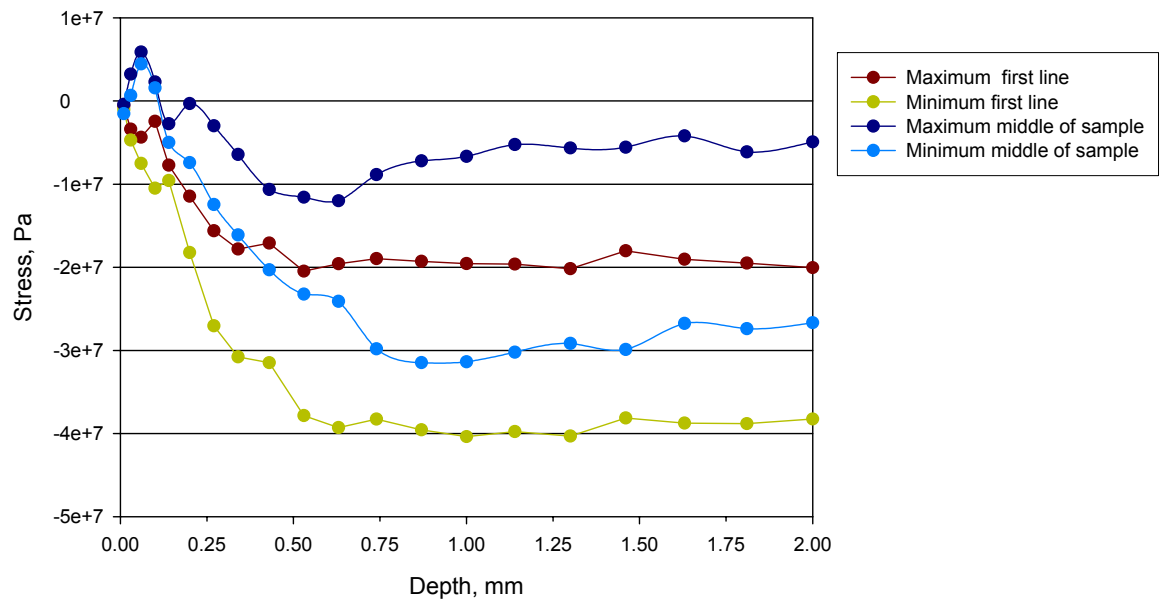
Figure 4.65: Plot of relieved residual stress versus hole depth – 20mm
LASER SIDE

The measurement taken at the middle of the sample indicates a slight tensile stress in the surface layer whereas the measurement on the first line indicates stress of a compressive nature.

4.8.3.2 Reverse side

Measurements on the reverse side of the sample were taken at the following positions:

- Middle of sample
- Last line

The strain relaxation curves as a function of hole depth is shown in Figure 4.66.
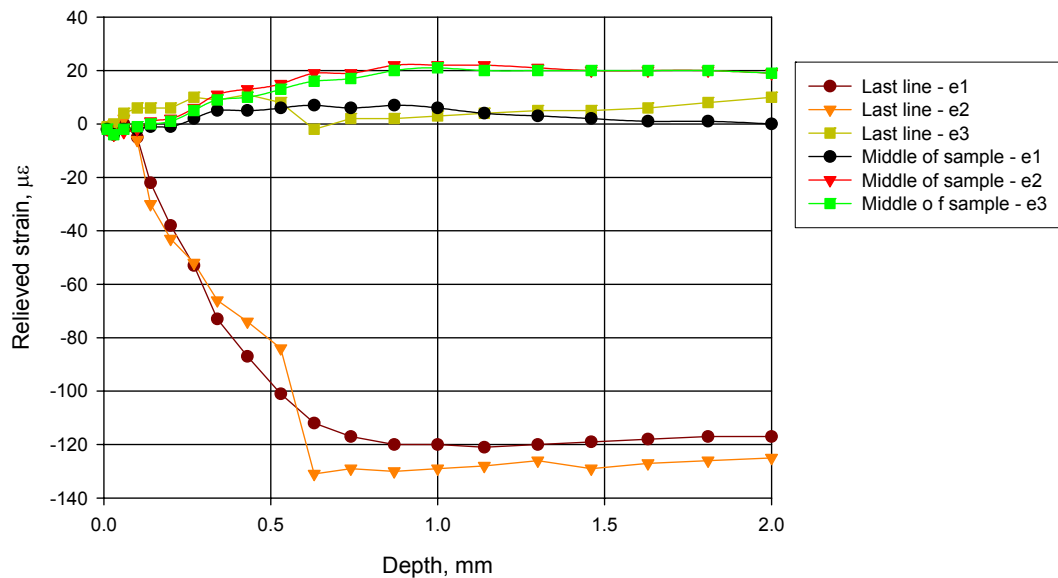
Figure 4.66: Strain relaxation curves for 'middle of sample' and 'last line' locations – (20mm)

From the above figures it is clear that there is no correlation between the measurements taken. The calculated principal stress results with their corresponding angles are given in Appendix F. A graphic illustration of the principal stresses versus hole depth is shown in Figure 4.67. Once again no correlation could be observed between the various curves.
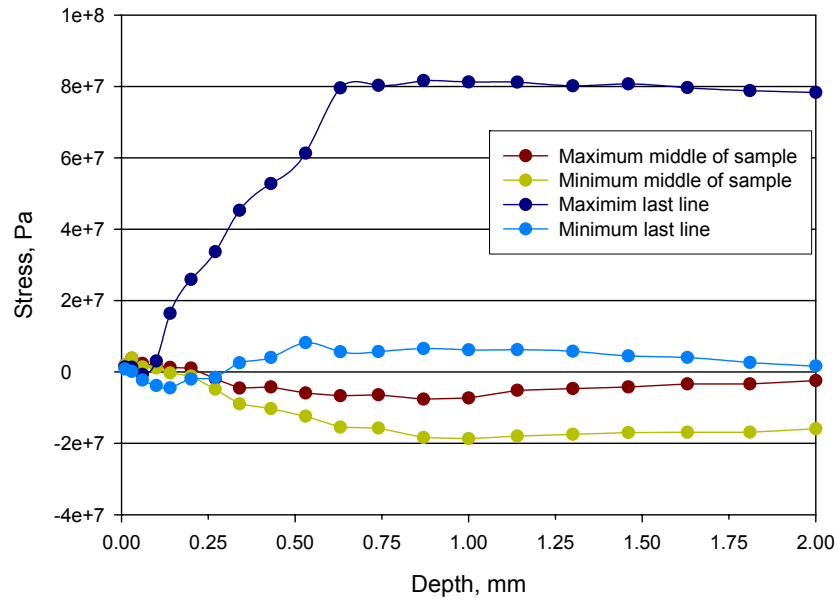
Figure 4.67: Relieved residual stress vs. hole depth – 20mm REVERSE SIDE

4.8.4 Combined curves

Due to the inconsistent nature of the results obtained, it was decided to group the relieved maximum stress versus hole depth curves according to measurement location.
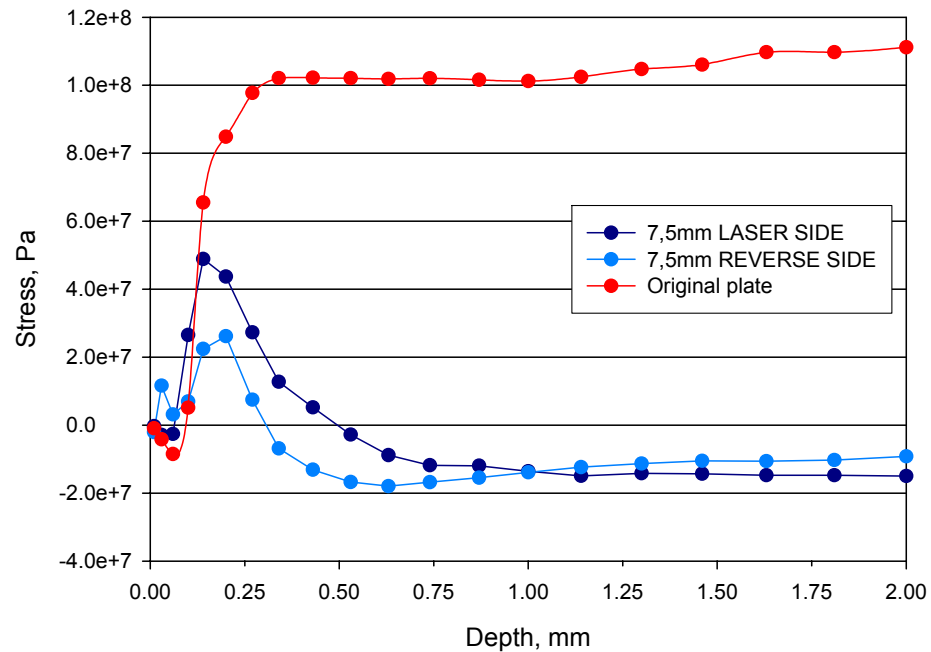
Figure 4.68: Plot of relieved residual stress versus hole depth – 'between the lines' location

Only the maximum (most tensile) relieved stress will be plotted since it is
the tensile residual surface stresses that have the most detrimental effect
on fatigue life. Figure 4.68 shows the curves for the 'between the lines'
location, with the curve of the original plate also indicated.

From Figure 4.68 it can be observed that the two curves for the laser
formed specimens follow a similar trend. The relieved stresses in the
deeper layers are compressive whereas for the original plate, the
relieved stresses are tensile. The original plate and laser side
specimen indicates a slight compressive surface residual stress with the
reverse side specimen indicating a slight tensile residual stress. The
residual stress in the reverse side specimen is on average lower than for
the laser side specimen. This is probably because the laser side surface
is being heated and thus experiences a steeper temperature gradient
during the heating/cooling cycle. For the specimens formed by the
7,5mm beam diameter, there is only a small difference in surface
residual stress distribution. Figure 4.69 indicates curves for the 'last line'
location point. The curve of the original plate is included as a reference.
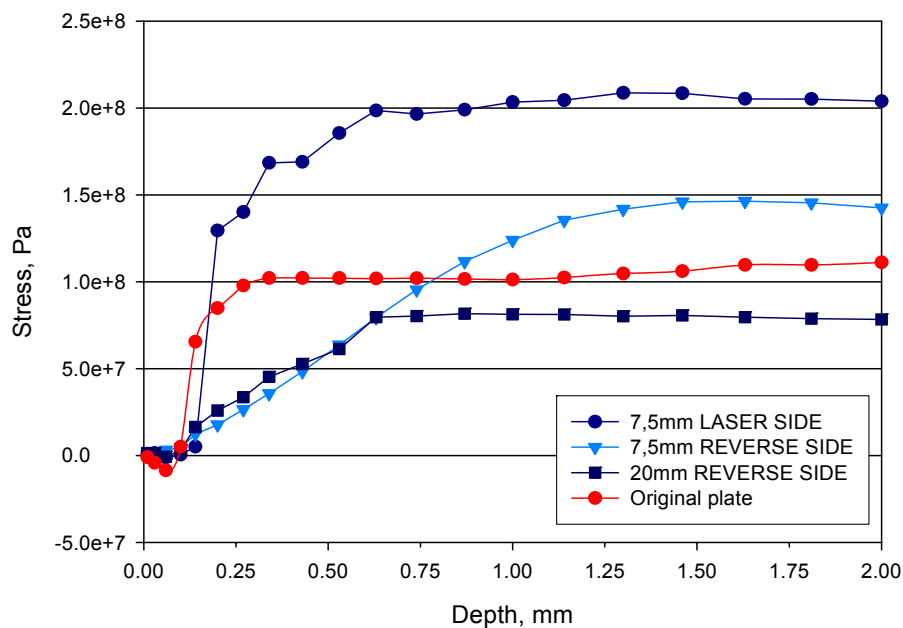
Figure 4.69: Plot of relieved residual stress versus hole depth – 'last line'
location

The most obvious difference between these and the previous results are the magnitude of relieved residual stress and its tensile nature in the deeper layers. This is not a big concern since the fatigue samples were cut from the centre section of the laser formed specimens. Note should be taken of this tendency for commercial forming processes.

Figure 4.70 shows relieved stress curves for the location 'middle' of the various samples, with the original plate's values included as a reference.
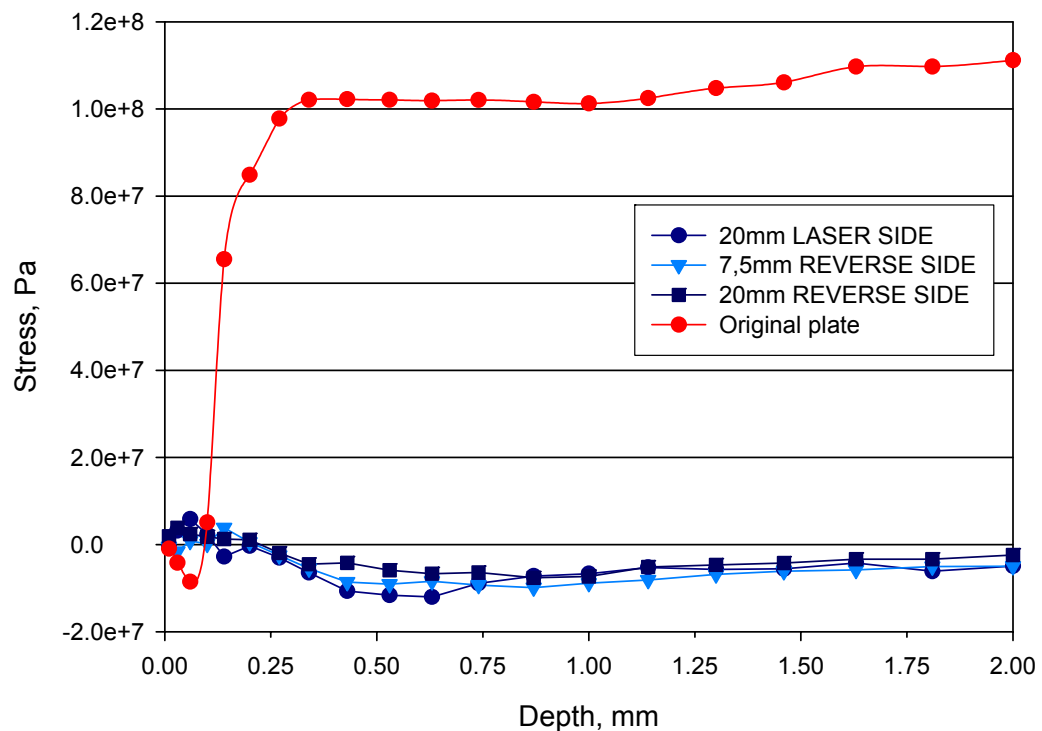
Figure 4.70: Plot of relieved residual stress versus hole depth – 'middle' of sample' location

These sets of results are the most important of all, since this location also coincides with the middle of the fatigue specimens. From Figure 4.70 it can be observed that there is a great reduction in residual stress magnitude between the original plate and the laser formed specimens. All laser formed specimens showed a slight tensile residual stress distribution at the surface layers. This slight tensile residual stress might be large enough to have an adverse effect on fatigue life.

4.8.5 Visual inspection of drilled hole

A typical cross-sectional view of the drilled hole is shown in Figure 4.71. It can be seen that the hole has a slight taper towards the bottom of the hole as well as an uneven bottom surface. The location of this specific hole was at the 'between the lines' location for the 7,5mm LASER SIDE sample. This change in shape could be due to the relieving of residual stresses, but it is unlikely, since the residual stress magnitudes observed were relatively small.
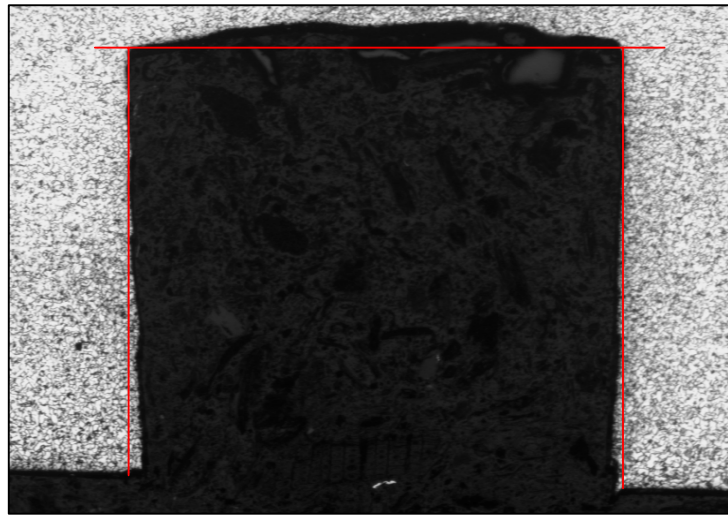
Figure 4.71: Cross-sectional view of drilled hole – 7,5mm LASER SIDE between the lines

From Section 4.5 it is clear that the microstructures in the surface region of the samples for the 7,5mm beam diameter samples are very different to that of the original plate. In the surface layers, phases like Widmanstätten ferrite with an aligned second phase (carbide), was present. This difference in microstructure could be a contributing factor for the tapered appearance of the hole observed as the surface layer consisted of harder phases than the layers towards the centre of the sample.

4.8.6 Microhardness correlation

It is well documented in literature that there is a correlation between residual stress magnitude and hardness. Figure 4.72 shows Vickers

hardness and relieved residual stress as a function of depth below the irradiated surface on the same graph.
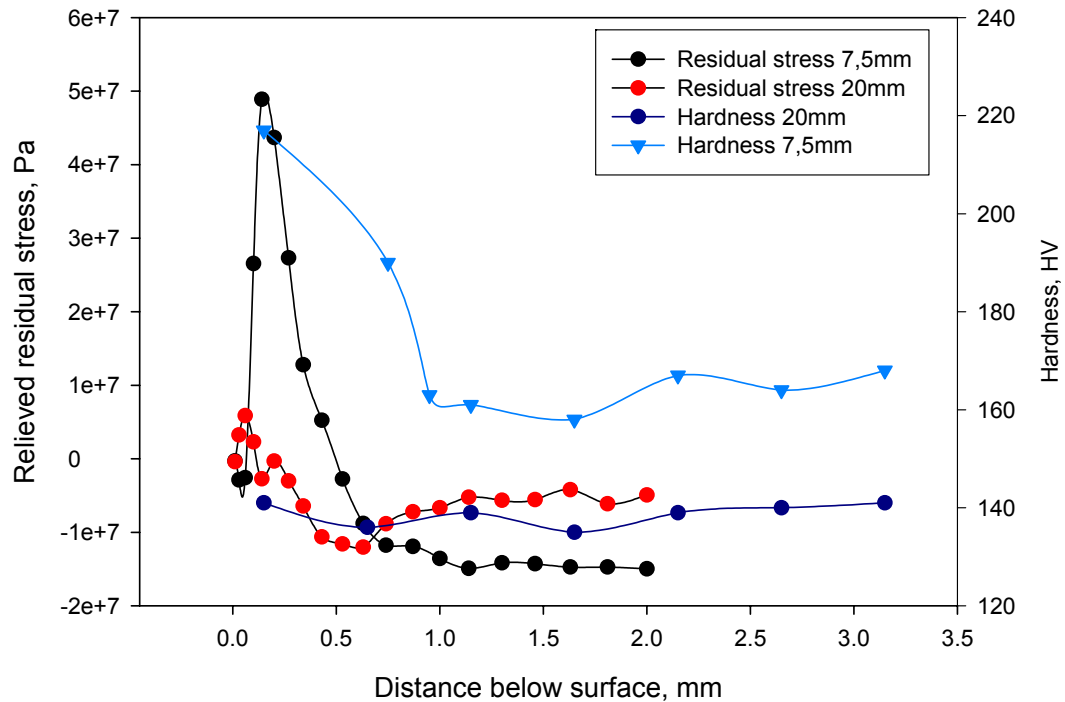
Figure 4.72: Plot of relieved residual stress and Vickers hardness as a function of depth below the laser irradiated surface

From Figure 4.72 it can be observed that the sample which showed a steep residual stress gradient also exhibited a steep hardness gradient in the surface layers. The residual stress magnitude is also much higher than for the sample irradiated with the 20mm beam diameter. For the 20mm beam diameter sample the residual stress profile is less dramatic which corresponds well with its hardness plot.

Microhardness comparison along the length of the sample was also conducted. Figure 4.73 indicate the positions where residual stress measurements were taken. From the result obtained in Figure 4.73, it can be predicted that there should be a greater difference in relieved residual stress results for areas between the irradiated lines for the 7,5mm beam diameter samples than the areas on the heated line.
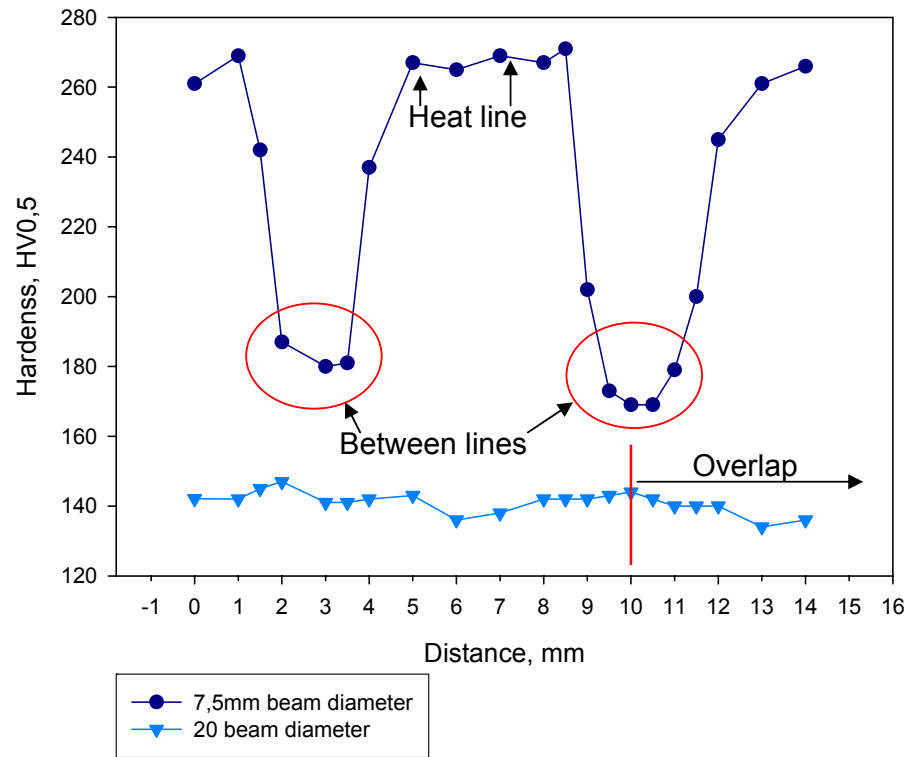
Figure 4.73: Microhardness evaluation along the length of the samples

One has to remember that there are not really any non-irradiated areas between the heated lines for the 7,5mm beam diameter samples, there is just no overlap. The hardness profile evident is because of the donut shaped laser beam used for irradiation. The beam intensity is higher towards the centre than at the edges.

According to literature, the elastic limit of a material can be determined by a simple hardness test using a pyramidal indenter as in the Vickers hardness test[41]. Using Vickers and Meyer hardness, an empirical equation was found that allowed for the calculation of the yield strength.

$$\sigma_{0,2} = \frac{HV}{3}(0,1)^{m-2} \tag{4.9}$$

Where: HV = Vickers hardness and m is the Meyer exponent.

Due to the fact that there is a correlation between hardness and strength, the change in yield strength ($\Delta\sigma_y$), relative to the original yield strength of the material (σ_{yo}), can easily be estimated based on the change in hardness (ΔHV), relative to the hardness of the original material (HV_o)[41].

$$\frac{\Delta\sigma_y}{\sigma_{yo}} = \frac{\Delta HV}{HV_o}$$
(4.10)

This information is of great importance, since residual stress values bigger than 60 percent of the material's yield strength is considered to contain errors[41]. According to literature this value can be as low as 50 percent of yield strength and as high as 80 percent of yield strength. Therefore to estimate the yield strength of the surface layer of the specimens, one can apply equation 4.10 to the specimens' hardness results.

Table 4.9 shows the hardness and yield strength results estimated for the various samples analysed.

Table 4.9: Hardness and estimated yield strength results

	Original	7,5mm beam diameter		20mm beam diameter
		On line	Between lines	
HV$_o$	157	266	175	141
ΔHV	-	109	18	-16
σ$_{yo}$	341,25 MPa	-	-	-
Δσ$_y$	-	236,92 MPa	39,12 MPa	-34,77 MPa
Estimated σ$_y$	-	578,17 MPa	380,37 MPa	306,48 MPa
60% of σ$_{y(est)}$	204,75 MPa	346,90 MPa	228,22 MPa	183,89 MPa

From the results in Table 4.9 it is clear that there is also a hardness / yield strength gradient through the thickness of the specimens. Surface layers have much higher yield strengths than the centre of the specimens. The 20mm beam diameter samples show a decrease in yield strength which should be significant when considering fatigue loading conditions. The row indicating 60 percent of yield shows the maximum magnitude of allowable residual stress measurements with only a small percentage of error present.

4.9   FATIGUE TESTING

The following results were obtained by means of the bend fatigue test (as close as possible to the condition where R=-1 i.e. zero mean stress conditions and A=∞).

4.9.1 Original flat plate specimens

Fatigue specimens were machined from the original blanks as indicated in Figure 4.74. The rolling direction of the plate is indicated by an arrow.

Figure 4.74: Blank of dual phase steel indicating rolling direction

The fatigue samples were tested at a minimum of three different loads in order to obtain an equation for the straight line portion of the fatigue curve. The results obtained by testing the original flat specimens are shown in Table 4.10 and Figure 4.75(a) and (b).

Table 4.10: Fatigue data of original flat plate specimens

Alternating stress (MPa)	Number of cycles to failure (Nf)	Standard deviation	Average number of cycles to failure
356,992	194 740 340 510 193 620 242 957 196 880	63 194	233 741 *Range: 146 890
317,061	381 430 482 950 325 120 396 500 379 140	57 090	393 028 Range: 157 830
287,362	910 820 799 560 556 300 941 670 930 550	161 961	827 780 *Range: 385 370

* Range = Nf_{max} - Nf_{min}
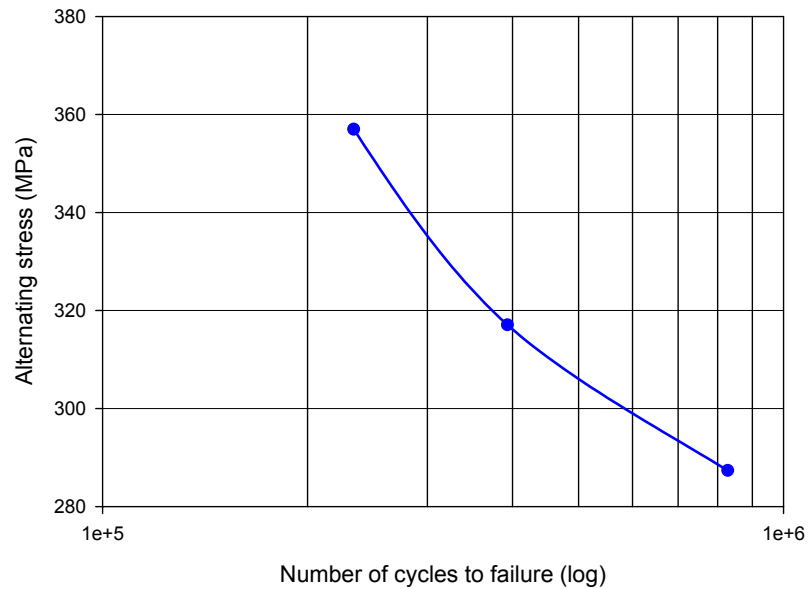
Figure 4.75: (a) S-N curve plotted with average results - original

Run-out was taken to be 2×10^6 cycles, as it was shown by previous research that laboratory specimens showed a direct relationship to fatigue values obtained by testing a complete wheel rim.

$$y = -47{,}844 \ln x + 939{,}54$$
$$R^2 = 0{,}8611$$
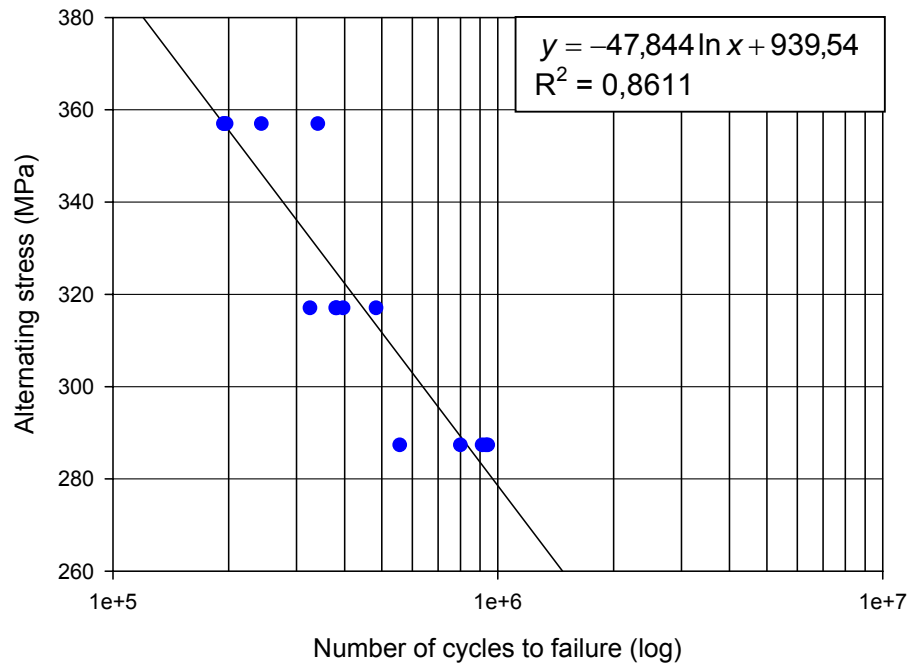
Figure 4.75: (b) S-N curve plotted with actual results showing linear
regression line and equation - original

The plate specimens were tested at loads below the yield strength of the material as it is unlikely that design specifications would recommend use within the plastic range. The yield strength of the material (0,2% proof stress) was determined by tensile testing and found to be 341,25MPa. Table 4.11 shows the alternating stress magnitude as a percentage in relation to the yield strength of the material.

Table 4.11: Alternating stress magnitude as a percentage of
yield strength - original

Load	Alternating stress (MPa)	% of Yield strength
1	356,992	104,6
2	317,061	92,9
3	287,362	84,2

From Table 4.11 it can be observed that even at loading conditions above the original yield strength of the material, the number of cycles to

failure was still above 200 000 (for this specific set of samples). The range of results obtained at the various loads indicates that at lower loads, the range in results increases. This is due to the fact that at higher loads, i.e. shorter lives (where crack propagation dominates), surface defects / surface finish has a lesser effect on the fatigue life [39]. At lower loads, the surface defects are more critical and affect fracture more dramatically than at higher loads. This trend can be observed on some of the other samples tested and will be shown in the sections to follow.

4.9.2 Pure bend specimens (PB)

Pure bend specimens were produced by bending flat plate by means of rollers. The apparatus used to produce the specimens is shown schematically in Figure 4.76. The rollers were set to produce a radius of curvature of approximately 130mm (similar to the laser formed specimens).

Figure 4.76: Schematic illustration of apparatus used to produce PB specimens

The term "pure bend" is used to describe these specimens to distinguish them from specimens deformed by means of stretch forming, where both ends of the specimen are clamped (fixed) and the specimen is then deformed by a stretch forming operation. The average radius of curvature of the pure bend specimens (after the rolling operation) was

determined to be approximately 110mm. The radius of curvature was measured after the specimen was deformed and removed from the apparatus. Appendix H shows the method used for calculation of radius of curvature. The actual fatigue results obtained by testing the pure bend specimens are shown in Table 4.12 and Figure 4.77(a) and (b).

Table 4.12: Fatigue data of pure bend specimens

Alternating stress (MPa)	Number of cycles to failure (Nf)	Standard deviation	Average number of cycles to failure
340,900	110 940 100 840 143 930 118 570 120 370	15 955	118 930 *Range: 43 090
286,468	388 790 285 460 405 733 408 230 542 950	91 633	406 233 Range: 257 490
264,118	1 087 250 1 128 480 1 094 270 1 103 333 1 010 002	44 558	1 084 667 *Range: 118 478

* Range = Nf_{max} - Nf_{min}
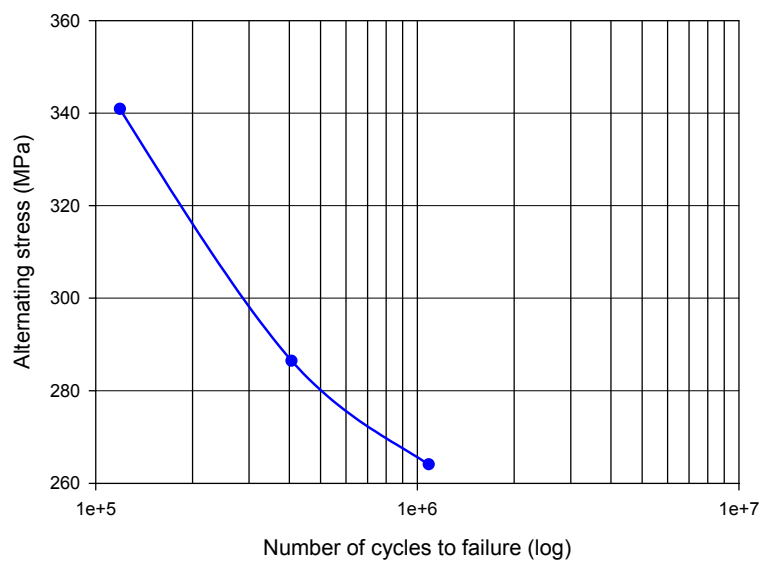
Figure 4.77: (a) S-N curve plotted with average results – PB

$$y = -34,205 \ln x + 735,78$$
$$R^2 = 0,9457$$
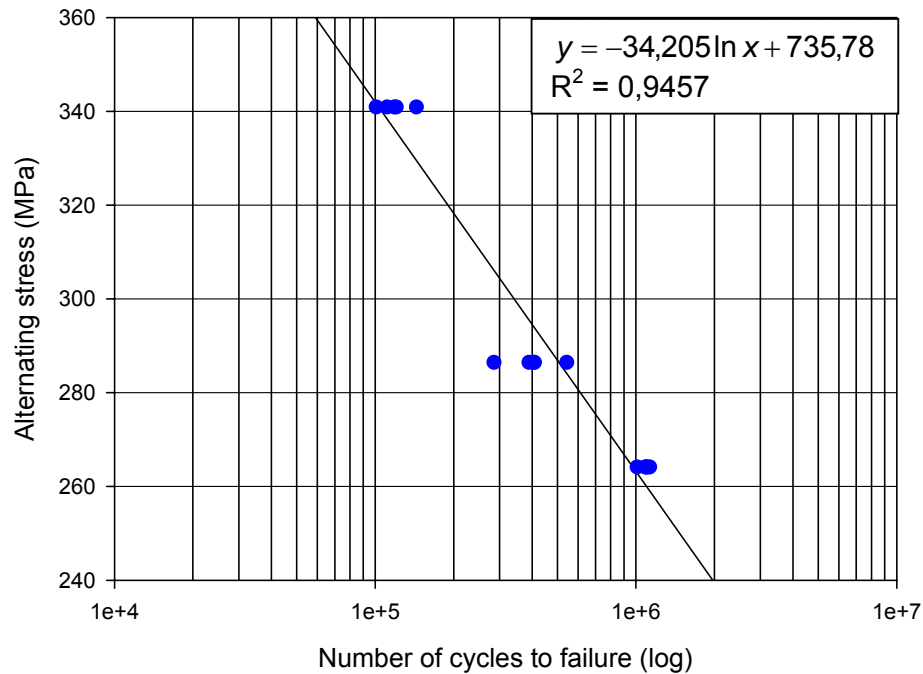
Figure 4.77: (b) S-N curve plotted with actual results showing linear regression
line and equation – PB

The loads given as a percentage of the material's yield strength (0,2%
proof stress) is listed in Table 4.13.

Table 4.13: Alternating stress magnitude as a percentage of yield strength
– PB

Load	Alternating stress (MPa)	% of Yield strength
1	340,900	99,9
2	286,468	84,0
3	264,118	77,4

Compared to the original flat plate specimens, the pure bend specimens
shows inferior fatigue strength. The specimen's shape changed and
hence its fatigue performance. This drop in fatigue strength could not be
attributed to microstructural changes since the pure bend did not induce
any microvoids or phase changes as the operation took place at room
temperature. At higher loads, e.g. 330 MPa a 58% reduction in number
of cycles can be predicted (calculated) when comparing Figure 4.74(b)
and Figure 4.77(b). At lower loads, e.g. 290MPa, a reduction of 42% can
be predicted.

4.9.3 Laser formed (LF) specimens – 7,5mm beam diameter

Specimens were deformed using the following laser parameters: 1,5kW, 7,5mm beam diameter, 1,2m/min scanning velocity and 7,5mm interval spacing between consecutive laser lines, i.e. 0% overlap. The average radius of curvature for these specimens was found to be approximately 137mm. Table 4.14 and Figure 4.78(a) and (b) shows the actual fatigue data obtained by fatigue testing the laser formed specimens.

Table 4.14: Fatigue data of laser formed specimens – 7,5mm beam diameter

Alternating stress (MPa)	Number of cycles to failure (Nf)	Standard deviation	Average number of cycles to failure
341,700	123 560 117 733 124 770 110 670 117 760	5 625	118 899 *Range: 14 100
285,574	330 590 609 200 333 610 407 430 573 730	132 540	450 912 Range: 278 610
265,310	750 640 1 484 510 852 830 993 670 747 620	306 796	965 854 *Range: 736 890

* Range = Nf_{max} - Nf_{min}

Table 4.15 shows the loads as a percentage of the material's yield strength (0,2% proof stress).

Table 4.15: Alternating stress magnitude as a percentage of yield strength – LF (7,5)

Load	Alternating stress (MPa)	% of Yield strength
1	341,700	100,1
2	285,574	83,7
3	265,310	77,8
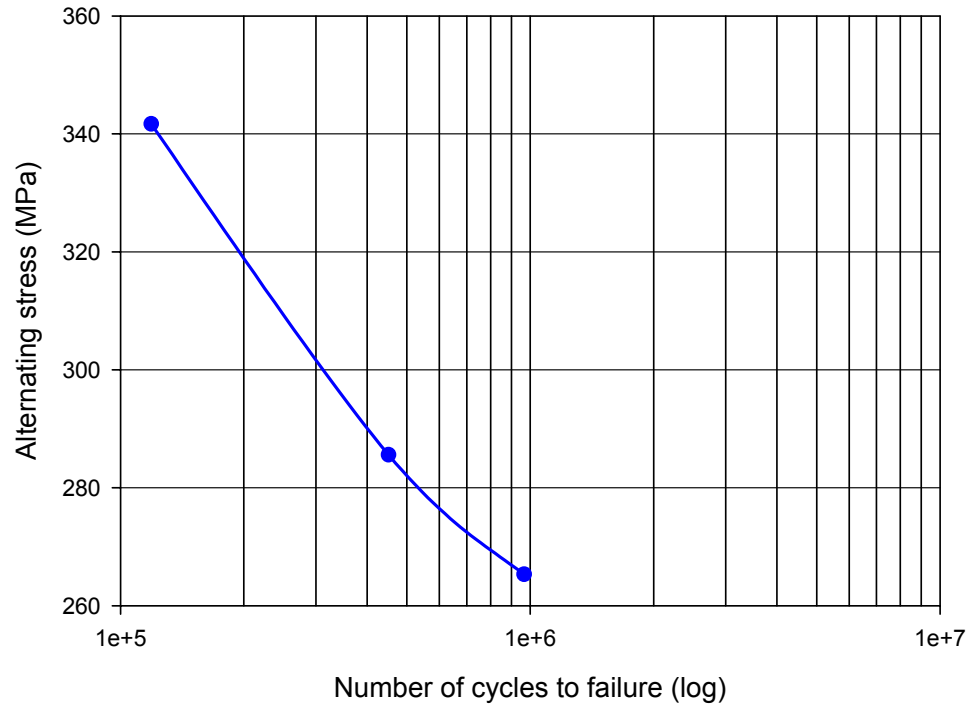
Figure 4.78: (a) S-N curve plotted with average results – LF (7,5)
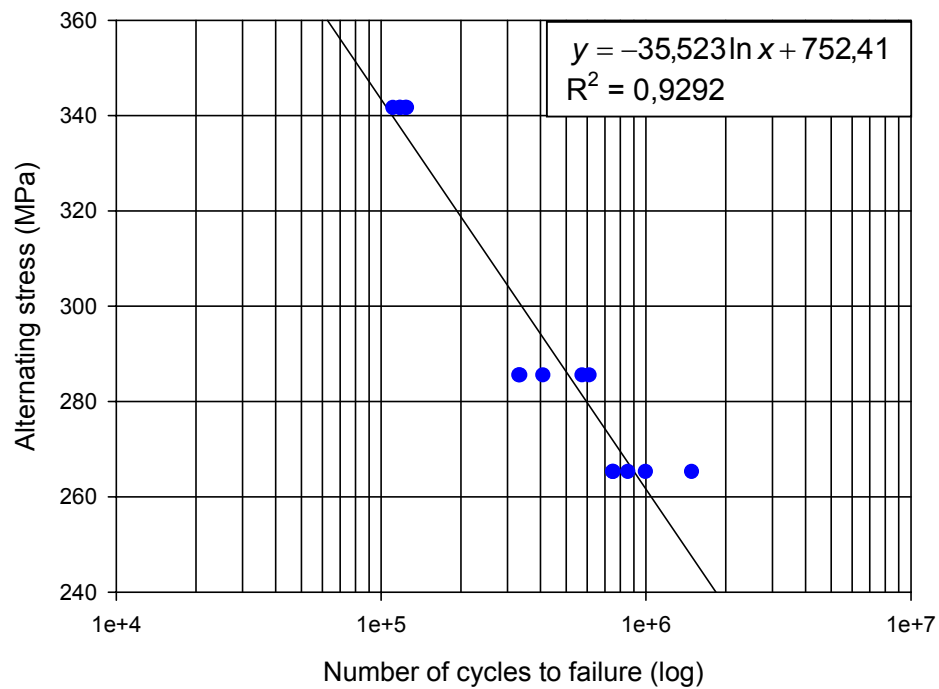
Figure 4.78: (b) S-N curve plotted with actual results showing linear
regression line and equation – LF (7,5)

From the equation obtained from Figure 4.78(b), it is clear that the laser formed specimens produced with this set of parameters, behaves similarly to the pure bend specimens when fatigue tested. It can thus be concluded that the laser forming operation did not greatly affect the material's fatigue strength compared to free bend specimens. It should be noted that no microvoids were formed during the deformation process of the pure bend specimens. A stretch forming operation on the other hand will lead to microvoid formation and thus a decrease in fatigue strength of the material.

4.9.4   Laser formed (LF) specimens – 20 mm beam diameter

The following laser parameters were used to produce the fatigue specimens: 5kW, 20mm beam diameter, 2,5m/min scanning velocity and a 10mm interval spacing between consecutive laser lines, i.e. 50% overlap. Results from the fatigue tests are shown in Table 4.16 and Figure 4.79(a) and (b).

Table 4.16: Fatigue data of laser formed specimens – 20mm beam diameter

Alternating stress (MPa)	Number of cycles to failure (Nf)	Standard deviation	Average number of cycles to failure
319,147	80 230 86 260 88 920 107 340 101 220	11 160	92 794 *Range: 27 110
285,574	92 970 164 500 119 560 132 760 171 320	32 372	136 222 Range: 78 350
265,310	403 368 353 570 519 580 518 520 391 580	76 843	437 324 *Range: 166 010
228,558	1 356 760 1 136 270 685 760 968 050 557 110	325 667	940 790 *Range: 799 650

* Range = Nf_{max} - Nf_{min}

The average radius of curvature was found to be approximately 122mm.
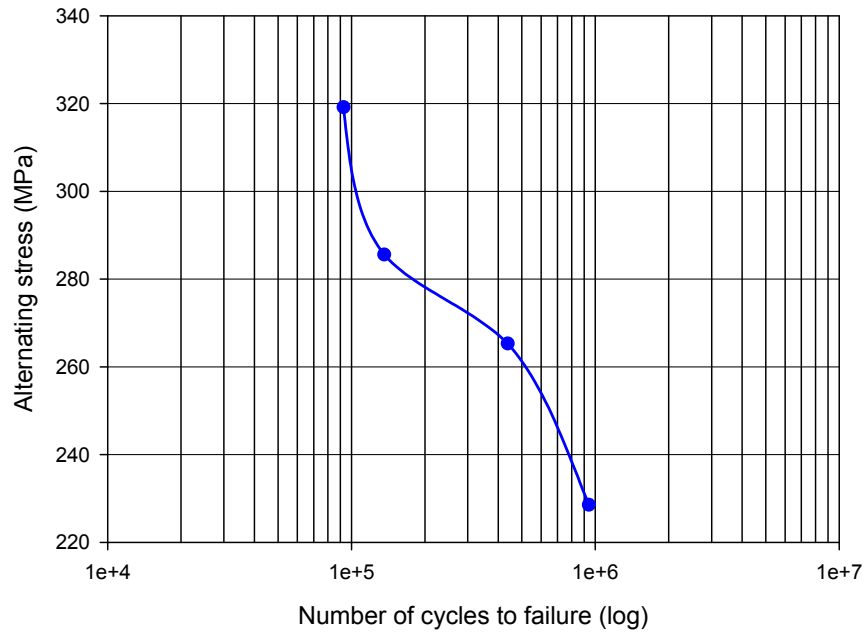
Figure 4.79: (a) S-N curve plotted with average results – LF (20)

$$y = -39{,}21 \ln x + 685{,}27$$
$$R^2 = 0{,}8785$$
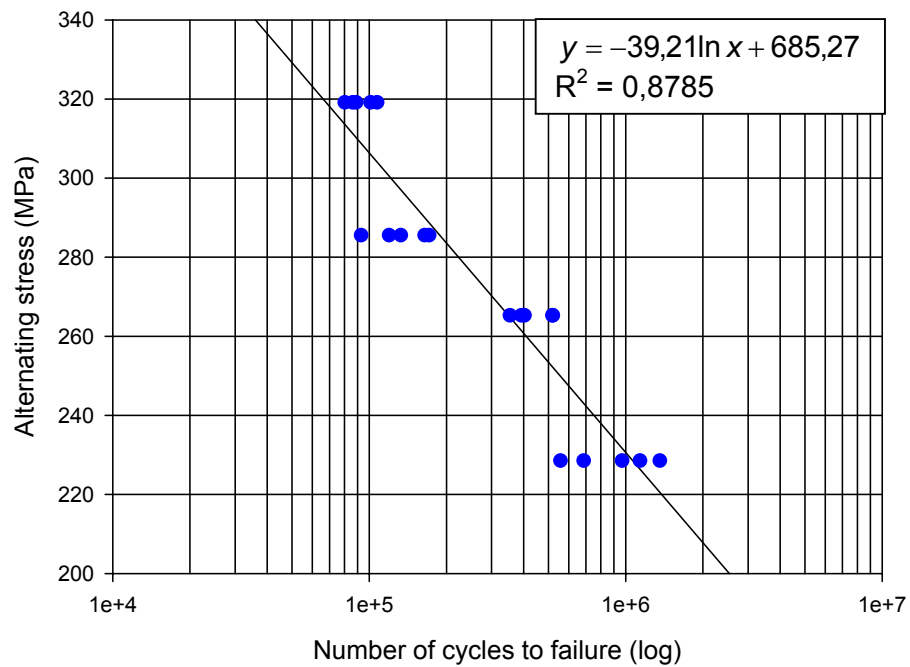
Figure 4.79: (b) S-N curve plotted with actual results showing linear regression line and equation – LF (20)

Table 4.17 shows the loads as a percentage of the material's yield strength (0,2% proof stress).

Table 4.17: Alternating stress magnitude as a percentage of
yield strength – LF (20)

Load	Alternating stress (MPa)	% of Yield strength
1	319,147	93,5
2	285,574	83,7
3	265,310	77,8
4	228,558	67,0

From Figure 4.79 (a) it should be noted that the S-N curve shows a peculiar shape. This is not desired when considering fatigue strength as there is a steep decline between the first two and last two loads. When considering the first two loads, a decrease of 10,5% in alternating stress magnitude leads to an increase in the number of cycles to failure of only 31,9%. Whereas between the second and third loads, the decrease in alternating stress magnitude is 7,1% with an increase in the number of cycles to failure by 68,9%. Similarly between the last two loads there was a decrease in alternating stress magnitude of 13,9% and an increase in the number of cycles to failure of 53,5%.

A steep slope of the S-N curve signifies that with only a small change in applied alternating stress, there will be a large difference in the number of cycles to failure. This is unwanted since close tolerances will have to be specified to ensure adequate fatigue properties. It is well documented that mean stress magnitude influences the slope of the S-N curve, therefore it can be said that since the amplitude ratio (A) equals $\frac{S_a}{\sigma_m}$, the amplitude ratio can also be an indication of the fatigue curve slope. Hence, curves with similar amplitude ratios should exhibit similar S-N curve slopes. By calculating the amplitude ratios for the various load conditions, one can attempt to explain the appearance of the fatigue

curve obtained. The test loads with their corresponding amplitude ratio (A) are given in Table 4.18. The specimens produced with this set of laser parameters exhibited the lowest fatigue strength of all the samples tested.

Table 4.18: Amplitude ratios for various test loads – 20mm beam diameter

	Alternating stress, S_a (MPa)	Effective mean stress, σ_m (MPa) - surface	Amplitude ratio, A
Load 1	319,15	1,003	318,20
Load 2	285,57	2,988	95,57
Load 3	265,31	1,198	221,46
Load 4	228,56	3,583	63,79

From Table 4.18 it can be seen that the amplitude ratios of load 1 and load 3 are of a much higher magnitude than load 2 and load 4. This trend was also evident from the fatigue curve when the average results were plotted. It therefore seems that two population sets are evident on the fatigue curve of the samples formed by the 20mm beam diameter, as displayed in Figure 4.80.
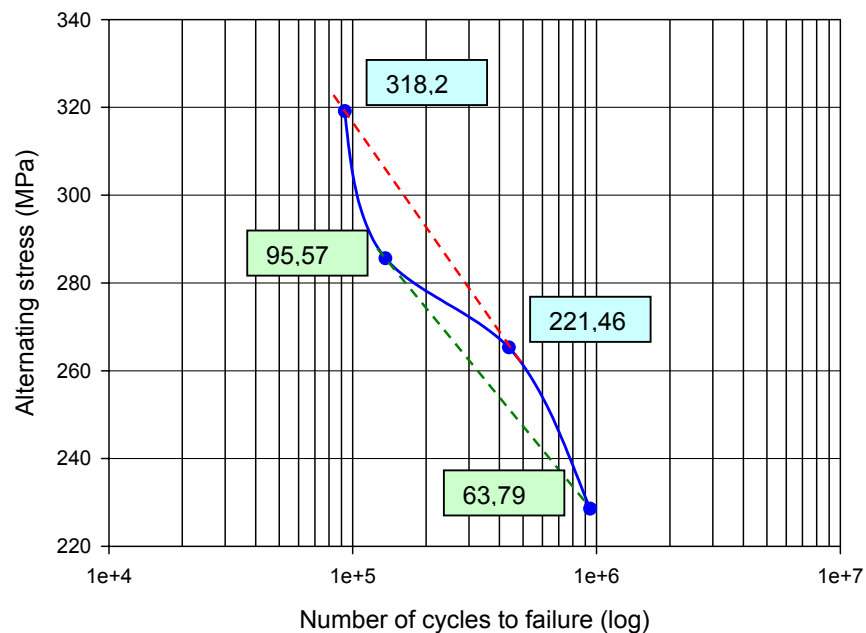
Figure 4.80: S-N curve showing two population sets – 20mm beam diameter

The previous section could be a possible explanation for the odd shape of the S-N curve of the samples formed with the 20mm beam diameter. The rest of the samples tested showed amplitude ratios of approximately similar magnitudes and therefore did not exhibit an odd shaped S-N curve. The amplitude ratios of the other samples as well as the stress ratios will be discussed in the following section.

4.9.5 Combined S-N curves

In order to obtain a better understanding of the fatigue performance of the various sets of fatigue samples tested, a single graph with the various S-N curves were generated. Figure 4.81 shows a plot of all samples tested with the average number of cycles to failure plotted against alternating stress. Actual results from previous research on the fatigue life of wheel centre disc specimens are also included on Figure 4.81.
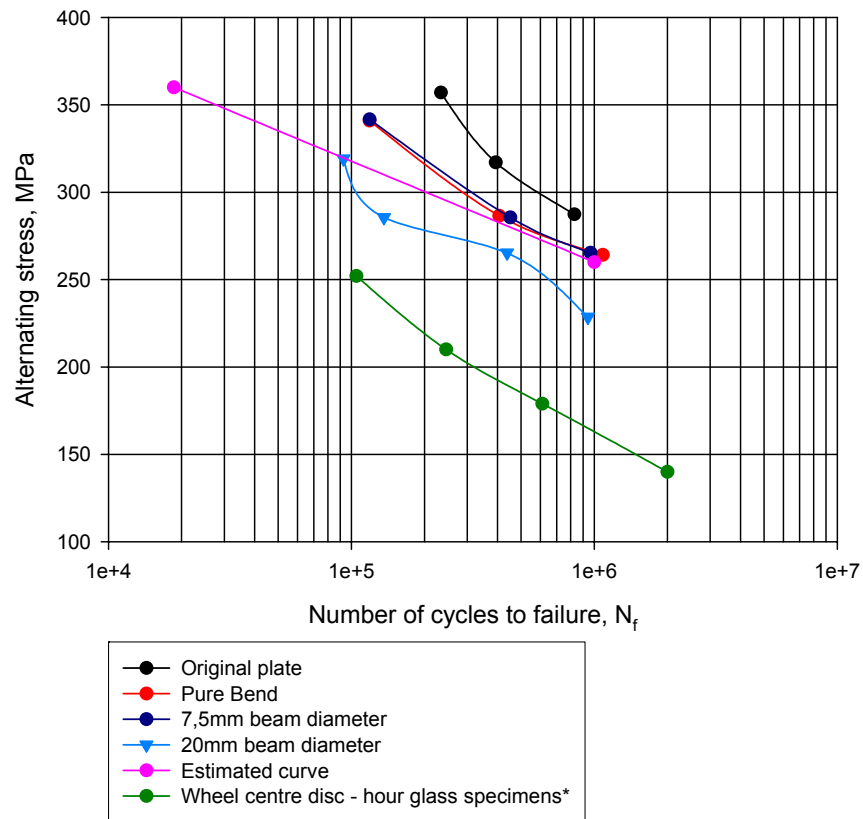
Figure 4.81: S-N curves plotted with average results of all fatigue samples tested (* Results obtained from previous research[36])

The general trends of the curves seem to be similar, except for the laser formed (LF) specimens with a 5kW laser power and 20mm beam diameter. The original flat plate material still exhibited the best properties. The pure bend specimens and the laser formed (LF) specimens formed with a 1,5kW and 7,5mm beam diameter showed very similar results. Figure 4.82 shows S-N curves with all actual results plotted and also show linear regression lines.
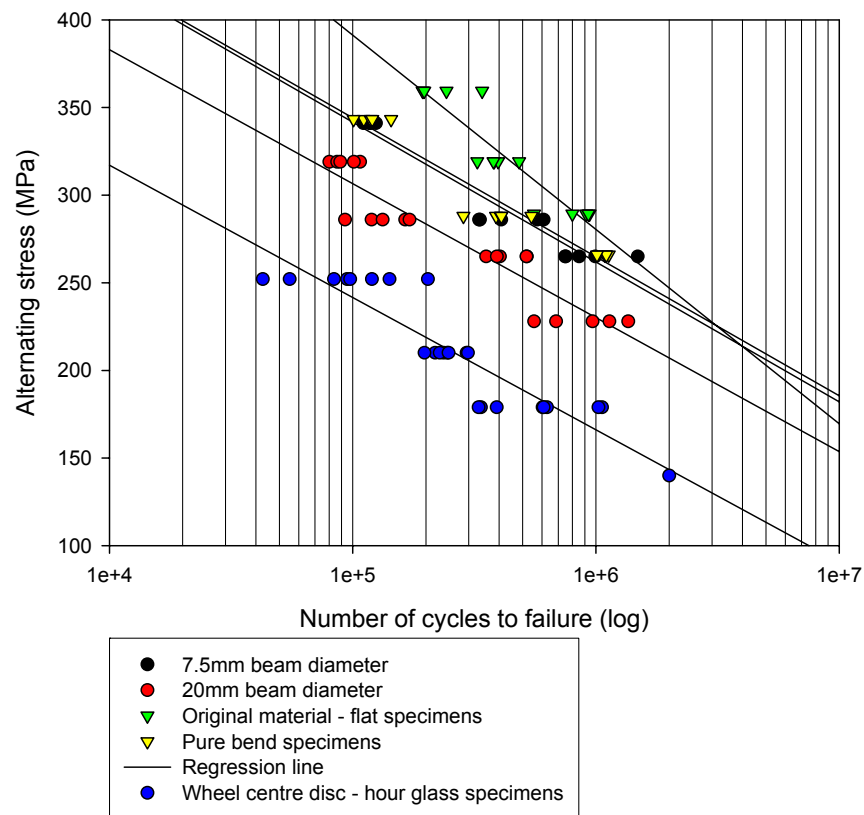
Figure 4.82: S-N curves plotted with actual results showing linear regression lines

Although the pure bend and 7,5mm beam diameter laser formed specimens show worse results than the original material, the results are still better than the estimated curve as predicted using the Juvinall and Marshek method. This indicates that the estimated curve predicts shorter lives than actually obtained. It is thus safe to assume that the

estimated curve can be used to give an approximation of fatigue life when no actual fatigue data are available. The estimated curve should not be used for predictions for the 20mm beam diameter laser formed specimens, as the material will fail sooner than predicted. All the samples tested still showed better fatigue strength than the hour glass samples machined from the finished product (wheel rim). The results obtained for the hour glass specimens of the wheel centre disc was obtained from previous research[42].

From Figure 4.82 it can be observed that the formed specimens all have approximately the same slope (parallel lines), except for the original flat plate specimens. This is also verified by the equations obtained by linear regression for the various curves. The various equations obtained by linear regression are shown below:

- Original flat plate: $S_a = -47,844 \, ln \, N_f + 939,54$ (4.11)
- Pure bend: $S_a = -34,205 \, ln \, N_f + 735,78$ (4.12)
- LF (7,5mm beam Ø) $S_a = -35,523 \, ln \, N_f + 752,41$ (4.13)
- LF (20mm beam Ø) $S_a = -39,21 \, ln \, N_f + 685,27$ (4.14)
- Estimated curve $S_a = -25,094 \, ln \, N_f + 606,68$ (4.15)
- Centre disc specimens $S_a = -32,784 \, ln \, N_f + 619,05$ (4.16)

Where: S_a = Alternating stress (MPa)

N_f = Number of cycles to failure

From Figure 4.82 it is also clear that the range of results for the pure bend and laser formed specimens is not as large as those results obtained for the hour glass specimens from the wheel centre disc. The last point on the graph for the wheel centre disc indicates run out at $2x10^6$ cycles. Actual tests at a load of 140MPa showed lives in excess of $2x10^6$ cycles.

4.10   FATIGUE, RESIDUAL STRESS AND MICROSTRUCTURE

Residual stress measurements were taken from the calculated maximum principal (most tensile) stress results as indicated in Appendix F. Readings were taken as shown on the illustration in Figure 4.83.
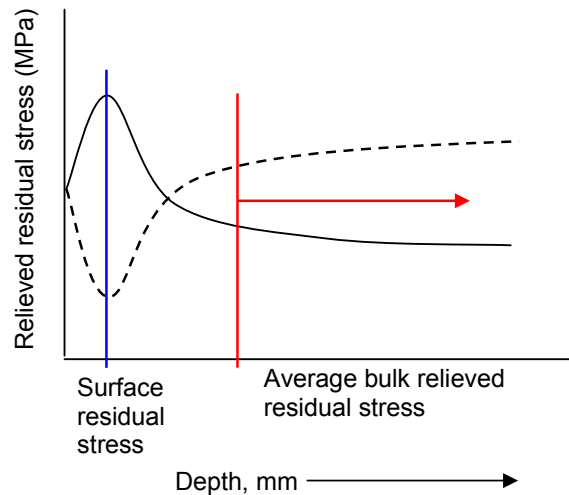
Figure 4.83: Schematic diagram illustrating measurement values of residual stress

The actual calculated results for the various specimens analysed are given in Table 4.19.

Table 4.19: Relieved residual stress results (most tensile)

Specimen	Surface residual stress	Bulk average residual stress
Original plate	-8,518MPa (2,5%)*	104,583MPa (30,6%)*
7,5mm beam ∅ LASER SIDE	48,884MPa (14,3%)*	-14MPa (4,1%)*
7,5mm beam ∅ REVERSE SIDE	0,8MPa (0,2%)*	-7,205MPa (2,11%)*
20mm beam ∅ LASER SIDE	5,868MPa (1,7%)*	-5,701MPa (1,7%)*
20mm beam ∅ REVERSE SIDE	2,427MPa (0,7%)*	-4,754MPa (1,4%)*

* Indicates result as a percentage of the material's original yield strength

Of the laser formed specimens, only the 'middle of sample' location's readings will be used since this location also coincides with the centre of the fatigue sample.

From Table 4.19 it is clear that all the results obtained are below the 60 percent threshold value as discussed in section 4.8.6, it is only the original plate that shows a slight compressive stress in the surface layer with a relatively large tensile bulk relieved residual stress. The laser formed specimens show relieved residual stresses of relatively small magnitude. The largest value was obtained on the laser irradiated side of the 7,5mm beam diameter samples. This value of 48,884MPa is only 14,3% of the original material's yield strength. Because the surface layer has a higher hardness than the bulk material (266HV vs 160HV), it indicates that the surface layer should have a higher yield strength as well. The surface layers for the 7,5mm beam diameter specimens have estimated yield strength of 578,17MPa according to Table 6.18. When taking this 'new' yield strength into account, the relieved residual stress value only constitutes 8,5% of the estimated yield strength. When considering all these factors, one has to evaluate whether the small magnitude of relieved residual stress obtained for the laser formed specimens actually influence fatigue life. The original plate still outperformed the laser specimens during fatigue testing. The bulk relieved residual stress of the original plate indicates a value of 104,853MPa (30,6% of yield stress) tensile and a surface residual stress of 8,518MPa compressive.

The 7,5mm beam diameter laser formed specimens showed better fatigue life than the 20mm beam diameter specimens. Even though the 7,5mm beam diameter specimens show a higher tensile surface residual stress value as well as a higher bulk relieved residual stress value. These results would suggest that the change in microstructure is far more detrimental than the residual stresses observed in the laser formed specimens.

Figure 4.84 shows a three dimensional graphic representation of relieved surface residual stress vs. fatigue life vs. hardness (Vickers). The xyz coordinates are shown by coloured lines.
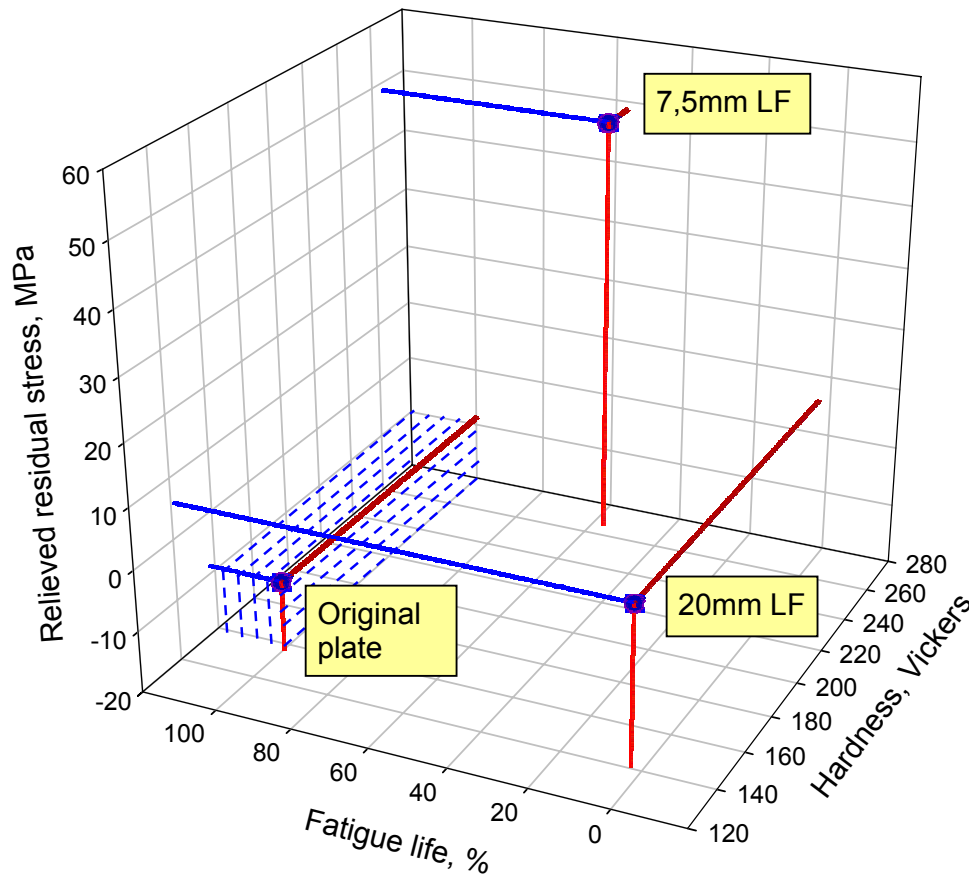
Figure 4.84: Three dimensional plot of relieved residual stress (surface) vs. fatigue life vs. hardness (HV)

When considering Figure 4.84 it is evident that the original plate (best fatigue performance) values result in the smallest volume (rectangular box – blue dashed lines) under the lines indicating the xyz coordinates. Whereas the 20mm beam diameter samples (worst fatigue performance) show the largest volume under the plot/lines. It is thus concluded that in this case the volume underneath the relieved residual stress (surface) vs. fatigue life vs. hardness (HV) coordination lines is an indication of the fatigue performance of the various specimens tested.

Table 4.20 is a summarizing table indicating forming parameters, fatigue life, residual stress, surface hardness and surface microstructure of the samples evaluated.

Table 4.20: Summary of results and parameters

	Line energy	Volumetric energy	% Overlap	Max Temp	Forming equation	Fatigue equation	Fatigue life*	Surface Res σ	Bulk Res σ	Surface hardness	Microstructure
Original plate	-	-	-	-	-	$S_a = -48\ln N_f + 940$	100%	-8,5MPa	104,6MPa	157HV (σ_y = 341MPa)	Ferrite & martensite, small grains
7,5mm beam ∅ 1,5kW	1250J/m	28,29MJ/m^3	0%	1377,7°C	$y = 35{,}9e^{0.0081x}$	$S_a = -36\ln N_f + 752$	57%	48,9MPa	-14MPa	266HV (σ_{yest}= 578MPa)	Widmanstätten ferrite & aligned second phase
20mm beam ∅ 5kW	2000J/m	6,37MJ/m^3	50%	1486,2°C	$y = 34{,}8e^{0.0082x}$	$S_a = -39\ln N_f + 685$	3%	5,9MPa	-5,7MPa	141HV (σ_{yest}= 306MPa)	Ferrite & ferrite carbide aggregate, grain growth

* Based on an alternating stress of 290MPa, where number of cycles to failure for the original plate = 100%.

4.10.1 Fatigue life prediction models

It has been proved by previous research that the endurance limit for dual phase steel equals approximately 25% of the material's tensile strength. A modified Juvinall and Marshek method allows the plotting of an estimated S-N curve with the following points:

$S_e = 0,25S_u = 0,25(577,78) = 144,45$MPa at 2×10^6 cycles and
$S_{1000} = 0,9(S_u) = 0,9(577,78) = 520,02$MPa at 10^3 cycles.

Plotting these points on a log-normal scale resulted in the curve shown in Figure 4.85.
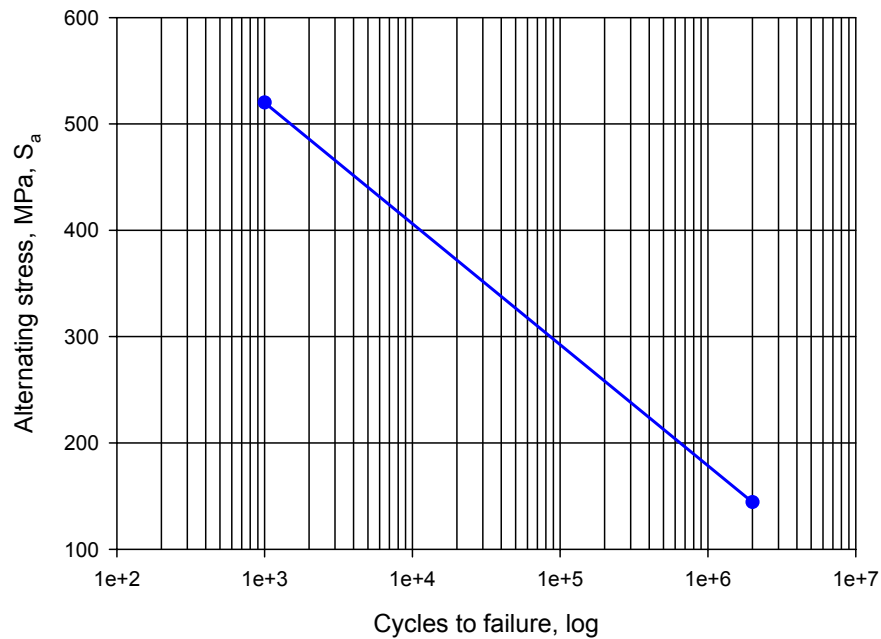
Figure 4.85: Estimated S-N curve for dual phase steel

Life prediction can now be determined by using the following relationship of the straight line portion between 10^3 and 1×10^6 cycles:

$$S_a = -49,411 \ln N_f + 861,34 \qquad\qquad (4.17)$$

4.10.2 Determination of the fully reversed alternating stress, S_n

Using the equations as defined in section 2.18 the mean stress and alternating stress for each loading condition were determined taking into account the residual stress magnitude. The effective mean residual stress magnitudes are shown in Table 4.21. Residual stress values obtained from the laser irradiated side of the specimen were used in the calculation, since most of the fractures initiated from the top surface of the specimen.

Table 4.21: Fatigue test parameters

Test load (MPa)	Stress ratio, R $R = \dfrac{\sigma_{min}}{\sigma_{max}}$	Amplitude ratio, A $A = \dfrac{S_a}{\sigma_m}$		Stress range (MPa)	Alternating stress, S_a (MPa)	Effective mean stess* (MPa)	
Original flat sheet		Surface mean stress	Bulk average mean stress			Surface	Bulk average
357,0	-1,06	-18,2	3,8	714,0	357,0	-19,64	93,46
317,06	-1,04	-21,9	3,2	634,2	317,06	-14,48	98,62
287,36	-1,03	-22,5	2,9	574,7	287,36	-12,79	100,31
7,5mm Beam diameter							
341,70	-1,03	7,8	-17,5	683,3	341,7	43,32	-19,57
285,57	-1,02	6,2	-16,9	571,1	285,57	46,00	-16,88
265,31	-1,04	6,0	-14,2	530,6	265,31	44,21	-18,67
20mm Beam diameter							
319,15	-1,03	318,2	-30,2	638,3	319,15	1,003	-10,60
285,57	-1,02	95,6	-33,3	571,1	285,57	2,988	-8,58
265,31	-1,04	221,5	-25,6	530,6	265,31	1,198	-10,37
228,56	-1,02	63,8	-28,6	457,1	228,56	3,583	-7,99

*Effective mean stress: $\sigma_{meff} = \sigma_m + \sigma_{res}$

Both the bulk average effective mean stress and surface effective mean stress was used to calculate the fully reversed alternating stress values,

S_n, and the results are shown in Table 4.22. The Gerber prediction model was used to determine the S_n values, since it was proved by previous research there is a close correlation when analysing dual phase steel for fatigue properties.

Gerber mean stress model: $\dfrac{S_a}{S_n} + \left(\dfrac{\sigma_m}{S_u}\right)^2 = 1$ (4.18)

Table 4.22: Fully reversed alternating stress values according to the Gerber model

S_a, original plate (MPa)	Effective mean stress value used (MPa)			
	Surface (S_{n1})	Difference*	Bulk ave (S_{n2})	Difference*
356,995	357,41	0,42	366,59	9,60
317,06	317,26	0,20	326,58	9,52
287,36	287,50	0,14	296,29	8,93
7,5mm Beam diameter	Surface (S_{n1})	Difference*	Bulk ave (S_{n2})	Difference*
341,7	343,63	1,93	342,09	0,39
285,57	287,39	1,82	285,81	0,24
265,31	266,87	1,56	265,59	0,28
20mm Beam diameter	Surface (S_{n1})	Difference*	Bulk ave (S_{n2})	Difference*
319,15	319,15	0	319,26	0,11
285,57	285,58	0,01	285,63	0,06
265,31	265,31	0	265,40	0,09
228,56	228,57	0,01	228,60	0,04

*Difference (MPa) = S_a - S_n

From Table 4.22 it is clear that the difference between the calculated stress values (incorporating the residual stress magnitudes) and the actual applied alternating stress magnitudes does not vary considerably. It can thus be expected that the residual stress magnitude in the case of

laser forming of dual phase steel, does not increase the alternating stress values significantly. By substituting the calculated S_n values in place of S_a in the life prediction equation of Juvinall and Marshek, one can determine if this prediction model will be adequate to apply to laser formed dual phase steel components. The results are tabulated in Table 4.23.

Table 4.23: Estimated number of cycles to failure according to the Juvinall and Marshek prediction model

Original plate	Actual Results	Calculated[1]	Calculated[2]
Load 1	S_a = 356,995MPa N_f = 233 741	S_{n1} = 357,41MPa N_{f1} = 26 869	S_{n2} =366,59MPa N_{f2} = 22 314
Load 2	S_a = 317,06MPa N_f =393 028	S_{n1} = 317,26MPa N_{f1} = 60 555	S_{n2} = 326,58 N_{f2} = 50 146
Load 3	S_a = 287,36MPa N_f =827 780	S_{n1} = 287,50 N_{f1} = 110 593	S_{n2} = 296,29 N_{f2} = 92 569
7,5mm Beam diameter	Actual Results	Calculated[1]	Calculated[2]
Load 1	S_a = 341,7 MPa N_f = 118 899	S_{n1} = 343,63MPa N_{f1} = 35 512	S_{n2} = 342,09MPa N_{f2} = 36 636
Load 2	S_a = 285,57MPa N_f = 450 912	S_{n1} = 287,39MPa N_{f1} = 110 839	S_{n2} = 285,81MPa N_{f2} = 114 441
Load 3	S_a = 265,31MPa N_f = 965 854	S_{n1} = 266,87 N_{f1} = 167 900	S_{n2} = 265,59MPa N_{f2} = 172 307
20mm Beam diameter	Actual Results	Calculated[1]	Calculated[2]
Load 1	S_a = 319,15MPa N_f = 92 794	S_{n1} = 319,15MPa N_{f1} = 58 283	S_{n2} = 319,26MPa N_{f2} = 58 153
Load 2	S_a = 285,57MPa N_f =136 222	S_{n1} = 285,58MPa N_{f1} = 114 975	S_{n2} = 285,63MPa N_{f2} = 114 858
Load 3	S_a = 265,31MPa N_f = 437 324	S_{n1} = 265,3MPa N_{f1} = 173 321	S_{n2} = 265,40MPa N_{f2} = 172 971
Load 4	S_a = 228,56MPa N_f = 940 790	S_{n1} = 228,57MPa N_{f1} = 364 491	S_{n2} = 228,60MPa N_{f2} = 264 270

Calculated[1] = using S_{n1} values; Calculated[2] = using S_{n2} values

From the previous results it is clear that the Juvinall and Marshek prediction model together with the Gerber mean stress model does not yield results even remotely near to those obtained by actual testing. The Goodman mean stress model showed even less of a correlation. The Soderberg mean stress model is seldom used as it is considered to be very conservative. It is therefore recommended that the Juvinall and Marshek prediction model not be used when considering laser formed dual phase steel samples.

4.11   INCONSISTENCIES OBSERVED DURING LASER FORMING

During production of the fatigue specimen by laser forming, certain inconsistencies were observed. The fatigue specimens were produced by placing ten flat plate specimens next to each other followed by laser irradiation along the length of the setup. The setup is illustrated in Figure 4.86. This setup followed the same time cycle as was used to form single specimens. During the forming process it was observed that the samples bend to various radii of curvature for the same set of forming parameters.
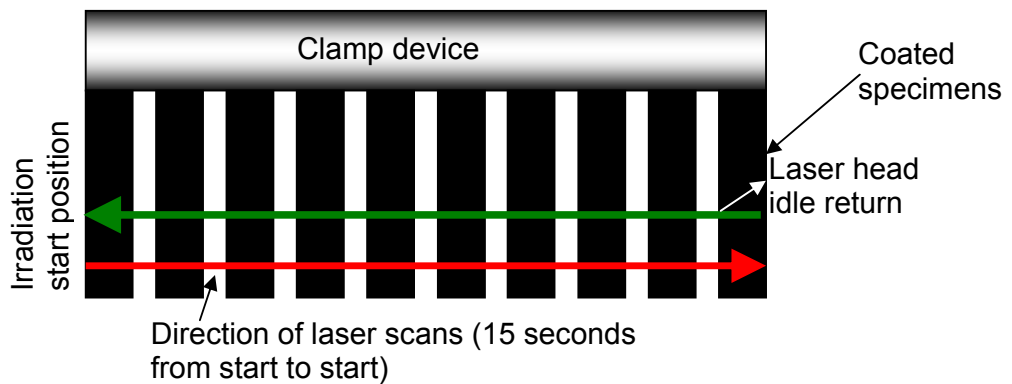
Figure 4.86: Schematic illustration of laser forming operation

The samples further from away from the starting position showed a decrease in bend radius (tighter bend). This can clearly be seen by some of the samples taken from the setup and is shown in Figure 4.87.
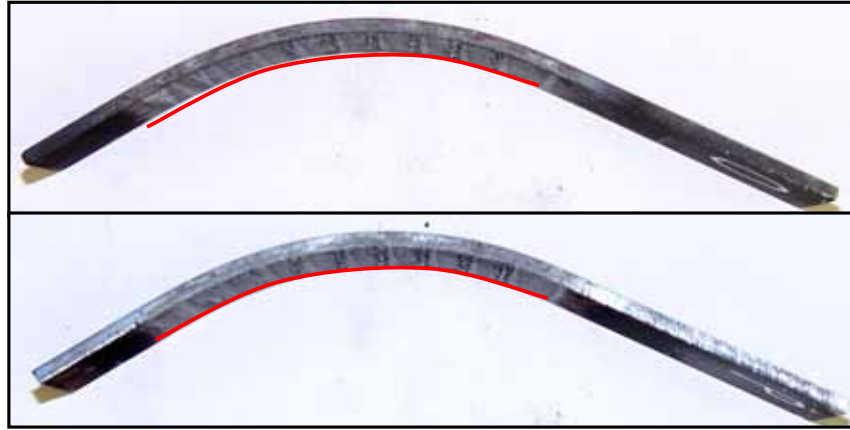
Figure 4.87: Samples showing slight difference in radius of curvature for the same set of laser parameters (indicated by red line)

Since it was known and later confirmed that there was no material change (all the samples were from the same batch), the change in results was attributed to the laser system used. After discussions with the operator, it seemed almost impossible for the system to be at fault. On examination of the irradiated surface of the specimens, it was found that there was indeed a discrepancy in visual laser line width on the samples, indicating that the beam diameter and hence radiating energy density was not constant across the samples being irradiated. This is clearly shown in Figure 4.88 on the surface of samples produced with a 7,5mm beam diameter.
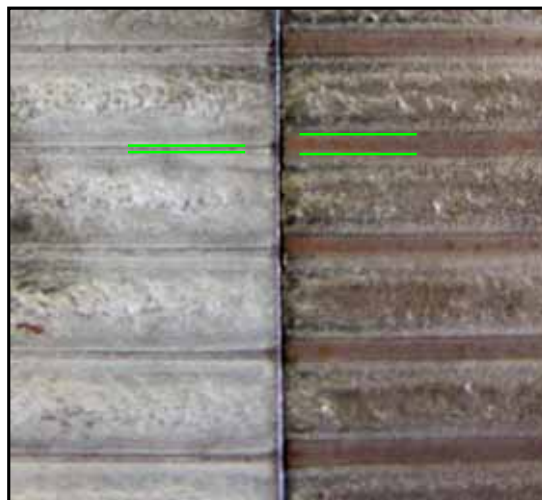
Figure 4.88: Specimen surface indicating difference in width between laser lines (green lines)

This could not be confirmed with the samples produced with a 20mm beam diameter since there was a 10mm overlap between consecutive laser line scans, making it difficult to determine the start/finish position of each line width. The system must therefore first be calibrated for larger length of specimens before extrapolating the results obtained for small specimens with a 50mm width. It is envisaged that this discrepancy does not significantly influence the fatigue results, since the fatigue specimens were machined from the centre of each plate specimen and the difference in deformation was observed more at the free end of the plate specimen from which irradiation started.

4.12   FATIGUE FAILURE

Fracture surface analysis indicated that fatigue cracks initiated from the laser irradiated surface, with a small number of samples where crack initiation was from the bottom surface. Crack initiation from the bottom surface was due to corrosion pits, and these samples were disregarded. Multiple crack initiation sites are clearly visible on Figure 4.89.
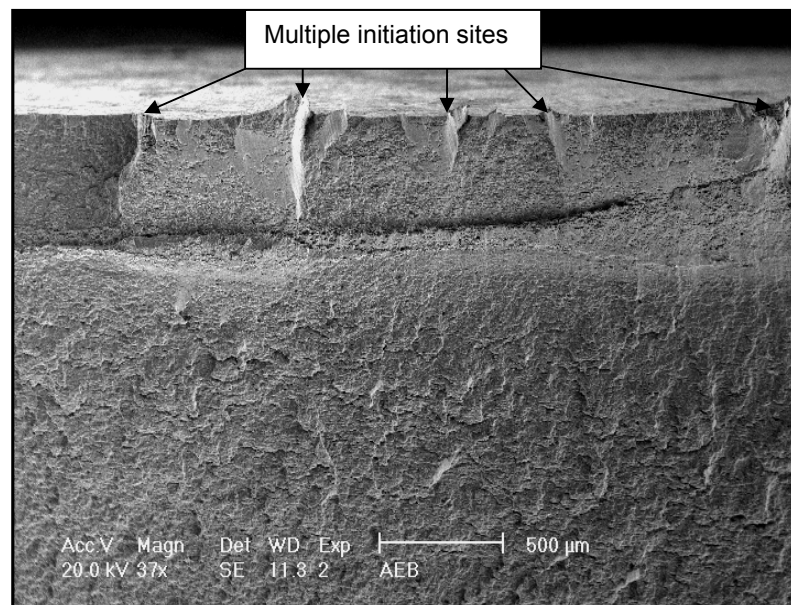
Figure 4.89: Multiple initiation sites on top surface

Investigation of these initiation sites yielded no results as the fracture surface showed a high degree of mechanical damage (rubbing action). It was thus not possible to clearly identify the cause of crack initiation at these sites. Figure 4.90 shows evidence of mechanical damage at one of these initiation points. The most probable cause for crack initiation is surface irregularities, i.e. corrosion pits, thickening effect due to laser irradiation, etc.
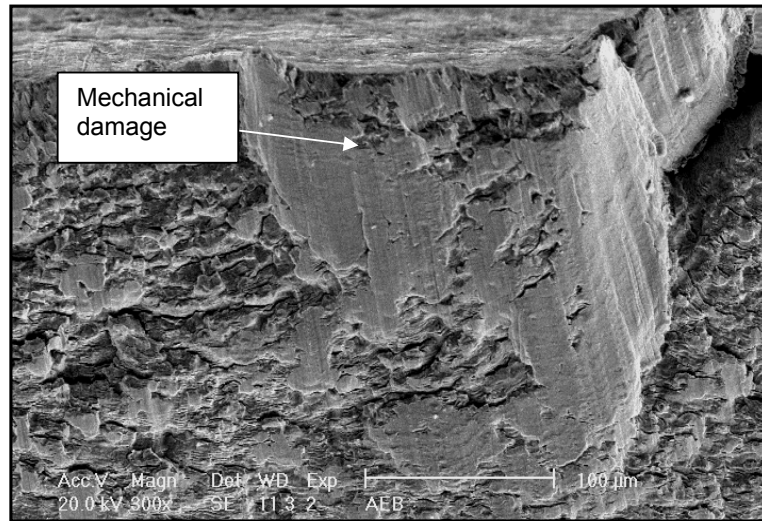
Figure 4.90: Evidence of mechanical damage at initiation point

A typical fatigue fracture surface is shown in Figure 4.91, indicating the semi-elliptical shape of the fatigue region and the fast fracture region.
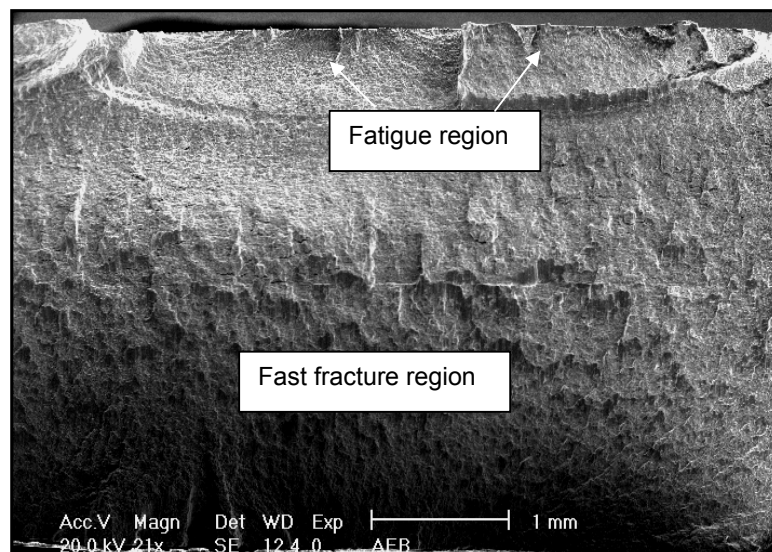
Figure 4.91: Typical fatigue fracture surface

On further investigation of the fatigue fracture region, some evidence of striations was observed, although on certain sections, this evidence was once again destroyed by mechanical damage. Evidence of striations is shown in Figure 4.92.
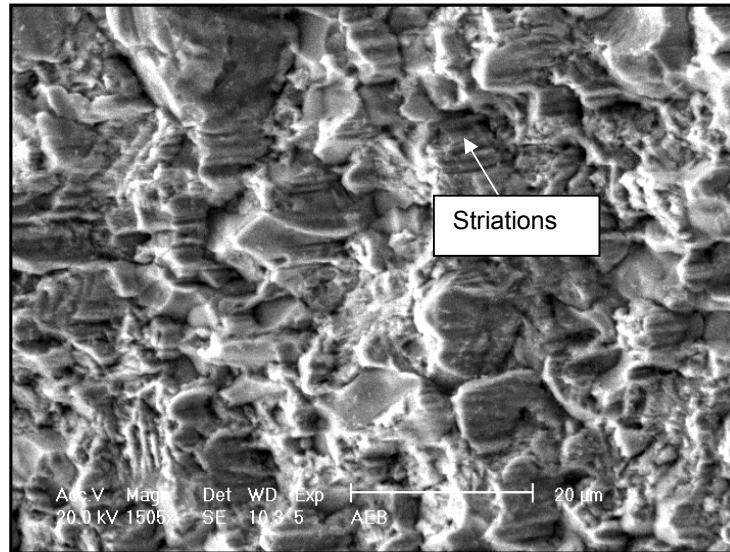
Figure 4.92: Evidence of striations in fatigue fracture region

It is expected that a metallurgical change (phase change; hardness) at the top surface (irradiated surface) is the major cause of crack initiation as it sets up a metallurgical notch/inconsistency. On the 7,5mm beam diameter samples, a difference of 63HV units can be observed between the surface and material at the bottom surface. A phase / microstructure change was also observed and was discussed in detail in Section 4.5.

4.13 SUMMARY

From these results it is evident that it was possible to produce specimens of similar geometrical shapes using various laser parameters. The optimum set of parameters will be dependant on the mechanical properties required of the specimens (this will change as the required mechanical properties change). A change in the microstructure (for dual phase steel) due to the heat is inevitable, but these changes did not result in the formation of any microvoids as were experienced during mechanical stretch forming.

Specimens of similar geometries for fatigue testing were produced by
employing the following settings:

- 5kW, 20mm beam diameter, 2,5 m/min, 10 mm interval spacing
- 1,5kW, 7,5mm beam diameter, 1,2m/min, 7,5 mm interval spacing

It is assumed that any sets of parameters between 5kW and 1,5kW and
line energies of 2000J/m and 1250J/m will yield similar results.
The generalised forming equation given in equation 4.6 can be used to
predict bend height changes due to laser forming. The equation is only
valid for dual phase steel in the power range of 1,5kW to 5kW. The
master diagram for the laser deforming of dual phase steel can be used
to predict settings that will result in specimens with a 130mm radius of
curvature.

It is evident that residual stress analysis is a very complex process. The
residual stress distribution profile is probably the most important result
obtained from testing. Actual results should be used with care since the
rosette strain gauge used for measurements had a relatively small gauge
diameter. The average stress method is only an approximate method
and results should not be used as absolute values. It has been found by
previous research that the hole-drilling results are affected when the
residual stress exceeds 60 percent of the bulk material's yield strength.
Trends were observed at the same location of the samples, regardless if
measurements were taken on the laser irradiated side or reverse side of
the specimen. The only difference was the magnitude of relieved
residual stress. In most cases the obtained relieved residual stress was
much smaller in magnitude than that of the original plate (in the bulk of
the material). The surface indicated a slight tensile residual stress for
most samples evaluated. Only two readings were higher than the
original plate's for the bulk of the material. These two were both for the
7,5mm beam diameter specimens where measurements were taken at
the 'last line' location (REVERSE and LASER SIDE). A good correlation
in distribution profile was obtained between microhardness and relieved

residual stress distribution at the 'middle of sample' location. This indicates that an increase in hardness indicates an increase in residual stress magnitude for the laser formed specimens.

From the results obtained it is clear that the laser forming process has potential to be employed as a production stage in the manufacture of wheel centre discs while maintaining adequate fatigue strength. Large beam diameters which cause heat penetration through the thickness of the specimen and hence microstructure breakdown should be avoided, since it was shown that these specimens exhibited worse properties than those produced with a smaller laser beam diameter. The CO_2 laser system needs to be controlled more accurately as inconsistencies influence the final radius of curvature of the specimen. It is suggested that peak temperature reached by the specimen be used as a control measure for the CO_2 laser system and not only laser parameters. This means that the system should be able to vary laser head velocity to ensure constant peak temperature of the specimen surface.

CHAPTER 5

FINAL CONCLUSIONS

5.1   INTRODUCTION

The aim of this investigation was to establish the effect of process parameters on the final product's shape/bend angle and to characterize the effect of the laser forming process on the material's mechanical properties and structural integrity. It has been proven in the previous Chapter that both these main objectives have been met.

5.2   FINAL CONCLUSIONS

The final conclusions of this investigation can be summarized as follows:

- Laser materials processing is a common manufacturing process in industry. Laser forming on the other hand has been used mainly for deforming very thin sheet on the micro scale. In order to establish laser forming as a competitive production process, the effect of process parameters, material properties and initial cost are all important considerations that need to be fully investigated and analysed.

- The literature study indicated that the main parameters to consider during laser forming are the laser power (P), laser head velocity (v) and laser beam diameter (mm). Plate thickness and laser beam profile (energy distribution) will be kept constant. Microstructural changes are important to note, as the flow stress at high temperatures are more significantly influenced by microstructural changes.

- The results of preliminary tests indicated that the following laser parameters resulted in specimens with approximately the same radius of curvature:
    - 5kW, 20mm beam diameter, 10mm interval spacing, 2,5m/min
    - 3,1kW, 14mm beam diameter, 10,5mm interval spacing, 2m/min
    - 1,5kW, 7,5mm beam diameter, 0mm interval spacing, 1,2m/min

- The above parameters resulted in the following mean forming equation being obtained:

$$y = 35{,}3e^{0{,}008x}$$

  Where y = bend height (mm) and x = distance from free end.

- Other important points to note include:
  - Highest increase in bend height was obtained during the first five laser scans, subsequent scans only marginally increased bend height.
  - Bend height increases linearly with the number of laser scanning cycles.
  - Percentage overlap is an important factor which could be beneficial or detrimental for increasing bend height.
  - Definite microstructural changes occurred at all laser parameters used. Grain growth as high as 60 percent higher than the original grain size was observed.
  - These microstructural changes also influenced the hardness profile between top and bottom surfaces.

- A forming master diagram was obtained for laser forming of dual phase steel between the 5kW and 1,5kW parameters.

- The 7,5mm beam diameter specimens behaved almost exactly the same as mechanically pure bend specimens.

- During fatigue testing, the original flat plate showed superior fatigue strength compared to all the other specimens tested.

- The 20mm beam diameter specimens showed the lowest fatigue life, although still better than the results obtained for the wheel centre disc as indicated by previous research.

- The estimated curve can be used as a prediction model when no fatigue data is available, but only when considering the original plate, pure bend and 7,5mm beam diameter specimens.

- From the S-N curves obtained for the various specimens, the following equations were obtained:
    - Original flat plate: $S_a = -47,844 \, ln \, N_f + 939,54$
    - Pure bend: $S_a = -34,205 \, ln \, N_f + 735,78$
    - LF (7,5mm beam Ø) $S_a = -35,523 \, ln \, N_f + 752,41$
    - LF (20mm beam Ø) $S_a = -39,21 \, ln \, N_f + 685,27$
    - Estimated curve $S_a = -25,094 \, ln \, N_f + 606,68$
    - Centre disc specimens $S_a = -32,784 \, ln \, N_f + 619,05$

- Inconsistencies were observed during the laser forming process with evidence that the laser beam diameter is not constant for all samples produced, even though the same settings were programmed.

- Maximum temperatures observed on the various specimens are indicated below:
    - 7,5mm beam diameter: 1451,6°C
    - 14mm beam diameter: 1444,4°C
    - 20mm beam diameter: 1486,2°C

- The fastest cooling rate was observed on the 14mm beam diameter specimens at a rate of 471°C/s.

- The fastest heating rate was on the 20mm beam diameter specimens at a rate of 76°C/s.

- On average the 20mm beam diameter specimens showed higher temperatures at all points of measurement, followed by the 14mm beam

diameter specimens with the 7,5mm beam diameter specimens reaching the lowest temperatures.

- Dramatic microstructural changes were observed on the specimens subjected to the 1,5kW laser parameters. The microstructure after the forming process consisted of bainitic / Widmanstätten ferrite and aligned second phase (at the surface). This structure indicated a maximum hardness of 266HV vs. 157HV for the original material.

- The specimens produced by the 5kW laser parameters indicated a total breakdown of the martensite phase. The microstructure at the top surface indicated excessive grain growth with ferrite and ferrite/carbide aggregate as the dominant phases.

- The original plate showed compressive relieved residual stresses at the surface and tensile residual stresses in the bulk of the material.

- There is a good correlation in relieved residual stress results of measurements taken at the middle of the sample location i.e. measurements taken in the centre of the sample. All laser formed specimens indicated a tensile surface residual stress and a compressive bulk relieved residual stress.

- Residual stress magnitudes are relatively small, with a maximum value of 48,884MPa (14,3% of S_y) at the surface and a maximum value of -14MPa (4,1% of S_y) in the bulk of the material.

- There was a good relation between the microhardness profile and the relieved residual stress profile vs. depth below the irradiated surface.

- The microstructural changes observed on the samples have the most detrimental effect on fatigue life since the residual stress values are

relatively small and thus resulted in a very small mean stress condition, thereby having little effect on the crack initiation process.

- Laser forming can be successfully carried out on dual phase steel, even though a change in microstructure was observed. However, as a result of the deleterious behaviour it is suggested that dual phase steel is not suitable for this forming application unless the laser parameters have been investigated and are closely controlled. On the other hand, if fatigue performance is not of significance, then this process may be recommended.

FUTURE WORK

Through this research it has been proved that the laser forming process can be a viable forming process. It is important to know the material's properties and microstructure beforehand in order to choose proper forming parameters. For dual phase steel, the following future work will enhance the understanding of the forming process:

- Laser forming of dual phase steel with a Nd:YAG laser system:
    - Are the process variables more controllable, i.e. can a specimen with a constant bend angle be reproduced?
    - Higher efficiency of laser system?

- Temperature control below the martensite breakdown temperature:
    - Bending possible at such low temperatures?
    - What are the possible bending mechanisms?

- Attempt forming specimens and maintain the ferrite/martensite microstructure without grain growth:
    - Can microstructure be maintained without any degradation?
    - Will it be possible to characterise small changes in microstructure, e.g. precipitation of phases, etc?
    -
- Forming of three dimensional shapes, e.g. bulge:
    - Establish the correct heating pattern and cycle to form a three dimensional bulge.
    - Control of mechanical properties and microstructure.

The laser forming process can be developed for local industry as a possible production stage, especially where very hard and difficult to mechanically deform alloys are used. Another area of interest is an investigation into the viability of the laser forming process for high strength aluminium alloys for the aviation industry.

REFERENCE LIST

1.   Rofin-Sinar. 2000. *Introduction to industrial laser materials processing.*
        Rofin-Sinar: Hamburg. pp1-159

2.   Namba, Y. 1987. *Laser forming of metals and alloys.* Conference
        proceedings: LAMP'87. pp601-610

3.   Masubuchi, K. 1992. *Studies at MIT related to applications of laser
        technologies to metal fabrication.* Conference proceedings: LAMP'92.
        pp939-946

4.   Silve, S, et al. 1999. *Laser forming – a new vocabulary for objects.*
        Conference proceedings: ICALEO 1999. pp87-96

5.   Vollersten, F, et al. 1995. *The laser bending of steel foils for microparts
        by the buckling mechanism – a model.* Modelling Simul. Mater. Sci. Eng.
        pp107-119

6.   Marya, M and Edwards, GR. *Factors affecting the laser bending of Ti-
        6Al-2Sn-4Zr-2Mo.* Journal of Laser applications.

7.   Chan, KC, et al. 2000. *Laser bending of thin stainless steel sheets.*
        Journal of laser applications. Laser Institute of America. pp34-40

8.   Kutsuna, M, et al. 1998. *Study on laser plate bending of stainless steels
        and aluminium alloys.* Conference proceedings: Taiwan International
        Welding Conference'98. pp285-290

9.   Marya, M & Edwards, GR. 1998. The laser forming of titanium alloys.
        Conference proceedings: Trends in welding research – 5th International
        Conference. pp982-987

10.   Magee, J, et al. 1998. *Development of an integrated laser forming
        demonstrator system for the aerospace industry.* Conference
        proceedings: ICALEO 1998. pp141-149

11.   Tong, K. 1998. *A numerical study on laser forming of titanium plates.*
        Conference proceedings: ICALEO 1998. pp131-139

12.   Hsiao, Y, et al. 1997. *Finite element modeling of laser forming.*
        Conference proceedings: ICALEO 1997. pp31-40

13.   Li, W & Yao, YL. 1999. *Effects of strain rate in laser forming.*
        Conference proceedings: ICALEO 1999. pp107-116

14.   Son, KJ, et al. 2000. *Analysis of angular distortion in weldments using
        laminated plate theory.* Journal of Science and Technology of welding
        and joining. Volume 5. No. 4. pp245-249

15.   Tong, K. 1999. *Analysis on laser forming of 0.063" thick titanium sheets.*
      Conference proceedings: ICALEO 1999. pp97-106

16.   Marya, M & Edwards, GR. 1999. *Heat flow analysis for the optimization
      of the laser forming of titanium Ti-6Al-2Sn-4Zr-2Mo* submitted to ASME
      Transactions, Journal of Engineering Materials and Technology.

17.   Scully, K. 1987. *Laser line heating.* Journal of Ship Production. Vol3.
      No4. pp 237-246

18.   Cheng, J and Yao, YL. 2002. *Microstructure integrated modeling of
      multiscan laser forming.* Journal of Manufacturing Science and
      Engineering. Vol 124, May. pp379-388

19.   Higgins, RA. 1993. *Engineering metallurgy.* 6th ed. Edward Arnold:
      Great Britain. pp239-283

20.   *Constant temperature transformation TTT curves*
      http://www.key-to-steel.com/ViewArticle.asp?OD=17

21.   Roberts, WL. 1978. *Hot rolling of steel.* Marcell Dekker: USA. pp66-68

22.   ASM International. 1991. Atlas *of time-temperature diagrams for irons
      and steels.* ASM: USA. pp558

23.   Gorni, AG; Vieira, RR. 1996. *The effect of finishing temperature and
      cooling rate on the microstructure and mechanical properties of an as-
      hot-rolled dual-phase steel.*
      http://www.geocities.com/agorni/dpabst.html

24.   Bouaziz, O, et al. 2001. *Physical modeling of microstructure and
      mechanical properties of dual-phase steel.* Journal De Physique.
      September 2001. EDP Sciences: Les Ulis Cedexa

25.   Huper, T, et al. 1999. *Effect of volume fraction of constituent phases on
      the stress-strain relationship of dual phase steels.* ISIJ International:
      Tokyo

26.   Avner, SH. 1974. *Introduction to physical metallurgy.* 2nd ed. McGraw-
      Hill: Singapore. pp 350-355

27.   Reed-Hill, RE and Abbaschian, R. 1994. *Physical metallurgy principles.*
      3rd ed. PWS: USA. pp 674-685

28.   Won, JN, Bae, CM. 1999. *Microstructural evolution and its relation to
      mechanical properties in a drawn dual-phase steel.* Journal of Materials
      Science. Kluwer Academic Publihsers. pp 5661-5668

29.   Dieter, GE.1988. *Mechanical metallurgy*. SI Metric ed. McGraw-Hill: Singapore. pp557-559

30.   Askeland, DR. 1994. *The science and engineering of materials*. 3rd ed. PWS: USA. pp185-186

31.   Zuccarello, B. 1999. *Optimal calculation steps for the evaluation of residual stress by the incremental hole-drilling method*. Experimental Mechanics Vol.39, No.2. SAGE publications. pp117-124

32.   Measurements Group. 1988. *Measurement of residual stresses by the hole-drilling strain gauge method*. Tech Note (TN-503-3)

33.   American Society for Testing and Materials (CD) Vol 03.01. 2002. *Standard test method for determining stresses by the hole-drilling strain gage method*. ASTM: USA

34.   Dowlling, NE. 1999. *Mechanical behaviour of materials*. Prentice Hall: USA. pp 351-475

35.   Bannantine, J, et al. 1990. *Fundamentals of metal fatigue analysis*. Prentice Hall: USA. pp 1-30

36.   Das, AK. 1997. *Metallurgy of failure analysis*. McGraw Hill: USA. pp79-80

37.   Holman, JP. 1992. *Heat transfer*. 7th ed. McGraw-Hill: Singapore. pp664-665

38.   FLIR Systems. 2002. *ThermaCAM^{TM} Researcher 2002 - Operating manual*. FLIR Publications: USA. pp38-40

39.   Bhadeshia. HKDH. *Widmanstätten Ferrite*. Course Material: Part II Course C9, Alloys.

40.   Lancaster, JF. 1993. *Metallurgy of Welding*. 5th ed. Chapman & Hall: Great Britain. pp182-185

41.   Nobre, JP, et al. 2004. An empirical methodology to estimate a local yield stress in work-hardened surface layers. Experimental Mechanics Vol.44, No.1. SAGE Publications. pp76-84

42.   McGrath, PJ. 2001. *An investigation of residual stresses induced by forming processes on the fatigue resistance of automotive wheels* (PhD Thesis). PE Technikon: SA. pp91-96

Additional references:

43.   Magee, J, et al. 1998. *Advances in laser forming.* Journal of Laser Applications. Vol 10. No.6. pp235-245

44.   Li, W and Yao, YL. 2001. *Laser bending of tubes, mechanism, analysis, and prediction.* Journal of Manufacturing Science and Engineering. Vol 123. November. pp674-681

45.   Bao, J and Yao, YL. 2001. *Analysis and prediction of edge effects in laser bending.* Journal of Manufacturing Science and Engineering. Vol 123 February. pp53-61

46.   Erdogan, M. 2002. The *effect of new ferrite content on the tensile fracture behaviour of dual phase steels.* Journal of Materials Science 37. Kluwer Academic Press. pp3623-3630

47.   American Society for Testing and Materials (CD) Vol 03.01. 2002. *Analysis of strain gage rosette Data* (E1561-93). ASTM: USA

48.   Nobre, JP. Et al. 2000. *Use of the hole-drilling method for measuring residual stresses in highly stressed shot-peened surfaces.* Experimental Mechanics Vol.40, No.3. SAGE Publications. pp289-297

49.   Rumzan, I and Schmitt, DR. 2003. *Three dimensional stress-relief displacements from blind-hole drilling: a parametric description.* Experimental Mechanics Vol. 43, No.1. SAGE Publications. pp52-60

50.   *An evaluation of four hole drilling analysis techniques with respect to non-uniform residual stress fields.* http://midas.npl.co.uk/midas/content/ma31.html

51.   Burroughs, W. 1982. *Understanding Lasers.* Longman:Milan

52.   Luxon, JT & Parker, DE. 1985. *Industrial lasers and their applilcations.* Prentice-Hall:New Jersey

53.   Muncheryan, HM. 1983. *Principles and practice of laser technology.* TAB:USA

54.   Eloy, JF. 1987. *Power lasers.* Wiley:Great Britain

55.   *Lasers in manufacture* http://www.me.iastate.edu/graduate/programs/lasers/lasers.html

56.   *Theoretical model of laser cutting process* http://greenmfg.me.berkeley.edu/lml/research/cutting/

57.   *Improving laser cutting quality for two dimensional contoured paths* http://www.columbia.edu/~ylyl/di2d.htm

58.   *Job Shop Technology*
        http://www.jobshoptechnology.com/

59.   Callister, WD (Jr). 1999. *Materials Science and Engineering.* 5th ed.
        Wiley: New York. pp658-667

60.   Shackelford, JF. 2000. *Materials Science for Engineers.* 5th ed.
        Prentice-Hall: New Jersey. pp354-389

61.   Hannah, RL and Reed SE (editors). 1992. *Strain Gage User's
        handbook.* Elsevier: Great Britain. pp1-79

62.   Ross, B. 1995. *Investigating mechanical failures.* Chapman & Hall:
        Great Britain. pp113-187

63.   Smallman, RE. 1985*. Modern physical metallurgy.* 4th ed. Butterworth-
        Heinemann: England. pp423-434

64.   Easterling, K. 1992. *Introduction to physical metallurgy.* 2nd ed.
        Butterworth-Heinemann: Great Britain. pp27-30; 126-180

65.   Llewellyn, DT. 1992. *Steels: Metallurgy and applications.* 2nd ed.
        Butterworth-Heinemann: Great Britain. pp26-30; 129-136

66.   Budinsky, KG and Budinski, MK. 1999. *Engineering Materials.* 6th ed.
        Prentice-Hall: USA. pp281-302

67.   Neely, JE. 1994. *Practical metallurgy and materials of industry.* 4th ed.
        Prentice-Hall: USA. pp142-177

68.   DeGarmo, EP, et al. 2003. *Materials and processes in manufacturing.*
        9th ed. Wiley: USA. pp66-103

69.   Halliday, D and Resnick, R. 1981. *Fundamentals of physics.* 2nd ed.
        Wiley: USA. pp340-342; 355-363

70.   Leco Corporation. 1992. Metallography principles and procedures.
        Leco: USA. pp35-57

71.   Higgins, RA. 1994. *Properties of engineering materials.* 2nd ed. Edward
        Arnold: Great Britain. pp198-237

APPENDIX A

DETERMINATION OF RADIUS OF CURVATURE

APPENDIX A

Consider a circle with radius R. Draw in a radius from the center of the circle to the top quadrant. Draw a line perpendicular to the radius at any distance H to the inside of the circle. From where the line intersects the circle at its ends, its length is L. Draw a line, with length R from the center of the circle to one of the intersection points of the perpendicular line to form an angle θ. Draw a line from where the perpendicular line intersects the circle to the top quadrant from where H was measured, to form an angle ϕ.
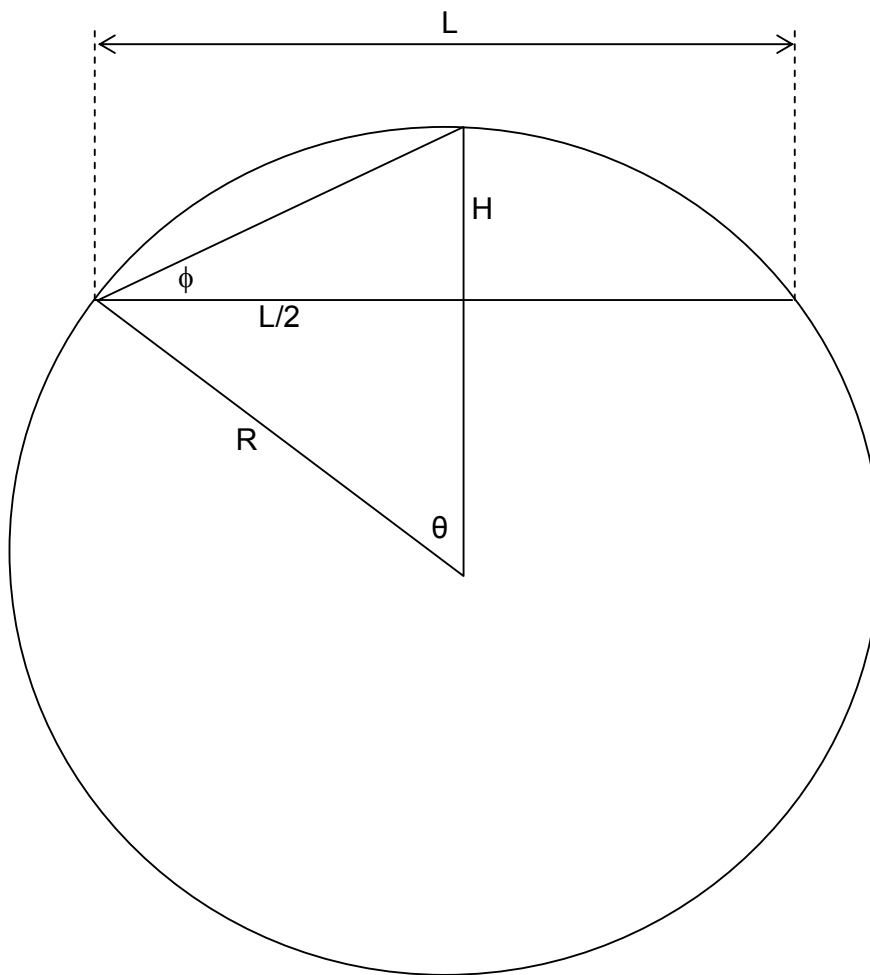
DERIVATION

$$\frac{L/2}{R} = \frac{L}{2R}$$

$$\sin\theta = \frac{L}{2R}$$

$$\therefore \theta = \sin^{-1}\left(\frac{L}{2R}\right)$$

Where θ is measured in degrees.

$$\frac{H}{L/2} = \frac{2H}{L}$$

$$\tan\phi = \frac{2H}{L}$$

$$\therefore \phi = \tan^{-1}\left(\frac{2H}{L}\right)$$

Where φ is measured in degrees.

$$\frac{\theta}{\phi} = 2$$

$$\therefore \theta = 2\phi$$

METHOD OF APPLICATION

Use $\boxed{\phi = \tan^{-1}\left(\frac{2H}{L}\right)}$ to find φ.

Use $\boxed{\theta = 2\phi}$ to find θ.

Manipulate $\sin\theta = \left(\frac{L}{2R}\right)$ into $\boxed{R = \frac{L}{2\sin\theta}}$ to find R.

APPENDIX B

TIME-TEMPERTURE RESULTS

APPENDIX B

1,5kW, 0% Overlap

Temperature	Individual time	Cumulative time
1451.6000	0.0000	0.0000
745.3000	7.1600	9.1010
517.9000	9.4600	18.5610
495.1000	2.6800	21.2410
516.5000	1.2590	22.5000
548.7000	4.3000	26.8000
560.2000	1.8010	28.6010
579.5000	4.4600	33.0610
584.9000	1.5000	34.5610
594.1000	4.5990	39.1600
606.6000	1.6200	40.7800
604.2000	4.5000	45.2800
617.6000	1.5200	46.8000
579.5000	9.1610	55.9610
503.5000	10.6000	66.5610
488.2000	1.1800	67.7410
489.7000	1.2990	69.0400
482.9000	4.6810	73.7210
486.4000	1.4590	75.1800
482.9000	4.4600	79.6400
488.2000	1.6400	81.2800
489.7000	4.2810	85.5610
495.1000	1.7390	87.3000
500.0000	4.3800	91.6800
505.0000	1.4800	93.1600
475.7000	16.8400	110.0000
455.7000	4.2010	114.2010
455.7000	1.3800	115.5810
434.4000	4.6600	120.2410
438.5000	1.5390	121.7800
434.4000	3.8010	125.5810

432.3000	2.1790	127.7600
426.1000	4.4000	132.1600
432.3000	1.5410	133.7010
424.0000	4.4390	138.1400
434.4000	1.8210	139.9610
428.3000	8.5590	148.5200
406.9000	12.1600	160.6800
410.8000	1.7810	162.4610
404.3000	4.2800	166.7410
399.4000	1.7590	168.5000
389.8000	4.2800	172.7800
387.2000	1.3600	174.1400
376.8000	4.6400	178.7800
382.3000	1.6610	180.4410
365.9000	4.4200	184.8610
371.6000	1.8600	186.7210
362.9000	7.4190	194.1400
367.3000	8.8800	203.0200
355.5000	4.2800	207.3000
367.3000	1.3010	208.6010
352.2000	4.8190	213.4200
358.7000	1.7010	215.1210
338.6000	4.2400	219.3610
338.6000	1.6790	221.0400
328.3000	4.2810	225.3210
328.3000	2.2190	227.5400
320.5000	3.7600	231.3000
324.1000	1.9210	233.2210
320.5000	7.5390	240.7600
306.7000	12.6600	253.4200
311.5000	1.9410	255.3610
306.7000	4.4190	259.7800
310.9000	2.0000	261.7800
290.4000	4.0610	265.8410

301.1000	1.4590	267.3000
279.7000	4.5800	271.8800
285.2000	1.5810	273.4610
279.7000	4.3800	277.8410
289.7000	1.8190	279.6600
295.1000	6.1810	285.8410
272.6000	15.2600	301.1010
252.9000	15.1200	316.2210
232.7000	16.9800	333.2010

3,1kW , 25% Overlap

Temperature	Individual Time	Cumulative Time
1426.3000	0.0000	0.0000
971.4000	1.3600	1.3600
842.2000	2.8800	4.2400
751.6000	4.2010	8.4410
645.9000	11.4590	19.9000
660.0000	0.7810	20.6810
653.6000	3.6990	24.3900
667.3000	0.7400	25.1200
668.4000	3.0200	28.1400
680.6000	1.5410	29.6810
680.6000	3.4000	33.0810
692.7000	0.9600	34.0410
693.7000	3.5990	37.6400
707.4000	0.7200	38.3600
652.5000	13.2800	51.6400
618.4000	6.5200	58.1600
615.6000	1.1200	59.2800
586.6000	3.6410	62.9210
591.9000	0.7190	63.6400
569.1000	3.6610	67.3010
576.0000	0.7600	68.0610
559.3000	3.6200	71.6810
567.8000	0.8390	72.5200
552.1000	3.6000	76.1200
557.8000	0.7400	76.8600
544.4000	8.6810	85.5410
519.6000	11.3800	96.9210
524.5000	0.9390	97.8600
508.4000	3.6010	101.4610
510.1000	0.8990	102.3600
496.8000	3.4810	105.8410

501.8000	0.9190	106.7600
485.1000	3.5610	110.3210
485.1000	0.9590	111.2800
472.5000	3.4800	114.7600
474.3000	1.0410	115.8010
457.9000	8.0590	123.8600
430.7000	16.2010	140.0610
436.7000	0.9390	141.0000
428.6000	3.2400	144.2400
430.7000	1.0200	145.2600
415.9000	3.6000	148.8600
422.3000	0.8210	149.6810
407.2000	3.5400	153.2210
415.9000	1.0390	154.2600
398.8000	12.0410	166.3010
391.4000	7.6600	173.9610
396.3000	0.9190	174.8800
379.2000	3.6000	178.4800
389.5000	0.9000	179.3800
373.8000	3.5200	182.9000
376.5000	1.0410	183.9410
371.2000	3.4590	187.4000
374.1000	0.8800	188.2800
365.9000	3.5410	191.8210
368.7000	0.9800	192.8010
354.3000	5.5990	198.4000
329.4000	18.0210	216.4210
312.0000	10.0400	226.4610

5kW, 50% Overlap

Temperature	Individual time	Cumulative time
1423.0000	0.0000	0.0000
1122.7000	1.1790	1.1790
866.3000	7.4610	8.6400
721.5000	10.6200	19.2600
1247.0000	0.9390	20.1990
814.2000	1.5410	21.7400
1107.0000	2.3800	24.1200
820.3000	3.3390	27.4590
1116.6000	0.6400	28.0990
851.2000	2.9800	31.0790
1157.1000	0.9000	31.9790
868.7000	3.0610	35.0400
1175.3000	0.8400	35.8800
859.6000	5.0400	40.9200
733.7000	10.6790	51.5990
708.1000	0.8800	52.4790
719.6000	3.6810	56.1600
680.5000	3.3990	59.5590
696.4000	0.6810	60.2400
666.1000	3.1600	63.4000
683.5000	0.7790	64.1790
657.6000	3.2210	67.4000
679.4000	0.5790	67.9790
660.8000	3.2000	71.1790
674.5000	0.9000	72.0790
643.5000	13.8010	85.8800
629.5000	5.7600	91.6400
631.9000	0.8190	92.4590
626.1000	3.2010	95.6600
627.1000	0.8990	96.5590
606.8000	3.0200	99.5790

604.5000	0.9610	100.5400
589.2000	3.0190	103.5590
590.5000	0.8800	104.4390
566.2000	10.6600	115.0990
525.9000	16.3210	131.4200
488.0000	16.5800	148.0000
461.2000	15.7400	163.7400
456.6000	13.6400	177.3800
431.7000	7.4000	184.7800
405.7000	21.1000	205.8800
375.5000	26.5400	232.4200
364.4000	6.7200	239.1400

APPENDIX C

FATIGUE SETUP PROCEDURE

APPENDIX C
FATIGUE SETUP PROCEDURE

Fatigue testing setup procedure

The specimens should be machined as shown in the technical drawing (see Figure 7.6). Pitting marks and deep scratches were removed from the machined specimen's surface with a flapper wheel attached to a pneumatic pencil grinder. The specimen's surface was then prepared further for strain gauge application. The surface was sanded to a near polished appearance using a circular technique. After sanding, the specimen was cleaned using acetone and a strain gauge was then fitted.

Installing a specimen in grips of the machine:

- Before any specimen installation, the stroke of the machine should be set as close to zero as possible.
- Before the specimen is clamped in the grips, the specimen strain gauge should be connected to the strain amplifier and calibrated (set for zero).
- At all times must the thickness centre of the specimen be 6.5mm above the base of the main grip. Make use of spacers to achieve this.
- Insert the specimen in the main grips.
- Loosely fasten the four off M8 cap screws.
- Ensure that the specimen is well aligned with the main grips.
- Torque the four off M8 cap screws.

Setting up and adjusting the machine:
Adjusting the machine for initial zero:

- Ensure that the main switch is off to prevent accidental start of the motor.
- The stroke should still be set as close to zero as possible and the ten off M8 cap screws on the flywheel properly tightened.
- Slightly undo the five off M12 hexagon bolts on the motor base.

- Adjust the motor base using the adjustment screw to obtain a zero or offset strain. By rotating the flywheel by hand and observing the indicated strain, the zero or offset can be set.
- Tighten the five off M12 hexagon bolts on the motor base.
- Verify the zero or required offset strain value.

Adjusting the stroke for the required strain amplitude:
- Undo the ten off M8 locking cap screws on the flywheel.
- Adjust the eccentricity of the flywheel by small increments.
- Slightly tighten four off the M8 locking cap screws on the flywheel and observe the indicated strain as before.
- Repeat above until the correct strain amplitude is introduced.
- Tighten all the ten off M8 locking cap screws on the flywheel.
- Verify the strain amplitude by rotating the flywheel by hand.

APPENDIX D

SURFACE ROUGHNESS RESULTS

APPENDIX D

Surface Roughness			Ra	Ry	Rz	Rq
Sample 1,5kW	Outside (no laser)	Reading 1	0.82	6.91	6.91	1.07
		Reading 2	1.01	6.48	6.48	1.22
		Reading 3	1.10	7.46	7.46	1.32
		Ave	0.98	6.95	6.95	1.20
	Inside (on laser)	Reading 1	0.92	5.87	5.87	1.16
		Reading 2	1.11	5.77	5.77	1.32
		Reading 3	0.99	6.33	6.33	1.21
		Ave	1.01	5.99	5.99	1.23
	Inside (between laser)	Reading 1	0.99	6.24	6.24	1.20
		Reading 2	0.83	4.78	4.78	1.00
		Reading 3	0.64	4.46	4.46	0.81
		Ave	0.82	5.16	5.16	1.00
Sample 5kW	Outside (no laser)	Reading 1	0.94	6.22	6.22	1.16
		Reading 2	1.19	7.40	7.40	1.47
		Reading 3	0.90	5.92	5.92	1.10
		Ave	1.01	6.51	6.51	1.24
	Inside (on laser)	Reading 1	1.06	6.58	6.58	1.32
		Reading 2	1.00	6.45	6.45	1.23
		Reading 3	0.87	5.92	5.92	1.09
		Ave	0.98	6.32	6.32	1.21
	Inside (between laser)	Reading 1	0.65	4.63	4.63	0.82
		Reading 2	0.88	6.11	6.11	1.12
		Reading 3	0.69	3.93	3.93	0.84
		Ave	0.74	4.89	4.89	0.93

APPENDIX E

LASER EXPERIMENTAL PARAMETERS

Power kW	Beam diameter mm	Scan velocity m/min	No. of scans	P/V J/m	Interval spacing mm	Deformation
1	2	50	10	20	10	None
2	2	50	10	40	10	None
3	2	50	10	60	10	None
1	2	40	10	25	10	None
2	2	40	10	50	10	None
1	2	30	10	33,3	10	None
1	2	20	10	50	10	None
1	4	50	10	20	10	Slight
1	4	40	10	25	10	Reverse bend
1	4	20	10	50	10	Reverse bend
1	4	5	10	200	10	Slight
2	4	20	10	100	10	Slight
2	4	10	10	200	10	Slight
2	4	5	10	400	10	Bending, melting
1	2	5	10	500	10	Slight, melting
1	2	15	10	66,7	10	None, slight melting
1	2	10	10	100	10	Slight
1	2	7,5	10	133,3	10	Reverse bend, marked melting
1	7	5	10	200	10	None
2	7	5	10	400	10	Slight
2	7	10	10	200	10	Slight
3	7	5	10	600	10	Bending
3	7	10	10	300	10	Bending
4	7	10	10	400	10	Bending, melting
4	7	15	10	266,7	10	Bending
2	10	5	10	200	10	Slight
3	10	5	10	600	10	Significant

Power kW	Beam diameter mm	Scan velocity m/min	No. of scans	P/V J/m	Interval spacing mm	Deformation
4	10	5	10	400	10	Significant, melting
4	10	10	10	400	10	Significant
2	15	5	10	400	10	Slight
3	15	5	10	600	10	Significant
4	15	5	10	800	10	Significant
1	2	12	10	83,3	1	Slight
2	4	7,5	10	266,7	2	Slight
2	4	10	10	200	2	Slight
2	5	10	10	200	2,5	Slight
2	7	5	10	400	3,5	Slight
3	10	5	10	600	5	Slight
3	10	5	20 (5/line)	600	5	Significant
4	15	5	20 (5/line)	800	7,5	Significant*
2	7	5	20 (5/line)	400	7	Bending
3	10	5	20 (5/line)	600	10	Significant*
4	15	5	20 (5/line)	800	15	Significant*
2	7	5	20 (5/line)	400	3,5	Significant
4	15	5	20 (5/line)	800	7,5	Significant*
5	30	2,5	20 (5/line)	2000	10	Significant*
2,5	20	0,34	20 (5/line)	7353	20	Bending
1,256	20	0,17	20 (5/line)	7388	20	None
1,256	20	0,5	20 (5/line)	2512	20	Significant
5	20	2,5	20 (5/line)	2000	10	Significant*
5	20	3	20 (5/line)	1666,7	5	Significant

Power kW	Beam diameter mm	Scan velocity m/min	No. of scans	P/V J/m	Interval spacing mm	Deformation
1,875	7,5	1	10 (5/line)	1875	7,5	Significant, melting
1,5	7,5	1	20 (5/line)	1500	7,5	Significant
1,5	7,5	1,20	20 (5/line)	1250	7,5	Significant*
3,5	14	2,8	20 (5/line)	1250	7	Significant
3,5	14	2,55	20 (5/line)	1373	7	Significant
3,5	14	2,55	20 (5/line)	1373	10,5	Significant
3,1	14	2	20 (5/line)	1550	10,5	Significant*

* Test specimens evaluated in more detail, see Chapter 4.

Details of deformation:

- Less than 0,3 mm change in bend height   =   Slight

- Between 0,3 - 0,6 mm change in bend height   =   Bending

- More than 0,6 mm change in bend height   =   Significant

- Melting refers to the surface of the specimen being melted by the heat
  generated due to laser irradiation

APPENDIX F

TABULATED RESIDUAL STRESS RESULTS

APPENDIX F

Original plate

Depth (mm)	e1 (µe)	e2 (µe)	e3 (µe)	σ_{max} (Pa)	σ_{min} (Pa)	Angle (°)
0.01	3	4	2	-932351	-1961879	35.8
0.03	10	12	8	-4180087	-6239144	35.8
0.06	14	21	21	-8511834	-1.2E+07	-22.5
0.10	-11	-9	3	5116004	-485235	17.8
0.14	-46	-42	-119	65504840	30004775	24.0
0.20	-51	-50	-157	84833492	35566508	22.8
0.27	-43	-47	-185	97770714	34206209	21.7
0.34	-35	-48	-198	1.02E+08	32774711	20.0
0.43	-30	-51	-202	1.02E+08	32049963	18.5
0.53	-24	-52	-205	1.02E+08	30470872	17.3
0.63	-19	-55	-208	1.02E+08	29515115	15.9
0.74	-16	-56	-210	1.02E+08	28780977	15.2
0.87	-14	-59	-211	1.02E+08	28627086	14.3
1.0	-13	-60	-211	1.01E+08	28424173	13.9
1.14	-16	-63	-213	1.02E+08	30091032	13.8
1.30	-20	-67	-217	1.05E+08	32406416	13.8
1.14	-22	-68	-219	1.06E+08	33412118	14.0
1.63	-28	-73	-225	1.1E+08	36730932	14.3
1.81	-28	-73	-225	1.1E+08	36730932	14.3
2.0	-32	-76	-227	1.11E+08	38753227	14.4

7,5mm LASER SIDE between lines

Depth (mm)	e1 (µe)	e2 (µe)	e3 (µe)	σ_{max} (Pa)	σ_{min} (Pa)	Angle (°)
0.01	1	0	1	-289914	-999667	α
0.03	4	4	8	-2865001	-4872487	22.5
0.06	3	8	9	-2589218	-5148270	-16.8
0.10	-5	12	-37	26555439	525768.3	32.1
0.14	-4	18	-74	48883819	1409852	29.2
0.20	11	27	-70	43691002	-5648353	27.2
0.27	28	43	-44	27311845	-1.7E+7	27.4
0.34	40	57	-19	12772100	-2.6E+07	28.8
0.43	50	69	-6	5229315	-3.4E+07	29.6
0.53	55	75	8	-2765130	-3.8E+07	30.8
0.63	62	86	20	-8813651	-4.4E+07	32.5
0.74	64	88	25	-1.2E+07	-4.6E+07	32.9
0.87	63	88	26	-1.2E+07	-4.5E+07	33.5
1.0	64	91	30	-1.4E+07	-4.7E+07	34.4
1.14	63	89	32	-1.5E+07	-4.6E+07	34.8
1.30	61	87	31	-1.4E+07	-4.5E+07	35.0
1.14	60	87	32	-1.4E+07	-4.5E+07	35.6
1.63	59	86	33	-1.5E+07	-4.5E+07	36.0
1.81	59	86	33	-1.5E+07	-4.5E+07	36.0
2.0	58	84	33	-1.5E+07	-4.4E+07	36.0

7,5mm LASER SIDE last line

Depth (mm)	e1 (µe)	e2 (µe)	e3 (µe)	σ$_{max}$ (Pa)	σ$_{min}$ (Pa)	Angle (°)
0.01	-1	0	1	318978.8	-318979	0
0.03	-1	-5	3	1453505	-2581294	35.8
0.06	1	2	9	-1224578	-4414366	18.4
0.10	-5	1	17	470869.1	-7237602	12.2
0.14	-13	-9	12	5103700	-4539508	17.1
0.20	-28	-74	-270	1.29E+08	38610858	15.9
0.27	-48	-107	-293	1.4E+08	52131278	13.7
0.34	-70	-109	-340	1.68E+08	62758477	17.7
0.43	-101	-136	-336	1.69E+08	77414969	17.5
0.53	-135	-162	-362	1.86E+08	94608311	18.7
0.63	-163	-172	-377	1.99E+08	1.06E+08	21.2
0.74	-179	-185	-370	1.97E+08	1.13E+08	21.6
0.87	-190	-190	-371	1.99E+08	1.17E+08	22.5
1.0	-197	-202	-381	2.03E+08	1.23E+08	21.7
1.14	-205	-198	-377	2.04E+08	1.24E+08	23.6
1.30	-212	-206	-385	2.09E+08	1.28E+08	23.5
1.14	-213	-202	-382	2.08E+08	1.27E+08	24.2
1.63	-210	-199	-376	2.05E+08	1.25E+08	24.3
1.81	-209	-196	-375	2.05E+08	1.24E+08	24.6
2.0	-206	-191	-372	2.04E+08	1.22E+08	24.9

20mm LASER SIDE first line

Depth (mm)	e1 (µe)	e2 (µe)	e3 (µe)	σ$_{max}$ (Pa)	σ$_{min}$ (Pa)	Angle (°)
0.01	2	2	1	-591984	-1027967	22.5
0.03	9	9	6	-3395903	-4703853	22.5
0.06	12	6	10	-4367860	-7511781	-39.3
0.10	13	-1	11	-2460236	-1E+07	-42.8
0.14	19	16	13	-7714879	9564599	0
0.20	33	37	22	-1.1E+07	-1.8E+07	30.0
0.27	48	56	31	-1.6E+07	-2.7E+07	31.3
0.34	54	64	36	-1.8E+07	-3.1E+07	32.3
0.43	57	65	33	-1.7E+07	-3.1E+07	29.5
0.53	67	79	41	-2E+07	-3.8E+07	31.3
0.63	69	83	40	-2E+07	-3.9E+07	31.5
0.74	67	81	39	-1.9E+07	-3.8E+07	31.7
0.87	69	84	40	-1.9E+07	-4E+07	31.9
1.0	70	86	41	-2E+07	-4E+07	32.3
1.14	70	84	40	-2E+07	-4E+07	31.3
1.30	71	85	41	-2E+07	-4E+07	31.3
1.14	67	81	37	-1.8E+07	-3.8E+07	31.3
1.63	68	82	39	-1.9E+07	-3.9E+07	31.5
1.81	68	82	40	-2E+07	-3.9E+07	31.7
2.0	68	80	40	-2E+07	-3.8E+07	30.8

20mm LASER SIDE middle

Depth (mm)	e1 (μe)	e2 (μe)	e3 (μe)	σ_{max} (Pa)	σ_{min} (Pa)	Angle (°)
0.01	0	1	3	-406077	-1528295	9.2
0.03	-5	-6	-1	3213898	654845.7	25.2
0.06	-10	8	6	5868079	4448572	0
0.10	-4	-3	-2	2289249	1579495	0
0.14	7	3	5	-2746525	-4990963	-35.8
0.20	6	-4	6	-319976	7417511	α
0.27	15	-1	9	-3002842	-1.2E+07	-38.5
0.34	23	5	12	-6437462	-1.6E+07	-33.1
0.43	32	13	16	-1.1E+07	-2E+07	-27.0
0.53	37	14	17	-1.2E+07	-2.3E+07	-26.2
0.63	39	15	17	-1.2E+07	-2.4E+07	-24.9
0.74	42	3	18	-8858328	-3E+07	-33.0
0.87	42	-2	18	-7215447	-3.1E+07	-34.7
1.0	42	-3	17	-6664172	-3.1E+07	-34.5
1.14	41	-5	14	-5242804	-3E+07	-33.7
1.30	41	-3	13	-5660837	-2.9E+07	-32.5
1.14	41	-4	14	-5569770	-3E+07	-33.4
1.63	37	-5	11	-4196816	-2.7E+07	-32.9
1.81	39	-1	13	-6130091	-2.7E+07	-32.1
2.0	38	-3	11	-4925741	-2.7E+07	-31.9

7.5mm REVERSE SIDE middle

Depth (mm)	e1 (μe)	e2 (μe)	e3 (μe)	σ_{max} (Pa)	σ_{min} (Pa)	Angle (°)
0.01	0	1	3	-477563	-1726505	9.2
0.03	1	4	6	-1564483	-3578342	-5.7
0.06	-2	5	5	852870.2	-3056938	-22.5
0.10	-2	3	6	159043.1	-3097800	-7.0
0.14	-9	-3	8	3866613	-3131924	8.2
0.20	-3	-1	10	550943.5	-5693769	17.3
0.27	4	1	10	-2493418	-7792233	31.7
0.34	12	4	11	-5480225	-1.1E+07	-43.1
0.43	21	8	13	-8599910	-1.6E+07	-33.0
0.53	29	8	12	-9090977	-2.1E+07	-27.9
0.63	32	7	10	-8396586	-2.2E+07	-25.9
0.74	38	7	11	-9270683	-2.7E+07	-26.2
0.87	41	8	11	-9847942	-2.8E+07	-25.1
1.0	41	7	9	-8855571	-2.8E+07	-24.2
1.14	40	6	8	-8120882	-2.7E+07	-24.2
1.30	40	4	6	-6828559	-2.7E+07	-24.1
1.14	39	3	5	-6093869	-2.6E+07	-24.1
1.63	39	2	5	-5796191	-2.7E+07	-24.8
1.81	38	1	4	-5061501	-2.6E+07	-24.8
2.0	37	1	4	-4972490	-2.5E+07	-24.9

7.5mm REVERSE SIDE between lines

Depth (mm)	e1 (μe)	e2 (μe)	e3 (μe)	σ$_{max}$ (Pa)	σ$_{min}$ (Pa)	Angle (°)
0.01	3	4	4	-2023414	-2528534	-22.5
0.03	4	55	12	11645623	-2.2E+07	-42.6
0.06	5	51	26	3143352	-2.3E+07	-36.8
0.10	6	-38	47	6940924	-4.1E+07	36.2
0.14	5	-91	75	22419830	-7.4E+07	37.5
0.20	11	-118	116	26191894	-1.1E+07	36.9
0.27	14	-76	157	7485100	-1.2E+07	33.1
0.34	15	-43	200	-6808888	-1.3E+07	29.2
0.43	11	-26	231	-1.3E+07	-1.4E+07	26.6
0.53	7	-17	262	-1.7E+07	-1.6E+07	25.0
0.63	3	-14	284	-1.8E+07	-1.7E+07	24.1
0.74	-3	-16	301	-1.7E+07	-1.8E+07	23.7
0.87	-7	-19	311	-1.5E+07	-1.8E+07	23.5
1.0	-10	-23	317	-1.4E+07	-1.9E+07	23.6
1.14	-12	-27	319	-1.2E+07	-1.9E+07	23.7
1.30	-13	-30	320	-1.1E+07	-1.9E+07	23.9
1.14	-14	-32	320	-1E+07	-1.9E+07	24.0
1.63	-12	-34	320	-1.1E+07	-1.9E+07	24.3
1.81	-11	-36	319	-1E+07	-1.9E+07	24.5
2.0	-12	-38	316	-9195256	-1.9E+07	24.6

7.5mm REVERSE SIDE last line

Depth (mm)	e1 (μe)	e2 (μe)	e3 (μe)	σ$_{max}$ (Pa)	σ$_{min}$ (Pa)	Angle (°)
0.01	0	-1	0	463942.1	-463942	α
0.03	0	-1	-1	769209.6	113096.4	-22.5
0.06	-1	-4	-4	3189935	1221595	-22.5
0.10	0	-6	-6	4615257	678578.2	-22.5
0.14	-3	-13	-17	12356337	5289782	-11.6
0.20	-3	-18	-25	17782586	6921980	-10.0
0.27	-3	-25	-38	26470385	9704157	-7.2
0.34	-2	-33	-52	35750174	11894346	-6.7
0.43	-3	-46	-70	48359080	16049252	-7.9
0.53	-4	-61	-92	63636476	21064892	-8.2
0.63	-5	-75	-115	79387123	26489587	-7.6
0.74	-8	-89	-138	95464741	33351923	-6.9
0.87	-11	-104	-161	1.12E+08	40094567	-6.7
1.0	-11	-116	-179	1.24E+08	43648536	-7.0
1.14	-11	-125	-196	1.35E+08	47260039	-6.5
1.30	-9	-131	-206	1.42E+08	47867020	-6.7
1.14	-6	-134	-213	1.46E+08	47267508	-6.7
1.63	-1	-134	-215	1.46E+08	44202716	-6.8
1.81	4	-133	-215	1.45E+08	40704028	-7.0
2.0	9	-130	-212	1.42E+08	36610757	-7.2

20mm REVERSE SIDE last line

Depth (mm)	e1 (µe)	e2 (µe)	e3 (µe)	σmax (Pa)	σmin (Pa)	Angle (°)
0.01	-2	-1	-1	1405000	837887.2	- 22.5
0.03	-2	0	0	1314742	180516.3	-22.5
0.06	0	2	4	-693240	-2297277	0
0.10	-5	-6	6	3040656	-3788286	24.9
0.14	-22	-30	6	16438075	-4476010	28.8
0.20	-38	-43	6	25928477	-2004346	25.4
0.27	-53	-52	10	33656808	-1508757	22.0
0.34	-73	-66	9	45283287	2564974	19.8
0.43	-87	-74	11	52792457	4027353	18.2
0.53	-101	-84	8	61293570	8235935	17.3
0.63	-112	-131	-2	79588262	5641454	26.7
0.74	-117	-129	2	80290081	5687264	25.1
0.87	-120	-130	2	81646813	6573419	24.7
1.0	-120	-129	3	81252644	6219959	24.5
1.14	-121	-128	4	81218337	6254266	24.0
1.30	-120	-126	5	80173500	5803844	23.8
1.14	-119	-129	5	80717071	4512644	24.6
1.63	-118	-127	6	79666475	4067982	24.4
1.81	-117	-126	8	78827946	2663624	24.4
2.0	-117	-125	10	78345422	1650890	24.2

20mm REVERSE SIDE middle

Depth (mm)	e1 (µe)	e2 (µe)	e3 (µe)	σmax (Pa)	σmin (Pa)	Angle (°)
0.01	-2	-2	-2	1924627	1924627	α
0.03	-4	-4	-4	3849254	3849254	α
0.06	-2	-3	-2	2426547	1422707	α
0.10	-2	-2	-1	1798381	1088559	22.5
0.14	-1	1	0	1274762	-312449	-35.8
0.20	-1	2	1	1122328	-1122328	-31.7
0.27	2	6	5	-1904761	-4831433	-29.5
0.34	5	11	9	-4491539	-8980850	-31.7
0.43	5	13	10	-4184989	-1E+07	-32.8
0.53	6	15	13	-5869859	-1.2E+07	-28.8
0.63	7	19	16	-6676597	-1.5E+07	-29.5
0.74	6	19	17	-6398478	-1.6E+07	-26.9
0.87	7	22	20	-7620452	-1.8E+07	-26.3
1.0	6	22	21	-7301574	-1.9E+07	-24.3
1.14	4	22	20	-5120048	-1.8E+07	-25.7
1.30	3	21	20	-4668354	-1.7E+07	-24.1
1.14	2	20	20	-4197048	-1.7E+07	-22.5
1.63	1	20	20	-3360980	-1.7E+07	-22.5
1.81	1	20	20	-3360980	-1.7E+07	-22.5
2.0	0	19	19	-2398666	-1.6E+07	-22.5

APPENDIX G

RESIDUAL STRESS COMPONENTS

APPENDIX G

RESIDUAL STRESS COMPONENTS

1.   **Mechanical and optical device**

This device contains the vertical drilling head which incorporates an optical device and a high speed air turbine motor. The device is supported by three adjustable leveling screws which are footed with swivel mounting pads to allow attachment to uneven surfaces. The drilling head houses an air turbine motor which rotates at 300 000rpm under a pressure of 4,5 bar. An inverted end mill is taper locked to the centre bore of the air turbine. The optical device allows for the alignment of the end mill with the drilling location on the strain rosette as well as for hole measurement after the drilling operation. The drilling head is controlled by a stepper motor providing the vertical feed during the drilling operation. The software allows for two types of drilling operations:

- Manually (Step by step), where the operator instruct the software to start the drilling stage;
- Automatic, where the software programme controls the entire operation.

Stress analysis is either by the linear method (all steps are equal in size) or polynomial method (smaller steps closer to the surface, with larger steps as the depth increases). The parameters to be selected by the test operator are:

- Number of steps for a particular hole depth.
- Delay time setting.
- Feed rate of the end mill.
- Evaluation method (linear / polynomial)

2.   **MGC amplifier**

The three elements of the strain rosette are individually connected to separate channels of the MGC amplifier. This device records the strain

readings at the end of each incremental cut after the delay time has elapsed to allow for cooling.

3.   Electronic device

This unit forms an important part of the whole system, as it interfaces the computer signals with the solenoid valve that controls the air supply to the turbine motor and with the stepper motor during the drilling operation.

APPENDIX H

NUMERICAL COEFFICIENTS $\overline{a}$ and $\overline{b}$

APPENDIX H

Numerical values of coefficients $\overline{a}$ and $\overline{b}$

Rosette A	$\overline{a}$					$\overline{b}$				
Blind hole	Hole Diameter, D_0/D					Hole Diameter, D_0/D				
Depth/D	0.30	0.35	0.40	0.45	0.50	0.30	0.35	0.40	0.45	0.50
0.00	.000	.000	.000	.000	.000	.000	.000	.000	.000	.000
0.05	.027	.037	.049	.063	.080	.051	.069	.090	.113	.140
0.10	.059	.081	.108	.138	.176	.118	.159	.206	.255	.317
0.15	.085	.115	.151	.192	.238	.180	.239	.305	.375	.453
0.20	.101	.137	.177	.223	.273	.227	.299	.377	.459	.545
0.25	.110	.147	.190	.238	.288	.259	.339	.425	.513	.603
0.30	.113	.151	.195	.243	.293	.279	.364	.454	.546	.638
0.35	.113	.151	.195	.242	.292	.292	.379	.472	.566	.657
0.40	.111	.149	.192	.239	.289	.297	.387	.482	.576	.668
Through Hole	.090	.122	.160	.203	.249	.288	.377	.470	.562	.651

APPENDIX I

TECHNICAL CONFERENCE PAPER

23rd International Congress on Applications of Lasers & Electro-Optics

2004

Presented October 2004

UTILISING LASER FORMING AS A NOVEL WAY OF FORMING DUAL PHASE STEEL FOR AUTOMOTIVE COMPONENTS

Annelize Els-Botes[1], Patrick J McGrath[2]

[1] Manufacturing Technology Research Centre, Faculty of Engineering, Port Elizabeth Technikon, Port Elizabeth, 6000, South Africa
[2] Faculty of Engineering, Tshwane University of Technology, Pretoria, 0001, South Africa

Abstract

Dual phase steel is commonly used in the manufacture of automotive components. The component under consideration for this paper is the centre disc of a pressed wheel. It has been proved by previous research that the reduction in fatigue life of samples machined from the various production stages of the pressed wheel, is as great as 83%. The maximum reduction occurred during the first production stage (production of a bulge shape). This paper covers experimental work on two dimensional samples shaped by various laser parameters to similar radii of curvature as those produced by the first draw production stage of the mechanical forming operation. A CO_2 Trumpf laser system was used for the production of laser formed specimens. The heat generated during the laser forming process affected the dual phase (ferrite and $\pm$ 25% islands of martensite) microstructure at the surface being irradiated. Laser powers as high as 5kW was employed in the production of two dimensional samples. Fatigue testing revealed that there is a wide range of results obtained from the samples formed to the same radius of curvature and then tested by the bend fatigue test. This paper will give a brief outline of the effect of laser parameters (laser power, laser scanning velocity, and number of laser scans, beam diameter and interval spacing) on the bend and fatigue characteristics of automotive dual phase steel.

Introduction

Fatigue properties of materials have become progressively more prevalent as technology has developed a greater amount of machinery that is subjected to repeated loading and vibration (e.g. automobiles). It is expected that laser forming will have a lesser effect on the reduction on fatigue strength of dual phase steel compared to the mechanical stretch forming operations currently used to manufacture automotive wheel rims. During conventional forming operations, microvoids are formed between the hard (martensite) and soft (ferrite) phases in dual phase steel. These microvoids leads to a decrease in fatigue strength of the material since these microvoids can be considered as 'microcracks' already existing in the material. It is envisaged that the heat absorbed by the material during laser forming will influence the microstructure and hence the fatigue performance, but to a lesser degree than conventional stretch forming since no microvoids will be generated within the microstructure.

Material Characteristics

Dual phase steel can be produced directly from the rolling mill by the use of a thermo-mechanical treatment (TMT) well suited to the alloy composition [1]. The finishing temperature of the rolling process must be close to the upper critical temperature to maximize the acceleration effect that the hot deformation has on the ferrite reaction and avoiding simultaneously the intercritical rolling that can result in the formation of work hardened ferrite that is detrimental to the cold formability of the steel. The coiling temperature is another important factor, and must be kept below 600°C in order to avoid the formation of pearlite which suppresses the continuous yielding of the metal during tensile testing and lowers its work hardening rate. Amongst the various hardening mechanisms of steels the distribution of a hard second phase in the ferritic matrix is one of the best methods to optimize the strength/ductility ratio [2]. To achieve weight reductions and fuel saving in automobiles, designers have concentrated on dual phase steels (DPS) containing ferrite and martensite phases. It has been documented that the volume fraction and shape of grains in

dual phase steels strongly influences the material's stress-strain behaviour [3]. The ferrite-martensite structure is obtained by heating the steel to approximately 800°C, which is in the austenite-ferrite region, and quenching it back to room temperature. The structure that is quenched contains ferrite and austenite that is enriched in carbon. The exceptional properties of dual phase steel are, a low yield strength and a high work hardening rate. The importance of a high work hardening rate is that the strength of the steel increases rapidly as it is deformed. A high work hardening rate is considered to be typical of a mixed microstructure consisting of a hard phase in a soft matrix [4]. It has been found that dual phase steels frequently contain, in addition to ferrite and martensite, between two and nine percent of retained austenite. These particles of retained austenite increase the work hardening rate during the first several percent strain during a tensile test. This is due to strain-induced transformation of the retained austenite into martensite [5].

Chemical Composition

The chemical composition of the dual phase steel used in this study is shown in table 1.

Table 1: Chemical composition of dual phase steel (DPS)

% Carbon	0,09	% Copper	0,025
% Silicon	0,22	% Tin	0,004
% Manganese	0,90	% Vanadium	0,001
% Sulphur	0,04	% Aluminium	0,04
% Chromium	0,71	% Titanium	0,004
% Nickel	0,04	% Boron	0,0003
% Molybdenum	0,01	% Iron	96,696
% Phosphorus	0,04		

The main difference in chemical composition as compared to C2 steel (conventional steel used for manufacture of wheel rims) is given in table 2.

Table 2: Difference in main alloying elements between C2 and dual phase steel (DPS)

Alloying element	C2	DPS
% Silicon	0,03	0,22
%Phosphorus	0,015	0,04
% Chromium	0,05	0,71

The matrix microstructure of C2 consists of ferrite and pearlite compared to the ferrite and martensite matrix of dual phase steel. Elements such as nickel, aluminium, silicon and copper are all found largely dissolved in ferrite [6]. The carbide forming tendencies of some of these elements are only apparent when there is a significant amount of carbon present. Any element dissolved in ferrite increases its hardness and strength due to solid solution strengthening. The strengthening effect of the dissolved elements contributes relatively little to the overall strength of the steel [4].

The change in critical temperature produced by the presence of alloying elements is important in the heat treatment of alloy steels, since it will either raise or lower the hardening temperature as compared to plain-carbon steel. All alloying elements tend to reduce the carbon content of the eutectoid, but only nickel and manganese reduce the eutectoid temperature.

Mechanical Properties

The mechanical properties, as determined by the tensile test, are given in table 3.

Table 3: Mechanical properties of dual phase steel

0,2% Proof Stress	341,3MPa
Tensile Strength	577,8 MPa
Modulus of Elasticity	198,7GPa
% Elongation	23,8
% Reduction of Cross-sectional Area	52,5

The average hardness of the material in the as-received condition (rolled sheet) was found to be approximately $HV_{0,5}$ 157. From table 3 it is clear that the material has a high ductility, based on percentage elongation and percentage reduction in cross-sectional area.

Experimental Setup

Dual phase steel samples of dimensions 50x200x3,5 mm were irradiated with a laser beam with various powers, scanning velocities and beam diameters. The specimens were graphite coated to maximize absorptivity of laser energy. The energy distribution of the laser beam (beam's mode) was kept constant as a donut shape during all trials. A non-dimensional sketch of the beam profile is illustrated in figure 1.
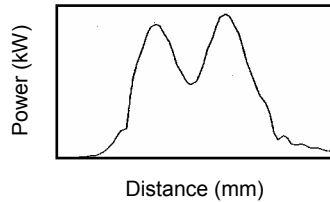
Figure 1: Non-dimensional beam profile

A 5kW Trumpf continuous wave CO_2 laser system was used for the forming of the dual phase steel samples. Gas flow through the laser head was 10l/min and the gas was Argon. The Trumpf laser system used for the experiments is shown in figure 2. The unit is classified as a Class 1 laser system and has a maximum output power of 5kW.
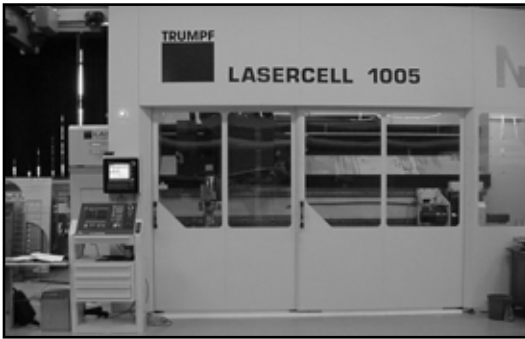

Figure 2: Trumpf laser system

Actual bend height (i.e. the change in height due to bending) was measured after various scanning intervals. The specimens to be irradiated were clamped at one end in a clamping device and radiation was started from the free end of the specimen. The experimental setup is shown in figure 3.
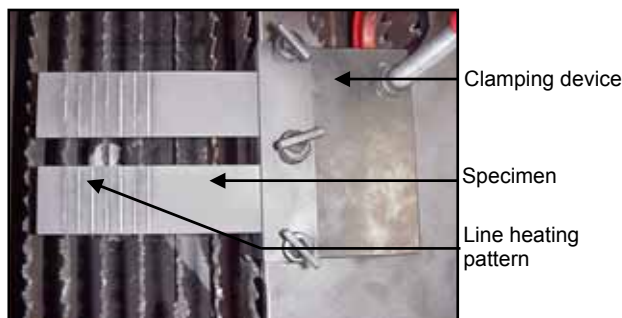

Figure 3: Experimental setup

Typical bend specimens formed during laser line heating are shown in figure 4. Measurements were taken from the free end as indicated in figure 4.
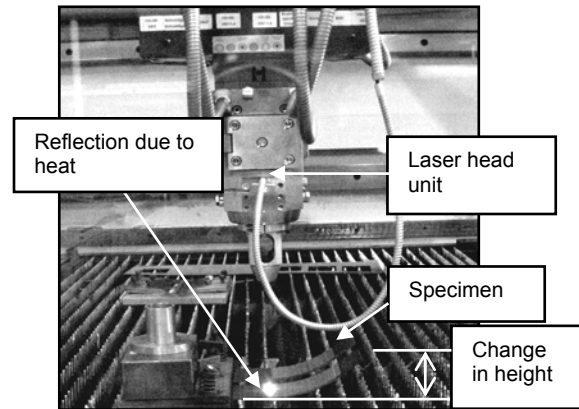

Figure 4: Typical bend specimens during laser line heating

Results and Discussion

Dimensional Analysis

Table 4 shows the various experimental settings investigated. Only those settings that yielded significant results were investigated further (e.g. microstructure analysis and microhardness profiling). Details of deformation: More than 0,6 mm change in bend height = Significant. The number of scans for all experiments was fifteen scans per line.

Table 4: Experimental parameters

kW	Beam $\varnothing$ (mm)	Velocity (m/min)	Scans	Interval (mm)
4	15	5	20	7,5
3	10	5	20	10
4	15	5	20	15
4	15	5	20	7,5
5	30	2,5	20	10
5	20	2,5	20	10
1,5	7,5	1,2	20	7,5
3,1	14	2	20	10,5

Figure 5 graphically shows the increase in actual bend height versus distance from the free end of the various specimens tested. The values indicated by arrows on figure 5, are the line energies associated with the various test parameters used. Line energy is the quotient of laser power (W) and scanning velocity (m/min), and the resultant unit is J/m. At first glance there does not seem to be any correlation between line energy and bend characteristics. For the same line energy with different laser powers and scanning velocities, there is a difference in the bending characteristics of the specimen. Therefore, even if the line energy is

kept constant, there does not seem to be a constant corresponding bend angle.
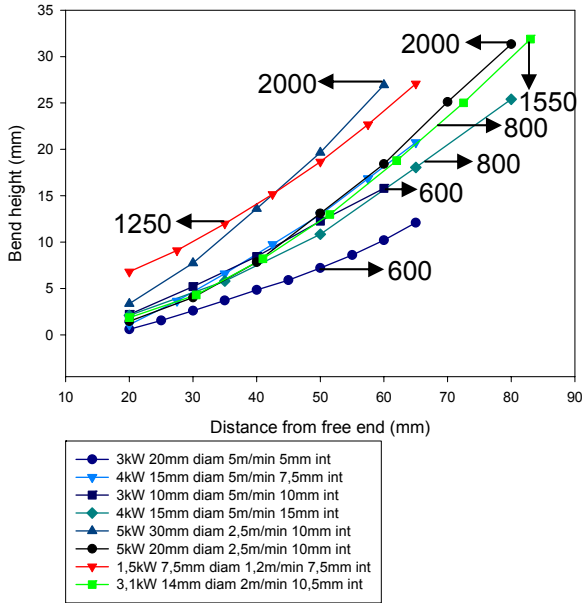

Figure 5: Comparison after 15 scans/line for various settings

On further investigation, it became apparent that the interval spacing between scanning lines or percent overlap by consecutive heating lines is a very important consideration. Figure 6 (a) and (b) shows the comparison of two settings with various interval spacing (percent overlap).
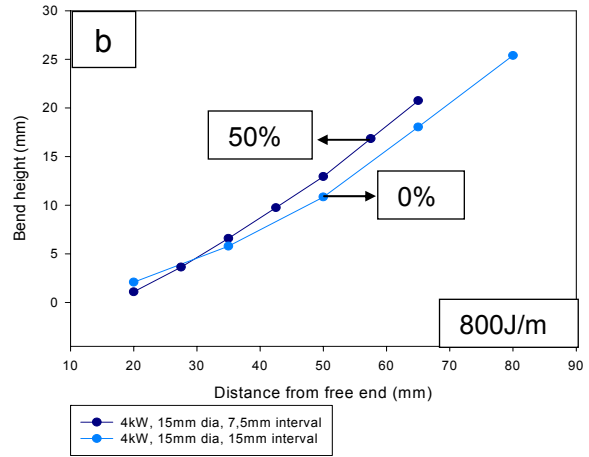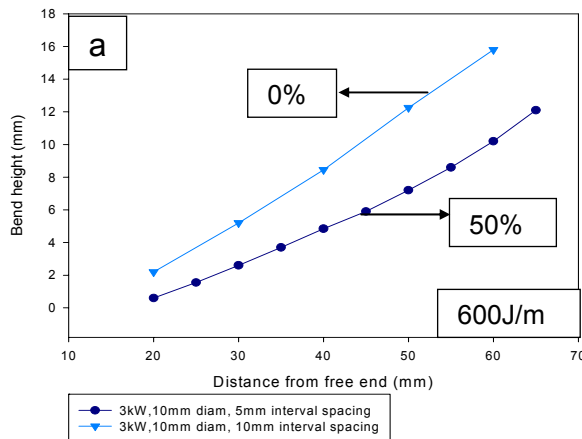

Figure 6 (a) and (b): Effect of percentage overlap between scan lines and bend characteristics

For lower line energies like those indicated in figure 6(a), the temperature gradient mechanism (TGM) seems to play the major role in the deformation experienced by the specimen. The deformation mechanisms experienced by these specimens are a combination of the temperature gradient mechanism and the buckling mechanism (BM). At higher line energies like those indicated in figure 6(b), the buckling mechanism is the foremost deformation mechanism with the temperature gradient mechanism only contributing a small part of the total deformation. Therefore, at lower line energies, as the percentage overlap increase, the specimen is heated to a great extent and thereby destroys the temperature gradient through the thickness of the sheet specimen. The buckling mechanism does not contribute a great deal either, since the temperature reached by the specimen is not sufficient to ensure a plasticized zone (yielded zone) of adequate size. The increase in temperature did not lower the flow stress of the material enough so that plastic deformation can take place with ease. As the line energy increase, the main deformation mechanism changes to the buckling mechanism. The temperature reached by the specimen penetrates through the thickness of the plate and generates a plastic zone of adequate width (w) and depth (d). Yielded widths and depths smaller than the sheet thickness is unlikely to create noticeable distortions when heat flow is two dimensional [7].

$$\theta_{Bending} = \frac{\alpha(T - T_o)wd}{2D^3}(3\pi D - 8d) \qquad (1)$$

Equation 1 shows that bend angle increase (based on w and d) with an increase in plasticized zone (yielded zone) when the buckling mechanism is the main contributor to deformation. There is an optimum plastic zone width to plastic zone depth ratio (w:d), exceeding this ratio will not lead to an increased bend angle as the limiting element for plastic zone depth is the material thickness. Percentage overlap does not cause an increase in the ratio of plastic zone width to plastic zone depth (w:d) and therefore it can be concluded that the only reason that there is a better response in terms of bend height is that the radius of curvature for the higher percentage overlap specimens is smaller (i.e. tighter bend).
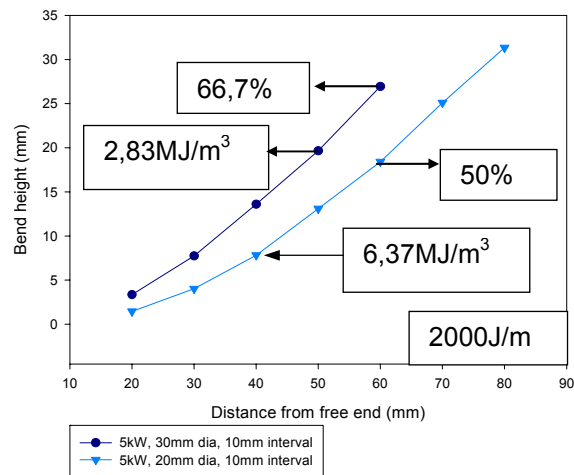

Figure 7: Constant laser power but different laser beam spot size, and percentage overlap

There seems to be a correlation between figure 6(b) and figure 7. An increase in percentage overlap for constant line energy, increased the bending response of the specimen. On the other hand, if one looks at the volumetric energy density of the two specimens in figure 7, the two specimens are not similar, since the one employs a 20mm beam diameter and the other a 30mm beam diameter. If volumetric energy distribution is measured in J/m^3, the 20mm beam diameter sample is exposed to a higher value than the 30mm beam diameter sample since the power settings are the same. Specimens for evaluation were reproduced according to the settings shown in table 5 based on findings on preliminary testing. These settings were found to produce specimens with approximately the same radius of curvature (approximately 130mm).

Table 5: Settings to produce specimens of similar geometry

kW	Beam ∅ mm	% Overlap	Velocity m/min	Energy J/m
5	20	50	2,5	2000
3,1	14	25	2	1550
1,5	7,5	0	1,2	1250

From figure 8 it can be seen that the graph lines are very close to each other. It can thus be concluded that when graphs follow the same path on the bend height vs. distance from free end plot, the geometrical shape will be similar if all other variables (ambient temperature, etc.) are kept constant.
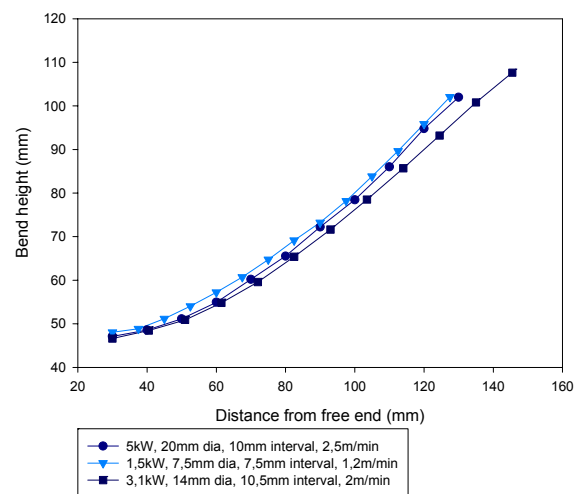

Figure 8: Graphical representation of specimens produced with settings in table 5

Mathematical solution to the graphs in figure 8 yielded the following equations, all with an R^2 = 0,99. The specimens will be identified by the lasers powers as indicated in table 5.

5kW: $\qquad\qquad y = 34,8e^{0,0082x}$ $\qquad$ (2)

3,1kW: $\qquad\qquad y = 35,1e^{0,0077x}$ $\qquad$ (3)

1,5kW: $\qquad\qquad y = 35,9e^{0,0081x}$ $\qquad$ (4)

In above equations 2, 3, and 4, y represents bend height (mm) and x represents the distance

from the free end (mm). It is clear that all the curves follow the same trend and are similar to the formula used to characterize the flow curve area of the stress-strain curve of a tensile test. The flow curve equation is given below:

$$\sigma_{true} = K\varepsilon^n \qquad (5)$$

Where n = strain hardening exponent
Equation 5 is frequently used in calculations with regard to plastic deformation in the plastic regime of the stress-strain curve. Equations 2, 3 and 4 can be combined to form a generalised equation valid only for dual phase steel between line energies of 1250J/m and 2000J/m. Combined equation:

$$y = 35,3e^{0,008x} \qquad (6)$$

The constants 35, 3 and 0,008 are only valid for dual phase steel and settings as given in table 5. The influence of number of laser scans per line on the resulting bend height was also investigated and typical results are shown in figure 9(a) and (b). It is clear from figure 9 that for all the consecutive laser lines with a line energy of 600J/m, the most deformation was observed during the first five scans of the scanning cycle of 15 scans per line. Continuing to laser scan the same position more than five scans will not result in a significant increase in bend height and hence bend angle. There is also a better consistency in results for the specimens with zero percent overlap than those produced by employing a 50 percent overlap (see figure 9b).
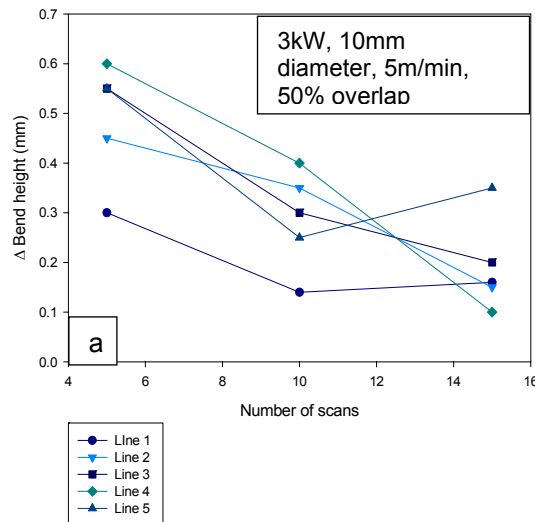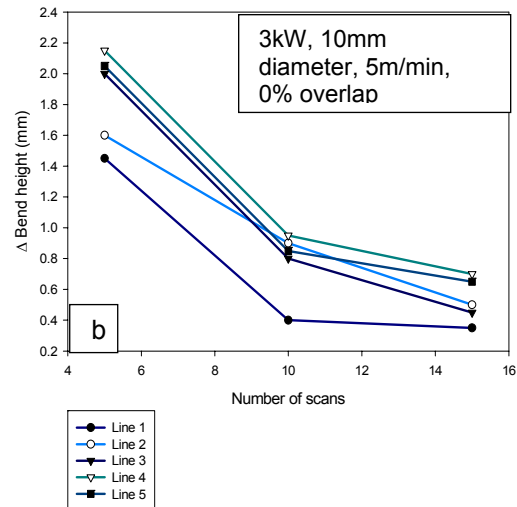
Figure 9 (b): Influence of number of laser scans on bend characteristics

Figure 10(a) and (b) also indicates that the specimen experiences the most deformation during the first five laser scans. The specimens were irradiated with a line energy of 800J/m and it is now clear that the specimens that were irradiated with a zero percent overlap behaved differently to those who employed a 50 percent overlap. The zero percent overlap samples shows that there is less of a difference between the first five scans and the second five scans, except for the very last scanning line. The difference in change of bend height is more drastic for the specimens where the laser line pattern did not employ any overlap between scanning lines.

Figure 9(a): Influence of number of laser scans on bend characteristics
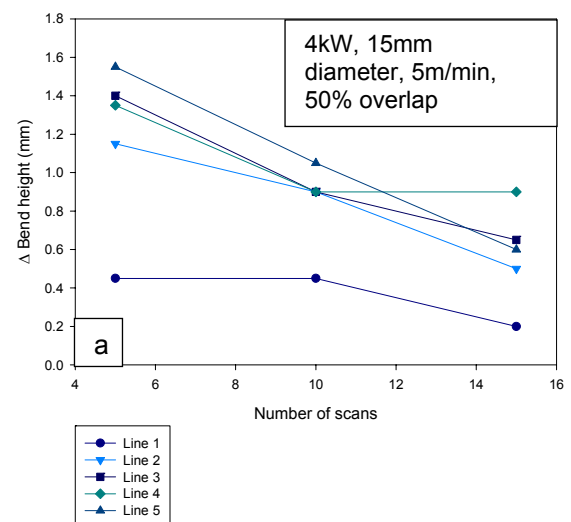
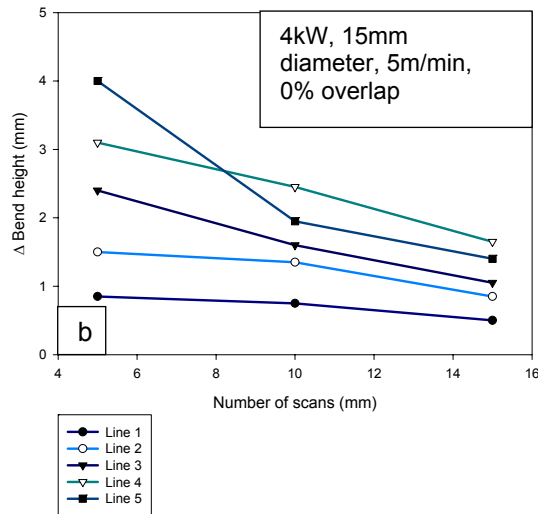Figure 10 (a): Influence of number of laser scans on bend characteristics

Figure 10 (b): Influence of number of laser scans on bend characteristics

The change in total bend height between each set of five laser scans shows that the increase in bend height is approximately linear in nature. This trend is graphically illustrated in figure 11, which shows the difference in total bend height vs. number of scans per line.
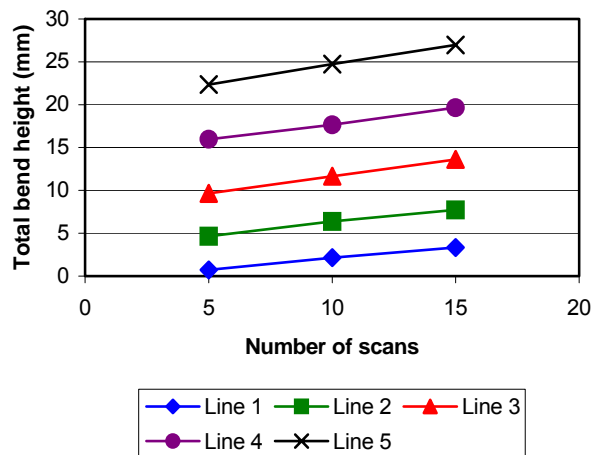

Figure 11: Graphical representations of difference in total bend height vs. number of scans per line (5kW, 30mm beam diameter, 2,5m/min, 10mm interval spacing)

The bend height increases more rapidly with an increase in number of line heating cycles the sample has already experienced. The lines shown on figure 11 are all linear in nature and approximately parallel to each other. The distance between the lines is an indication that deformation is taking place more rapidly with time or number of line scans.

Microhardness Analysis

Analysis the microhardness values through the thickness of the specimens deformed by laser line heating yielded results as illustrated in figure 12. Vickers microhardness measurements were done using a 500g load.
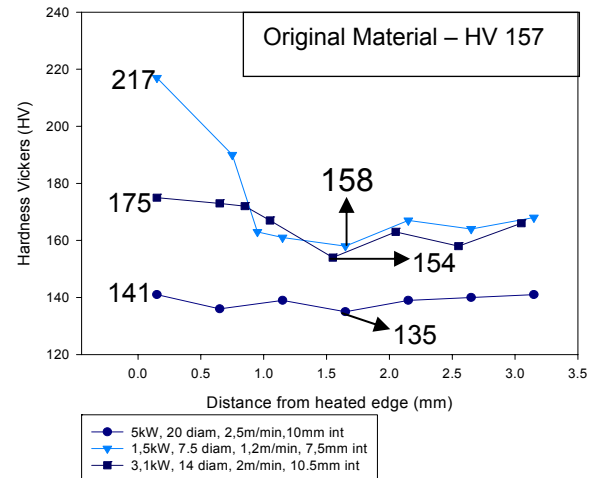

Figure 12: Microhardness analysis of laser formed specimens

It is clear from figure 12 that the most dramatic change in hardness can be seen on the specimen irradiated with the 1,5kW laser power. The magnitude of difference between the various maximum and minimum readings for the various laser parameters used is shown below:

5kW: 6 HV units
3,1kW: 21 HV units
1,5kW: 59 HV units

Preliminary Fatigue Results

The deformed plate were then set up and laser cut into the shape (hour-glass) of the fatigue specimen. The specimen appearance after the laser cutting operation is shown in figure 13. The melted edge was removed during the final machining operation on the CNC milling machine. After final machining, the specimen surfaces were cleaned using a flapper wheel with a120 grit roughness. Run-out was taken to be 2×10^6 cycles, as it was shown by previous research that laboratory specimens showed a direct relationship to fatigue values obtained by testing a complete wheel rim.
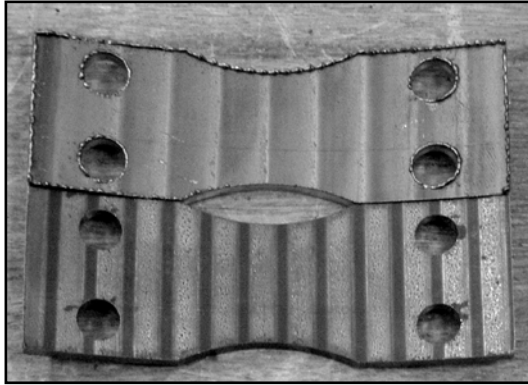
Figure 13: Specimen appearance after laser cutting from plate specimens

A non-dimensional graphical presentation of the preliminary fatigue results are shown in figure 14. The general trends of the curves seem to be similar, except for the laser formed (LF) specimens with a 5kW laser power and 20mm beam diameter. The original flat plate material still exhibited the best properties.
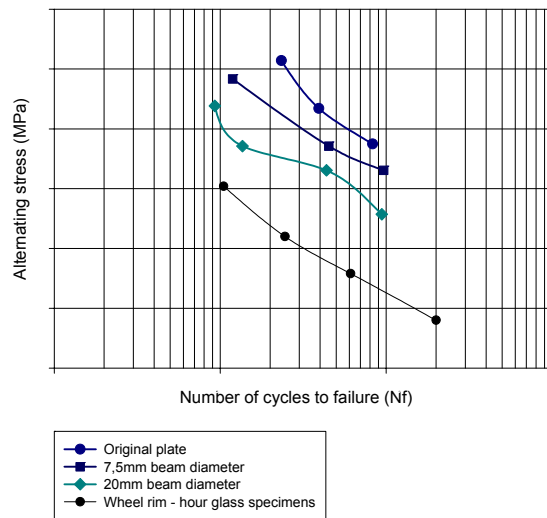

Figure 14: Graphical representation of preliminary fatigue results

Conclusion

From this preliminary work it is evident that it will be possible to produce specimens of similar geometrical shapes using various laser parameters. The optimum set of parameters will be determined by the mechanical properties of the resultant specimens produced by the various settings. Ideally the properties of such specimens should be similar or even better than the original material's properties. Changes in the microstructure due to the heat are inevitable,

but if these changes are more detrimental to the materials properties than the changes occurring during conventional forming the process will have to be re-analysed. It is assumed that any set of parameters between 5kW and 1,5kW and line energies of 2000J/m and 1250J/m will yield similar results. The above two settings are the two outer limits within which laser forming of dual phase steel can be conducted without difficulty.

From the results obtained it is clear that the laser forming process has potential to be employed as a production stage in the manufacture of wheel centre discs. Large beam diameters which cause heat penetration through the thickness of the specimen and hence microstructure breakdown should be avoided, since it was shown that these specimens exhibited worse fatigue properties than those produced with a smaller laser beam diameter. The CO_2 laser system needs to be controlled more accurately as inconsistencies influence the final radius of curvature of the specimen. If the CO_2 laser system can not be better controlled, this laser system can not be recommended for forming processes which require close tolerances. It is suggested that peak temperature reached by the specimen be used as a control measure for the CO_2 laser system and not only laser parameters. This means that the system should be able to vary laser head velocity and laser beam diameter to ensure constant peak temperature of the specimen.

References

1. Gorni, AG; Vieira, RR. 1996. *The effect of finishing temperature and cooling rate on the microstructure and mechanical properties of an as-hot-rolled dual-phase steel.* http://www.geocities.com/agorni/dpabst.html
2. Bouaziz, O, et al. 2001. *Physical modeling of microstructure and mechanical properties of dual-phase steel.* Journal De Physique. September 2001. EDP Sciences: Les Ulis Cedexa
3. Huper, T, et al. 1999. *Effect of volume fraction of constituent phases on the stress-strain relationship of dual phase steels.* ISIJ International: Tokyo
4. Avner, SH. 1974. *Introduction to physical metallurgy.* 2nd ed. McGraw-Hill: Singapore. pp 350-355

5. Reed-Hill, RE and Abbaschian, R. 1994. *Physical metallurgy principles*. 3rd ed. PWS: USA. pp 674-685

6. Chan, KC, et al. 2000. *Laser bending of thin stainless steel sheets*. Journal of laser applications. Laser Institute of America. pp34-40

7. Marya, M and Edwards, GR. *Factors affecting the laser bending of Ti-6Al-2Sn-4Zr-2Mo.* Journal of Laser applications.